UNIVERSITY OF CALIFORNIA, SAN DIEGO

Tolerance of Metal-Organic Frameworks to Functionalization

A Dissertation submitted in partial satisfaction of the requirements for the degree

Doctor of Philosophy

in

Chemistry

by

Corinne An-Li Allen

Committee in Charge:

Professor Seth Cohen, Chair
Professor Pieter Dorrestein
Professor Brian Maple
Professor Tadeusz Molinski
Professor Charles Perrin
Professor Arnold Rheingold

2014

The Dissertation of Corinne An-Li Allen is approved, and it is acceptable in quality and form for publication on microfilm and electronically:

Chair

University of California, San Diego

2014

DEDICATION

To those who make my world go ‘round, thank you.

TABLE OF CONTENTS

LIST OF SYMBOLS AND ABBREVIATIONS

Å	Ångström, 10^{-10} m
bdc	1,4 – benzene dicarboxylic acid
BET	Brunauer-Emmett Teller
Bn	Benzyl
Boc	*tert*-butyloxycarbonyl
btb	4,4',4''-benzene-1,3,5-triyl-tribenzoic acid
°C	Degree Celsius
°	Degree
δ	Chemical Shift (ppm)
d	Doublet (NMR Splitting)
DEF	Diethylformamide
DMF	Dimethylformamide
DMPA	2,2-Dimethoxy-2-phenylacetophenone
ESI-MS	Electrospray Ionization Mass Spectrometry
Et	Ethyl
F_o	Observed Electron Density
F_c	Calculated Electron Density
g	Gram
G.O.F.	Goodness of Fit
h	Hour
HCl	Hydrochloric Acid
Hex	*n*-Hexane
HK	Horvath-Kawazoe
iPr	Isopropyl

IRMOF	Isoreticular Metal-Organic Framework
K	Kelvin
M	Molar (mol/L)
m	*meta*
m	Multiplet (NMR Splitting)
MD	Molecular Dynamics
MIL	Material Institute Lavoisier
mL	Mililiter
mmol	Millimoles
MOF	Metal-Organic Framework
MOP	Metal-Organic Polyhedra
MW	Molecular Weight (g/mol)
nm	Nanometer
NMR	Nuclear Magnetic Resonance
o	Ortho
OAc	Acetate
p	Para
P	Powder
ppm	Parts per Million
PSD	Postsynthetic Deprotection
PSM	Postsynthetic Modification
q	Quartet (NMR Splitting)
RT	Room Temperature
s	Second
s	Singlet (NMR Splitting)

SBU	Secondary Building Unit
SEM	Scanning Electron Microscopy
SCSC	Single Crystal to Single Crystal
t	Triplet (NMR Splitting)
θ	Theta
THF	Tetrahydrofuran
TGA	Thermogravimetric Analysis
TMS	Trimethylsilyl
UiO	University of Oslo
UMCM	University of Michigan Crystalline Material
UV	Ultraviolet
Vis	Visible
XRD	X-ray Diffraction

LIST OF FIGURES

LIST OF SCHEMES

LIST OF TABLES

ACKNOWLEDGEMENTS

I would like to first thank my grandmother for reminding me not to drink more than five cups of coffee a day and that a Ph.D. is about the approach, not the answer. Also, for the eight AM weekly phone calls reminding me of such that always ended with 'don't worry, be happy.' Secondly, my parents, who encouraged me to find what I enjoy doing and to follow that path wherever it may go. Again, also for the reminder that your writing ability has nothing to do with completion of a dissertation. Yes, I will leave that as a fragment, thank you word processor.

I would also like to thank my advisor, Prof. Seth M. Cohen, who always had my best interests in mind and pushed me to let the water roll off the feathers.

Completion of this dissertation, and Ph.D. program, is nothing if not a team effort. And don't it always seem to go that you don't know what you got 'til it's gone? I'm feeling nostalgic, so here we go, from Jess to Johny, I have learned so much from every person who has walked through our lab door. I cannot express my gratitude in enough ways but I shall immortalize a few of you. Min, TCrizzle, Piper, Matthieu, Arpeetz, Serg, Dav-id, KDizzle, Gabry, PVD, MSD (SS), C5, DP, and Jess, thank you for your never-ending support in literally every context possible. I have been lucky to be surrounded by your level of talent and intellect but most importantly your compassion for my skewed perspective of this whole ordeal.

Min. What on earth would I be doing right now if it were not for you? Thank you for being the calming force within my life. Meeting you was one of the best parts of being here.

And to my dearest Dr. David C. Stone, in lieu of a crude homage to my musical idol, you were my physical rock who kept me in the playing field that is this

reality. As in you took me climbing when the experiments failed, brought me down, and kept kicking.

Texts, schemes, and figures in Chapter 2 are, in part, reprints of the material in the following publications as listed: Tanabe, K. K.; Allen, C. A..; Cohen, S. M. Photochemical Activation of a Metal-Organic Framework to Reveal Functionality *Angew. Chem. Int. Ed.* **2010**, *49*, 9730-9733. Allen, C. A..; Cohen, S. M. Near-UV Photo-Induced Modification in Isoreticular Metal-Organic Frameworks *J. Mater. Chem.* **2012**, *22*, 10188-10194.

Texts, schemes, and figures in Chapter 3 are, in part, reprints of the material in the following publications as listed: Chao, C.; Allen, C. A..; Cohen, S. M. Tandem Postsynthetic Modification of Metal-Organic Frameworks Using an Inverse-Electron-Demand Diels-Alder Reaction *Inorg. Chem.* **2011**, *50*, 10534-10536.

Texts, schemes, and figures in Chapter 4 are, in part, reprints of the material in the following publications as listed: Allen, C. A..; Boissonnault, J. A.; Cirera, J.; Paesani, F.; Gulland, R.; Cohen, S. M. Chemically Crosslinked Metal-Organic Frameworks *Chem. Commun.* **2013**, *49*, 3200-3202. Allen, C. A..; Cohen, S. M. Exploration of Chemically Crosslinked Metal-Organic Frameworks *Inorg. Chem.* **2014**, *53* (13), 7014-7019.

The dissertation author was the primary researcher and author on all but one publication listed above. The co-authors listed also contributed to the research. Permission to reproduce these publications was granted by John Wiley and Sons, Inc., copyright 2010, American Chemical Society, copyright 2014 and 2011, and The Royal Society of Chemistry, copyright 2013 and 2012.

Th- th- that's all folks.

VITA

EDUCATION

University of California, San Diego 2014
Ph.D., Chemistry
Advisor: Prof. Seth M. Cohen

University of California, San Diego 2011
M.S., Chemistry
Advisor: Prof. Seth M. Cohen

University of Oregon 2009
B.S., with Honors, Chemistry

AWARDS AND PROFFESSIONAL AFFILIATIONS

Nation Science Foundation Graduate Research Fellow 2011 – 2014

Association for Women in Science - Member 2012 – present

American Chemical Society - Member 2009 – present

National Science Foundation Alliance for Graduate Education and the Professoriate Fellow 2009 - 2010

Teaching Assistant 2009 - 2010
University of California, San Diego

Recipient of Clarence and Lucille Dunbar Scholarship 2009
University of Oregon

Recipient of Sara J. Staggs Undergraduate Transition Award 2009
University of Oregon

Peer Learning Assistant 2008 - 2009
University of Oregon

Research Assistant 2007 - 2009
University of Oregon
Advisor: Prof. Darren W. Johnson

Recipient of Non-resident Dean's Scholarship 2005 - 2009
University of Oregon

PRESENTATIONS

1.) "Tolerance of Metal-Organic Frameworks for Functionalization." C. A. Allen and S. M. Cohen. Seminar at University of California, San Diego. May 30, 2014. (Lecture)

2.) "Series of Chemically Cross-Linked Isoreticular Metal-Organic Frameworks." C. A. Allen, J. B. Cirera, F. Paesani and S. M. Cohen. 245th ACS National Meeting in New Orleans, LA. April 11, 2013. (Lecture)

3.) "Combining Orthogonal Postsynthetic Methods in a Single Isoreticular Metal-Organic Framework." C. A. Allen and S. M. Cohen. 243th ACS National Meeting in San Diego, CA. March 25, 2012. (Poster)

4.) "Postsynthetic Deprotection: Light-Revealed Functionality in Metal-Organic Frameworks." C. A. Allen, K. K. Tanabe and S. M. Cohen. 241st ACS National Meeting in Anaheim, CA. March 27, 2011. (Poster)

5.) "Self-Assembled Supramolecular Pnictogen Containing Macromolecules." C. A. Allen, V. M. Cangelosi and D. W. Johnson. ACS Summer School on Green Chemistry and Sustainable Energy in Golden, CO. July 27, 2009. (Poster)

6.) "Self-Assembled As(III)-Thiolate Macromolecules." C. A. Allen, V. M. Cangelosi and D. W. Johnson. Dalton Discussion 11 in Berkeley, CA. June 23, 2008. (Poster)

7.) "Supramolecular Arsenic Coordination Chemistry; Strategy and Execution." C. A. Allen, V. M. Cangelosi and D. W. Johnson. Pacific Northwest Undergraduate Symposium on Organic Chemistry in Corvallis, OR. August 11, 2008. (Lecture)

PUBLICATIONS

1.) Allen, C. A. and Cohen, S. M., "Exploration of Chemically Crosslinked Metal-Organic Frameworks" *Inorg. Chem.* **2014**, *53*, 7014-7019, DOI: 10.1021/IC500951B

2.) Allen, C. A., Boissonnault, J. A., Cirera, J., Gulland, R., Paesani, F., Cohen, S. M., "Chemically Crosslinked Metal-Organic Frameworks" *Chem. Commun.*, **2013**, *49*, 3200-3202, DOI: 10.1039/C3CC40635K

3.) Kim, M., Boissonnault, J. B., Allen, C. A., Dau, P., Cohen, S. M., "Functional Tolerance in an Isoreticular Series of Highly Porous Metal-Organic Frameworks" *Dalton Trans.*, **2012**, *41*, 6277-6282, DOI: 10.1039/C2DT30120B

4.) Allen, C. A., Cohen, S. M., "Near-UV Photo-Induced Modification in Isoreticular Metal-Organic Frameworks" *J. Mater. Chem.*, **2012**, *22*, 10188-10194, DOI: 10.1039/C2JM15183A

5.) Chao, C., Allen, C. A., Cohen, S. M., "Tandem Postsynthetic Modification of Metal-Organic Frameworks Using an Inverse-Electron-Demand Diels-Alder Reaction" *Inorg. Chem.*, **2011**, *50*, 10534-10536, DOI: 10.1021/ic2017598

6.) Tanabe, K. K.†, Allen, C. A.†, Cohen, S. M., "Photochemical Activation of a Metal-Organic Framework to Reveal Functionality" *Angew. Chem. Int. Ed.*, **2010**, *49*, 9730-9733, DOI: 10.1002/anie.201004736 †Equal Contributors

7.) Cangelosi, V. M., Pitt, M. A., Vickaryous, W. J., Allen, C. A., Zakharov, L. N., Johnson, D. W., "Design Considerations For the Group 15 Elements: The Pnictogen-π Interaction as a Complementary Component in Supramolecular Assembly Design" *Cryst. Growth Des.*, **2010**, *10*, 3531-3536, DOI: 10.1021/cg100444n

8.) Allen, C. A., Cangelosi, V. M., Zakharov, L. N., Johnson, D. W., "Supramolecular Organization Using Multiple Secondary Bonding Interactions" *Cryst. Growth Des.*, **2009**, 9, 3011-3013, DOI: 10.1021/cg900395w

ABSTRACT OF THE DISSERTATION

Tolerance of Metal-Organic Frameworks to Functionalization

by

Corinne An-Li Allen

Doctor of Philosophy in Chemistry

University of California, San Diego, 2014

Professor Seth Cohen, Chair

Metal-Organic Frameworks (MOFs) are porous coordination polymers with the potential to excel in catalysis and gas storage/separation. This dissertation will first discuss relevant types of MOFs, their characteristics, and previous functionalization methods. To fully gauge the utility of MOFs, novel materials with tunable properties are required as are appropriate design strategies to create these materials.

Of specific interest is MOFs embedded with secondary metal binding groups. Chapter 2 will discuss a mild method to incorporate these functional groups into

MOFs. The utilization of photocleavable protecting groups, a nitrobenzyl ether masking an aryl hydroxyl group, allows for the liberation of secondary metal binding sites upon photoirradiation. By combining mixed MOF systems with photochemical and chemical modification methods, multifunctional materials can be accessed from a single starting MOF.

Exploration of new postsynthetic modification reactions is explored in Chapter 3. Initial studies focused on a radical initiated photochemical-click reaction to modify a terminal alkene with a free thiol to create a thioether. Depending on the chemical stability and pore size of the MOF material, this reaction was moderately successful at best. Additionally, optimization proved to be difficult due to the number of chemical species present during the course of the reaction. A simpler click Diels-Alder cycloaddition was studied as an alternative route to modify a terminal alkene embedded inside the MOF. The cycloaddition was found to proceed only if there was sufficient space available within the MOF pores and around the alkene moiety.

Finally, in Chapter 4, chemically crosslinked organic ligands are studied to probe the tolerance of certain MOFs for geometrically restricted components. Extended oligomeric ligands based on these criteria are also discussed. Even using ligands with up to four organic struts tethered together, the canonical IRMOF structure can still be formed. This indicates that the limitations of coordination polymers are much less stringent than originally thought.

1. Introduction

1. I. Introduction

Metal-organic frameworks (MOFs) are porous 2D/3D materials comprised of metal ions or metal ion clusters linked together through bridging multitopic organic ligands. The overall topology of the MOF is based on two individual factors, the geometry of the metal cluster, known as the secondary building unit (SBU), and the geometry by which they are connected, dictated by the shape of the coordinating ligand(s). Judicious choice of each building block, metal source and organic ligand, can easily provide access to many different topologies giving MOFs a structural diversity beyond many other inorganic materials (Figure 1.1).

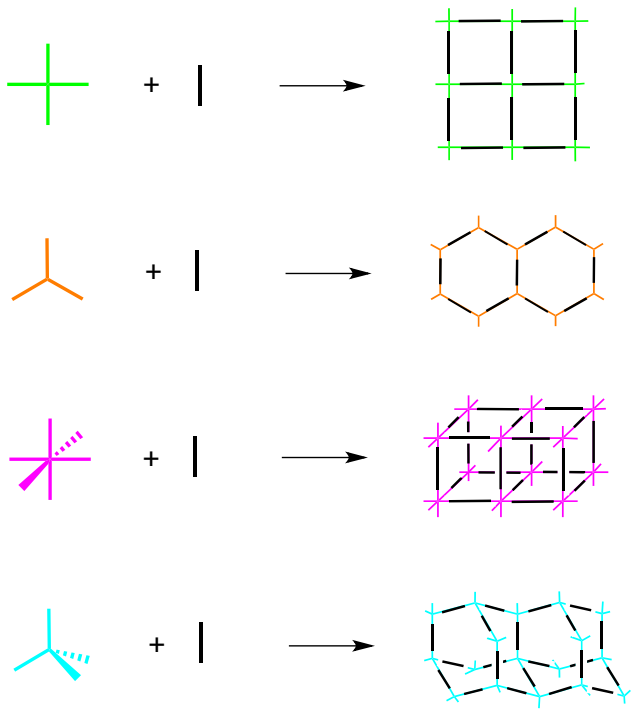

Figure 1.1. Cartoon representation of how different building blocks can lead to a variety of topologically distinct materials. In this illustration, the colored nodes represent the SBU and the rods represent a linear ditopic coordinating ligand.

MOFs are a specific type of coordination polymer that bridges organic polymers and zeolites. Organic polymers are generally known as being a soft and amorphous material whose properties can be tailored through the choice of starting monomer(s) and the reaction conditions.[1,2] On the other hand, zeolites are purely inorganic microporous aluminosilicates that are valued for their robust and porous nature. Zeolites are routinely used as commercial catalysts and adsorbents because of their rigid architectures and micropores.[3] MOFs can be considered a hybrid of these two materials depending on the initial components. Combining the predictable coordination geometry of various metals with various coordinating group(s) (i.e. carboxylate, pyridine, imidazole, phosphates, etc.)[4,5] can create rationally designed topologies. In turn, the organic linking portions can allow for additional modulation within the preset architectures. Taking the strengths of both materials, modularity, porosity, predictable coordination, and blending them into a highly crystalline and ordered coordination polymer is why MOFs are of keen interest for the applications discussed at the end of the chapter.

1. II. Types of MOFs

The most iconic MOF, known as MOF-5 or as isoreticular metal-organic framework (IRMOF)-1, is a coordination polymer derived from a single linear organic ligand and a single metal source. The metal nodes are actually Zn_4O clusters bridged by six 1,4-benzenedicarboxylic acid (bdc) molecules.[6] In particular, this SBU is identical to the structure obtained when subliming zinc acetate ($Zn_4O(OAc)_6$); a structure that has been known for decades.[7] To prepare the material, H_2bdc and $Zn(NO_3)_2 \cdot 4H_2O$ are dissolved in diethylformamide (DEF) and heated to 85-105 °C for 10-22 h, to give the product as single-crystalline clear blocks (Figure 1.2). Each zinc ion is tetrahedrally coordinated with a single bond to the central oxo ligand and the

remaining three sites are filled by the carboxylates of three bdc ligands. While the individual metal centers are tetrahedral, the overall cluster geometry is octahedral leading to the cubic topology. Single crystal X-ray diffraction (XRD) demonstrates the reticulation, the creation of a net or net like structure; of the Zn_4O tetrahedron SBUs by the benzene based ligands into a cubic structure (Figure 1.2, top right). The angle of the benzene rings creates two distinct pores, in a checkerboard pattern, within the material. Taking into account van der Waals radii, one has a window size of 15 Å and the other is 11 Å. The experimental Brunauer-Emmett-Teller (BET) surface area was found to be 3100 m^2g^{-1}, notably higher than the microporous zeolites.

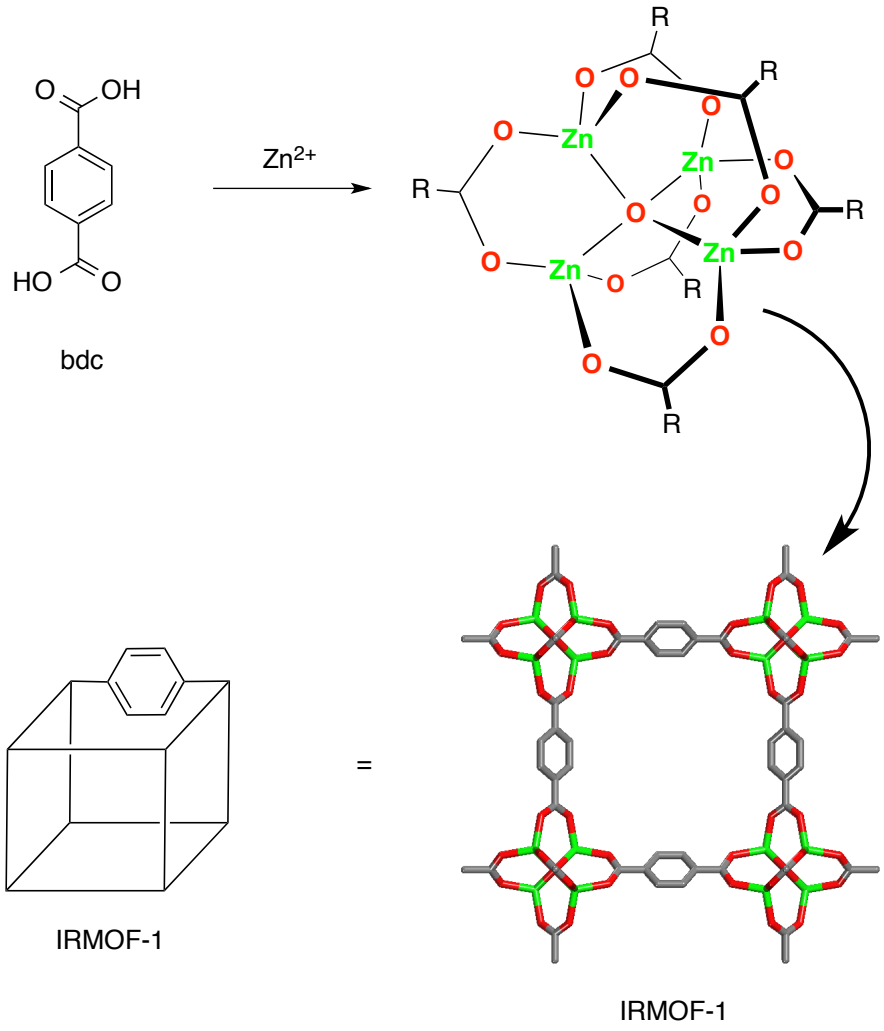

Figure 1.2. Synthesis of IRMOF-1 from H_2bdc and Zn (top). While each Zn atom is tetrahedrally coordinated, the overall shape is octahedral (based on the methyl groups) of the acetate ligands. The X-ray crystal structure verifies the cubic topology and shows the reticulation (bottom right). Carbon atoms are in grey, oxygen is in red, and zinc is in green. Hydrogen atoms are omitted for clarity. The nodes in the cartoon (bottom left) are indicative of the entire Zn_4O SBU.

An expansion of the zinc-carboxylate MOF is through the use of two geometrically distinct organic ligands. Using both components of IRMOF-1, the same Zn_4O SBU and bdc linker, in addition to a tritopic carboxylate based linker, H_3btb, a new copolymeric zinc-carboxylate MOF was obtained and designated University of

Michigan Crystalline Material (UMCM-1).[8] The copolymerization of both bdc and btb ligands, H_2bdc, H_3btb and $Zn(NO_3)_2 \bullet 4H_2O$ in DEF at 85 °C for 48 h, results in clear needle crystals. UMCM-1 consists of the same Zn_4O SBUs coordinated together by two bdc and four btb ligands creating an overall polyhedral framework (Figure 1.3). The use of two organic linkers manifests in two highly unique pores, one micro- (14 Å) and one mesopore (32 Å) (Figure 1.3, bottom left). The micropores come together in an edge-sharing method to create the larger mesopore. In general, mesoporous materials are more difficult to obtain due to pore instability upon removal of solvent molecules. In this case, the hexagonal mesopore is surrounded by the more structurally sound micropores, stabilizing the overall structure. These two pores are also identified through dinitrogen sorption at 77 K, which shows a distinct step at low pressures. This step is indicative of multiple pore sizes that are in agreement with the crystallographic data. The experimental BET surface area was found to be 4092 m^2g^{-1}. UMCM-1 is thus an example of how utilizing two organic ligands can result in topologically distinct MOFs with various pore structures.

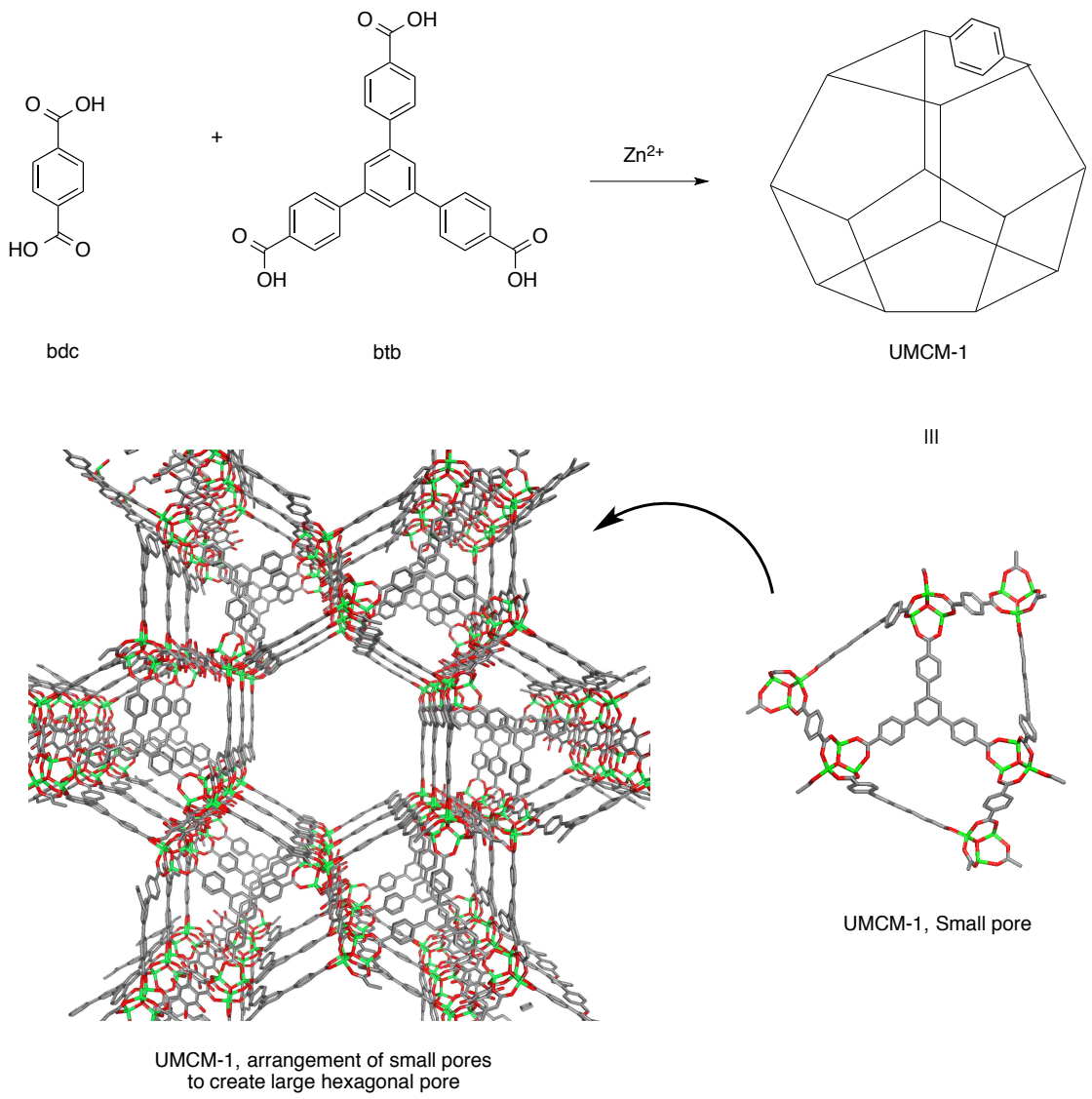

Figure 1.3. Schematic illustrating the synthesis of UMCM-1 using H_2bdc and H_3btb (top). The X-ray structure in comparison to the cartoon representation is also included starting with the micropore (bottom right) and showing how the micropores align to create the central mesopore (bottom left). The nodes in the cartoon are indicative of the entire Zn_4O SBU. Carbon atoms are in grey, oxygen is in red, and zinc is in green.

Zinc-carboxylate based MOFs are highly crystalline and have many benefits but they are easily susceptible to degradation by moisture and protic solvents. To create more chemically robust materials, MOFs comprised of stronger metal-

carboxylate bonds were sought. Utilizing trivalent metals, Materials Institut Lavoisier (MIL)-68 has been synthesized by heating H_2bdc in N,N-dimethylformamide (DMF) with vanadium, at 200 °C for 72 h to make MIL-68(V), gallium at 100 °C for 10 h for MIL-68(Ga), and indium at 100 °C for 48 h for MIL-68(In) as single crystalline materials in the shape of rods.[9,10] Two unique channels are formed in MIL-68. Similar to the UMCM system where smaller channels surround a larger channel, the edges of delimiting triangular channels create larger hexagonal channels (16 Å, Figure 1.4, bottom right). Instead of discrete metal nodes bridged by ligands, the MIL family of frameworks contains an infinite chain of octahedral SBUs, where SBUs are connected by a hydroxyl bridge and two carboxylates (Figure 1.4, top right). TGA analysis shows framework stability until ~400 °C which is higher than the Zn-carboxylate based MOFs suggesting a stronger coordination bond or that the inifinite SBU has additional stability over discrete metal nodes. Experimental Langmuir surface areas were 847, 1139, and 1410 m^2g^{-1} and BET surface areas were 603, 746, and 1117 m^2g^{-1} for MIL-68(V), (In), and (Ga) respectively. These diminished surface areas are expected for MIL-68 based on different pore structure.

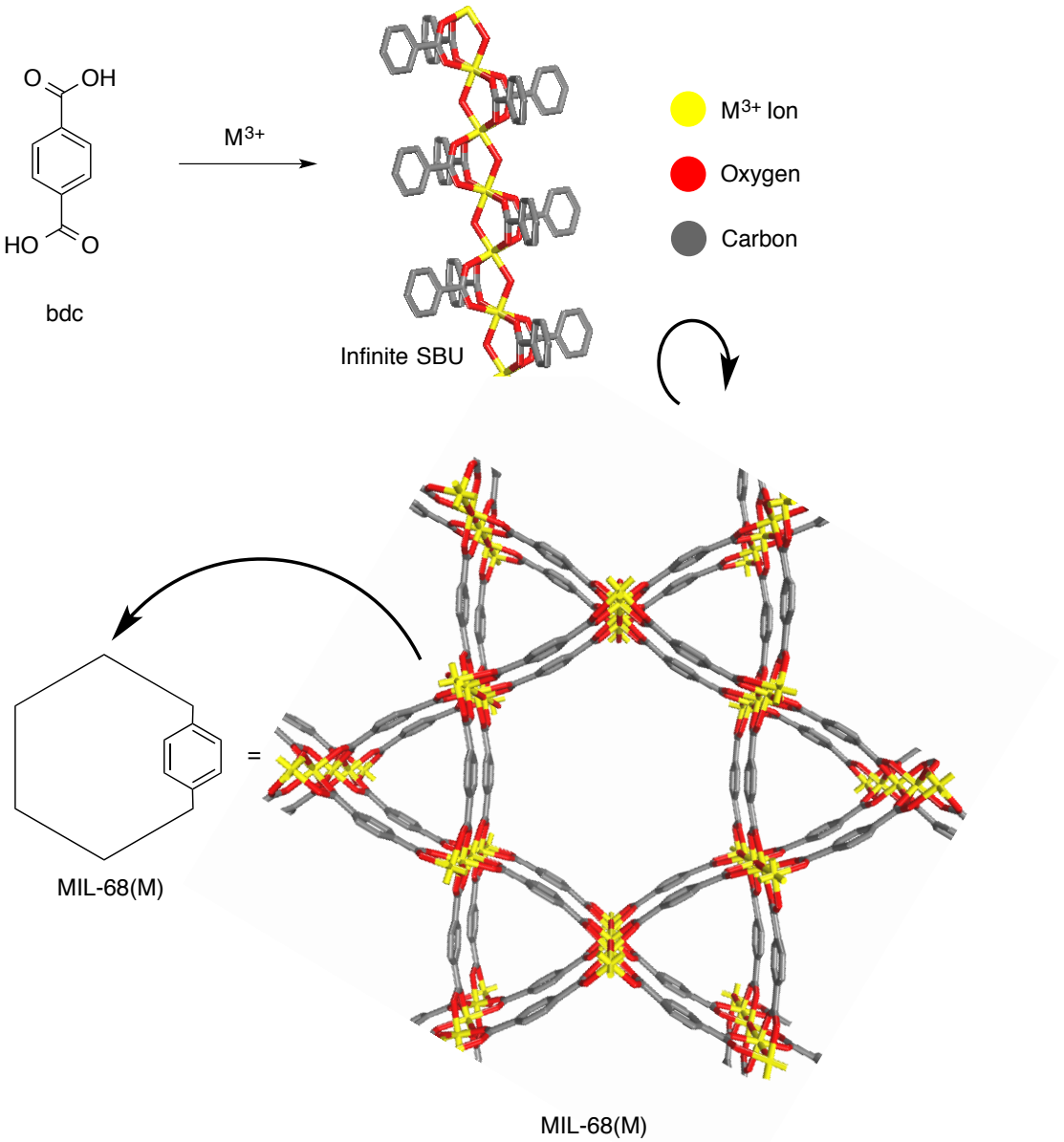

Figure 1.4. Synthesis of MIL-68(M) from H_2bdc and M^{3+} (top). Carbon atoms from the ligand are in grey, oxygen is in red and the trivalent metal is in yellow. Multiple trivalent metals can be used in this synthesis and the infinite SBU remains the same with two bridging carboxylates and a hydroxyl group. The X-ray structure and cartoon depiction are also included (bottom). The hexagonal pore is comprised of the edges of six triangular pores.

The chemical stability achieved by using a trivalent metal ion, instead of Zn^{2+}, lead to the exploration of even more robust materials using group four metals with H_2bdc. Due to increased oxophilicity, utilization of a group four metal(s) should create an even stronger coordination bond than any described previously possibly increasing the framework stability. Indeed, the University of Oslo (UiO) MOF no longer has infinite channels, as seen in the MIL materials, but distinct pores comprised of H_2bdc and Zr. Heating $ZrCl_4$ with H_2bdc in DMF at 120 °C for 24 h results in a microcrystalline powder, UiO-66, that scanning electron microscopy (SEM) shows are intergrown cubic crystals.[11] While the initial crystallites were too small for single XRD analysis, PXRD analysis uncovered the framework topology. This particular SBU has the most coordinating moieties of any MOF, creating an overall octahedron coordinated by 12 bdc carboxylates to the $Zr_6O_4(OH)_4$ core (Figure 1.5, top right). The terminal hydroxyl groups can be reversibly removed depending on the temperature without any interruption of the SBU shape. This unique Zr-carboxylate SBU drastically increases the thermal stability of this MOF to ~500 °C in comparison to the ~350 °C seen for Zn-carboxylate based materials. Either the stronger Zr-O bonds or the shape of the SBU could result in this stability increase. However, the use of H_2bdc ligands only allows for a 6 Å window which is much smaller than many MOFs. This can be modulated to 8 and 10 Å by the addition of one (1,4- biphenyldicarboxylic acid, UiO-67) or two benzene rings (1,4-terphenyldicarboxylic acid, UiO-68) between the carboxylic acids with minimal effects on the thermal stability of the framework. The experimental Langmuir surface is for UiO-66 1187 m^2g^{-1} thus demonstrating how topology can affect the physical properties of MOFs.

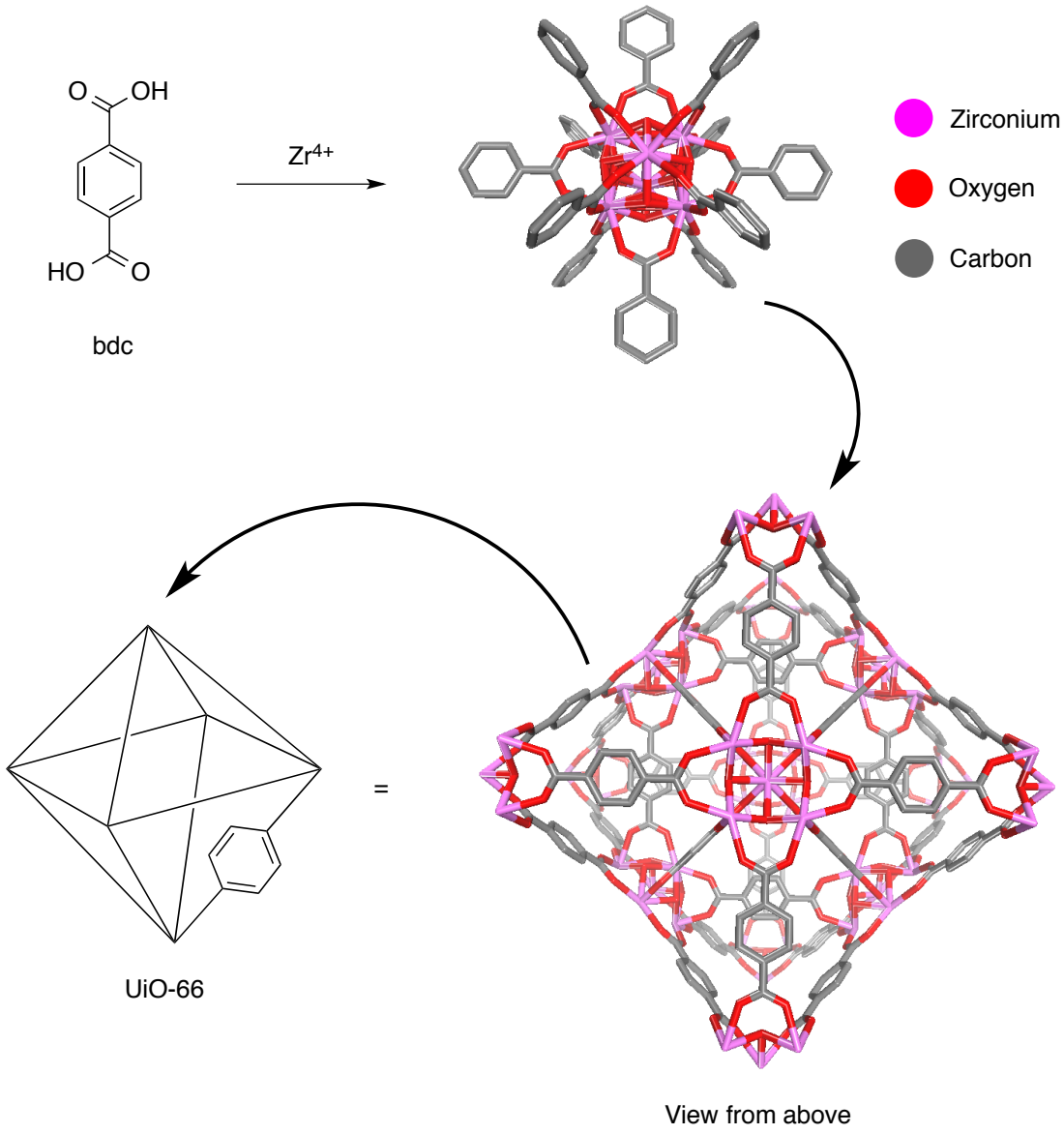

Figure 1.5. Synthesis of the SBU from H_2bdc and Zr (top). Connectedness of the SBUs to form UiO-66 (bottom). Zirconium is in pink, oxygen is in red, and carbon is in grey. Cartoon schematic of UiO-66 synthesis in comparison to the X-ray structure.

1. III. Characterization Methods for MOFs

Determination of the components and arrangement of species within a porous material has been critical in order to make improvements in the materials. In

general, characterization of porous materials has been easily adopted for MOFs. Due to their hybrid nature, many MOFs can be dissolved in acidic or basic media. This dissolution allows for indirect methods to confirm the identify of the organic portion of the material such as nuclear magnetic resonance (NMR) spectroscopy, commonly ^{1}H and ^{13}C, and electrospray ionization mass spectrometry (ESI-MS) analysis.

Topology can be identified through single crystal XRD if the material is suitably crystalline. PXRD can also be used to identify the crystallographic parameters of the bulk material, can be used to quickly identify if related materials are of similar topologies to those previously examined, and verify bulk crystallinity and phase purity. TGA is used to analyze the amount of solvent and water present in a sample and any degradation events that are thermally triggered by measuring the sample mass as a function of temperature. With MOFs, there is a large difference between the degradation of the organic species by itself (<200 °C) in comparison to the organic species within the lattice of a framework (>360 °C). Both the temperature and profile of degradation can reveal information about thermal stability. For example, a slow and undulated loss of mass can indicate a multi-step degradation process whereas a steep and smooth curve can indicate a single event.

Lastly, gas adsorption measurements are used to evaluate the porosity of MOFs. It has been established that activation of the MOF materials, evacuation of any residual solvent, followed by dinitrogen adsorption measurements at 77 K can provide information about the porosity and accessible surface area of the materials.[12] MOF adsorption measurements rely on the identity of the adsorbent, the temperature, and one of two mathematical models used to convert gas adsorption measurements to surface area values. The difference between accessible surface area and the

more commonly thought of van der Waals surface area, is based on the size of the adsorbent molecule; generally, the smaller the adsorbent molecule, the more accurate of an estimate. The Langmuir model assumes a monolayer of adsorbent molecules, which has been computationally determined to be an over estimate for the actual adsorption capabilities for materials with pores larger than a single layer of adsorbent. The BET model assumes a multilayer adsorption, which provides a more accurate porosity measurement for MOFs than the Langmuir model.[13] MOF papers have reported numbers in terms of m^2g^{-1} and the larger the value, in general, the larger the porosity of any given material. While accessible surface areas can be determined from low-pressure adsorption, obtaining measurements up to atmospheric pressure can provide details about the pore size and distribution. For many MOFs, a type 1 isotherm is seen where an increased partial pressure of adsorbent leads to an exponentially increased adsorption until a saturation pressure is reached. This typically indicates homogenous micropores in the material. At the saturation pressure, there is an equilibrium between the adsorbed molecules of the material and the freely available headspace molecules where an increased pressure has no affect on the adsorption. Also, for a type 1 isotherm, the profile of the adsorption curve is followed exactly by the desorption curve. If two isotherms from different samples are plotted together, a lower saturation pressure can discern a smaller accessible surface area from one another. Other types of isotherms are characteristic for larger macroporous materials or heterogeneity of the pore sizes within a material such as for UMCM-1 which has a type IV isotherm. Hysteresis, common among these materials, is when the adsorption trace does not overlap with the desorption trace, i.e. adsorbent molecules are staying bound to a material at lower pressures than when they were introduced. All of these characterization techniques, in conjunction with basic understanding of

the binding preferences of metal with certain types of coordinating groups, have provided improvements to the design of a MOF material and the means to determine the properties.

1. IV. Modulating MOF Properties

All of the above systems are based on aryl carboxylates as the key-coordinating moiety and although other coordinating groups have been explored will not be discussed here.[14-16] Within just the class of metal-carboxylate based MOFs, introducing pendant functional groups, in lieu of one or more C-H bonds, is a viable method for modifying the final MOF material. Simply using 2-substituted-1,4-benzenedicarboxylic acid (Figure 1.5), in addition to or instead of H_2bdc, in the solvothermal synthesis of any of the above MOFs, reveals isostructural MOFs with a pendant functional group at the two position. For analogues to IRMOF-1, 2-bromo-1,4-dicarboxylic acid (Br-bdc) forms IRMOF-2 as clear cubes under slightly modified conditions and 2-amino-1,4-benzenedicarboxylic acid (NH_2-bdc) forms IRMOF-3 as amber cubes.[17] To create a singly brominated or aminated framework of UMCM-1, MIL-68, and UiO-66 variants, the same technique can be employed.[18-21] Incorporating functionality into a framework by using 'pre' functionalized building blocks has been designated 'prefunctionalization.' Using up to eight different bdc ligands into the solvothermal synthesis can create 'multivariate' MOFs that are very versatile and can be further modified.[22] However, there are some limitations for the variety and placement of functional groups that can be incorporated in this fashion. Since the MOFs are comprised of metal-ligand coordination bonds, directly incorporating secondary metal sites can be cumbersome, if not impossible. Solubility and steric constraints also must be taken into consideration, as the new functional group must not physically interfere with the formation of the coordination bonds or lattice. Lastly,

solvothermal syntheses are at high temperatures for extended periods of time and the organic moiety must withstand these conditions.

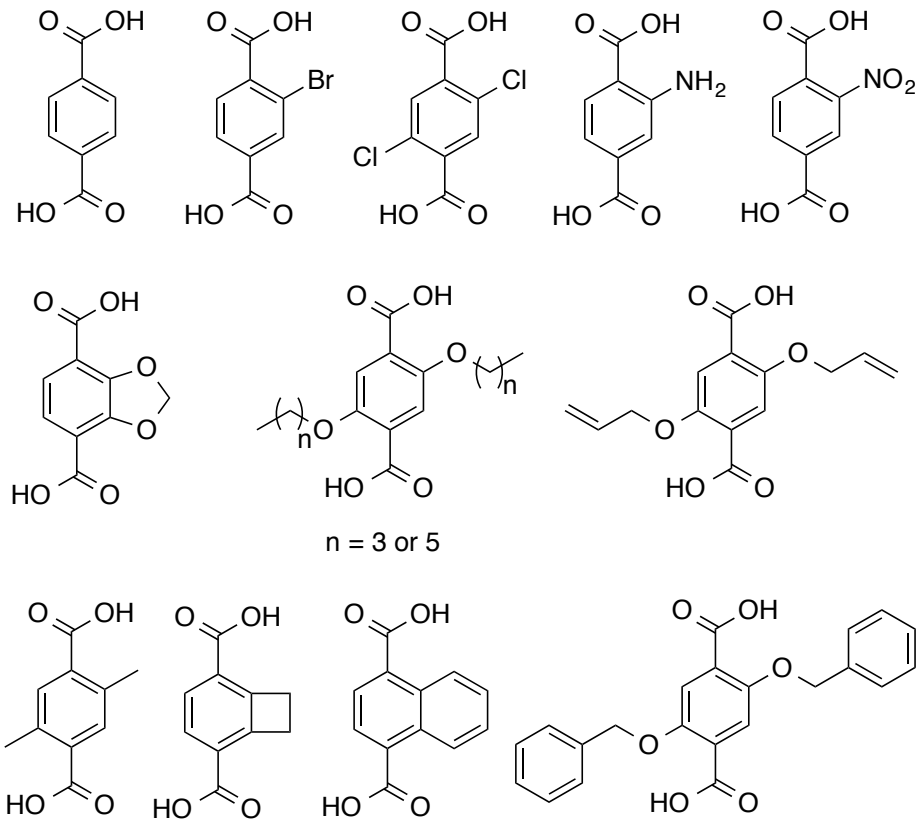

Figure 1.6. Ligands that have successfully been incorporated into an IRMOF framework through direct solvothermal synthesis.

To circumvent these limitations, directly incorporated groups can be utilized as chemical 'handles' for transformations after the lattice has been created. Porous materials allow for diffusion of guest and solvent molecules and should the identity of this guest molecule be a reactant, chemical transformations could be designed that act directly on the porous material. This tactic of incorporating functional groups after the framework has been synthesized was deemed 'postsynthetic modification' (PSM)

in contrast to 'presynthetic' methods. In this fashion, many of the previous complications associated with functionalization of the ligands can be avoided entirely. However, reaction conditions that can incorporate the desired functional group must be mild enough to not affect the structural integrity of the parent MOF material. Depending on the design strategy to obtain the final MOF, identifying suitable reaction conditions may not be a trivial task.

An initial PSM study was on the aniline decorated IRMOF-3. This was exposed to acetic anhydride resulting in the complete transformation the aniline to the acetamide without affecting crystallinity (Figure 1.7, A and B).[23] However, conditions were later found that could directly incorporate a prefunctionalized acetamide bdc (Figure 1.7, C and D). Following a similar procedure, alkyl amides with up to 18 carbon tails were installed inside an IRMOF lattice.[24] This was one of the first examples where PSM demonstrated utility because direct access to that MOF material was impossible due to solubility and steric issues of the requisite bdc building block. Additionally, the physical properties of IRMOF-3 in comparison to IRMOF-3-AM18 had a dramatic alteration in the hydrophobicity of the crystals.[25] Since it was proven that altering the functional groups lining the pores of MOFs could alter their properties, PSM could be a viable method of tuning the materials to be more effective in any future applications.

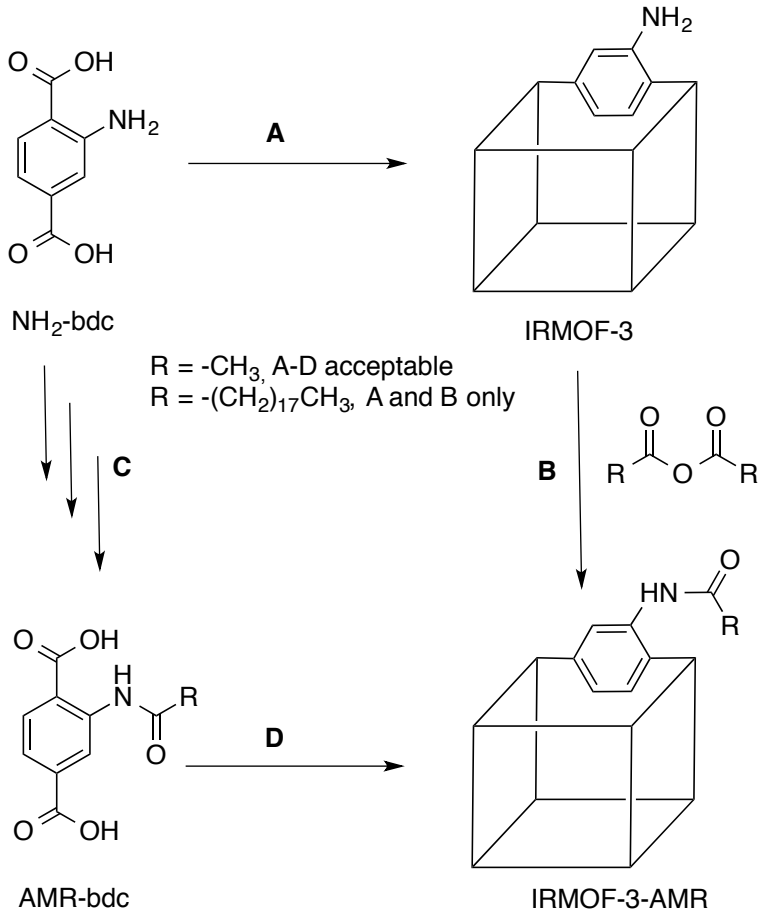

Figure 1.7. Synthesis of MOFs via postsynthetic modification (A and B) in comparison to presynthetic modification (C and D) is illustrated. When the R group is $-CH_3$, either route is viable to IRMOF-3-AMR. However, when R is a longer alkyl group than simply a methyl, C and D are no longer viable and PSM is the only method to obtain IRMOF-3-AMR. This is critical for designing a synthetic route to obtain a final material.

After these initial reports, many new studies were reported using PSM to add in functionality, specifically to enhance catalytic and gas storage capabilities. The aniline groups of IRMOF-3 were condensed with salicyaldehyde to modify 40% of the amine sites, creating a secondary metal binding site for vanadium (Figure 1.8).[26] Most importantly, the creation of this new metal chelating site did not affect the structural integrity of the IRMOF materials. In another example, the aniline groups of UMCM-1-

NH_2 were condensed with 2-pyridinecarboxyaldehyde to create a Schiff base complex also capable of coordinating metals.[27] Successful metalation with palladium in the new metal binding site did not affect the integrity of the Zn-carboxylate bonds. Post PSM and subsequent metalation, the BET surface area dropped from 3200 m^2g^{-1} (UMCM-1-NH_2) to 1700 m^2g^{-1}. These are just two of many examples where PSM was used to modify the 'NH_2' chemical handle that was installed via presynthetic modification to introduce a metal binding group that does not interfere with the Zn-carboxylate bonds. In these cases, the available surface area dropped dramatically but still maintained enough porosity to demonstrate catalytic conversions post metalation.

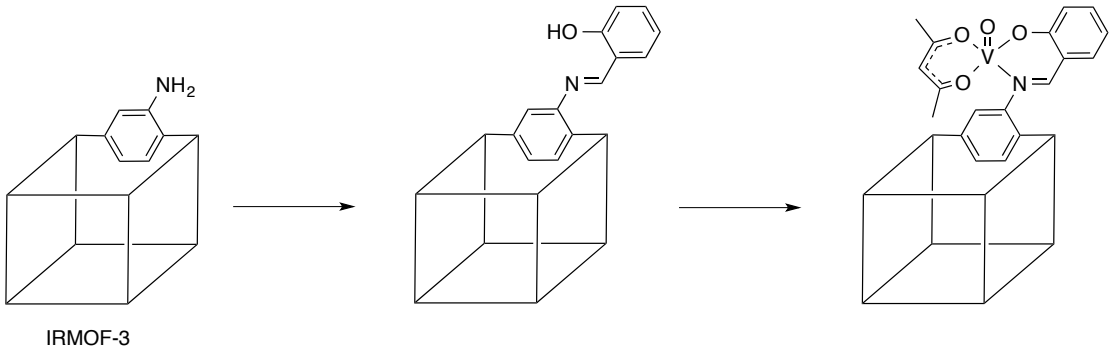

Figure 1.8. PSM of IRMOF-3 to create a secondary metal binding group followed by metalation with V.

1. V. Applications of MOFs

Based on the previously discussed IRMOF, UMCM, MIL-68 and UiO-66, it is evident that building blocks in the initial solvothermal synthesis can access a multitude of materials with a range of properties and topologies (Figure 1.9). One of the many

benefits of using MOFs is their inherent modularity. Unlike purely inorganic porous materials (i.e. zeolites) or porous organic materials (i.e. activated carbon), MOFs have the capability of combining the benefits of organic and inorganic porous solids into a rationally designed material.[5,6,17,28,29] This makes MOFs a promising candidate for next generation porous materials in a wide variety of fields including catalysis and gas storage/separation.[30-34] While much of MOF research has been dedicated to applications such as sensors,[35,36] drug delivery systems,[37-40] and others,[41-51] those areas will not be discussed here.

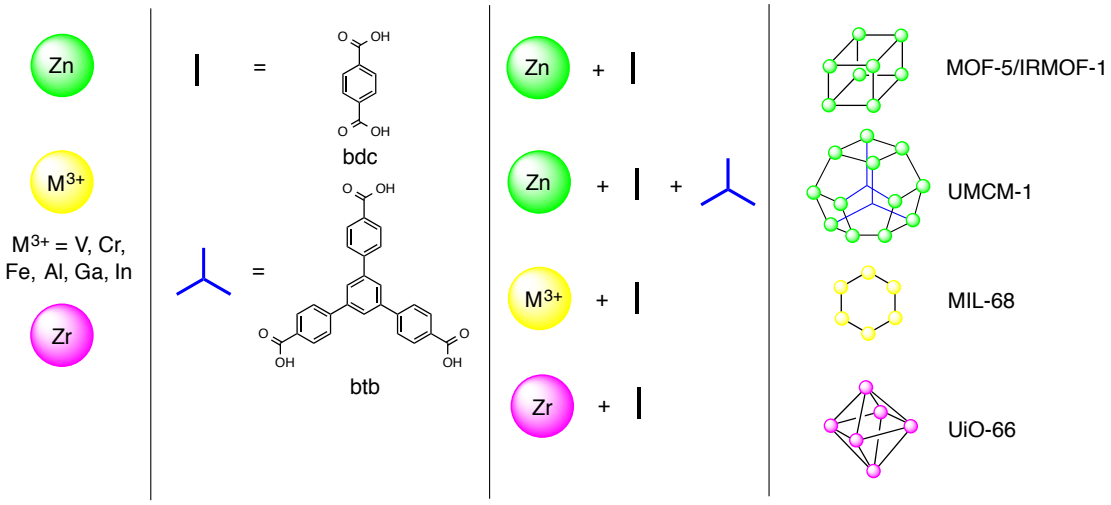

Figure 1.9. Summary of MOF syntheses, that were discussed above, and their stick representations. The spheres are present to indicate where the SBU would be and will be omitted in the rest of the thesis.

Ideally, catalytic material will have easy accessibility for the substrate(s) to the catalytical active site, a high turnover frequency, mild reaction conditions, simple separation and indefinite reusability.[52] Using MOFs, the pore and aperture dimensions

can be designed for a particular class of substrate(s). Depending on the identity of the metal(s) in the solvothermal synthesis, one or more catalytically active species can be directly incorporated into the host framework or can be designed as a handle for PSM incorporation. Additionally, separation could be as easy as a filtration of the MOF from the reaction conditions, and the stability of the coordination bonds can be tuned to suit the reaction of interest. The organic strut can also contain secondary metal binding groups available for the incorporation of another metal. In this fashion, a periodic spacing of identical catalyst sites can be organized within the MOF lattice. Many homogeneous catalysts suffer from aggregation and dimerization as the inactivating mechanism; immobilization of the catalyst in the structure of the MOFs would eliminate that problem.

The affinity for guest molecules, specifically in the gas phase, towards a porous solid arises from two specific forces. First, there are simple van der Waals interactions that can be used to create physisorption capable areas. To increase physisorption, a tunable pore size (substrate specific) and positive surface area contacts (i.e. large aryl groups or 'corners' that are simply a high density of accessible surface contacts, inherent within MOF lattices) are effective.[17,30,34,53-58] Second, additional functional groups can be incorporated to create chemisorption sites such as secondary metal binding sites similar to those that were discussed in context of catalysis.[59] Both computationally and experimentally, accessible coordination sites on metal ions have provided a significant increase in the heats of adsorption for MOFs in regard to CO_2 or H_2.[60-64] Pendant amines were also computationally determined to be beneficial to increase affinity for CO_2 as they can covalently interact with CO_2 molecules thus polarizing the interior of the material and increase the number of positive contacts for additional CO_2 molecules which has been experimentally validated.[65,66]

The following chapters will explore the tolerance of various MOFs to chemical and physical modification of the organic struts. Chapter 2 will specifically analyze photochemical modifications to create Zn-carboxylate based MOFs with secondary metal binding groups. Next, combining photochemical and covalent chemical modification in mixed ligand Zn based MOFs will allow access to multiple MOFs from a single starting material. Chapter 3 will explore PSM via click reactions in multiple MOFs. The goal is to specifically correlate PSM conversion and either the aperture size or chemical robustness of the MOF for multi-reagent and single reagent reactions. Lastly, Chapter 4 will exploit 'presynthetic' modification to chemically crosslink organic bdc struts prior to MOF formation. By doing so, restrictions on the degrees of freedom are created and orientation of ligand sets around an SBU can be rationally controlled during the crystallization process. This can provide another method for the positional control of functional groups within a crystalline lattice.

1. VI. References

(1) Wood, C. D.; Tan, B.; Trewin, A.; Su, F.; Rosseinsky, M. J.; Bradshaw, D.; Sun, Y.; Zhou, L.; Cooper, A. I. *Adv. Mater.* **2008**, *20*, 1916.

(2) Wigmans, T. *Carbon* **1989**, *27*, 13.

(3) Weitkamp, J. *Solid State Ionics* **2000**, *131*, 175.

(4) Medishetty, R.; Tandiana, R.; Koh, L. L.; Vittal, J. J. *Chem.--Eur. J.* **2014**, *20*, 1231.

(5) Ferey, G. *Chem. Soc. Rev.* **2008**, *37*, 191.

(6) Li, H.; Eddaoudi, M.; O'Keeffe, M.; Yaghi, O. M. *Nature* **1999**, *402*, 276.

(7) Koyama, H.; Saito, Y. *Bull. Chem. Soc. Jpn.* **1954**, *27*, 112.

(8) Koh, K.; Wong-Foy, A. G.; Matzger, A. J. *Angew. Chem. Int. Ed.* **2008**, *47*, 677.

(9) Barthelet, K.; Marrot, J.; Ferey, G.; Riou, D. *Chem. Commun.* **2004**, 520.

(10) Volkringer, C.; Meddouri, M.; Loiseau, T.; Guillou, N.; Marrot, J.; Ferey, G.; Haouas, M.; Taulelle, F.; Audebrand, N.; Latroche, M. *Inorg. Chem.* **2008**, *47*, 11892.

(11) Cavka, J. H.; Jakobsen, S.; Olsbye, U.; Guillou, N.; Lamberti, C.; Bordiga, S.; Lillerud, K. P. *J. Am. Chem. Soc.* **2008**, *130*, 13850.

(12) Düren, T.; Millange, F.; Férey, G.; Walton, K. S.; Snurr, R. Q. *J. Phys. Chem. C* **2007**, *111*, 15350.

(13) Walton, K. S.; Snurr, R. Q. *J. Am. Chem. Soc.* **2007**, *129*, 8552.

(14) Gagnon, K. J.; Perry, H. P.; Clearfield, A. *Chem. Rev.* **2011**, *112*, 1034.

(15) Shimizu, G. K. H.; Vaidhyanathan, R.; Taylor, J. M. *Chem. Soc. Rev.* **2009**, *38*, 1430.

(16) Clearfield, A. *Dalton Trans.* **2008**, 6089.

(17) Eddaoudi, M.; Kim, J.; Rosi, N.; Vodak, D.; Wachter, J.; O'Keeffe, M.; Yaghi, O. M. *Science* **2002**, *295*, 469.

(18) Garibay, S. J.; Wang, Z.; Tanabe, K. K.; Cohen, S. M. *Inorg. Chem.* **2009**, *48*, 7341.

(19) Kim, M.; Boissonnault, J. A.; Allen, C. A.; Dau, P. V.; Cohen, S. M. *Dalton Trans.* **2012**, *41*, 6277.

(20) Kim, M.; Cahill, J. F.; Fei, H.; Prather, K. A.; Cohen, S. M. *J. Am. Chem. Soc.* **2012**, *134*, 18082.

(21) Garibay, S. J.; Cohen, S. M. *Chem. Commun.* **2010**, *46*, 7700.

(22) Deng, H.; Doonan, C. J.; Furukawa, H.; Ferreira, R. B.; Towne, J.; Knobler, C. B.; Wang, B.; Yaghi, O. M. *Science* **2010**, *327*, 846.

(23) Wang, Z.; Cohen, S. M. *J. Am. Chem. Soc.* **2007**, *129*, 12368.

(24) Tanabe, K. K.; Wang, Z.; Cohen, S. M. *J. Am. Chem. Soc.* **2008**, *130*, 8508.

(25) Nguyen, J. G.; Cohen, S. M. *J. Am. Chem. Soc.* **2010**, *132*, 4560.

(26) Ingleson, M. J.; Barrio, J. P.; Guilbaud, J.; Khimyak, Y. Z.; Rosseinsky, M. J. *Chem. Commun.* **2008**, 2680.

(27) Doonan, C. J.; Morris, W.; Furukawa, H.; Yaghi, O. M. *J. Am. Chem. Soc.* **2009**, *131*, 9492.

(28) Tranchemontagne, D. J.; Mendoza-Cortes, J. L.; O'Keeffe, M.; Yaghi, O. M. *Chem. Soc. Rev.* **2009**, *38*, 1257.

(29) O'Keeffe, M.; Yaghi, O. M. *Chem. Rev.* **2011**, *112*, 675.

(30) Han, S. S.; Mendoza-Cortes, J. L.; Goddard Iii, W. A. *Chem. Soc. Rev.* **2009**, *38*, 1460.

(31) Duren, T.; Bae, Y.; Snurr, R. Q. *Chem. Soc. Rev.* **2009**, *38*, 1237.

(32) Lee, J.; Farha, O. K.; Roberts, J.; Scheidt, K. A.; Nguyen, S. T.; Hupp, J. T. *Chem. Soc. Rev.* **2009**, *38*, 1450.

(33) Li, J.; Kuppler, R. J.; Zhou, H. *Chem. Soc. Rev.* **2009**, *38*, 1477.

(34) Murray, L. J.; Dinca, M.; Long, J. R. *Chem. Soc. Rev.* **2009**, *38*, 1294.

(35) Kreno, L. E.; Leong, K.; Farha, O. K.; Allendorf, M. D.; Van Duyne, R. P.; Hupp, J. T. *Chem. Rev.* **2011**, *112*, 1105.

(36) Hu, Z.; Deibert, B. J.; Li, J. *Chem. Soc. Rev.* **2014**, *43*, 5815.

(37) Horcajada, P.; Gref, R.; Baati, T.; Allan, P. K.; Maurin, G.; Couvreur, P.; Férey, G.; Morris, R. E.; Serre, C. *Chem. Rev.* **2011**, *112*, 1232.

(38) Horcajada, P.; Serre, C.; Vallet-Regí, M.; Sebban, M.; Taulelle, F.; Férey, G. *Angew. Chem., Int. Ed.* **2006**, *45*, 5974.

(39) Horcajada, P.; Serre, C.; Maurin, G.; Ramsahye, N. A.; Balas, F.; Vallet-Regí, M.; Sebban, M.; Taulelle, F.; Férey, G. *J. Am. Chem. Soc.* **2008**, *130*, 6774.

(40) Kundu, T.; Mitra, S.; Patra, P.; Goswami, A.; Díaz, D.; Banerjee, R. *Chem.--Eur. J.* **2014**, *20*, 10514.

(41) Zhang, W.; Xiong, R. *Chem. Rev.* **2011**, *112*, 1163.

(42) Allendorf, M. D.; Bauer, C. A.; Bhakta, R. K.; Houk, R. J. T. *Chem. Soc. Rev.* **2009**, *38*, 1330.

(43) Czaja, A. U.; Trukhan, N.; Muller, U. *Chem. Soc. Rev.* **2009**, *38*, 1284.

(44) Kurmoo, M. *Chem. Soc. Rev.* **2009**, *38*, 1353.

(45) Miras, H. N.; Vila-Nadal, L.; Cronin, L. *Chem. Soc. Rev.* **2014**, *43*, 5679.

(46) Orilall, C. M.; Wiesner, U. *Chem. Soc. Rev.* **2011**, *40*, 520.

(47) Shekhah, O.; Liu, J.; Fischer, R. A.; Woll, C. *Chem. Soc. Rev.* **2011**, *40*, 1081.

(48) Uemura, T.; Yanai, N.; Kitagawa, S. *Chem. Soc. Rev.* **2009**, *38*, 1228.

(49) Zhang, T.; Lin, W. *Chem. Soc. Rev.* **2014**, *43*, 5982.

(50) Zhang, Z.; Zaworotko, M. J. *Chem. Soc. Rev.* **2014**, *43*, 5444.

(51) Zhu, Q.; Xu, Q. *Chem. Soc. Rev.* **2014**, *43*, 5468.

(52) Yoon, M.; Srirambalaji, R.; Kim, K. *Chem. Rev.* **2011**, *112*, 1196.

(53) Hong, S.; Oh, M.; Park, M.; Yoon, J. W.; Chang, J. S.; Lah, M. S. *Chem. Commun.* **2009**, 5397.

(54) Yan, Y.; Lin, X.; Yang, S. H.; Blake, A. J.; Dailly, A.; Champness, N. R.; Hubberstey, P.; Schroder, M. *Chem. Commun.* **2009**, 1025.

(55) Getman, R. B.; Bae, Y.; Wilmer, C. E.; Snurr, R. Q. *Chem. Rev.* **2011**, *112*, 703.

(56) Suh, M. P.; Park, H. J.; Prasad, T. K.; Lim, D. *Chem. Rev.* **2011**, *112*, 782.

(57) He, Y.; Zhou, W.; Qian, G.; Chen, B. *Chem. Soc. Rev.* **2014**, *43*, 5657.

(58) Kumar, M. R.; Sundar, V. J.; Subramanian, V. *Int. J. Hydrogen Energy* **2012**, *37*, 16070.

(59) Fracaroli, A. M.; Furukawa, H.; Suzuki, M.; Dodd, M.; Okajima, S.; Gándara, F.; Reimer, J. A.; Yaghi, O. M. *J. Am. Chem. Soc.* **2014**, *136*, 8863.

(60) Zheng, B. S.; Bai, J. F.; Duan, J. G.; Wojtas, L.; Zaworotko, M. J. *J. Am. Chem. Soc.* **2011**, *133*, 748.

(61) Britt, D.; Furukawa, H.; Wang, B.; Glover, T. G.; Yaghi, O. M. *Proc. Natl. Acad. Sci. U. S. A.* **2009**, *106*, 20637.

(62) Rowsell, J. L. C.; Spencer, E. C.; Eckert, J.; Howard, J. A. K.; Yaghi, O. M. *Science* **2005**, *309*, 1350.

(63) Queen, W. L.; Hudson, M. R.; Bloch, E. D.; Mason, J. A.; Gonzalez, M. I.; Lee, J. S.; Gygi, D.; Howe, J. D.; Lee, K.; Darwish, T. A.; James, M.; Peterson, V. K.; Teat, S. J.; Smit, B.; Neaton, J. B.; Long, J. R.; Brown, C. M. *Chem. Sci.* **2014**.

(64) Yazaydın, A. Ö.; Benin, A. I.; Faheem, S. A.; Jakubczak, P.; Low, J. J.; Willis, R. R.; Snurr, R. Q. *Chem. Mater.* **2009**, *21*, 1425.

(65) López-Maya, E.; Montoro, C.; Colombo, V.; Barea, E.; Navarro, J. A. R. *Adv. Funct. Mater.* **2014**, Early View.

(66) Fracaroli, A. M.; Furukawa, H.; Suzuki, M.; Dodd, M.; Okajima, S.; Gándara, F.; Reimer, J. A.; Yaghi, O. M. *J. Am. Chem. Soc.* **2014**, *136*, 8863.

2. Photochemical Postsynthetic Modification in Metal-Organic Frameworks

2. I. Introduction

As described in Chapter 1, the utility of MOFs would be enhanced if their architectures and characteristics could be designed down to the molecular level. Previous efforts, in the manipulation of MOFs, have focused on the organic building blocks. The introduction of new functional groups can easily create an altered chemical atmosphere inside the material. This has been explored through both 'prefunctionalization' and PSM methods. PSM has been found to be a powerful tool for introducing new functional groups as a means to modulate the physical and chemical properties of the MOF materials. Generally, PSM has been described in the context of treating MOFs with reagents that can react with an available chemical "handle" on the MOF framework. As described in Chapter 1, the addition of atoms can lead to a substantial decrease in accessible surface area potentially affecting their application capabilities.[1-7] In contrast, the removal of chemical groups on and within a MOF to reveal new chemical functionality is far less studied. In this manner, both pre- and post-functionalization methods can be used to create versatile and highly functionalized materials without diminishing porosity.

A small number of studies have described the cleavage of protecting groups within a MOF lattice using either chemical reagents or thermal treatment.[8,9] Telfer et al. performed postsynthetic deprotection (PSD) by using heat to remove a thermally labile protecting group (e.g. , Boc = tert- butoxycarbonyl) to yield a free amino group within a larger, biphenyl dicarboxylate, based MOF (Figure 2.1).[10] The MOF, which was prepared from Zn^{2+} and 2-(tert- butoxycarbonylamino)biphenyl-4,4'-dicarboxylic acid, was heated to >150 °C to remove the Boc protecting group. However, the crystal quality rapidly declined after thermolysis as evidenced by the inability to obtain porosity measurements. Hupp et al. demonstrated a chemical deprotection

prior to further functionalization (Figure 2.2).[8] In their case, a trimethylsilyl (TMS) protected acetylene tagged MOF was exposed to an aqueous solution of fluoride ion. The TMS group was cleaved into a terminal acetylene group.

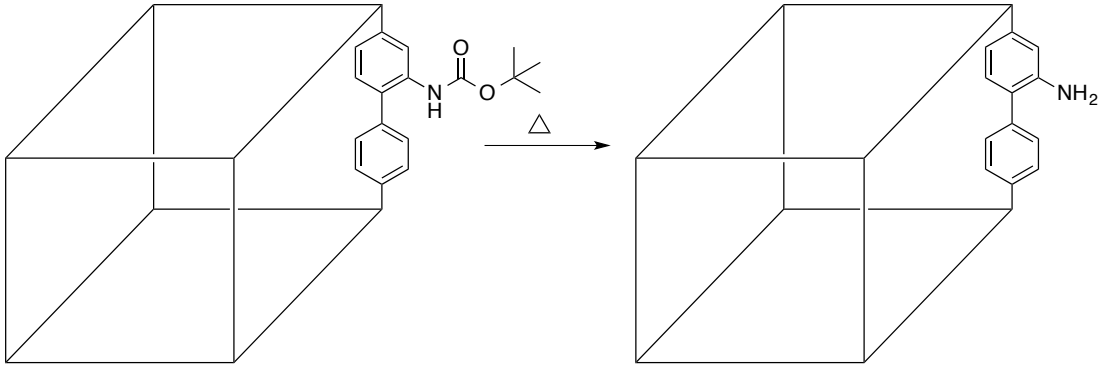

Figure 2.1. Deprotection via thermolysis of the BOC protecting group. While other MOFs can directly incorporate anilinic moieties, this MOF (right) cannot be synthesized directly. If the BOC group is not present, the MOF grows as interpenetrated networks.

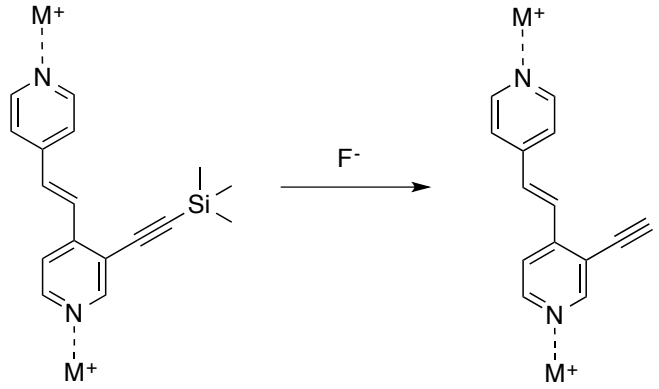

Figure 2.2. Chemical deprotection of a MOF decorated with trimethylsilyl (TMS) protected acetylene groups.

There are relatively few studies that have reported on the light-driven chemical modification or alteration of a MOF.[11-15] Light driven processes should be an

efficient and relatively gentle method to initiate and drive chemical reactions within a MOF lattice. Kitagawa and coworkers irradiated an azide tagged MOF to release a highly active nitrene species however they were unable to optimize greater than 70% conversion (Figure 2.3).[15] A particularly unique system, by Zhou et al., utilized photoirradiation to isomerize an azobenzene tagged MOF (Figure 2.4). In this system the physical adsorption of CO_2 can be modulated depending on the orientation of the azobenzene moiety. Most importantly, this was found to be a reversible process and could cycle indefinitely. On a different note, nitrobenzyl groups have been well established in the literature as photocleavable protecting groups for alcohols and amines.[16] An additional benefit of nitrobenzylether derivatives is that their cleavage wavelength can be tuned from the ultraviolet to visible range thus providing a modular system (Figure 2.5).

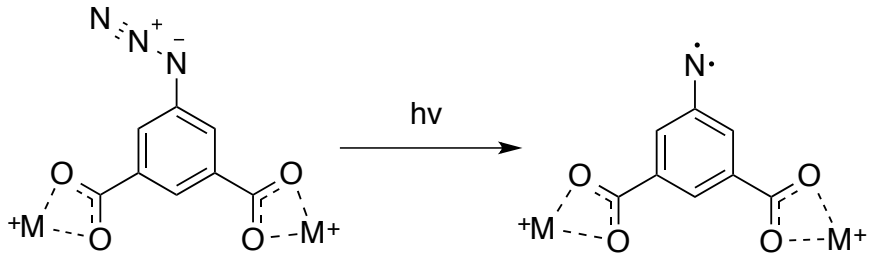

Figure 2.3. Photolysis of the azide group to reveal a MOF with radical species.

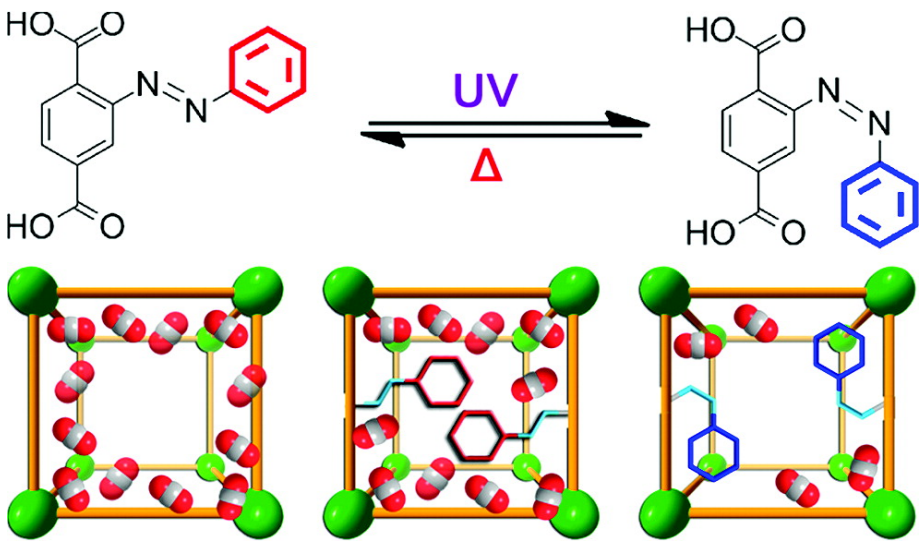

Figure 2.4. Photochemical isomerization that affects available surface area measurements. Reprinted with permission from Park, J., Yuan D., Pham, K. T., Li, J. R., Yakovenko, A., and Zhou, H., 'Reversible Alteration of CO_2 Adsorption upon Photochemical or Thermal Treatment in a Metal-Organic Framework,' *J. Am. Chem. Soc.*, 2012, *134* (1), 99-102. Copyright 2012 American Chemical Society.

In the first part of Chapter 2, the utilization of light to remove protecting groups from the organic components of a MOF lattice in a single-crystal-to-single-crystal (SCSC) fashion will be described. In this manner the MOF lattice is kept pristine, while unmasking new chemical functionality, free hydroxyl groups, throughout the pores of the MOF. This is significant, as reports of MOFs with free hydroxyl groups are rare due to their capacity to bind metal ions and general interference with MOF formation under solvothermal synthesis conditions.[17,18] Our findings suggest that this kind of PSD of MOFs may be an excellent strategy for producing porous materials that would otherwise be difficult to obtain.

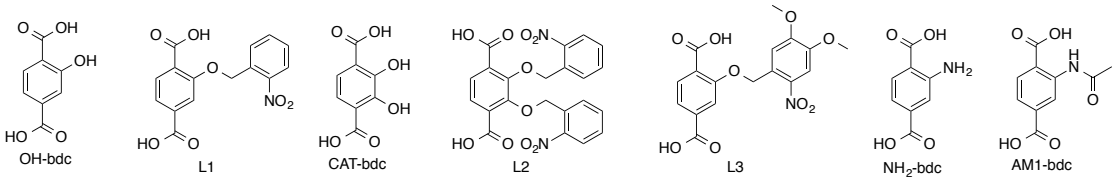

Figure 2.5. Relevant ligands and their names for Chapter 2. CAT stands for catechol, AM stands for the amide moiety and 1 indicates that there is a single carbon attached to the amide.

2. II. Results and Discussion – PSD

2-Hydroxy-1,4-benzenedicarboxylic acid (OH-bdc)[17] and 2,3-dihydroxy-1,4-benzenedicarboxylic acid (CAT-bdc, CAT = catechol)[19] were combined with o-nitrobenzyl bromide to generate protected dicarboxylate building blocks suitable for MOF construction (Scheme 2.1). The resulting ligands, 2-((2-nitrobenzyl)oxy)terephthalic acid (L1) and 2,3-bis((2-nitrobenzyl)oxy)terephthalic acid (L2), were used to prepare analogs of the porous UMCM-1 framework (Chapter 1). [20] L1 or L2 were combined separately with H_3btb[21] and $Zn(NO_2)_3•6H_2O$, under solvothermal reaction conditions as UMCM-1 to obtain UMCM-1-L1 and UMCM-1-L2 as colorless needles (Figure 2.6). Both UMCM-1-L1 and UMCM-1-L2 were found to be structural analogues of UMCM-1, as desired.[20] The structure and composition of UMCM-1-L1 and UMCM-1-L2 were conclusively established by several methods. Digestion of the MOFs in dilute acid, followed by ^1H NMR analysis showed that the materials contained both the btb and the appropriate nitrobenzyl-protected bdc ligand. PXRD of the MOFs gave patterns consistent with a UMCM-1 topology (Figure 2.7). Finally, gas sorption experiments with N_2 at 77 K indicated that UMCM-1-L1 and UMCM-1-L2 were highly porous and showed a characteristic step in the isotherm. The

BET surface areas of UMCM-1-L1 and UMCM-1-L2 were found to be 3219±150 m^2g^{-1} and 2661±172 m^2g^{-1}, respectively, consistent with the parent UMCM-1 material.[20]

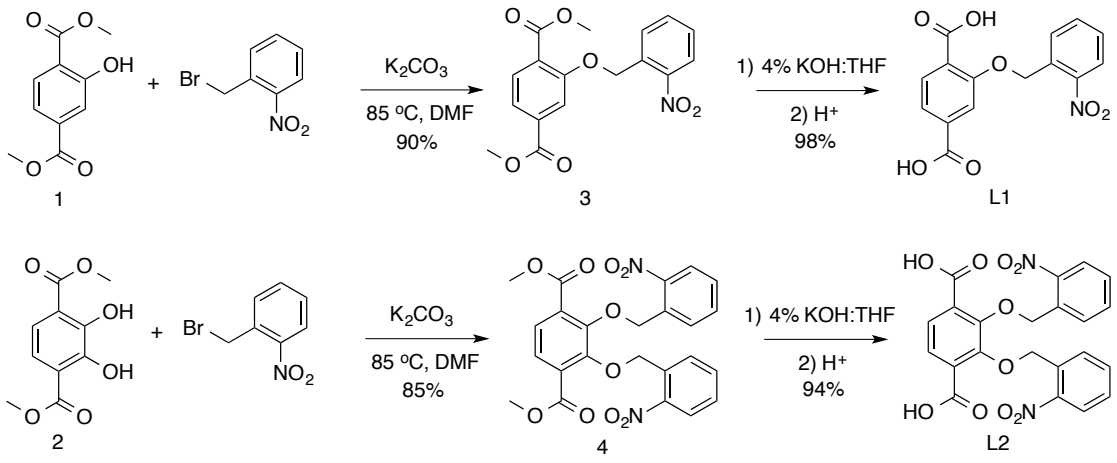

Scheme 2.1. Synthesis of photocleavable ligands for introducing secondary metal-binding sites into MOFs.

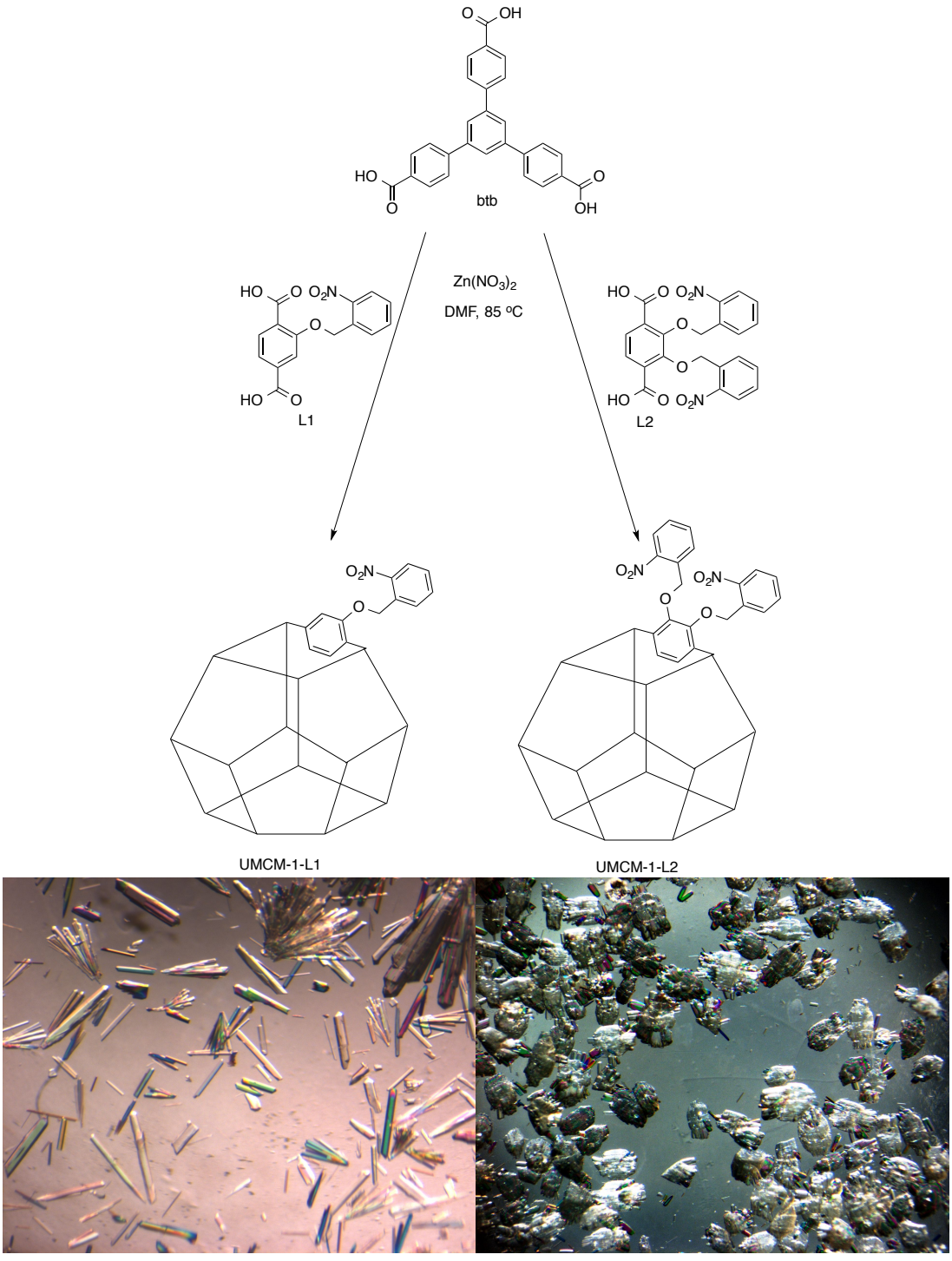

Figure 2.6. Synthesis of UMCM-1-L1 and UMCM-1-L2 (top). Optical microscopy photographs of as-synthesized UMCM-1-L1 (bottom left) and UMCM-1-L2 (bottom right). UMCM-1-L2 have a needle morphology however for UMCM-1-L2 the needles are stacked on top of each other as opposed to free needles seen in UMCM-1-L1.

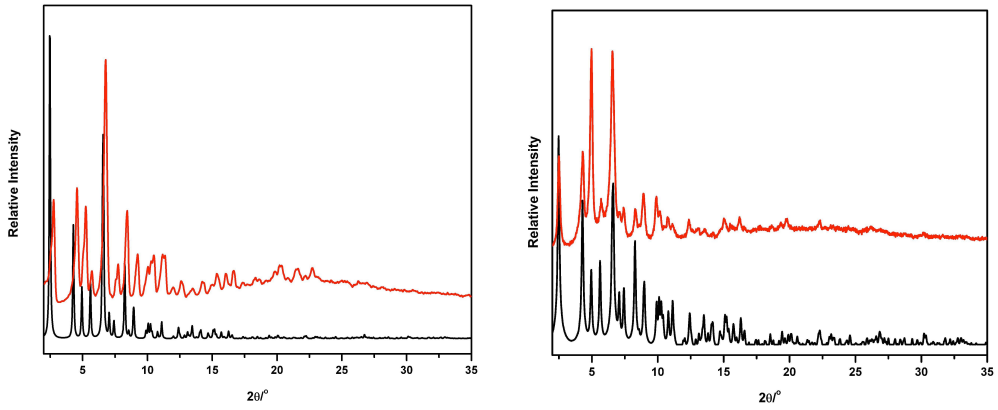

Figure 2.7. Experimental powder X-ray diffraction patterns (red) of UMCM-1-L1 (left) and UMCM-1-L2 (right) in comparison to their simulated powder patterns (black).

Single-crystal XRD of UMCM-1-L1 and UMCM-1-L2 unambiguously showed that both MOFs had the same topology as UMCM-1. A disordered oxygen atom was located and assigned on the bdc ligand of UMCM-1-L1; however, the nitrobenzyl substituent could not be located in the electron density map due to a large amount of positional disorder. Due to the asymmetry in the ligand, the nitrobenzyl group is averaged over four aryl positions, which cannot be resolved in the crystal structure. In contrast, both nitrobenzyl protecting groups could be located and assigned for the structure of UMCM-1-L2. Electron density for the NO_2 groups was located, but could not be effectively refined due to severe disorder (Figure 2.8).

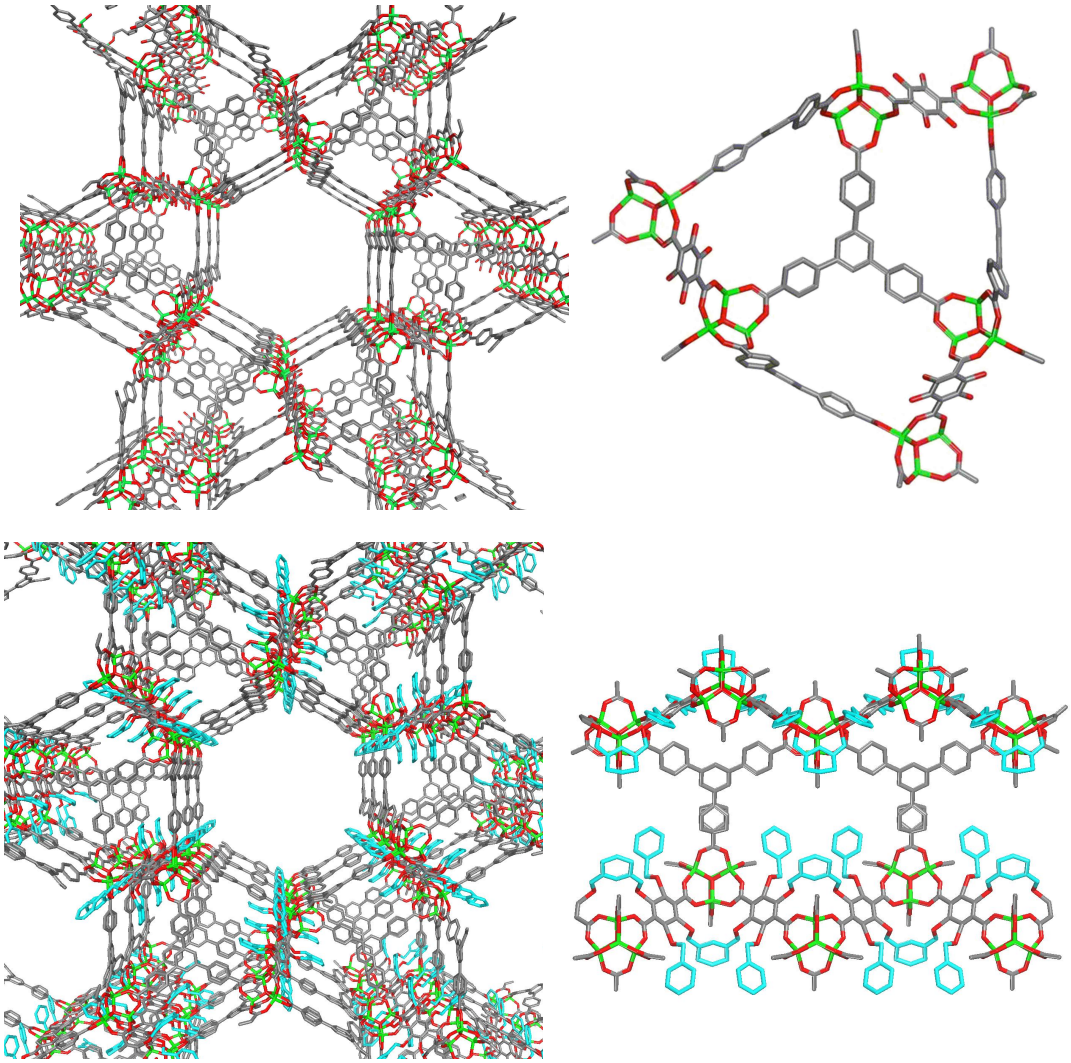

Figure 2.8 Structure of UMCM-1-L1 (top) and UMCM-1-L2 (bottom) from single crystal XRD. Overall UMCM structure (left) in comparison to the micropore (top right). The nitrobenzyl group could be mostly resolved in the crystal structure and is highlighted in cyan (bottom right). Carbon atoms are in grey, oxygen in red, and zinc in green.

UMCM-1-L1 and UMCM-1-L2 were irradiated with 365 nm light for 24–48 h; both MOFs underwent a distinct color change from colorless to orange (Figure 2.9), which was indicative of the photochemical reaction, and release of 2-nitrosobenzaldehyde (which was confirmed by UV-visible analysis (UV-Vis) and ESI-MS, data not

shown).[16,22,23] Examination by ^{1}H NMR spectroscopy, upon digestion of the MOFs in dilute acid, showed that the protecting groups were cleaved. UMCM-1-L1 readily underwent quantitative deprotection to UMCM-1-OH within 24 h of irradiation. UMCM-1-L2 required 48 h of irradiation to achieve ca. 75% deprotection to UMCM-1-CAT under the best conditions identified to date (Figure 2.10). As additional evidence for the deprotection process, UMCM-1-CAT was found to fluoresce blue (λ_{ex} = 365 nm), which is characteristic of the CAT-bdc ligand, while UMCM-1-L2 showed no fluorescence emission. TGA analysis also revealed differences between the protected and deprotected UMCM MOFs. The TGA trace for UMCM-1-L1 showed a weight loss beginning at 300 °C with a notable step at 375 °C prior to framework destruction at 400 °C, most likely due to thermal degradation of the nitrobenzyl sidechain (Figure 2.11). After irradiation this two-pronged weight loss is absent and suggests that the whole MOF stays intact until decomposition of the entire framework. However, in the case of L2, the difference between the TGA traces before and after irradiation are less defined due to incomplete deprotection. Thermal decomposition is evident <400 °C in both before (UMCM-1-L2) and after (UMCM-1-CAT) irradiation samples as there are still nitrobenzyl groups in both samples. This degradation profile is consistent with incomplete deprotection and follows the trend seen in UMCM-1-L1/UMCM-1-OH TGA traces where pendant organic moieties lead to a gradual thermal weight loss as opposed to a single drastic weight loss for the overall structure degradation.

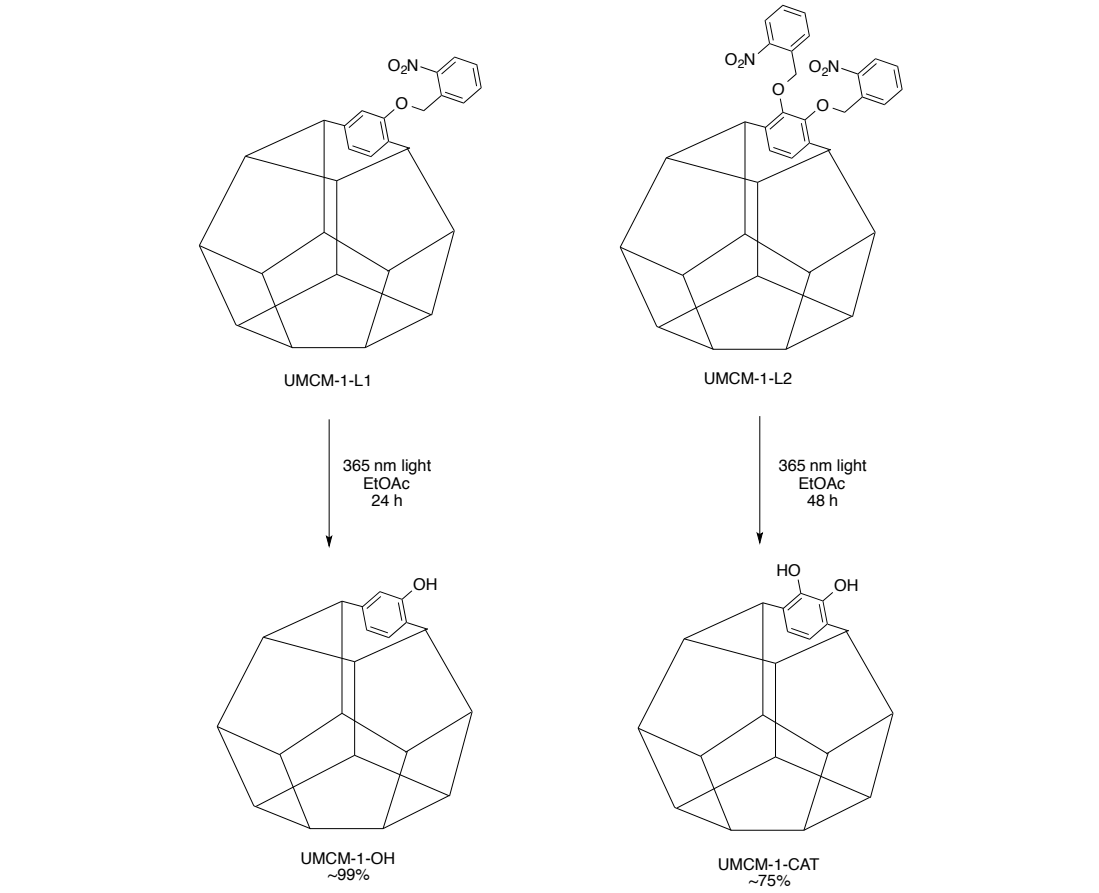

Figure 2.9. Photochemical deprotection of UMCM-1-L1 into UMCM-1-OH and UMCM-1-L2 to UMCM-1-CAT (top). UMCM-1-L1 was quantitatively deprotected after 24 hours whereas UMCM-1-L2 achieved only ~75% deprotection after 48h. Optical microscopy photographs of UMCM-1-OH (bottom left) and UMCM-1-CAT (bottom right) after photoirradiation. The color change is indicative of the photochemical release of the byproduct nitrosobenzaldehyde.

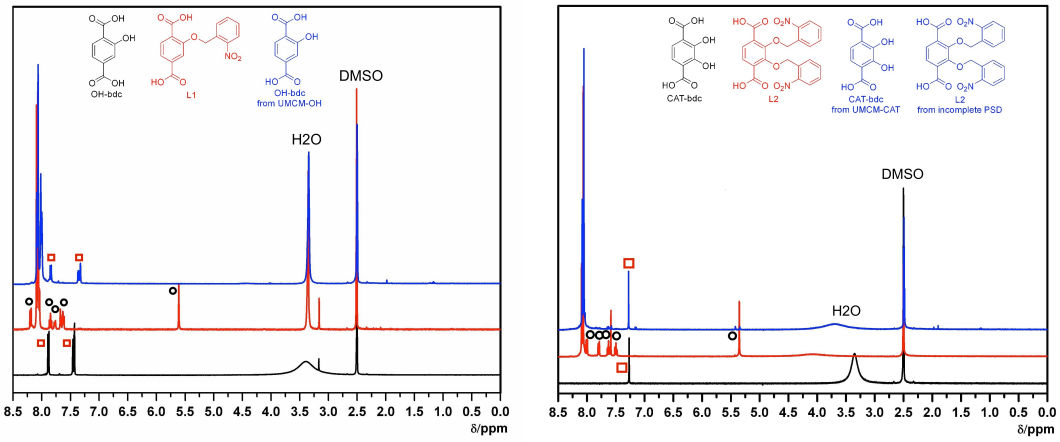

Figure 2.10. ^{1}H NMR spectra of digested UMCM-1-L1 (left) and UMCM-1-L2 (right) before (red) and after (blue) photoirradiation. The black trace is an authentic sample of the appropriate hydroxyl based bdc ligand for comparison. Deprotection quantitation was determined through integration of the benzylic protons ~5.5 ppm in comparison to the aryl protons ~7.2 ppm corresponding to the hydroxylated ligands.

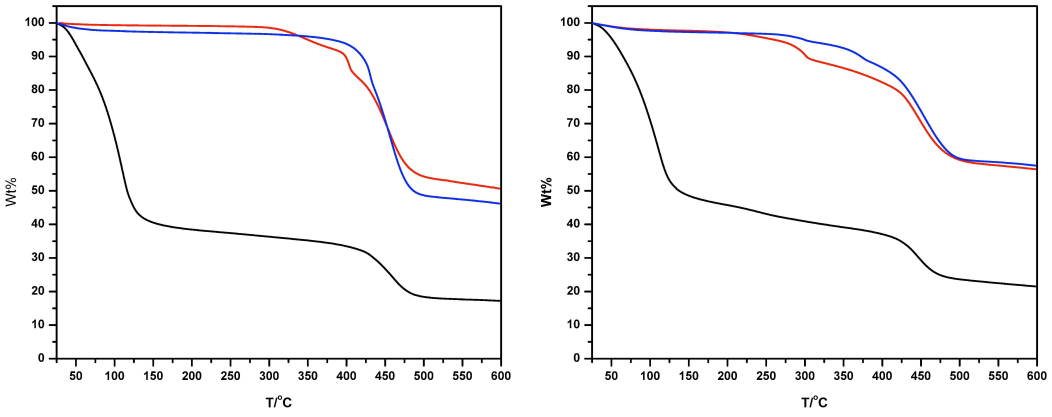

Figure 2.11. TGA traces of UMCM-1-L1 (top) and UMCM-1-L2 (bottom) as synthesized (black), dried (red) and after PSD (blue). Note the smooth curvature for UMCM-1-OH after complete removal of the nitrobenzyl group in comparison to the multistep degradation for ~75% deprotected UMCM-1-CAT.

Single-crystal XRD provided unambiguous evidence for removal of the nitrobenzyl groups in a SCSC fashion. The X-ray structure of UMCM-1-OH showed that the framework remained intact after irradiation however electron density for the hydroxy group on the bdc ligand was positionally disordered over all four aryl positions. Deprotection of UMCM-1- L2 to UMCM-1-CAT was readily evident by the X-ray structure with the disappearance of the nitrobenzyl protecting groups from the electron density map and appearance of the expected catechol group although still positionally disordered (Figure 2.12). PXRD patterns corroborate the framework remaining highly crystalline after irradiation (Figure 2.13).

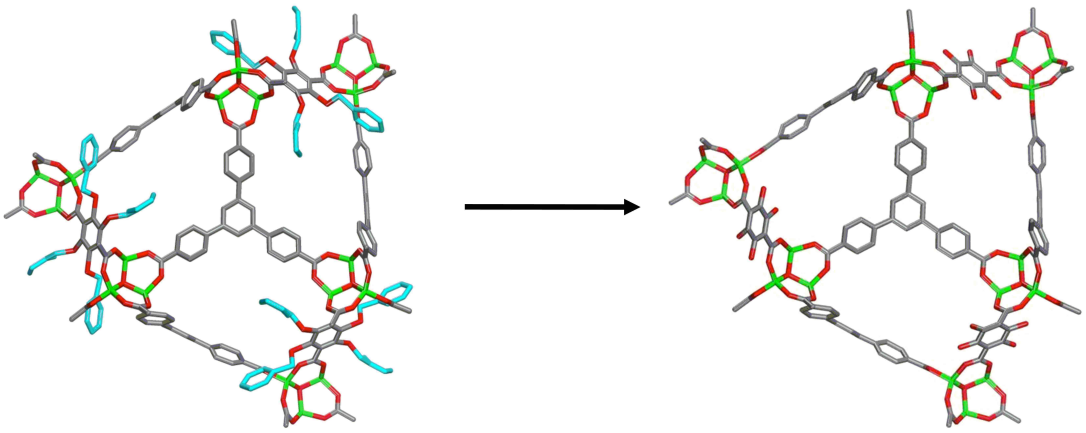

Figure 2.12. Crystallographic evidence for the loss of the nitro benzyl protecting group as evidenced in the UMCM-1-L2 system before (left) and after (right) exposure to light. The nitrobenzyl groups are positionally disordered in the UMCM-1-L2 structure and are highlighted in cyan. Carbon atoms are in grey, oxygen in red, and zinc in green.

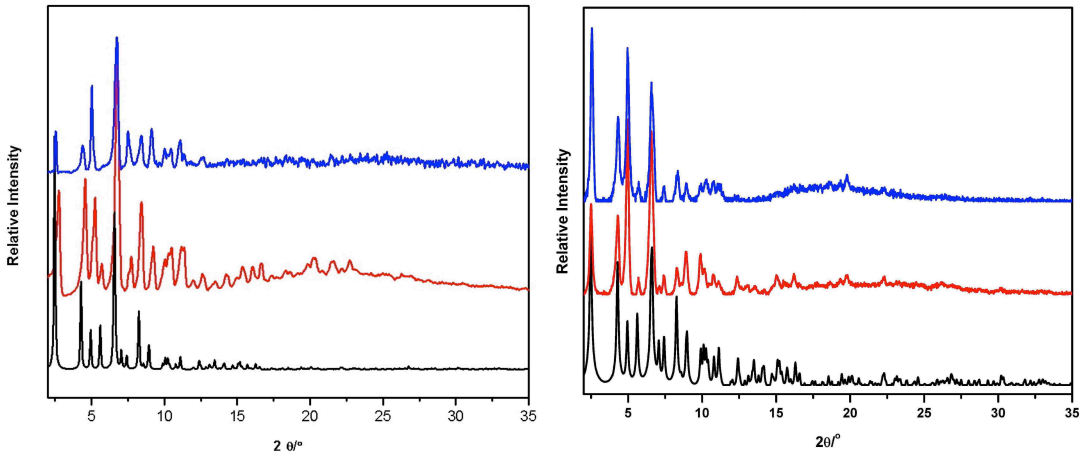

Figure 2.13. PXRD data of L1 system (left) and L2 system (right). Left: UMCM-1-OH in DMF (blue), UMCM-1-L1 in DMF (red), compared to the simulated powder pattern of UMCM-1-L1 from the single-crystal X-ray structure (black). Right: UMCM-1-CAT in toluene (blue) in comparison to UMCM-1-L2 in $CHCl_3$ (red) compared to the simulated powder pattern of UMCM-1-L2 from the crystal structure (black).

PSD of the MOFs was clearly manifest in the gas sorption behavior. N_2 isotherms (77 K) of UMCM-1-OH and UMCM-1-CAT showed significant increases in BET surface area. The BET surface areas were determined to be 3705±177 m^2g^{-1} and 3541±38 m^2g^{-1} for UMCM-1-OH and UMCM-1-CAT, respectively. The difference between the protected and deprotected MOFs is ca. 500 m^2g^{-1} and ca. 900 m^2g^{-1}, which is reasonable for the removal of either one (UMCM-1-OH) or two (UMCM-1-CAT) protecting groups from each structure. Although it is not intuitively obvious whether the surface area should increase or decrease upon removal of the protecting groups, calculated surface areas for UMCM-1-L2 and UMCM-1-CAT confirm that the there should be an increase upon removal of the protecting groups as space has opened up upon their release. Specifically, these measurements examine the accessible surface area by a dinitrogen molecule so the less space occupied in your material, the larger BET value, as described in Chapter 1.[24]

Furthermore, the changes in BET surface area are consistent with our observations in related systems, where upon introducing substituents by postsynthetic modification we see a decrease in BET surface area.[25-27] The complete gas sorption isotherms show a substantial increase in capacity at the saturation pressures, also consistent with removal of one or two nitrobenzyl protecting groups per bdc ligand (Figure 2.14). Overall, the gas sorption experiments indicate that the lattice is intact, the material is highly porous, and that the deprotection reaction results in the expected increase in surface area making PSD one of the few, if not only, postsynthetic modification methods to do so.

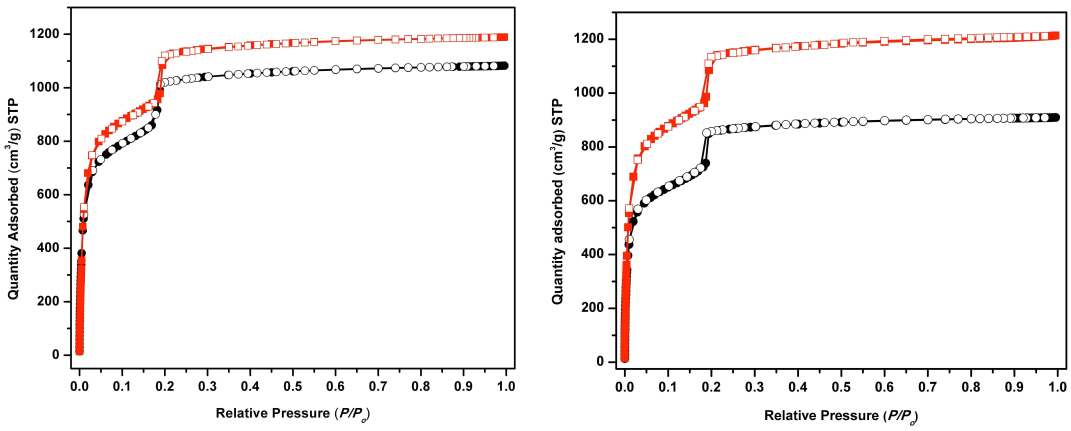

Figure 2.14. Dinitrogen isotherms of UMCM-1-L1 (left) and UMCM-1-L2 (right) before irradiation (black) and after (red) trace.

To show that the newly revealed functional groups are accessible, both UMCM-1-L2 and UMCM-1-CAT were treated with $[Fe(acac)_3]$ in EtOAc. After 24 h, UMCM-1-L2 was a light orange color while UMCM-1-CAT was a deep red-purple color. These color changes were confirmed by diffuse reflectance solid-state electronic

spectroscopy of UMCM-1-L2, UMCM-1- L2 treated with [Fe(acac)$_3$], UMCM-1-CAT, and UMCM-1-FeCAT, which showed clear differences in absorbance between non-metalated and metalated samples (Figure 2.16). The permanence of the color change is evidence of coordination between the free catechol groups and Fe. As expected, UMCM-1-L2 did not show any significant absorbance above 400 nm. Both UMCM-1-CAT and UMCM-1-L2 treated with [Fe(acac)$_3$] showed a transition at 500 nm. UMCM-1-CAT also had an additional shoulder around 400 nm, which was indicative of the catechol substituent. UMCM-1-FeCAT exhibited a smaller shoulder at 400 nm, but displayed a strong absorbance between 500 and 600 nm consistent with known Fe-catecholate complexes.

It is important to note that neither UMCM-1-OH nor UMCM-1-CAT could be prepared by direct solvothermal synthesis from OH-bdc and CAT-bdc (Figure 2.15). This is consistent with the hypothesis that the free hydroxyl groups interfere with the Zn-carboxylate coordination and prevent formation of the UMCM lattice directly. To create these MOFs by PSM, it would be difficult to devise a strategy to directly hydroxylate an aryl group without harsh reaction conditions which is unsuitable for many crystalline systems, thus demonstrating the usefulness of the PSD approach.

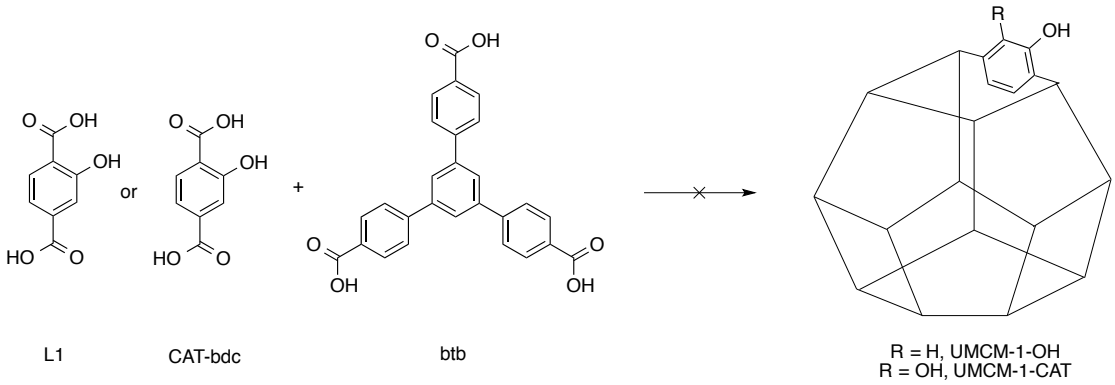

Figure 2.15. Direct synthesis attempts for UMCM-1-OH and UMCM-1-CAT.

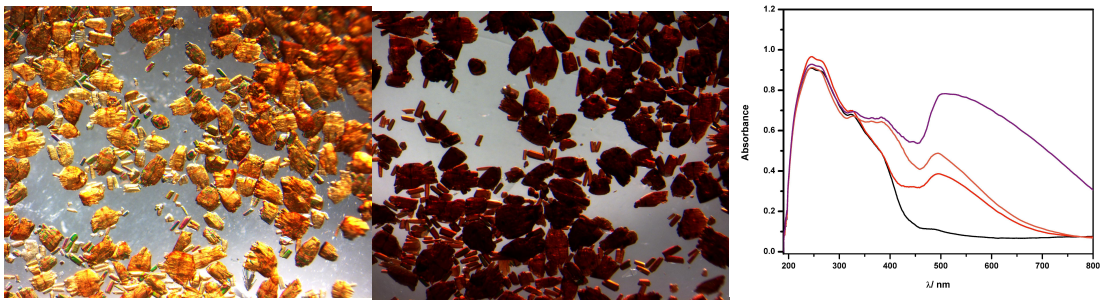

Figure 2.16. Optical microscopy photographs of UMCM-1-L2 after exposure with $Fe(acac)_3$ (left) and UMCM-1-FeCAT (middle). Solid state UV-Vis absorption spectra (right) of UMCM-1-L2 (black), UMCM-1-L2 + $Fe(acac)_3$ (red), UMCM-1-CAT (orange), and UMCM-1-FeCAT (purple).

2. III. Modulating PSD Capable Ligands

Chapter 1 described how multifunctional or 'multivariate' materials[28] have been realized using mixed-ligand strategies and various combinations of pre- and postsynthetic approaches.[28-33] Using a combination of these methods can lead to highly functionalized materials without complicating the synthetic conditions required to obtain the desired MOF. Above, a light-activated PSD reaction was utilized to

obtain materials with free metal binding groups inside a porous coordination polymer without destroying the integrity of the coordination bonds. There are no reports that compare the behavior of photolabile groups in a framework versus in solution. There is precedence for the MOF to modify solution state behavior as seen by Champness and George when monitoring charge transfer bands.[12] The remainder of Chapter 2 will explore a tandem PSD/PSM approach. Two different photolabile protected ligands (L1 and L3) will be used and their photocleavage at two different wavelengths will be investigated. L3, synthesized similarly to L1 and L2, was chosen as the additional methoxy groups has been shown to shift the λ_{max} in comparison to L1 (Scheme 2.2).[34]

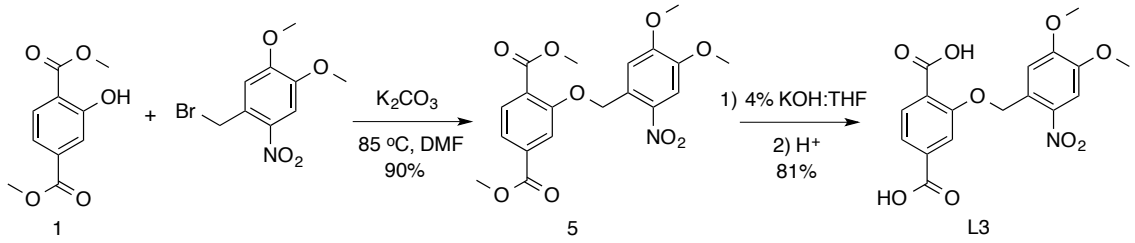

Scheme 2.2. Synthesis of protected ligand L3.

As described above, the incorporation of the relatively bulky L1 ligand into the UMCM-1 framework is well accommodated by the large pores in this material (14 and 32 Å).[20,35] However, we were somewhat surprised to find that both L1 and the dimethoxy analogue, L3, could be fully incorporated into an IRMOF lattice with relative ease (Figure 2.17).[1,36] Bulky ligands, such as 2,5-bis(benzyloxy)terephthalic acid have been incorporated into an IRMOF, but the degree of incorporation (with bdc as a co-ligand) was limited to ~30%, indicative of a steric restriction for bulky groups in the IRMOF lattice. All attempts to incorporate L2 into an IRMOF lattice were

unsuccessful, corroborating that steric interference could be a limiting factor. Combining L1 with $Zn(NO_2)_3•6H_2O$ in DMF or L3 with $Zn(NO_2)_3•6H_2O$ in DEF at 100 °C for 48 h produced cubic colorless or yellow crystals of IRMOF-1-L1 and IRMOF-1-L3, respectively (Figure 2.17). If DMF was used for the synthesis for IRMOF-1-L3, no crystals were obtained. The IRMOF lattice structure of both materials was directly confirmed by both PXRD (Figure 2.18) and single crystal XRD techniques. XRD structure determination of IRMOF-1-L1 and IRMOF-1-L3 unambiguously resolved the expected IRMOF lattice (Figure 2.19). In addition, diffuse electron density was found in the pores of both materials that was suggestive of the nitrobenzyl protecting groups; however, as seen in UMCM-1-L1 the substituents could not be clearly assigned due to severe disorder (Figure 2.19). The composition of the ligands in these frameworks was instead verified by other methods.

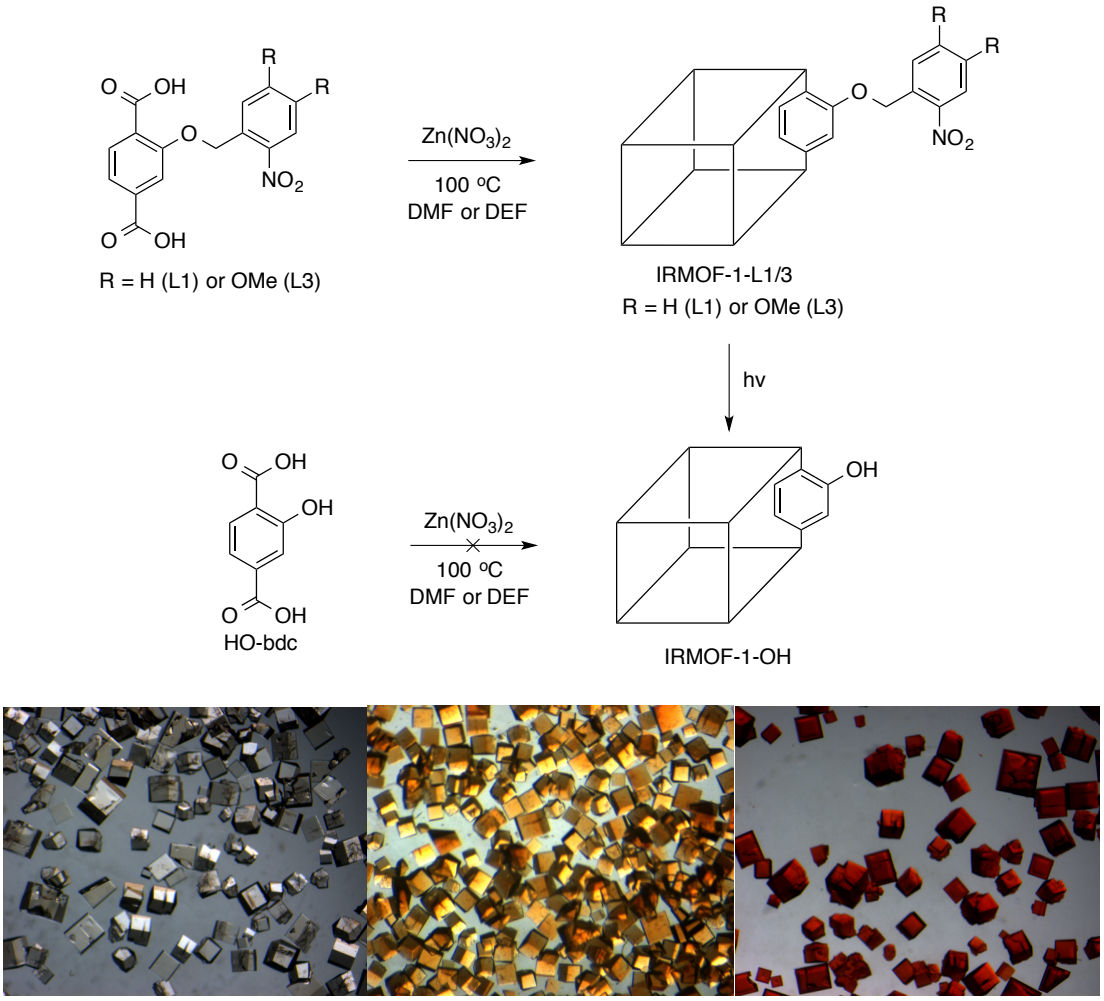

Figure 2.17. Schematic representation of synthesis and photochemical deprotection of IRMOF-1-L1/L3 to IRMOF-1-OH (top). Optical microscopy photographs of crystals of IRMOF-1-L1 (left), IRMOF-1-L3 (middle), and IRMOF-1-L1 post 365 nm (right) (bottom).

TGA of IRMOF-1-L1 displays a sharp weight loss at 260 °C (~40%) indicative of thermal liberation of the nitrobenzyl group (Figure 2.20). IRMOF-1-L3 does not show the same sharp weight loss, but has a gradual thermal trace that shows MOF degradation ~400 °C. Dissolution of IRMOF- 1-L1 and IRMOF-1-L3 crystals in dilute acid allowed for analysis of their chemical composition by ^{1}H NMR spectroscopy and ESI-MS. Both methods showed that ligands L1 and L3 were successfully incorporated into

the IRMOFs without degradation or loss of the protecting group prior to photoirradiation. BET surface area measurements with dinitrogen at 77 K gave values of 1407±36 m^2g^{-1} and 1164±17 m^2g^{-1} for IRMOF- 1-L1 and IRMOF-1-L3, respectively. Although these surface area values are lower than that of many other IRMOFs,[36] they are consistent with the introduction of the large nitrobenzyl groups into the framework pores.

IRMOF-1-L1 and IRMOF-1-L3 were irradiated in a photochemical reactor at one of two wavelengths, 365 or 400 nm, for 48 h to affect PSD of the materials and obtain IRMOFs with phenolic groups in the pores. The percent conversion of the PSD reaction was determined using ^{1}H NMR integrations after digesting the materials in acid. IRMOF-1-L1 gave 80–83% conversion to IRMOF-1-OH whether irradiated at either 365 nm or 400 nm. A concomitant increase in BET surface area, as observed in our previous studies, was found for the product IRMOF-1-OH, showing an average BET value of 2344±60 m^2g^{-1} (Figure 2.22). It should be noted that direct attempts to access IRMOF-1-OH were unsuccessful, similarly to direct incorporation in the UMCMs described above (Figure 2.15). IRMOF-1-L3 also did not show a substantial difference in PSD efficiency as a function of wavelength, giving between 53–58% conversion to IRMOF-1-OH whether irradiated at 365 or 400 nm. A steric effect may be contributing to this slow deprotection of IRMOF-1-L3, as the pores of this IRMOF are more restricted than IRMOF-1-L1 due to the additional methoxy groups on the protecting group. The dimethoxynitrosobenzaldehyde byproduct of the photochemical reaction may be more strongly retained in the pores and further interfere with the PSD reaction, due to the large extinction coefficient of dimethoxynitrosobenzaldehyde.[37] However, we find little evidence that these aldehyde byproducts remain in the framework (based on NMR and ESI-MS analysis of the final MOF products). All samples showed little to no

change in the PXRD patterns after irradiation, confirming the pristine nature of the crystals. Preservation of crystallinity was also readily apparent by visual inspection, where only a color change was observed, but the crystals appeared otherwise undisturbed as confirmed through single crystal XRD.

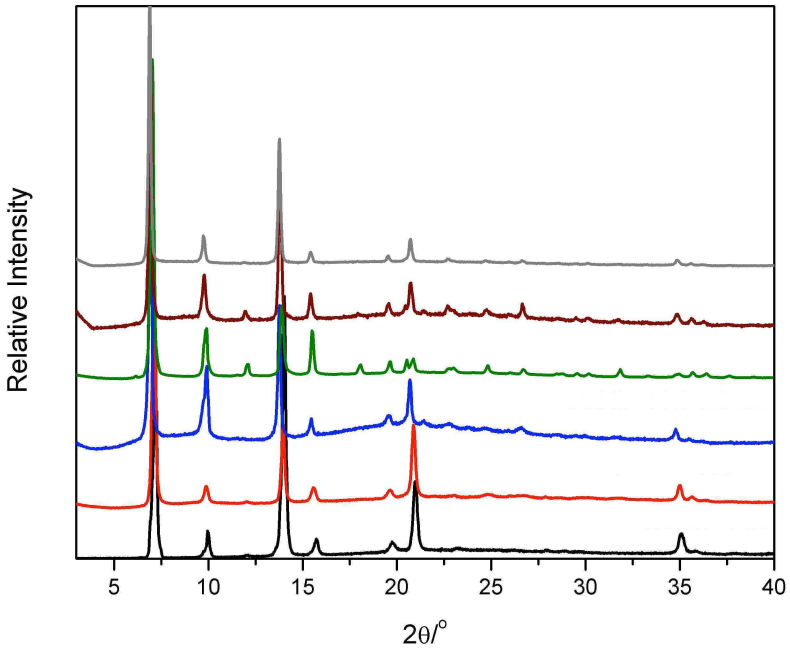

Figure 2.18. Powder X-ray diffraction of frameworks before and after PSD. From bottom to top: IRMOF-1-L1 (black), IRMOF-1-L1 365 nm (red), IRMOF-1-L1 400 nm (blue), IRMOF-1-L3 (green), IRMOF-1-L3 365 nm (maroon) and IRMOF-1-L3 400 nm (grey).

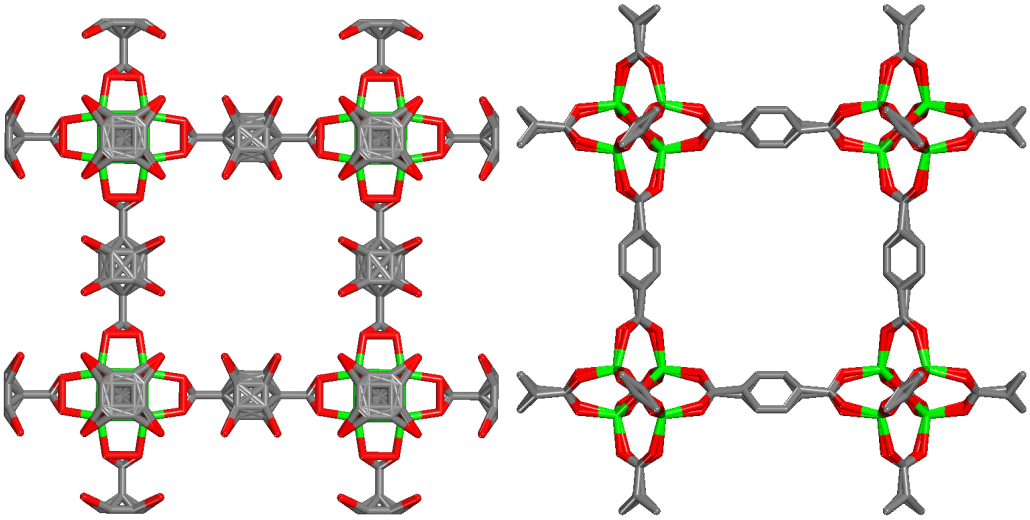

Figure 2.19. X-ray crystal structure for IRMOF-1-L1 (left) and IRMOF-1-L1 post 365 nm (right). Note the severe disorder of the oxygen atoms prior to PSD. Carbon atoms are shown in grey, oxygen in red, and zinc in green.

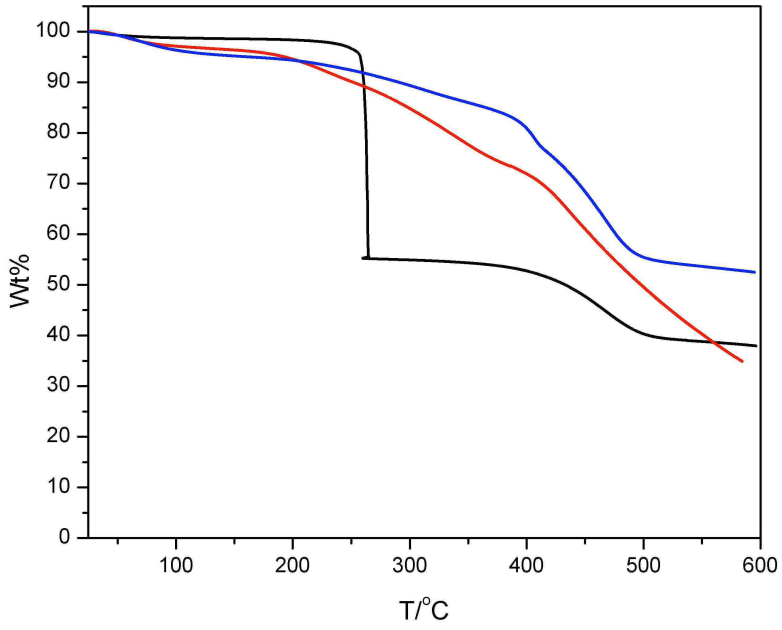

Figure 2.20. Thermogravimetric analysis trace of IRMOF-1-L1 (black), IRMOF-1-L3 (red), and IRMOF-1-L1 post exposure to 365 nm for 48 h (blue). The steep weight loss at 250 °C is consistent with the thermal liberation of the nitrobenzyl group as opposed to the degradation seen in UMCM-1-L1.

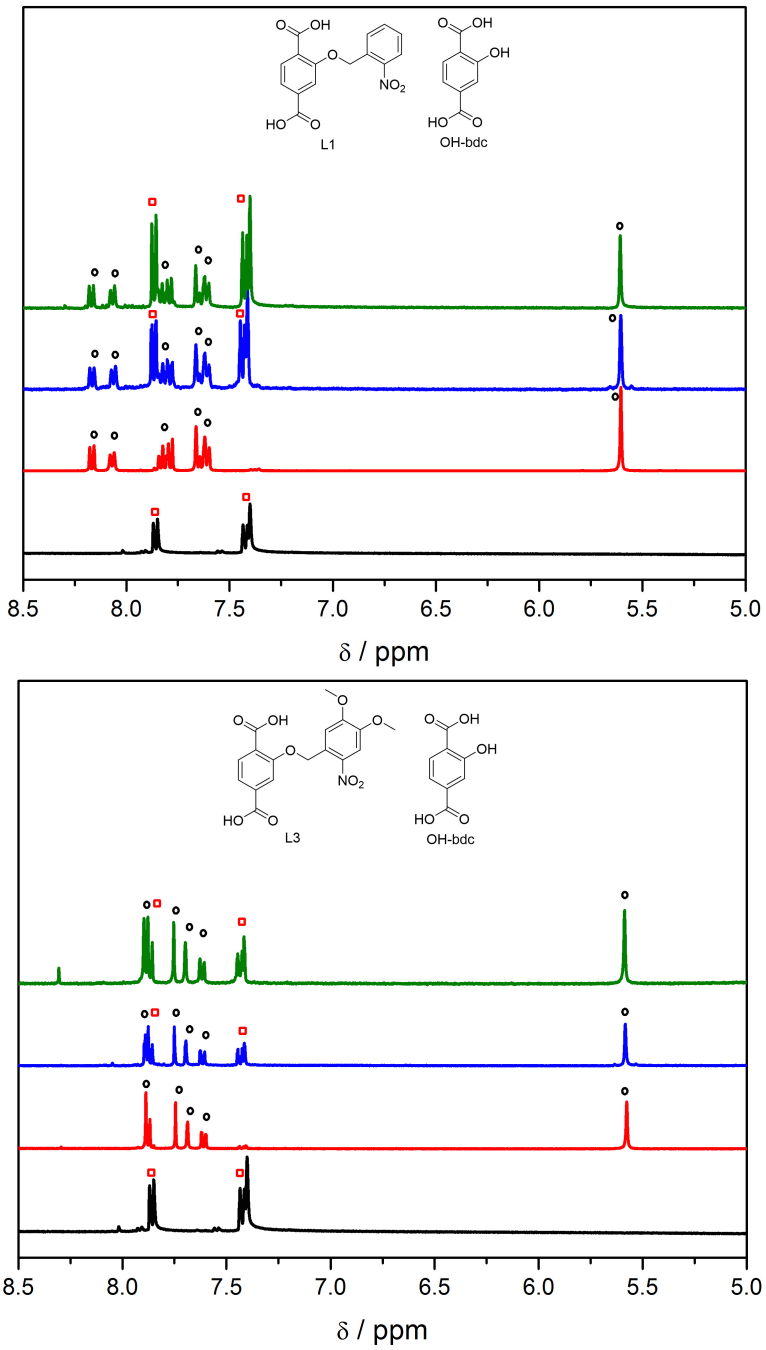

Figure 2.21. ^{1}H NMR spectra of digested MOFs before (red) and after PSD at 365 nm (blue) and 400 nm (green) for IRMOF-1-L1 (top) and IRMOF-1-L3 (bottom). The black trace is OH-bdc for reference. Quantitation was determined by the integration of the methylene peaks ~ 5.5 ppm in comparison to the aryl ~7.2 ppm peaks of OH-bdc. The starting ligands resonances are highlighted by black circles while the deprotected product is highlighted by red squares.

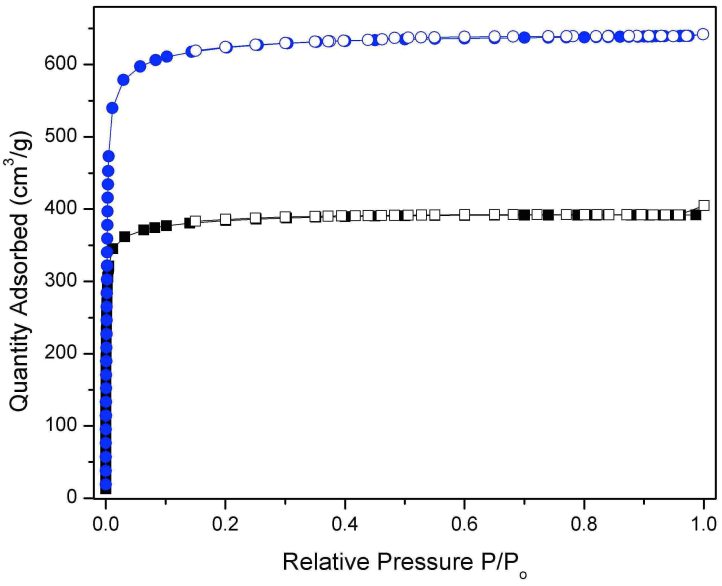

Figure 2.22. Dinitrogen isotherms of IRMOF-1-L1 before (black) and after (blue) exposure to 365 nm light. The large increase in saturation pressure is consistent with the deprotection of the nitrobenzyl group from majority of the bdc linkers.

Changing the electronics of the nitrobenzyl group is a common tactic used to shift the absorption wavelength for photocleavage.[34] Based on previous reports, it was expected that the nitrobenzyl group (L1) would cleave with a λ_{max} at 365 nm, while the dimethoxy derivative (L3) would cleave more effectively at 400 nm; however, in the MOFs the expected trend was not observed. Quantitative deprotection, as was seen in the UMCM system described above, was not achieved in these IRMOF materials, despite screening a variety of reaction conditions. The differences between the expected photochemical behaviour and our observations here may be due to a number of factors. As will be discussed below, we believe a combination of light absorption and scattering by the IRMOF explains, in part, the attenuation of the photochemical reactions. Both absorption and scattering diminish the amount of light that penetrates through the framework and thus impedes PSD.

2. IV. Results and Discussion - Tandem PSM/PSD

Mixed ligand approaches have been utilized to prepare highly functionalized MOF materials. Functional groups that can be introduced presynthetically can serve as chemical handles for PSM. In a recent study from our group, we investigated tandem PSM on a mixed ligand system. Two different BDC ligands, NH_2-BDC and Br-BDC, were incorporated into a UiO-66 framework and modified orthogonally via PSM.[38] In this case, the order in which the orthogonal PSM reactions were performed (i.e. PSM of NH_2-bdc before Br-BDC versus PSM of Br-BDC then NH_2-bdc) had no effect on the overall yields. Hence the PSM reactions could be performed in any order, allowing for the preparation of several bifunctional MOFs from a single parent material.

In order to investigate the possibility of performing tandem PSD-PSM, NH_2-bdc was chosen as the co-ligand to make mixed IRMOFs.[39] Upon mixing L1 and NH_2-BDC in a 3.8:1 ratio with $Zn(NO_2)_3$•$6H_2O$ in DEF at 100 °C for 48 h, amber-colored crystals of IRMOF-1-(L1)(NH_2) were obtained. The 3.8:1 ligand ratio gave the highest quality crystals based on visual inspection and PXRD analysis from a screening of a large number of ligand ratios and reaction conditions. ^{1}H NMR spectroscopy of the digested crystals indicate that NH_2-bdc comprised ~30% of the ligands of this IRMOF. PXRD (Figure 2.23) and single crystal XRD confirmed that IRMOF-1-(L1)(NH_2) possessed the correct topology, although the BDC substituents could not be assigned in the difference map. The BET surface area of IRMOF-1-(L1)(NH_2) was 1584±36 m^2g^{-1}, higher than IRMOF-1-L1, which is consistent with the smaller NH_2-bdc ligand being incorporated (Figure 2.23). TGA analysis shows a similar drop to IRMOF-1-L1 at 260 °C however only has a ~27% weight drop also indicative of a decreased amount of L1 in the material (Figure 2.24). Using similar conditions for L3 and NH_2-BDC in a 2:1 ratio,

amber blocks were obtained with ~40% NH_2-bdc incorporation. The more efficient incorporation of NH_2-bdc into IRMOF-1-(L1) (NH_2) and IRMOF-1-(L3)(NH_2) is attributed the greater solubility of NH_2-bdc when compared to L1 and L3. It is also possible that steric factors, L1 and L3 being much more bulky, play a role in the differences observed with respect to ligand integration and the overall low yields of IRMOF formation. IRMOF-1-(L3)(NH_2) gave a BET value 1615±10 m^2g^{-1}, understandably due to the larger L3 ligand, and a higher percentage of NH_2-bdc. TGA analysis was also similar to IRMOF-1-L3 as a steady weight loss is observed prior to framework degradation. Analogous to the orthogonal PSM mentioned previously, we explored two routes for tandem PSD-PSM: PSM followed by PSD (route 1), and PSD followed by PSM (route 2) (Scheme 2.3). These two routes were evaluated based on the best combination of percent PSM, percent PSD, and crystallinity of the final materials. It is worth noting that, like our previous study on tandem PSM, this methodology potentially leads to two intermediates and a final MOF from each starting framework.

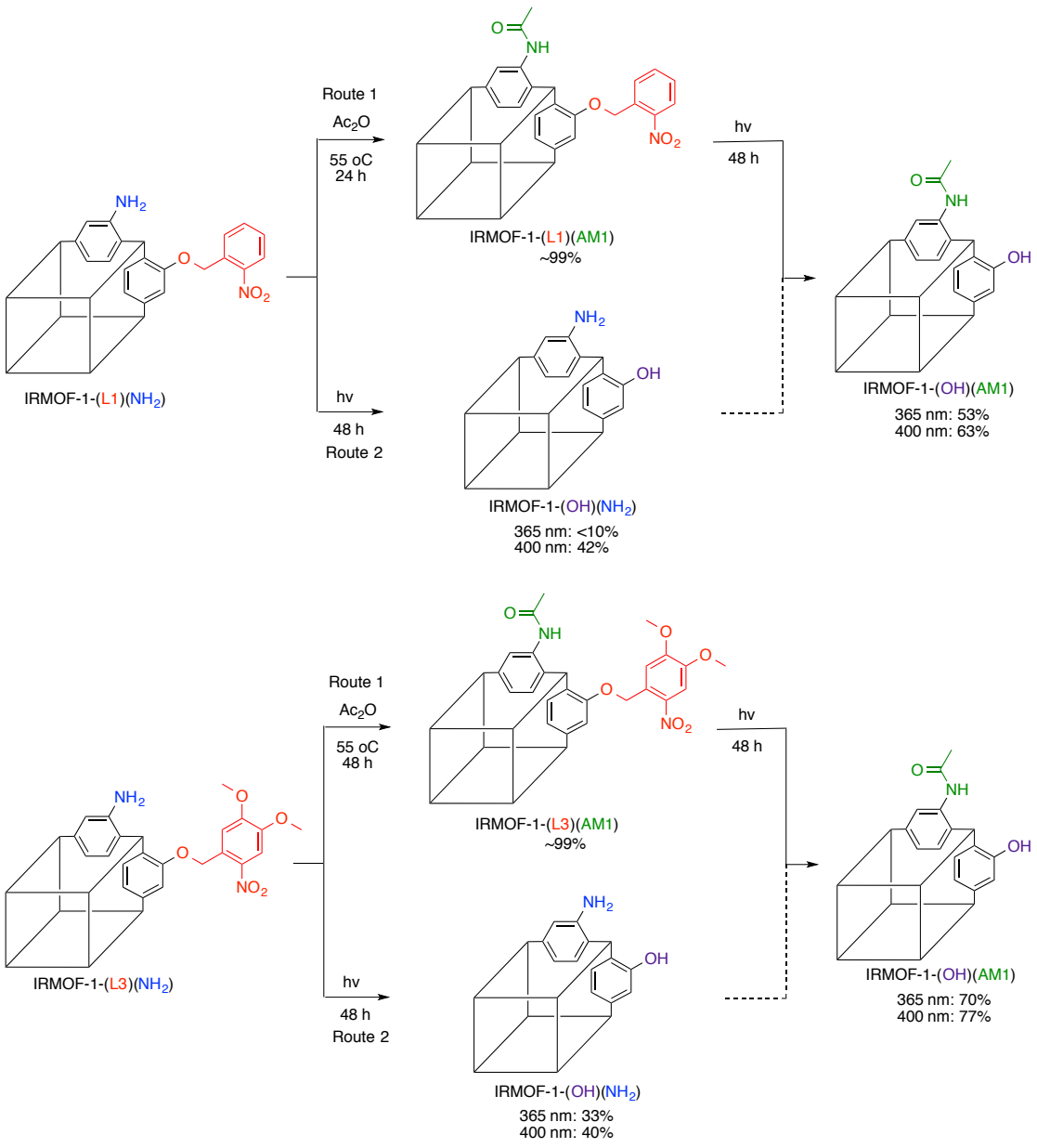

Scheme 2.3. Mixed MOF syntheses and subsequent PSD/PSM via two different routes. Route 1 is depicted through the top arrows and Route 2 is depicted on the bottom arrows.

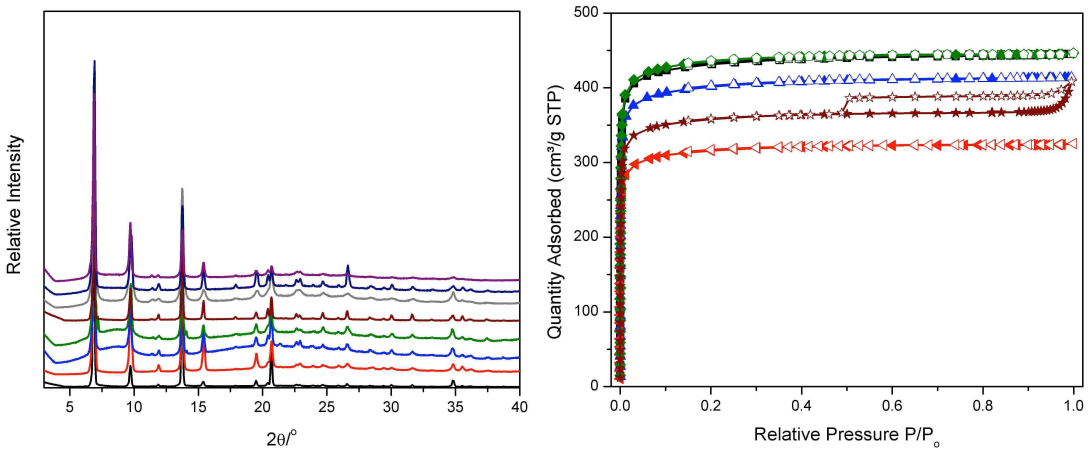

Figure 2.23. PXRD of mixed ligand IRMOFs (left). Starting from the bottom: IRMOF-1-(L1)(NH_2), IRMOF-1-(L1)(AM1), IRMOF-1-(L1)(AM1) 365 nm, IRMOF-1-(L1)(AM1) 400 nm, IRMOF-1-(L3)(NH_2), IRMOF-1-(L3)(AM1), IRMOF-1-(L3)(AM1) 365 nm, IRMOF-1-(L3)(AM1) 400 nm. Dinitrogen isotherms of mixed IRMOFs prior to PSD (right). IRMOF-1-(L1)(NH2) (black squares), IRMOF-1-(L1)(AM1) (blue triangles), IRMOF-1-(L3) (red triangles), IRMOF-1-(L3)(NH2) (green squares) and IRMOF-1-(L2)(AM1) (maroon stars).

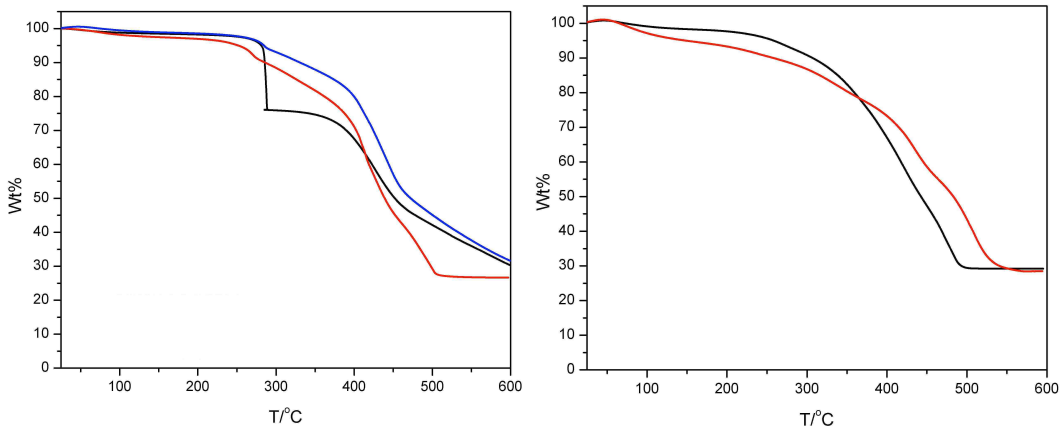

Figure 2.24. TGA traces of IRMOF-1-(L1)(NH_2) (black) following route 1 (left), IRMOF-1-(L1)(AM1) (red), and IRMOF-1-(L1)(AM1) post exposure to 365 nm (blue). Thermogravimetric analysis trace of IRMOF-1-(L3)(NH_2) (black) following route 2 (right) and IRMOF-1-(L3)(AM1) (red).

Using route 1, where PSM is performed before PSD, we found both IRMOF-1-(L1)(NH_2) and IRMOF-1-(L3)(NH_2) were quantitatively transformed to the acetamide IRMOF-1-(L1) (AM1) and IRMOF-1-(L3)(AM1), respectively. After PSM, PSD on IRMOF-1-(L1)(AM1) gave ~53–63% PSD at 365 or 400 nm (Figure 2.25). This is markedly lower than the photocleavage of IRMOF-1-L1 at either wavelength. Crushing the crystals gave only modest increases in the PSD yields of mixed IRMOFs (~10%). However, IRMOF-1-(L3)(AM1) gave ~70– 77% PSD at 365 or 400 nm, which is an improved yield when compared to IRMOF-1-L3 (Figure 2.26). Unfortunately, we were unable to identify reaction conditions where PSD in these IRMOFs would go to completion. Nonetheless, for route 1 it was found that L3 was a promising photochemical protecting group for PSD at both wavelengths in these mixed systems.

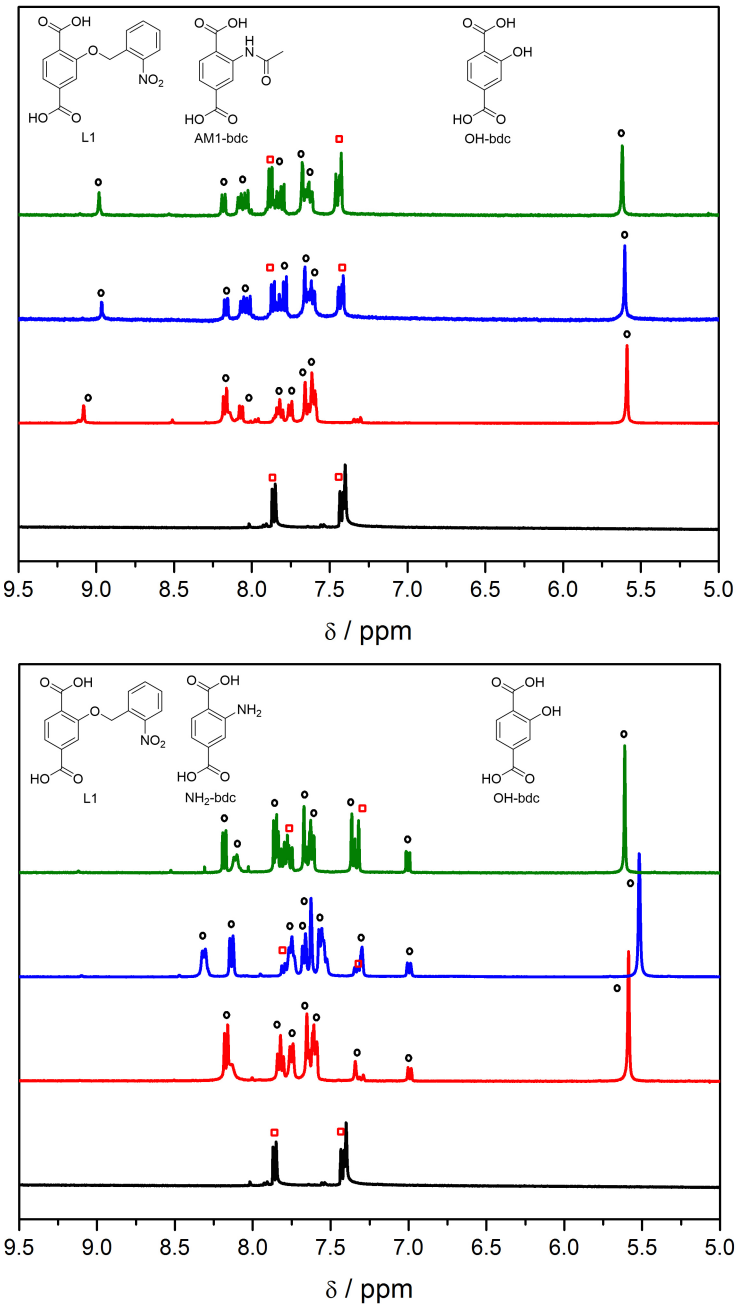

Figure 2.25. ^{1}H NMR of digested IRMOF-1-(L1)(AM1) (top, route 1) and IRMOF-1-(L1)(NH_2) (bottom, route 2) before (red trace) and after PSD at 365 nm (red) and 400 nm (green). Starting materials are marked with black circles and the product is marked by red squares. A ^{1}H NMR for an authentic sample of OH-bdc is provided (black) as reference. The resonances corresponding to the protected ligands are highlighted by black circles while the deprotected product is highlighted by red squares.

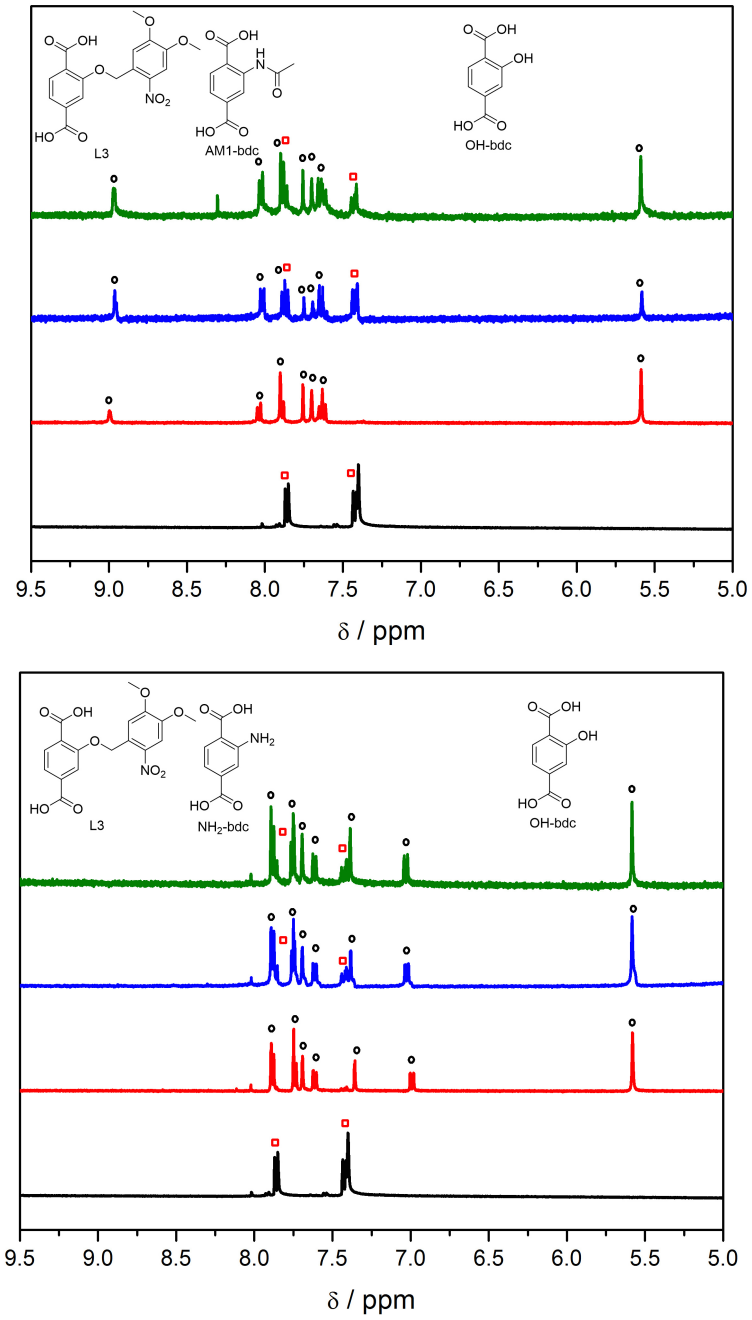

Figure 2.26. ^{1}H NMR of digested IRMOF-1-(L3)(AM1) (top, route 1) and IRMOF-1-(L3)(NH_2) (bottom, route 2) before (red trace) and after PSD at 365 nm (red) and 400 nm (green). Starting materials are marked with black circles and the product is marked by red squares. A ^{1}H NMR for an authentic sample of OH-bdc is provided (black) as reference. Resonances corresponding to the protected ligands are highlighted by black circles while the deprotected product is highlighted by red squares.

Route 2, where PSD was performed prior to PSM, gave less impressive results than route 1. Photolysis of IRMOF-1-(L1)(NH_2), at 365 nm shows minimal (<10%) PSD. The reason for this low yield is discussed in detail below. Additionally, this could be due to possible hydrogen bonding (with the NH_2 groups) that interferes the photochemical excitation required for the deprotection. At 400 nm, 42% PSD was observed, which is much lower than the 83% PSD observed for IRMOF-1-L1. Interestingly, IRMOF-1-(L3)(NH_2) shows 33% and 40% deprotection at 365 nm and 400 nm, respectively. This correlates better with the 53% and 58% PSD obtained with IRMOF-1-L3 at the same wavelengths. However, due to the generally lower than desired PSD results, route 2 was not further explored. Overall, it appears route 1 gives better PSD conversions than route 2. Unlike our previous study on tandem PSM, the order of PSD versus PSM was important for obtaining the desired materials. It should be noted that direct access to IRMOF-1-(OH)(NH_2) was unobtainable through direct solvothermal syntheses.

In order to understand the poor PSD at 365 nm for IRMOF-1-(L1)(NH_2), the absorption spectra of the homogeneous, free ligand systems were examined. UV-Vis spectroscopy studies on the methyl diester forms of the ligands provided some insight into the failure of these PSD reactions. Photocleavage of 2-nitrobenzyl groups has been well studied with the near-UV range (300–400 nm) providing the optimal wavelengths for promotion of this reaction. The λ_{max} for the methyl diesters forms of L1, NH_2-bdc, AM1-bdc, and HO-bdc were 310, 368, 330, and 325 nm, respectively (Figure 2.27). This indicates that the reduced PSD of L1 in IRMOF-1-(L1)(NH_2) can be attributed to the strong absorption by the NH_2-bdc ligands compared to L1 at 365 nm. Based on this hypothesis, the solution spectra suggest that the addition of the methoxy groups in L3 should alter the PSD behavior in IRMOF-1-(L3)(NH_2) as observed (vide supra).

Previous reports indicate that the addition of methoxy substituents allows photocleavage at wavelengths up to 420 nm. The broad and very intense absorption of L3 from 300–400 nm drastically increase the efficiency of L3 to absorb at 365 nm thus rendering the observed PSD in the presence of NH_2-bdc much more efficient.

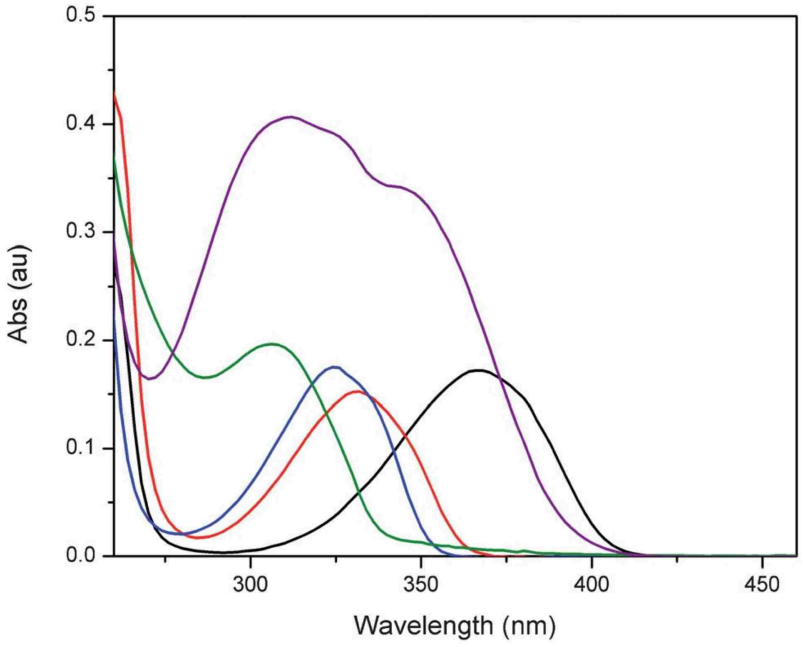

Figure 2.27. UV-Vis absorption spectra of the methyl diester form of several ligands (50 μM) in EtOAc. L3 (purple), L1 (green), OH-bdc (blue), AM1 (red), NH_2 (black).

The solution UV-Vis spectroscopy also assisted in our understanding of the more effective PSD achieved when using route 1. Acetylation of the amine group to give IRMOF-1-(L1)(AM1) blue-shifts the λ_{max} to 330 nm, thus reducing the interfering absorption at 365 nm and enhancing PSD. Additionally, IRMOF-1-(L3)(AM1) deprotects most out of all the mixed MOFs studied presumably due to a combination of the wide absorbing L3 comprises 60% of the material and the now unobtrusive AM1.

2. V. Conclusions

In summary, hydroxy and catechol moieties were successfully incorporated into a MOF by using postsynthetic photochemical deprotection. UMCM-1-OH and UMCM-1-CAT maintained their structural and thermal stabilities after exposure to the photochemical conditions. Moreover, UMCM-1-OH and UMCM-1-CAT exhibited significant increases in porosity, which is consistent with the liberation of the bulky nitrobenzyl substituents. PSD is the only method to leave the lattice untouched and reveal new functional groups while also freeing up pore space. Preliminary metalation tests with UMCM-1- CAT confirmed the presence of the catechol unit, as evidenced by binding of Fe^{3+} to the MOF. UMCM-1-OH and UMCM-1-CAT demonstrate the promise of postsynthetic deprotection to obtain MOFs with unprecedented functionality.

Research that followed this work devised a method to incorporate CAT-bdc into a more robust UiO framework.[40] After metalation, this MOF demonstrated the utility of a recyclable and reusable catalytic species embedded into a MOF lattice. This study validated the hypothesis developed during the work discussed above.

To elaborate upon the successful PSD in the UMCM system we also studied the effects of PSD of nitrobenzyl protected MOFs in comparison to the homogeneous systems. IRMOFs, comprised of a single photolabile protected ligand, showed moderate cleavages under the deprotection conditions but did not deprotect as anticipated based on homogenous studies, perhaps due to the larger density of cleavable groups in an IRMOF than in the UMCM system. The utility of multiple postsynthetic approaches (PSD and PSM) on a single, bifunctional IRMOF has been demonstrated and shown to be an effective method of obtaining multifunctional materials with minimal extraneous expenditure. However, optimization for the

material of interest is still required. The ability to combine pre- and various post-synthetic methods is a key step in obtained highly tailorable materials for technological applications.

2. VI. Experimental

Starting materials and solvents were purchased and used without further purification from commercial suppliers (Sigma-Aldrich, Alfa Aesar, EMD, TCI, Cambridge Isotope Laboratories, Inc., and others). $^{1}H/^{13}C$ NMR spectra were recorded on a Varian FT-NMR spectrometer (400 MHz). Elemental analysis was performed by NuMega Resonance Laboratories, San Diego, CA. H_3btb, OH-bdc, and CAT-bdc were synthesized according to literature procedures.[17,19,21]

2. VI. i. Ligand Synthesis

1. OH-bdc (2.42 g, 13.3 mmol) was dissolved in 250 mL of MeOH. Conc. H_2SO_4 (5 mL) was added and the solution was refluxed overnight (~18 h). Upon cooling the reaction to room temperature, the MeOH was removed under vacuum. The remaining solution was neutralized with saturated $NaHCO_3$(aq) solution and the product was extracted with $CHCl_3$ (3×50 mL). The organic layer was isolated, washed with brine (4×15 mL), and the $CHCl_3$ was removed under vacuum to obtain a white solid. Yield: 2.65 g (95%). ^{1}H NMR ($CDCl_3$, 400 MHz, 25°C): δ 3.92 (s, 3H; CO_2CH_3), 3.98 (s, 3H; CO_2CH_3), 7.52 (dd, J(H,H) = 8 Hz, J(H,H) = 1.6 Hz, ^{1}H; ArH), 7.63 (d, J(H,H) = 1.6 Hz, 1H; ArH), 7.90 (d, J(H,H) = 8.4 Hz, 1H; ArH). ^{13}C NMR ($CDCl_3$, 100 MHz, 25 °C): δ 52.5, 52.6, 115.7, 118.8, 119.7, 130.0, 136.4, 161.2, 165.9, 169.9. ESI-MS(+): m/z 209.23 $[M-H]^-$.

3. Compound 1 (1.83 g, 8.7 mmol) was dissolved in 40 mL of DMF. 2-nitrobenzyl bromide (2.26 g, 10.4 mmol) and K_2CO_3 (2.4g, 17.3 mmol) were added and the mixture was stirred at 85 °C for 2 h. After cooling to room temperature, the K_2CO_3 was

filtered off, and the solvent removed under vacuum to reveal a slightly orange solid. Yield: 2.74 g (90%) . ^{1}H NMR ($CDCl_3$, 400 MHz, 25°C): δ 3.95 (s, 3H; CO_2CH_3), 3.95 (s, 3H; CO_2CH_3), 5.62 (s, 2H, CH_2) 7.52 (t, *J*(H,H) = 8 Hz, *J*(H,H) = 0.8 Hz,1H; ArH), 7.74 (q, *J*(H,H) = 7.6 Hz, *J*(H,H) = 1.2 Hz, 3H; ArH), 7.92 (d, *J*(H,H) = 8 Hz, 1H; ArH), 8.22 (t, *J*(H,H) = 8 Hz, *J*(H,H) = 1.2 Hz, 2H; ArH). ^{13}C NMR ($CDCl_3$, 100 MHz, 25 °C): δ 52.3, 52.6, 67.7, 114.0, 122.0, 124.2, 124.9, 128.4, 128.8, 131.9, 133.1, 134.3, 134.8, 146.6, 157.3, 165.7, 165.9. ESI-MS(+): *m*/z 345.87[M+H] $^{+}$, 362.79[M+NH_4] $^{+}$, 368.07[M+Na]$^{+}$.

L1. Compound 3 (2.47 g, 7.1 mmol) was dissolved in 80 mL THF followed by the addition of 4% KOH (aq) (80 mL). After stirring the solution at room temperature for 2 h, the solution was diluted with water (50 mL) and washed with diethyl ether twice (25 mL). The aqueous layer was collected and acidified to pH~1 with concentrated HCl to precipitate out an off white solid. Th e solid was collected via vacuum filtration, washed with HO, and dried under vacuum with heat. Yield: 2.2 g (98%). ^{1}H NMR (DMSO-d_6, 400 MHz, 25 °C): δ 5.60 (s, 2H; CH_2), 7.62 (m, 3H; ArH), 7.78 (d, *J*(H,H) = 8 Hz, 1H; ArH), 7.82 (t, *J*(H,H) = 7.6 Hz, *J*(H,H) = 1.2 Hz, 1H; ArH), 8.06 (d, *J*(H,H) = 8 Hz, 1H; ArH), 8.16 (dd, *J*(H,H) = 8 Hz, *J*(H,H) = 1.2 Hz, 1H; ArH). ^{13}C NMR (DMSO-d_6, 100 MHz, 25 °C): δ 67.4, 114.2, 122.1, 125.3, 126.0, 129.2, 129.4, 131.4, 133.1, 134.6, 135.2, 147.2, 146.8, 166.9, 167.1. ESI-MS(-): *m*/z 316.17[M-H]$^{-}$.

2. CAT-bdc (10 g, 50 mmol) was dissolved in 250 mL MeOH. Conc. H_2SO_4 (~2 mL) was added and the solution was refluxed overnight. After cooling the reaction to room temperature, MeOH was removed under vacuum to yield a brown solid. The crude solid was neutralized with sat. $NaHCO_3$ and the product was extracted using $CHCl_3$. The organic layers were combined, dried with $MgSO_4$, filtered, and concentrated under vacuum to yield a light beige solid. Yield: 6.9 g (60%). ^{1}H NMR ($CDCl_3$, 400 MHz, 25°C): δ 3.99 (s, 6H), 7.34 (s, 2H), 10.94 (s, 2H). ^{13}C NMR ($CDCl_3$, 100

MHz, 25 °C): δ 52.9, 116.0, 118.5, 151.7, 170.3. ESI-MS(+): *m*/z 227.05 $[M+H]^+$, 243.93 $[M+NH_4]^+$.

4. Compound 2 (2.0 g, 8.8 mmol) was dissolved in 60 mL DMF. 2-nitrobenzyl bromide (4.2 g, 19 mmol, 2.2 eq) and K_2CO_3 (5.1 g, 37 mmol, 4.2 eq) were subsequently added and the mixture was left to stir at 80 °C for 2 h. After cooling the mixture to room temperature, H_2O was added to the solution to precipitate out the crude product. A pale yellow solid was isolated by vacuum filtration and was washed with copious amounts of H_2O to remove K_2CO_3 and DMF. T he solid was then washed with MeOH to remove any unreacted nitrobenzyl bromide. An off white solid was obtained and dried under vacuum. Yield: 3.7 g (85%). ^{1}H NMR ($CDCl_3$, 400 MHz, 25°C): δ 3.84 (s, 6H), 5.47 (s, 4H), 7.35 (dt, 2H, *J* = 0.8 Hz, 7.8 Hz), 7.54 (dt, 2H, *J* = 1.2 Hz, 7.6 Hz),7.68 (s,2H), 7.90(dd, 2H, *J* = 1Hz, 7.8Hz), 7.99 (dd, 2H, *J* = 1.2Hz, 8Hz). ^{13}C NMR ($CDCl_3$, 100 MHz, 25 °C): δ 52.8, 72.9, 124.7, 126.5, 128.1, 128.2, 130.0, 134.0, 134.3, 146.3, 152.7, 165.5. ESI- MS(+): *m*/z 519.17 $[M+NH_4]^+$, 520.19 $[M+Na]^+$.

L2. Compound 4 (2.0 g, 4.0 mmol) was dissolved in 80 mL of THF. 4% KOH (aq) (80 mL) was added to the solution and the reaction was left stirring at room temperature for 2 h. After removing THF under vacuum, the solution was filtered and washed once with diethyl ether. The solution was subsquently acidified to pH~1 using a 1M HCl solution resulting in an off white solid. The off white solid was collected by vacuum filtration, washed with copious amounts of H_2O, and dried under vacuum with heat. Yield: 1.7 g (94%). ^{1}H NMR (DMSO-d_6, 400 MHz, 25 °C): δ 5.36 (s, 4H), 7.50 (t, 2H, *J* = 7.6 Hz), 7.58 (s, 2H), 7.63 (t, 2H, *J* = 7.6 Hz), 7.79 (d, 2H, *J* = 8 Hz), 8.00 (d, 2H, *J* = 8.4 Hz). ^{13}C NMR (DMSO-d_6, 100 MHz, 25 °C): δ 72.9, 125.0, 126.3, 129.1, 129.2, 131.3, 133.5, 134.5, 146.9, 151.7, 166.9. ESI-MS(+): *m*/z 466.92 $[M+H]^-$.

5. Compound 1 (1.2 g, 5.6 mmol) was dissolved in 60 mL of DMF. 4,5-

Dimethoxy-2-nitrobenzyl bromide (2.0 g, 7.3 mmol) and K_2CO_3 (1.5 g, 11.1 mmol) were added and the mixture was stirred at 80 °C for 1 h. While hot, the K_2CO_3 was filtered off, and water was added to the filtrate to precipitate out the product. The pale yellow solid was isolated by vacuum filtration and washed with MeOH to remove any unreacted starting materials. Yield: 2.04 g (90%). ^{1}H NMR ($CDCl_3$, 400 MHz, 25°C): δ 3.89 (s, 3H; CO_2CH_3), 3.97 (s, 3H; OCH_3), 3.99 (s, 3H; OCH_3), 4.13 (s, 3H; CO_2CH_3), 5.62 (s, 2H, CH_2) 7.72 (d, 1H; Ar*H*), 7.80 (s, 2H; Ar*H*), 7.94 (d, 1H; Ar*H*), 8.06 (s, 1H; Ar*H*). ESI-MS(+): *m*/z 405.69$[M+H]^+$, 427.98$[M+Na]^+$.

L3. Compound 5 (1.68 g, 4.1 mmol) was dissolved in THF (500 mL) followed by the addition of 4% KOH (aq) (250 mL). After stirring the solution at room temperature for 2 h, the solution was diluted with water (100 mL) and washed with diethyl ether twice (50 mL). The aqueous layer was collected and acidified to pH~1 using concentrated HCl to precipitate out a yellow solid. The solid was isolated via vacuum filtration, washed with H_2O, and dried under vacuum at room temperature. Yield: 1.27 g (81%). ^{1}H NMR (DMSO-d_6, 400 MHz, 25°C): δ 3.88 (s, 3H; OCH_3), 3.94 (s, 3H; OCH_3), 5.58 (s, 2H, CH_2) 7.61 (d, 1H; Ar*H*), 7.69 (s, 1H; Ar*H*), 7.75 (s, 1H; Ar*H*), 7.88 (d, 2H; Ar*H*). ESI-MS(-): *m*/z 375.85 $[M-H]^-$.

2. VI. ii. MOF Synthesis

UMCM-1-L1. $Zn(NO_2)_3$•$6H_2O$ (3.26 g, 10.9 mmol), H_3btb (0.4 g, 0.91 mmol), and L1 (0.87 g, 2.75 mmol) were dissolved in 100 mL DMF. The solution was sonicated and divided into 10 mL portions and transferred to 10 scintillation vials (20 mL capacity each). The vials were placed in a sand bath and the bath was placed in an isothermal oven heated at 85 °C for 48 h. Clear needle clusters were found in each vial. Once the vials were cooled to room temperature, the mother liquor was decanted and the crystals were washed with DMF (3×10 mL), rinsed with $CHCl_3$ (2×10

mL) and left to sit for 3 days with fresh $CHCl_3$ added every 24 h. The crystals were stored in $CHCl_3$ until needed. The average yield of dried UMCM-1-L1 per vial was approximately 40 mg (37% based on BTB, 0.038 mmol per ligand). Anal. Calcd for $Zn_4O(C_{27}H_{15}O_6)_{1.33}$ ($C_{15}H_9NO_7$): C, 52.18; H, 2.49; N, 1.20. Found: C, 52.09; H, 3.78; N, 1.27. *Upon photochemical deprotection to UMCM-1-OH:* Anal. Calcd for $Zn_4O(C_{27}H_{15}O_6)_{1.33}$ ($C_8H_4O_5$): C, 50.87; H, 2.33; N, 0. Found: C, 50.99; H, 3.23; N, 0.43.

UMCM-1-OH Direct Synthesis Attempt. OH-bdc (0.51 g, 2.8 mmol), H_3btb (0.4 g, 0.91 mmol), and $Zn(NO_2)_3$•$6H_2O$ (3.26 g, 10.9 mmol) were dissolved in 100 mL DMF. The solution was sonicated, divided into 10 mL portions, and transferred to 10 scintillation vials (20 mL capacity each). The vials were placed in a sand bath and the bath was placed in an oven and heated to 85 °C for 48 h. No solid products were generated.

UMCM-1-L2. L2 (1.26 g, 2.7 mmol), H_3btb (0.34 g, 0.78 mmol), and $Zn(NO_2)_3$•$6H_2O$ (3.22 g, 12.3 mmol) was dissolved in 100 mL of DMF by sonication. The solution was split into 10 mL portions and placed into 20 mL scintillation vials. The vials were then transferred to an isothermal oven at 85 °C for 48 h. Colorless needle clusters were found in all vials. The needle clusters were washed with DMF (3×10 mL) and soaked in $CHCl_3$ (12 mL) overnight. After 24 h, the $CHCl_3$ was decanted from the vial and fresh $CHCl_3$ was added. The solution was replaced with fresh $CHCl_3$ every 24 h for a total of 3 days and the crystals were stored in $CHCl_3$ until further used. Yield: 50 mg (49% based on btb, 0.04 mmol per ligand). Anal. Calcd for $Zn_4O(C_{27}H_{15}O_6)_{1.33}$ ($C_{22}H_{14}N_2O_{10}$): C, 52.57; H, 2.59; N, 2.12. Found: C, 51.71; H, 3.95; N, 2.24. *Upon photochemical deprotection to UMCM-1-CAT:* Anal. Calcd for $Zn_4O(C_{27}H_{15}O_6)_{1.33}$ $(C_8H_4O_6)_{0.75}$ $(C_{15}H_9NO_8)_{0.125}$ $(C_{22}H_{14}N_2O_{10})_{0.125}$: C, 50.65; H, 2.36; N, 0.48. Found: C, 48.49; H, 3.82; N, 0.85.

UMCM-1-CAT Direct Synthesis Attempt. CAT-bdc (0.053 g, 0.027 mmol), H_3btb (0.034 g, 0.078 mmol), and $Zn(NO_2)_3$•$6H_2O$ (0.322 g, 1.23 mmol) were dissolved in either 10 mL of DEF or DMF with sonication. The vials were then transferred to an oven and heated at 85 °C for 48 h. A dark orange-brown solid was found in reaction mixtures using either DEF or DMF as solvent. PXRD analysis of the products indicated that neither material was UMCM-1-CAT.

Photochemical deprotection. UMCM-1-OH: One vial of UMCM-1-L1 (40 mg) was rinsed with EtOAc (3×10 mL) and transferred to a quartz vessel with 20 mL capacity. The solution was decanted and EtOAc (8 mL) was added. The vessel was placed inside a Rayonet RPR-200 photoreactor with 365 nm lamps. After irradiating the samples for 3 h, the yellow supernatant was decanted and the light orange crystals were rinsed with EtOAc (3×5 mL). Fresh EtOAc (8 mL) was added and the vessel was placed back inside the photoreactor chamber. This rinsing process was repeated once more at 20 h. After 24 h, the crystals were washed with EtOAc (3×10 mL) and exchanged back into $CHCl_3$ (2×10 mL) and soaked overnight in fresh $CHCl_3$ (10 mL). *UMCM-1-CAT:* One vial of UMCM-1-L2 (50 mg) was split into 10-15 mg portions and transferred to four scintillation vials (20 mL capacity). EtOAc (15 mL) was added to each vial and all four vials were placed inside a Rayonet RPR-200 photoreactor with 365 nm lamps. After irradiating the samples for 1-2 h the yellow supernatant was decanted. Fresh EtOAc (15 mL) was added to each vial and the vials were placed back inside the photoreactor chamber. In a typical 24 h period, the crystals were rinsed with $CHCl_3$ and resoaked in fresh EtOAc twice within a 12 hour span and were agitated once inbetween to ensure equal exposure. After 48 h, the four vials were recombined and the crystals were washed with EtOAc (3 x 10 mL). Samples for metallation were kept in EtOAc while gas sorption samples were washed with $CHCl_3$ (3

x 10 mL) and soaked overnight in fresh $CHCl_3$ (12 mL).

UMCM-1-L2 treated with Fe(acac)$_3$. $Fe(acac)_3$ (14 mg, 0.04 mmol) was added to UMCM-1-L2 in 2 mL of EtOAc. After 24 h at RT, the supernatant was decanted and the crystals were washed profusely with EtOAc (4×10 mL). The crystals were soaked in 10 mL of EtOAc overnight and the process was repeated for a total of 3 days or until the supernatant was colorless. The crystals were washed with $CHCl_3$ (3×10 mL) and stored in $CHCl_3$ (12 mL) until further needed.

UMCM-1-FeCAT: $Fe(acac)_3$ (14 mg, 0.04 mmol) was added to UMCM-1-CAT (40 mg) in 2 mL of EtOAc. After 24 h at RT, the supernatant was decanted and the crystals were washed profusely with EtOAc (4×10 mL). The crystals were soaked in 10 mL of EtOAc overnight and the process was repeated for a total of 3 days or until the supernatant was colorless. The crystals were washed with $CHCl_3$ (3×10 mL) and stored in $CHCl_3$ (12 mL) until further needed.

IRMOF-1-OH Direct Synthesis Attempt. Under identical conditions to IRMOF-1-L1 no solid material was obtained.

IRMOF-1-(OH)(NH_2) Direct Synthesis Attempt. Under identical solvothermal conditions to IRMOF-1-(L1)(NH_2), using varying ratios of NH_2-bdc to OH-bdc, no solids were obtained that incorporated both ligands in either DMF or DEF.

2. VI. iii. MOF Characterization Methods

Digestion and Analysis by ^1H NMR. Approximately 5 mg of MOF was dried under vacuum at 100 °C (or used immediately after BET analysis) and digested in 500 μL of DMSO-d_6 and 100 μL of dilute DCl (23 μL of 35% DCl in D_2O diluted with 1.0 mL of DMSO-d_6). All percentages of PSD are reported from two independent samples.

Digestion and Analysis by ESI-MS. ESI-MS was performed using a ThermoFinnigan LCQ-DECA mass spectrometer, and the data was analyzed using the

Xcalibur software suite. Samples for analysis by ESI- MS were prepared by either 10 μL of digested ^{1}H NMR solution diluted in 0.5~1 mL of MeOH or by digesting protected and deprotected MOF crystals (0.1~1 mg) in 1 mL of MeOH with sonication.

Thermal Analysis. Approximately 8-15 mg of protected and deprotected MOF (dried after gas sorption analysis) was used for TGA measurements. Samples were analyzed under a stream of dinitrogen using a TA Instrument Q600 SDT running from room temperature to 600 °C with a scan rate of 5 °C/min.

PXRD Analysis. Approximately 15 mg of MOF (soaked in DMF), except for UMCM-1-L2 (soaked in $CHCl_3$), or UMCM-1-CAT (soaked in toluene) was air dried before PXRD analysis. Powder X-ray diffraction (PXRD) data were collected at ambient temperature on a Bruker D8 Advance diffractometer at 40 kV, 40 mA for Cu Kα (α = 1.5418 Å), with a scan speed of 3 or 5 sec/step, a step size of 0.02° in 2θ, and a 2θ range of 2-35°.

BET Surface Area Analysis. Approximately 40-100 mg of protected and deprotected MOF (previously soaking in $CHCl_3$) was evacuated on a vacuum line for a minimum of 2 h (protected UMCM), a minimum of 5 min (all other MOFs). The sample was then transferred to a preweighed sample tube and degassed at 25 °C on an Micromeritics ASAP 2020 Adsorption Analyzer for a minimum of 12 h or until the outgas rate was <5 μmHg. The sample tube was re-weighed to obtain a consistent mass for the degassed protected or deprotected UMCM. BET surface area (m^2g^{-1}) measurements were collected on three independent samples of each MOF at 77 K by dinitrogen on a Micromeritics ASAP 2020 Adsorption Analyzer using the volumetric technique.

Single Crystal X-ray Diffraction. Single crystals of protected and deprotected MOFs in $CHCl_3$ were mounted on nylon loops with Paratone oil and placed under a

nitrogen cold stream (200 K). Data was collected on a Bruker Apex diffractometer using Mo Kα radiation (α = 0.71073 Å) controlled using the APEX 2010 software package. A semiempirical method utilizing equivalents was employed to correct for absorption. All data collections were solved and refined using the SHELXTL suite. All protected and deprotected UMCM were treated with the "squeeze" protocol in PLATON to account for electron density associated with the nitrobenzyl substituents and for partially occupied or disordered solvent (e.g., $CHCl_3$) within the porous framework. Structural details for UMCM (both protected and deprotected) are available at the CCDC under deposition numbers 786348, 786349, 786350, and 786351.

UV-Vis Spectroscopy. Absorption spectra of a 1.0 mL solution of methyl diester form of the ligands was prepared at 50 μM concentration in EtOAc and spectra were collected at room temperature.

Geometric Calculation of Surface Areas. The accessible surface area of each structure was calculated from a simple Monte Carlo integration technique, described previously,[41,42] where a probe molecule is effectively "rolled" over the framework surface. Briefly, a probe molecule was randomly inserted around each of the framework atoms in turn and checked for overlap with other framework atoms. The fraction of probe molecules that did not overlap with other framework atoms was then used to calculate the accessible surface area. The probe diameter was taken as the van der Waals diameter of nitrogen, 3.72 Å. By this method the calculated BET surface areas for UMCM-1-L2 and UMCM-1-CAT were 3493 and 4120 m^2g^{-1}, respectively.

2. VII. Acknowledgements

Texts, schemes, and figures in this thesis are, in part, reprints of the material in the following publications as listed: Allen, C. A..; Cohen, S. M. Near-UV Photo-Induced Modification in Isoreticular Metal-Organic Frameworks *J. Mater. Chem.* **2012**, *22*, 10188-10194. Tanabe, K. K.; Allen, C. A..; Cohen, S. M. Photochemical Activation of a Metal-Organic Framework to Reveal Functionality *Angew. Chem. Int. Ed.* **2010**, *49*, 9730-9733. The dissertation author was the primary researcher and the co-authors listed also contributed to the research. Permission to reproduce these publications was granted by John Wiley and Sons, Inc., copyright 2010, and The Royal Society of Chemistry, copyright 2012.

2. VIII. Appendix

Table 2.1. Crystal Data and structure refinement for UMCM-1-L1 before and after 365 nm PSD.

Identification code	UMCM-1-L1	UMCM-1-OH
Empirical formula	$C_{51}H_{29}NO_{16}Zn_4$	$C_{44}H_{24}O_{14}Zn_4$
Formula weight	1173.23	1038.11
Temperature	205(2) K	200(2) K
Wavelength	0.71073 Å	0.71073 Å
Crystal system	Hexagonal	Hexagonal
Space group	P 63/m	P 63/m
Unit cell dimensions	a = 41.275(2) Å α= 90°. b = 41.275(2) Å β= 90°. c = 17.5787(10) Å γ = 120°.	a = 41.381(13) Å α= 90°. b = 41.381(13) Å β= 90°. c = 17.548(5) Å γ = 120°.
Volume	25936(3) $Å^3$	26023(14) $Å^3$
Z	6	6
Density (calculated)	0.451 Mg/m^3	0.397 Mg/m^3
Absorption coefficient	0.569 mm^{-1}	0.563 mm^{-1}
F(000)	3540	3120
Crystal size	0.50 x 0.20 x 0.20 mm^3	0.40 x 0.15 x 0.10 mm^3
Theta range for data collection	1.51 to 25.36°	0.98 to 25.47°
Index ranges	-49<=h<=37, -47<=k<=49, -21<=l<=21	-49<=h<=46, -47<=k<=48, -21<=l<=21
Reflections collected	168049	.169995
Independent reflections	16395 [R(int) = 0.0869]	16596 [R(int) = 0.1827]
Completeness to theta = 25.00°	99.9 %	100.0 %
Absorption correction	Semi-empirical from equivalents	Semi-empirical from equivalents
Max. and min. transmission	0.8947 and 0.7641	0.9459 and 0.8062
Refinement method	Full-matrix least-squares on F^2	Full-matrix least-squares on F^3
Data / restraints / parameters	16395 / 0 / 288	16596 / 0 / 323
Goodness-of-fit on F^2	1.021	0.866
Final *R* indices [I>2sigma(I)]	R1 = 0.0600, wR2 = 0.1917	R1 = 0.0533, wR2 = 0.1005
R indices (all data)	R1 = 0.0867, wR2 = 0.2055	R1 = 0.1281, wR2 = 0.1135
Largest diff. peak and hole	2.090 and -0.587 $e.Å^{-3}$	0.420 and -0.398 $e.Å^{-3}$

Table 2.2. Crystal Data and structure refinement for UMCM-1-L2 before and after 365 nm PSD.

Identification code	UMCM-1-L2	UMCM-1-CAT
Empirical formula	$C_{58}H_{34}N_2O_{19}Zn_4$	$C_{47}H_{26}N_{0.40}O_{15}Zn_4$
Formula weight	1324.35	1097.76
Temperature	200(2) K	200(2) K
Wavelength	0.71073 Å	0.71073 Å
Crystal system	Hexagonal	Hexagonal
Space group	P 63/m	P 63/m
Unit cell dimensions	a = 41.288(2) Å α= 90°. b = 41.288(2) Å β= 90°. c = 17.5402(9) Å γ = 120°.	a = 41. 377(3) Å α= 90°. b = 41. 377(3) Å β= 90°. c = 17. 5217(13) Å γ = 120°.
V olume	25894(2) $Å^3$	25979(3) $Å^3$
Z	6	6
Density (calculated)	0.510 Mg/m^3	0.421 Mg/m^3
Absorption coefficient	0.574 mm^{-1}	0.566 mm^{-1}
F(000)	4008	3305
Crystal size	0.35 x 0.25 x 0.20 mm^3	0.40 x 0.10 x 0.07 mm^3
Theta range for data collection	1.29 to 25.36°.	1.50 to 25.33°.
Index ranges	-44<=h<=49, -49<=k<=45, -21<=l<=20	-49<=h<=49, -49<=k<=47, -21<=l<=15
Reflections collected	140103	117586
Independent reflections	16358 [R(int) = 0.0797]	16376 [R(int) = 0.1218]
Completeness to theta = 25.00°	99.9 %	100.0 %
Absorption correction	Semi-empirical from equivalents	Semi-empirical from equivalents
Max. and min. transmission	0.8938 and 0.8243	0.9615 and 0.8054
Refinement method	Full-matrix least-squares on F^2	Full-matrix least-squares on F^2
Data / restraints / parameters	16358 / 0 / 307	16376 / 0 / 286
Goodness-of-fit on F^2	0.981	0.839
Final *R* indices [I>2sigma(I)]	R1 = 0.0609, wR2 = 0.1753	R1 = 0.0477, wR2 = 0.1067
R indices (all data)	R1 = 0.0964, wR2 = 0.1861	R1 = 0.1075, wR2 = 0.1165
Largest diff. peak and hole	0.565 and -0.563 $e.Å^{-3}$	0.451 and -0.471 $e.Å^{-3}$

Table 2.3. Crystal Data and structure refinement for IRMOF-1-L1 before and after 365 nm PSD.

Identification code	IRMOF-1-L1	IRMOF-1-OH
Empirical formula	$C_{45}H_{21}N_3O_{22}Zn_4$	$C_{24}H_3O_{16}Zn_4$
Formula weight	1210.78	811.73
Temperature	200 (2) K	200 K
Wavelength	0.71073 Å	0.71073 Å
Crystal system	Cubic	Cubic
Space group	*Pm*-3*m*	*Fm*-3*m*
Unit cell dimensions	*a* = 12.8489(12) Å α = 90° *b* = 12.8489(12) Å β = 90° *c* = 12.8489(12) Å γ = 90°	*a* = 25.8059(14) Å α = 90°. *b* = 25.8059(14) Å β = 90°. *c* = 25.8059(14) Å γ = 90°.
V olume	2121.3(3) $Å^3$	17185.3(16) $Å^3$
Z	2	16
Density (calculated)	1.587 Mg/m^3	0.586 Mg/m^3
Absorption coefficient	2.318 mm^{-1}	1.124 mm^{-1}
F(000)	992	2944
Crystal size	0.50 x 0.50 x 0.10 mm^3	0.50 x 0.50 x 0.30 mm^3
Theta range for data collection	1.58 to 25.26°.	1.37 to 25.37°.
Index ranges	-15<=h<=13, -15<=k<=15, -15<=l<=15	-31<=h<=31, -31<=k<=31, -29<=l<=29
Reflections collected	12150	22285
Independent reflections	446 [R(int) = 0.0419]	850 [R(int) = 0.0342]
Completeness to theta = 25.37°	100.0 %	100.0 %
Max. and min. transmission	0.5431 and 0.3903	0.7292 and 0.6035
Refinement method	Full-matrix least-squares on F^2	Full-matrix least-squares on F^2
Data / restraints / parameters	446 / 1 / 32	850 / 0 / 30
Goodness-of-fit on F^2	1.644	1.124
Final R indices [I>2sigma(I)]	R1 = 0.1116, wR2 = 0.3415	R1 = 0.0925, wR2 = 0.2435
R indices (all data)	R1 = 0.1173, wR2 = 0.3490	R1 = 0.0966, wR2 = 0.2557
Largest diff. peak and hole	1.452 and -1.516 $e.Å^{-3}$	5.055 and -0.951 $e.Å^{-3}$

Table 2.4. Crystal Data and structure refinement for IRMOF-1-L3 and IRMOF-1-(L1)(NH_2).

Identification code	IRMOF-1-L3	IRMOF-1-(L1)(NH_2)
Empirical formula	$C_{51}H_{39}N_2O_{28}Zn_4$	$C_{38}H_{23}N_3O_{19}Zn_4$
Formula weight	1396.89	1080.81
Temperature	200 (2) K	200(2) K
Wavelength	0.71073 Å	0.71073 Å
Crystal system	Cubic	Cubic
Space group	*Fm*-3*m*	*Fm*-3*m*
Unit cell dimensions	*a* = 25.686(3) Å α = 90°. *b* = 25.686(3) Å β = 90°. *c* = 25.686(3) Å γ = 90°.	*a* = 25.545(14) Å α = 90°. *b* = 25.545(14) Å β = 90°. *c* = 25.545(14) Å γ = 90°.
V olume	16947(4) $Å^3$	16669(16) $Å^3$
Z	16	16
Density (calculated)	0.594 Mg/m^3	0.604 Mg/m^3
Absorption coefficient	1.139 mm^{-1}	1.158 mm^{-1}
F(000)	2944	2944
Crystal size	0.35 x 0.35 x 0.20 mm^3	0.50 x 0.50 x 0.30 mm^3
Theta range for data collection	1.37 to 25.31°.	1.59 to 25.70°.
Index ranges	-23<=h<=30, -30<=k<=10, -27<=l<=21	-31<=h<=31, -31<=k<=30, -28<=l<=30
Reflections collected	8788	34575
Independent reflections	836 [R(int) = 0.0458]	861 [R(int) = 0.0558]
Completeness to theta = 25.70°	100.0 %	99.9 %
Max. and min. transmission	0.8042 and 0.6912	0.7226 and 0.5951
Refinement method	Full-matrix least-squares on F^2	Full-matrix least-squares on F^2
Data / restraints / parameters	836 / 0 / 25	861 / 0 / 14
Goodness-of-fit on F^2	1.094	2.099
Final R indices [I>2sigma(I)]	R1 = 0.0650, wR2 = 0.1811	R1 = 0.1774, wR2 = 0.4137
R indices (all data)	R1 = 0.0827, wR2 = 0.1989	R1 = 0.2051, wR2 = 0.4524
Largest diff. peak and hole	1.075 and -0.398 $e.Å^{-3}$	2.072 and -1.050 $e.Å^{-3}$

2. IX. References

(1) Wang, Z.; Cohen, S. M. *J. Am. Chem. Soc.* **2007**, *129*, 12368.

(2) Morris, W.; Doonan, C. J.; Furukawa, H.; Banerjee, R.; Yaghi, O. M. *J. Am. Chem. Soc.* **2008**, *130*, 12626.

(3) Tanabe, K. K.; Wang, Z.; Cohen, S. M. *J. Am. Chem. Soc.* **2008**, *130*, 8508.

(4) Gadzikwa, T.; Farha, O. K.; Mulfort, K. L.; Hupp, J. T.; Nguyen, S. T. *Chem. Commun.* **2009**, 3720.

(5) Jones, S. C.; Bauer, C. A. *J. Am. Chem. Soc.* **2009**, *131*, 12516.

(6) Kawamichi, T.; Haneda, T.; Kawano, M.; Fujita, M. *Nature* **2009**, *461*, 633.

(7) Volkringer, C.; Cohen, S. M. *Angew. Chem., Int. Ed.* **2010**, *49*, 4644.

(8) Gadzikwa, T.; Farha, O. K.; Malliakas, C. D.; Kanatzidis, M. G.; Hupp, J. T.; Nguyen, S. T. *J. Am. Chem. Soc.* **2009**, *131*, 13613.

(9) Yamada, T.; Kitagawa, H. *J. Am. Chem. Soc.* **2009**, *131*, 6312.

(10) Deshpande, R. K.; Minnaar, J. L.; Telfer, S. G. *Angew. Chem. Int. Ed.* **2010**, *49*, 4598.

(11) Kaye, S. S.; Long, J. R. *J. Am. Chem. Soc.* **2008**, *130*, 806.

(12) Blake, A. J.; Champness, N. R.; Easun, T. L.; Allan, D. R.; Nowell, H.; George, M. W.; Jia, J.; Sun, X. *Nat. Chem.* **2010**, *2*, 688.

(13) Liu, Q.; Ma, J.; Dong, Y. *J. Am. Chem. Soc.* **2010**, *132*, 7005.

(14) Ohara, K.; Inokuma, Y.; Fujita, M. *Angew. Chem., Int. Ed.* **2010**, *49*, 5507.

(15) Sato, H.; Matsuda, R.; Sugimoto, K.; Takata, M.; Kitagawa, S. *Nat. Mater.* **2010**, *9*, 661.

(16) Mayer, G.; Heckel, A. *Angew. Chem. Int. Ed.* **2006**, *45*, 4900.

(17) Himsl, D.; Wallacher, D.; Hartmann, M. *Angew. Chem., Int. Ed.* **2009**, *48*, 4639.

(18) Devic, T.; Horcajada, P.; Serre, C.; Salles, F.; Maurin, G.; Moulin, B.; Heurtaux, D.; Clet, G.; Vimont, A.; Grenèche, J.; Ouay, B. L.; Moreau, F.; Magnier, E.; Filinchuk, Y.; Marrot, J.; Lavalley, J.; Daturi, M.; Férey, G. *J. Am. Chem. Soc.* **2010**, *132*, 1127.

(19) Raymond, K.; Xu, J. In *United States Patent and Trademark Office (Ed.: U.S.P.T. Office)*; The Regents of the University of California (Oakland, CA): US, 1999.

(20) Koh, K.; Wong-Foy, A. G.; Matzger, A. J. *Angew. Chem. Int. Ed.* **2008**, *47*, 677.

(21) Choi, S. B.; Seo, M. J.; Cho, M.; Kim, Y.; Jin, M. K.; Jung, D.; Choi, J.; Ahn, W.; Rowsell, J. L. C.; Kim, J. *Cryst. Growth Des.* **2007**, *7*, 2290.

(22) Karpishin, T. B.; Stack, T. D. P.; Raymond, K. N. *J. Am. Chem. Soc.* **1993**, *115*, 6115.

(23) Karpishin, T. B.; Stack, T. D. P.; Raymond, K. N. *J. Am. Chem. Soc.* **1993**, *115*, 182.

(24) Tanabe, K. K.; Allen, C. A.; Cohen, S. M. *Angew. Chem., Int. Ed.* **2010**, *49*, 9730.

(25) Tanabe, K. K.; Wang, Z.; Cohen, S. M. *J. Am. Chem. Soc.* **2008**, *130*, 8508.

(26) Doonan, C. J.; Morris, W.; Furukawa, H.; Yaghi, O. M. *J. Am. Chem. Soc.* **2009**, *131*, 9492.

(27) Kim, M.; Boissonnault, J. A.; Allen, C. A.; Dau, P. V.; Cohen, S. M. *Dalton Trans.* **2012**, *41*, 6277.

(28) Deng, H.; Doonan, C. J.; Furukawa, H.; Ferreira, R. B.; Towne, J.; Knobler, C. B.; Wang, B.; Yaghi, O. M. *Science* **2010**, *327*, 846.

(29) Marx, S.; Kleist, W.; Huang, J.; Maciejewski, M.; Baiker, A. *Dalton Trans.* **2010**, *39*, 3795.

(30) Burrows, A. D. *CrystEngComm* **2011**, *13*, 3623.

(31) Burrows, A. D.; Fisher, L. C.; Richardson, C.; Rigby, S. P. *Chem. Commun.* **2011**, *47*, 3380.

(32) Kim, M.; Cahill, J. F.; Prather, K. A.; Cohen, S. M. *Chem. Commun.* **2011**, *47*, 7629.

(33) Lescouet, T.; Kockrick, E.; Bergeret, G.; Pera-Titus, M.; Farrusseng, D. *Dalton Trans.* **2011**.

(34) Albini, A.; Fagnoni, M. *Handbook of synthetic photochemistry*; Wiley-VCH: Weinheim, 2010.

(35) Tanabe, K. K.; Allen, C. A.; Cohen, S. M. *Angew. Chem., Int. Ed.* **2010**, *49*, 9730.

(36) Eddaoudi, M.; Kim, J.; Rosi, N.; Vodak, D.; Wachter, J.; O'Keeffe, M.; Yaghi, O. M. *Science* **2002**, *295*, 469.

(37) Gaplovsky, M.; Il'ichev, Y. V.; Kamdzhilov, Y.; Kombarova, S. V.; Mac, M.; Schworer, M. A.; Wirz, J. *Photochem. Photobiol. Sci.* **2005**, *4*, 33.

(38) Cavka, J. H.; Jakobsen, S.; Olsbye, U.; Guillou, N.; Lamberti, C.; Bordiga, S.; Lillerud, K. P. *J. Am. Chem. Soc.* **2008**, *130*, 13850.

(39) Kleist, W.; Jutz, F.; Maciejewski, M.; Baiker, A. *Eur. J. Inorg. Chem.* **2009**, *2009*, 3552.

(40) Fei, H.; Shin, J.; Meng, Y. S.; Adelhardt, M.; Sutter, J.; Meyer, K.; Cohen, S. M. *J. Am. Chem. Soc.* **2014**, *136*, 4965.

(41) Walton, K. S.; Snurr, R. Q. *J. Am. Chem. Soc.* **2007**, *129*, 8552.

(42) Düren, T.; Millange, F.; Férey, G.; Walton, K. S.; Snurr, R. Q. *J. Phys. Chem. C* **2007**, *111*, 15350.

3. Postsynthetic Modification via Click Reactions

3. I. Introduction

As described in Chapter 2, photochemical reactions have provided access to MOFs with functional groups that were unobtainable through other synthetic methodologies (i.e. direct synthesis, PSM). In addition to the facile utilization of light, the mild reaction conditions did not degrade the crystallinity of the materials. The use of PSM methods that require harsher reaction conditions have proved problematic in prior PSM efforts,[1,2] making the use of photochemical transformations rather benign and attractive by comparison. Chapter 3 will describe efforts towards MOF modification through 'click' reactions. First, a photochemical click reaction between thiols and terminal alkene moieties will be discussed in both Zn- and In- based MOFs. Second, a somewhat related inverse electron demand Diels Alder click reaction will be explored in Zn- based MOFs.

The successful incorporation of secondary metal binding groups, described in Chapter 2, (e.g. phenols, catechol that are not involved in MOF formation/construction) suggested that softer metal binding groups (i.e. SH) would also be tolerated within certain MOFs. The design and synthesis of organic ligands with both a coordinating group capable of MOF formation (e.g. carboxylic acid, imidazole, pyridine, etc.) and a free thiol was found to be very difficult and abandoned early on in our efforts. Of initial interest was the thiol analogue to the H_2catbdc ligand described in Chapter 2, however the direct carboxylation of the thiol catechol group was low yielding.[3] Instead, a PSM approach was sought to integrate sulfur atoms into a MOF lattice. Based on our success with photochemical reactions and inspired by previous click reactions in MOFs,[4-7] methods to blend photo- and click- chemistry were explored. Because a click reaction implies short reaction times and high yields this would be an ideal PSM reaction. Additionally, bioconjugate and

polymeric materials have routinely used thiol-ene and thiol-yne click reactions, which involve the reaction between thiols and with terminal alkenes and alkynes, for the efficient functionalization.[8-12] In this manner, thioether moieties would be introduced into a MOF lattice without the potential of the new functional group (Figure 3.1).[13-17]

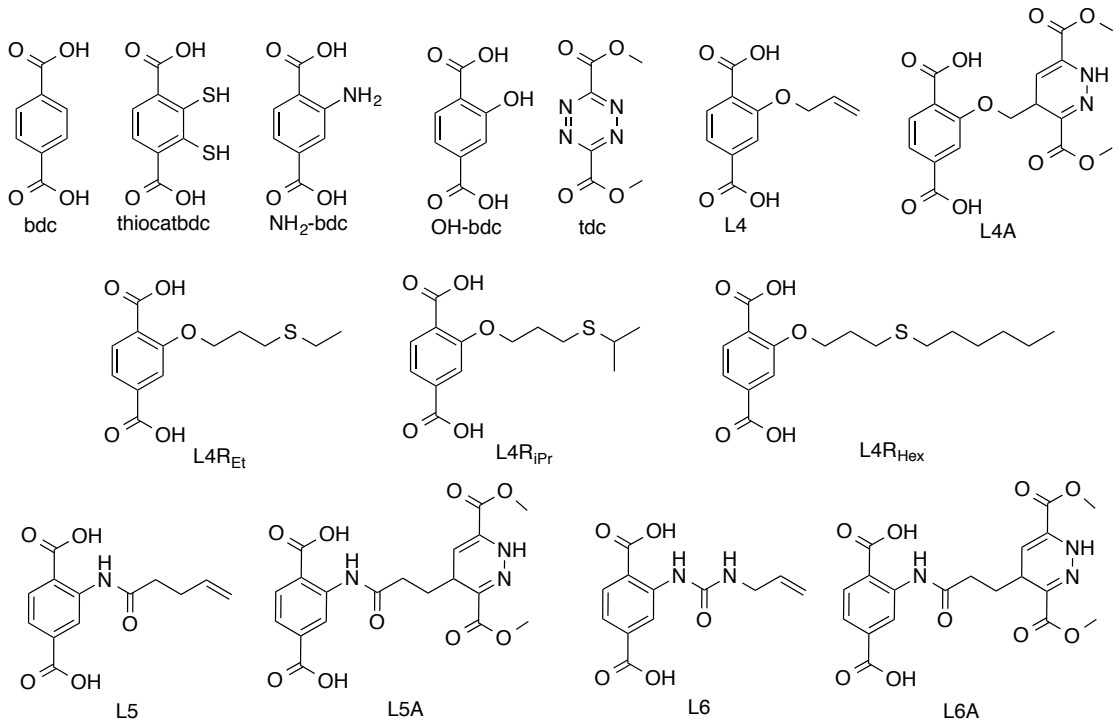

Figure 3.1. Naming scheme for ligands that will be discussed in Chapter 3.

3. II. Thiol-ene Click Reactions in Metal-Organic Frameworks

MOFs with terminal alkenes and alkynes have been previously reported though either functionalization by PSM, to install a single terminal alkene,[2] or through direct synthesis using a bdc ligand with two appended alkene moieites.[18,19] To simplify the system, a single terminal alkene was appended to a H_2bdc ligand (L4) (Scheme

3.1). This ligand was designed to display the alkene as a chemical 'handle' to access thiol-ene reactions on MOF substrates. One mechanism for thiol-ene reactions is through a base catalyzed reaction, however, Zn-carboxylate MOFs are intolerant to the presence of base therefore, a photoinitiated radical reaction was utilized. To perform these photoinitiated thiol-ene click reactions, a photocleavable catalyst, 2,2-dimethoxy-2-phenylacetophenone (DMPA)[20] is added to an alkene with an excess of thiol in a nonpolar organic solvent. A test reaction was performed on ligand L4 to verify its reactivity and to optimize the reaction conditions with the thiols of interest: 1-ethane thiol, 2-propane thiol, and 1-hexane thiol (Figure 3.2). Optimization attempts consisted of using 0.025-1 equivalent of DMPA, 1-5 equivalents of thiol, and 4-72 h of photoirradiation at 365 nm. The best conditions identified to date were 18-21 h of irradiation with 0.5 equivalents of DMPA and 2 equivalents of thiol in DMF (5 mL). DMF was chosen as the solvent, as opposed to the more common chlorobenzene, due to solubility issues with dicarboxylic acid L4. ^{1}H NMR analysis of the reaction showed the disappearance of the olefinic proton resonances, suggesting complete consumption of the starting material; however, the desired thiol-ether was obtained in only 50-65% isolated yield. ^{1}H NMR verified the appearance of new resonances in the expected aliphatic region of the spectrum (Figure 3.2). ESI-MS also corroborated the formation of the desired thioether product.

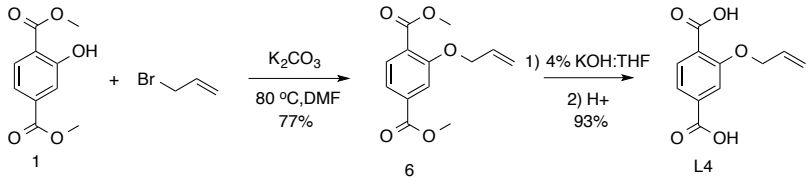

Scheme 3.1. Synthesis of L4 using the Williamson ether synthesis followed by hydrolysis.

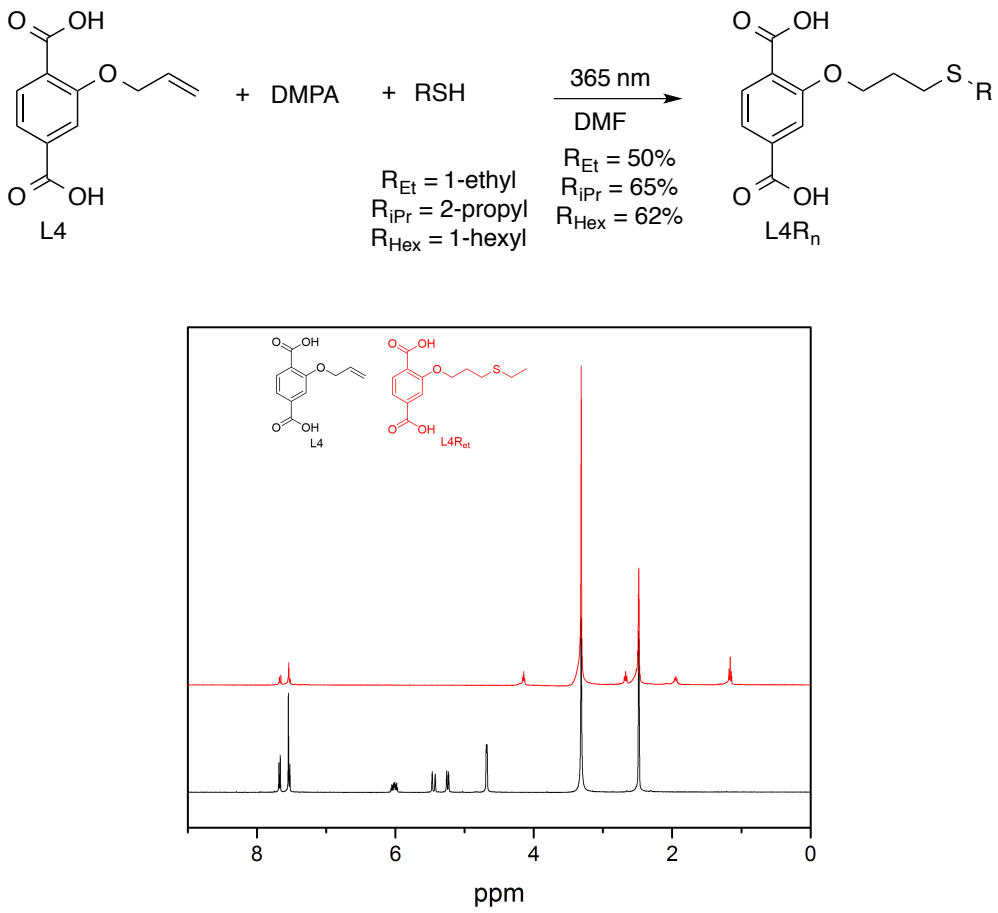

Figure 3.2. Proof-of-concept thiol-ene test reactions on L4 (top). ^{1}H NMR of L4 in DMSO (black) and $L4R_1$ in DMSO (red) (bottom). The disappearance of the olefinic proton resonances between 4-6 ppm are indicative of complete transformation as is the new resonances in the aliphatic range consistent with the formation of the thioether.

Synthesizing MOF substrates with the terminal alkene moiety was undertaken. First, dissolving L4 in DMF and heating to 100 °C in the presence of $Zn(NO_3)_2 \bullet 6H_2O$ resulted in clear block crystals indicative of an IRMOF topology (designated IRMOF-1-L4), which was verified through single-crystal XRD unit cell analysis and PXRD (Figure 3.3). Collection of a complete XRD data set and structure solution was not feasible as the crystals degraded during XRD data collection. Degradation of MOF crystals is

rather common and can usually be overcome by altering the collection temperature or solvent that the crystals soak in prior to XRD analysis, but neither approach was effective for IRMOF-1-L4. ^{1}H NMR and ESI-MS of the digested MOF material corroborated the formation of an allyloxy tagged IRMOF. Dinitrogen adsorption measurements show a type 1 isotherm, typical for IRMOFs with a BET value of 1290±116 m^2g^{-1}.

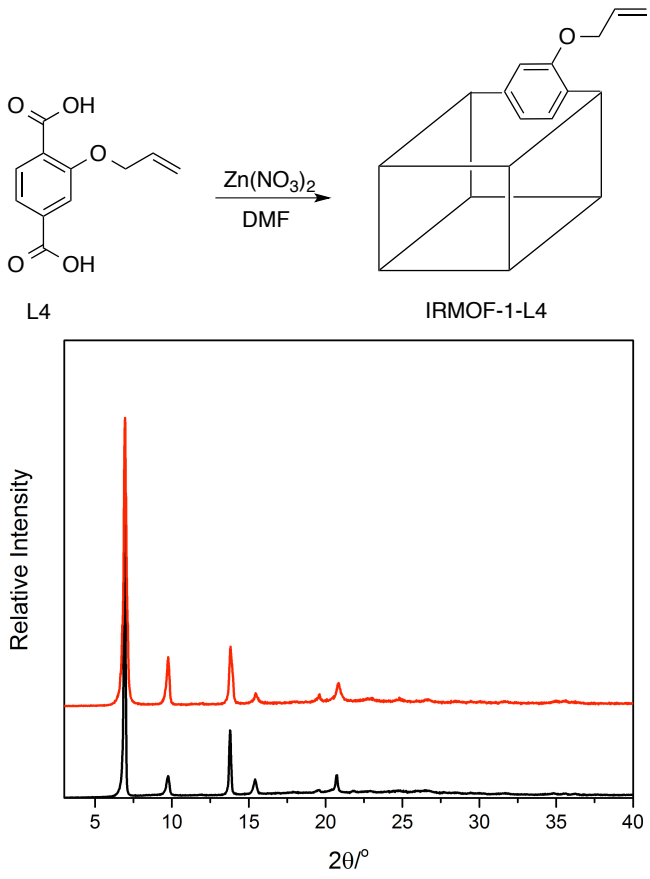

Figure 3.3. Synthesis of allyloxy tagged IRMOF-1-L4 (top). PXRD of IRMOF-3 (black) and IRMOF-1-L4 (red) from DMF (bottom).

Second, combining L4, H_3btb, and $Zn(NO_3)_2 \cdot 6H_2O$ in DMF with heating at 85 °C for 48 h easily afforded UMCM-1-L4 decorated with allyloxy groups (Figure 3.4). The resulting clear needle crystals were visually identical to the desired morphology of UMCM-1. ^{1}H NMR and ESI-MS of the digested MOF material clearly indicate both the btb and L4 ligands remain intact after the synthesis and subsequent digestion. XRD unit cell analysis and PXRD both corroborate the formation of a UMCM topology (Figure 3.4). Lastly, dinitrogen adsorption measurements showed a large BET value of 3655±142 m^2g^{-1} consistent with UMCM type materials.

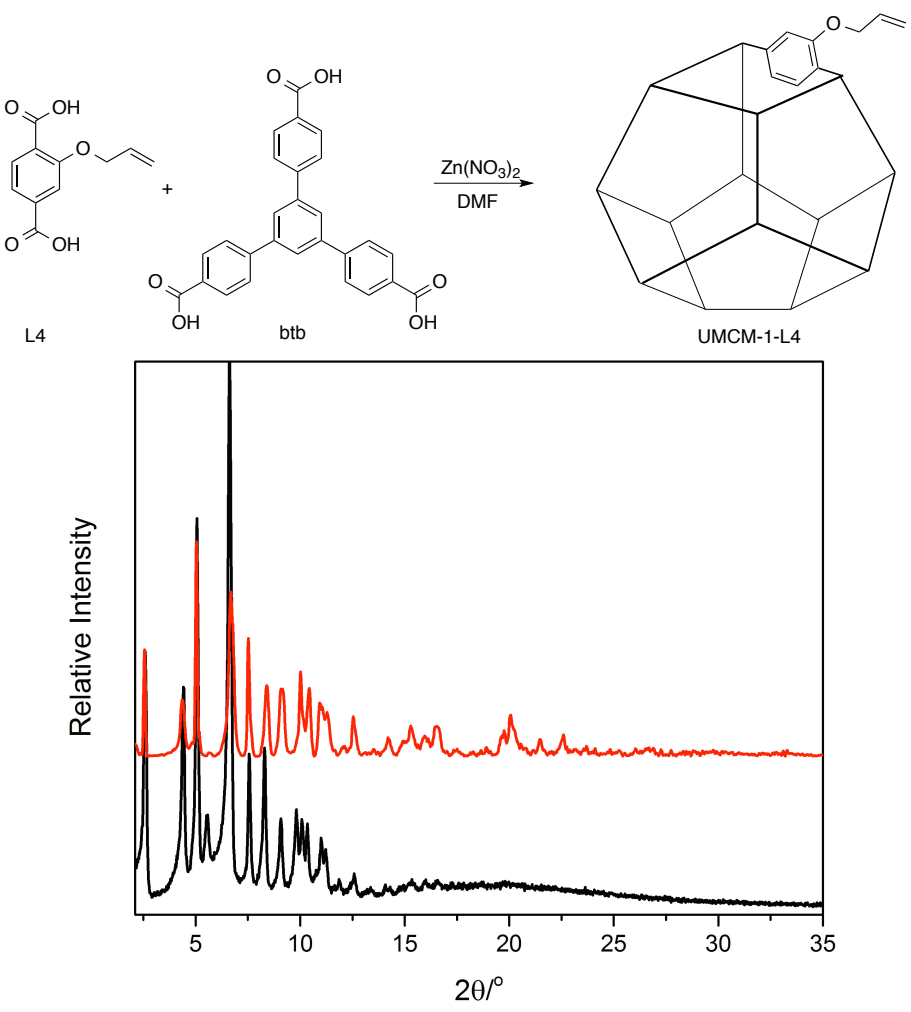

Figure 3.4. Schematic showing of the synthesis of allyloxy decorated UMCM-1-L4 (top). PXRD of UMCM-1 (black) compared to UMCM-1-L4 (red) from DMF (bottom).

Upon successful transformation of the allyloxy ligand (L4) to the thioether product, adaptation of this chemistry to the MOF was attempted. IRMOF-1-L4 and UMCM-1-L4 were treated with 0.5 equivalents DMPA and 2 equivalents of ethane thiol in one of the following solvents: $CHCl_3$, DMF, toluene, or EtOAc (4 mL) (Figure 3.5). While the crystals turned opaque in both DMF and toluene, the PXRD pattern indicated that the framework remained intact. In contrast, complete loss of

crystallinity was observed for the MOFs in $CHCl_3$ and EtOAc under these conditions as evidenced by the crystals turning opaque and an amorphous PXRD pattern (data not shown). The MOFs were found to be most stable in DMF and toluene when combined with only a single equivalent of thiol. To minimize degradation, a single equivalent of thiol was used in conjunction with replenishing of the solvent and reagents every 24 h. Unfortunately, neither of these Zn-carboxylate based MOFs were tolerant to the extended presence of ethane thiol in combination with photoirradiation as evidenced by the amorphous PXRD patterns post reaction. Zn-carboxylate based MOFs are known to be unstable in the presence of protic solvents due to protonation at the carboxylate sites and subsequent cleavage of the coordination bond. Additionally, high affinity of sulfur for Zn^{2+} species which could also be problematic for this system.

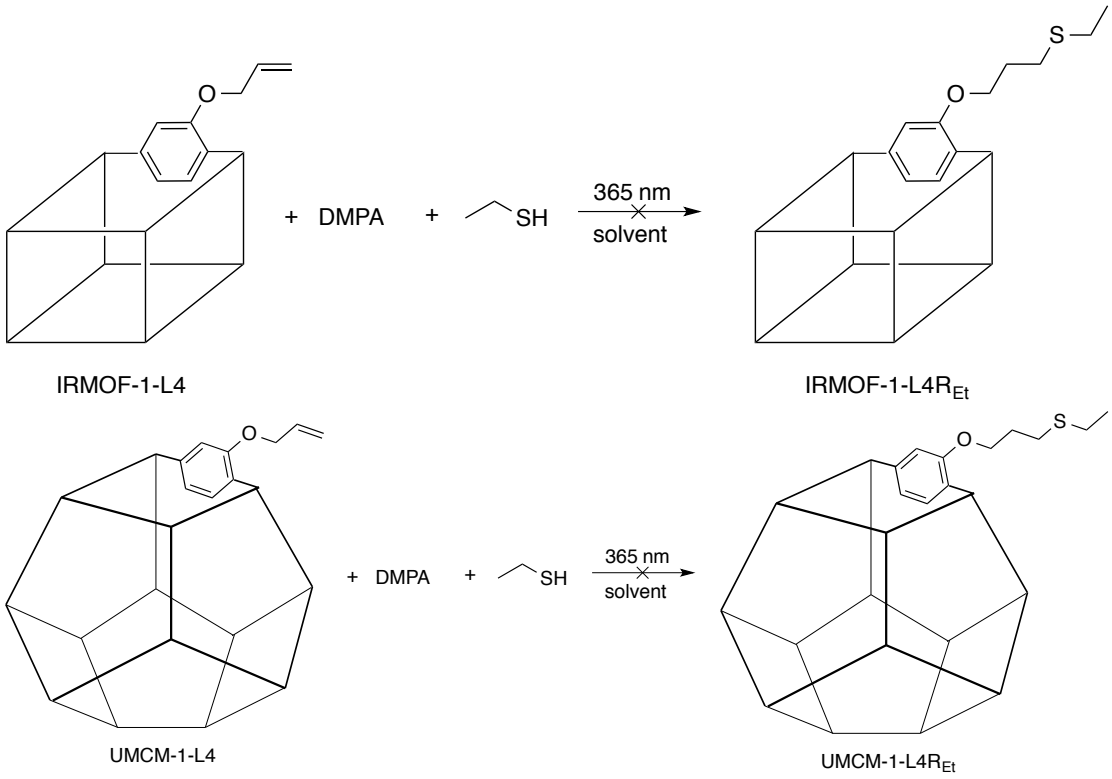

Figure 3.5 Schematic of thiol-ene reactions attempts on Zn-carboxylate based MOFs.

To avoid the decomposition and potential disruption of the Zn-carboxylate bonds by the free thiol discussed above, a similar study was undertaken using a more chemically robust MOF. UiO materials are one of the most robust MOFs known to date.[21] They are comprised of stronger Zr-carboxylate bonds that benefit from the inherent oxophilicity of Zr. However, the synthesis conditions for the UiO-66 framework, which involves heating $ZrCl_4$ with L4, lead to cleavage of the aryl-ether groups that were being explored for these MOFs. Attempts to synthesize UiO-66 derivatives with either L1 (from Chapter 2, to study PSD within a material with smaller pores) or L4, lead to a 50-75% cleavage of the 2-nitrobenzyl or allyl ether group creating a material mostly comprised mostly of OH-bdc as evidence by PXRD and ^{1}H NMR of the digested

materials (Figure 3.6). While this in situ deprotection may be useful for other studies the problems with incorporating the desired alkenyl groups into the UiO framework led us to explore other options for thiol-ene PSM.

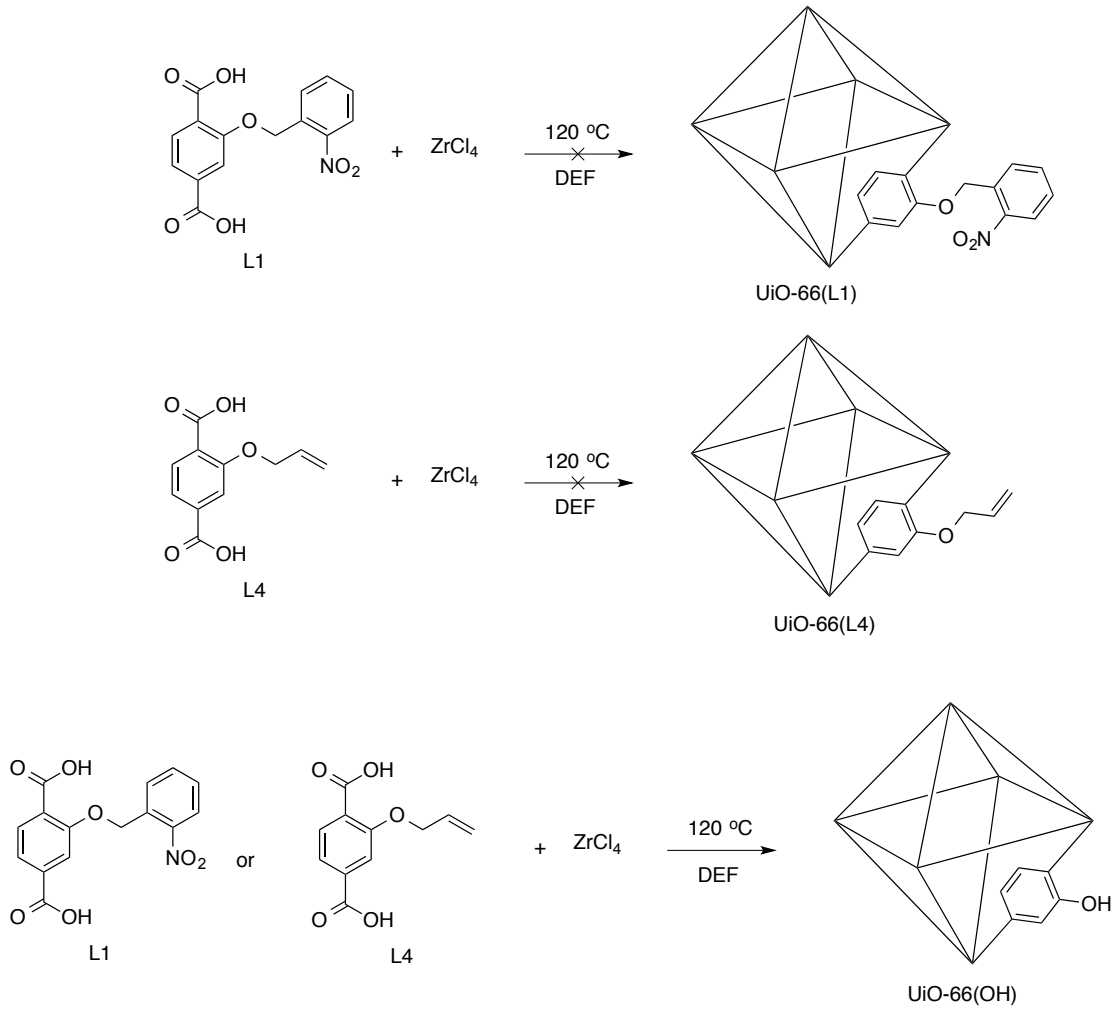

Figure 3.6. Attempts to synthesize arylether UiO materials lead to the cleavage of the ether group.

MIL-68, described in Chapter 1, is another framework that has been synthesized with a variety of metal sources, displays high porosity, and is also more chemically robust than Zn-based MOFs. An In-based MIL-68 was determined to be the easiest MIL-68 system to work with. Heating L4 and $In(NO_3)_2 \bullet xH_2O$ at 100 °C for 48 h resulted in the formation of a white powder. PXRD analysis showed that the material is isostructural with reported MIL-68 materials (Figure 3.7). ^1H NMR and ESI-MS confirmed that L4 remains intact after the synthesis. Additionally, TGA data showed a degradation event at 360 °C that matched previously reported TGA traces for MIL-68 materials.

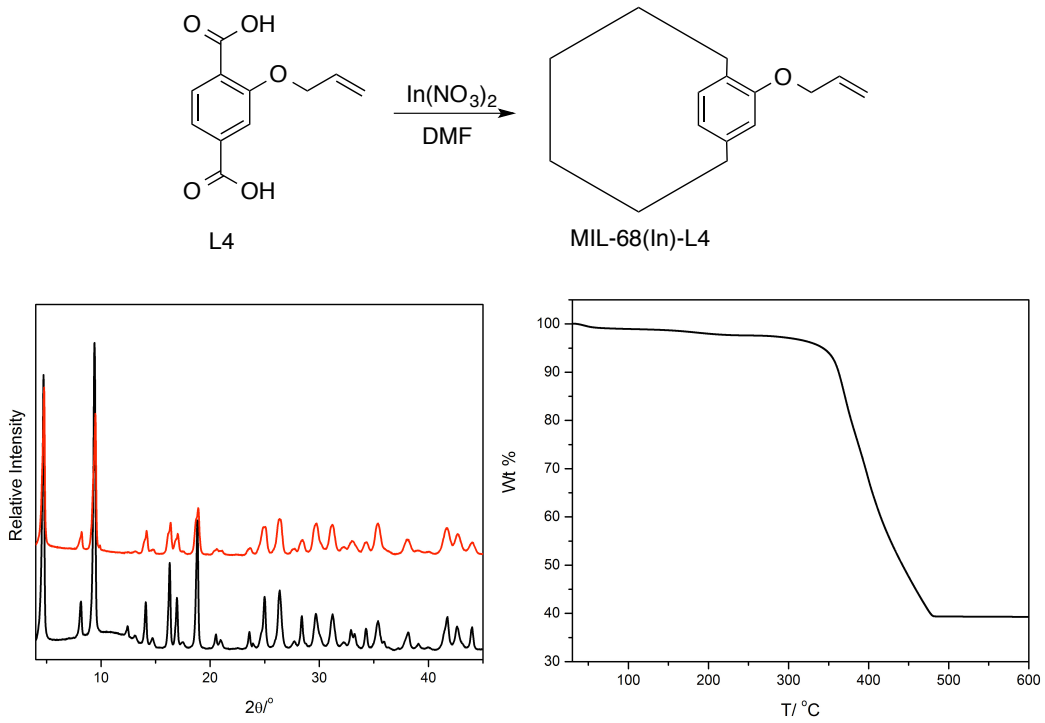

Figure 3.7. Synthesis of microcrystalline indium-carboxylate based MIL-68(In)-L4 (top). Comparison of PXRD from MIL-68(In)-NH_2 (black)and MIL-68(In)-L4 (red) (bottom left). TGA trace of MIL-68(In)-L4 after being fully evacuated of solvent indicative of a porous material (bottom right).

The In-carboxylate framework demonstrated a higher tolerance for protic solvents as washing with MeOH, which would generally destroy a Zn-based IRMOF or UMCM, did not disrupt the MIL-68(In)-L4. Additionally, thiols have a lower affinity for In^{2+} as In(II) is a harder Lewis acid than Zn^{2+} mitigating one of the potential problems in the initial study. MIL-68(In)-L4 was photoirradiated at 365 nm in the presence of 0.5 equivalent of DMPA and 4 equivalents of ethane thiol in DMF for 72 h . After 72 h, the material was washed with DMF to remove the excess thiol and byproducts. Under these reaction conditions, ~25-30% of the allyloxy groups were converted to the desired thioether determined by the ^{1}H NMR analysis of the digested material. The PXRD pattern confirmed that the MOF remained intact after exposure to the reaction conditions (Figure 3.8).

There are multiple possibilities for the modest conversion of the allyloxy functionality. The low conversion in MIL-68(In)-L4 may be due to inhibited diffusion of the requisite radical species throughout the entire lattice, (either the DMPA radical or the thiol radical). The free L4 ligand readily underwent conversion in milder conditions corroborating this hypothesis. In an attempt to mitigate diffusion issues, prior to the addition of thiol, DMPA was added to the MOF for 24 h in addition to increasing the equivalents of DMPA and daily exchanges of reagents. Unfortunately, none of these methods improved the yield. One other possible problem was a shifting of the λ_{max} of the reagents once inside the framework. There is precedence for this variation as discussed in Chapter 2. Instead of using 365 nm light, placing the reaction in direct sunlight was also tested. Surprisingly, this produced an increase in conversion to 85% after 7 days; however, these increased yields could not be reproduced under any controlled laboratory conditions, including use of broadband lamps, and was therefore not pursued further (Figure 3.9).

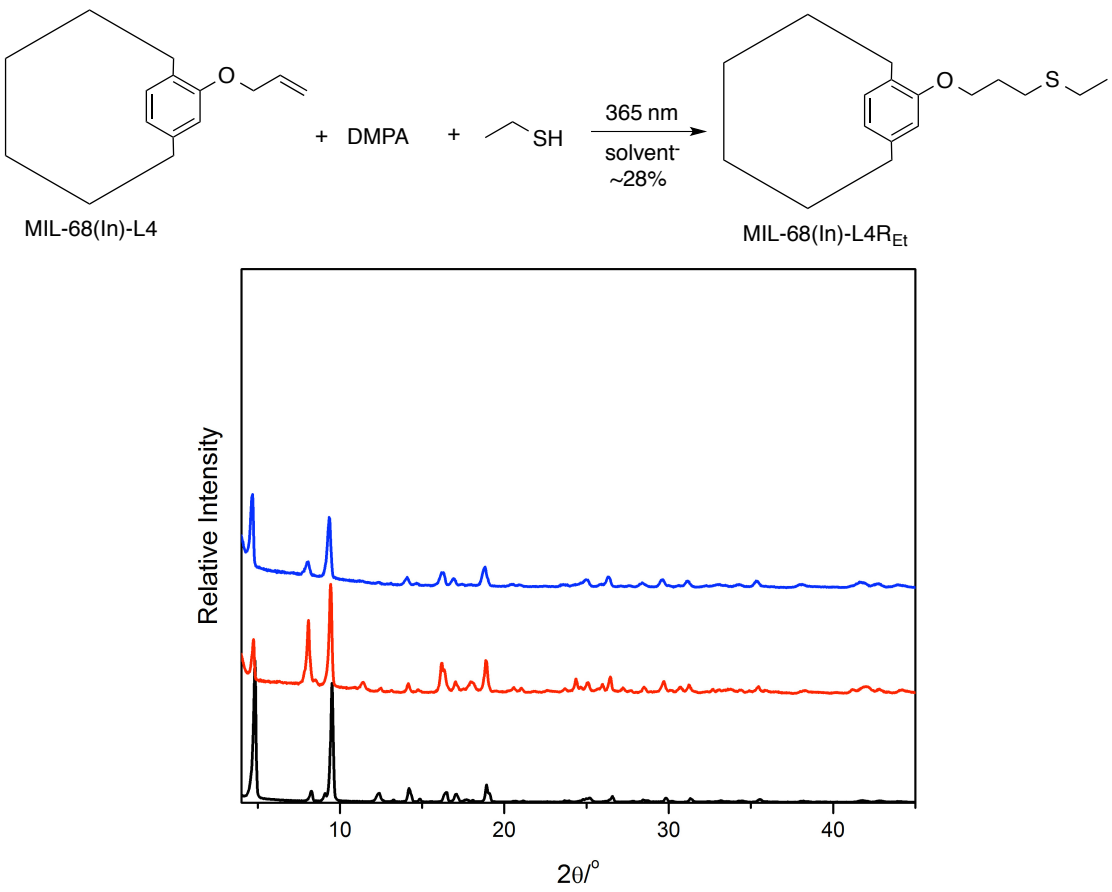

Figure 3.8. PSM incorporation of thio-ether moiety in the MIL-68 material (top). PXRD of MIL-68(In)-NH_2 (black) in comparison to MIL-68(In)-L4 (red) and MIL-68(In)-L4R_1 after 72h of thiol-ene conditions (bottom). Crystallinity is maintained after exposure to 4 equivalents of ethane thiol, 0.5 equivalents of DMPA and 72 h of 365 nm light.

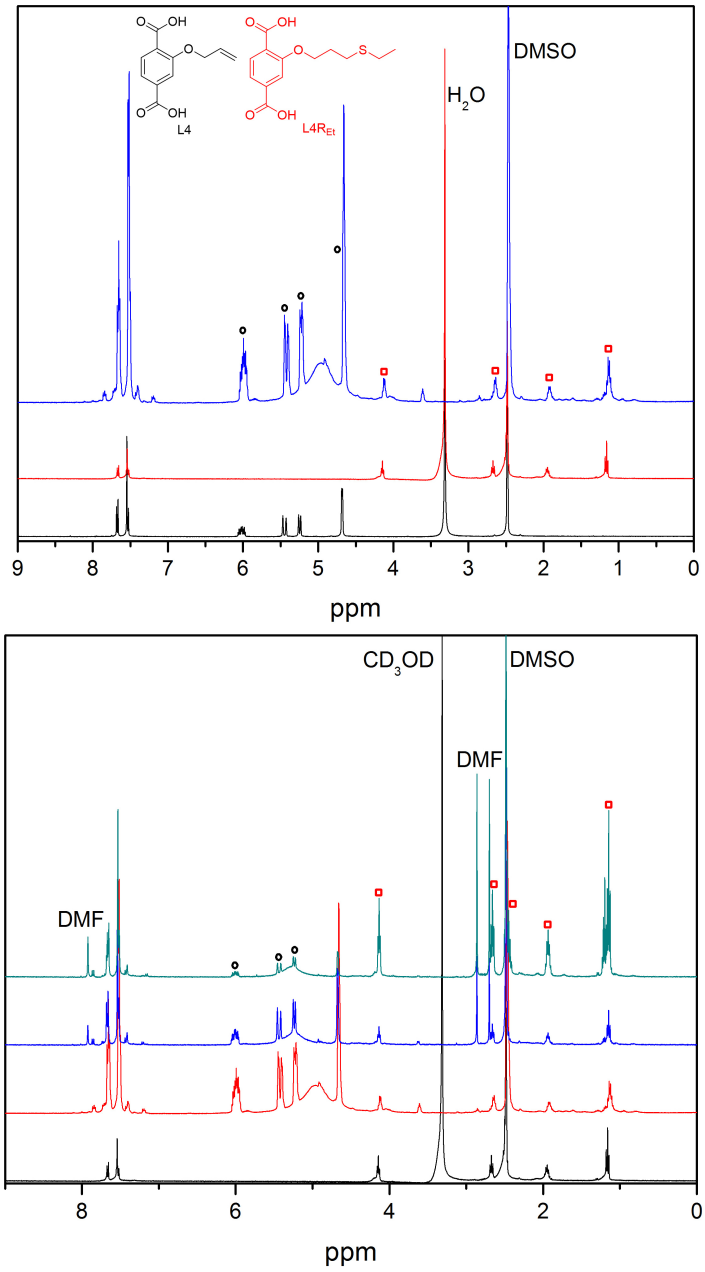

Figure 3.9. ^{1}H NMR in DMSO of L4 (black), L4R$_1$ (red) and MIL-68(In)-L4 after 72 h of thiol-ene click conditions (top). Modest conversion is evident by the appearance of new resonances in the aliphatic region that correspond to the thioether L4R$_1$. ^{1}H NMR of an authentic sample of L4R$_1$ (black) in comparison to MIL-68(In)-L4R$_1$ after 72 h with 365 nm light (red), 24 h with 365 nm light followed by 24 hours of sunlight (blue), and 7 days in sunlight (green, including evening) (bottom). The presence of DMF in the blue and teal traces suggests that the rinsing conditions are not successful after the reaction. The black circles indicate the starting ligand, L4, while the product is indicated by red squares.

3. III. Modifying MOFs Using an Inverse-Electron-Demand Diels-Alder Reaction

In addition to our efforts on thiol-ene click reactions on MOFs, we also investigated other click reactions on these materials. Both alkyne and azide handles have been introduced into MOFs for use in PSM click chemistry.[5,7] The classic [3 + 2] cycloaddition between an azide and terminal alkyne generally requires a Cu(I) catalyst to accelerate the reaction. However, the more reagents in a PSM reaction, the more difficult it becomes to purify and optimize the reaction. As an alternative, we investigated the functionalization of alkene decorated MOFs, in a PSM fashion, utilizing a tetrazine reagent that undergoes a "click" Diels-Alder cycloaddition.[22,23] While multiple reagents and radical species complicated the thiol-ene reaction, the tetrazine click reaction does not require a catalyst or other coreagents and liberates dinitrogen as the only byproduct, making this transformation very attractive for use in the PSM of MOFs. Electron deficient dienes, 1,2,4,5-tetrazines (also called s-tetrazines) and their derivatives rapidly react with electron-rich alkenes or alkynes by an inverse-electron-demand Diels-Alder reaction to yield dihydropyridazines or pyridazines (Figure 3.10). These reactions are facile and reliable, can be used to prepare various substituted pyridazines or fused heterocycles, and have been employed in the labeling of biomolecules and as key steps in the total synthesis of complex organic molecules.[23-27] Similarly to the thiol-ene click chemistry, the use of tetrazine click reactions has been recently described for the functionalization of polymers.[28]

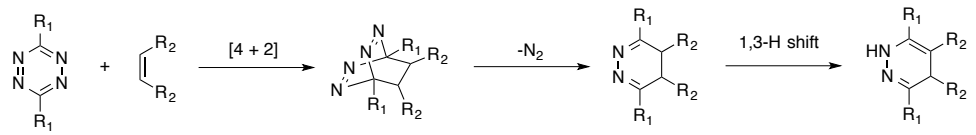

Figure 3.10. Inverse electron demand Diels-Alder [4+2] cycloaddition between a tetrazine and an olefin.

A stepwise, "tandem" approach was adopted for the PSM of MOFs by tetrazine reagents.[29,30] UMCM-1-NH_2 was selected because of its large pore size and previous success in many PSM reactions.[31,32] UMCM-1-NH_2 was quantitatively modified with pentenoic anhydride to produce UMCM-1-L5 with olefin groups appended to the bdc ligand through an amide linkage. The olefin-bearing UMCM-1-L5 was then treated with dimethyl-1,2,4,5-tetrazine-3,6-dicarboxylic acid (H_2tdc), which was synthesized using a modified literature procedure,[33] at room temperature in $CHCl_3$ for 24 h (Figure 3.11). Digestion of the resulting material followed by ^{1}H NMR analysis confirmed the formation of the expected Diels-Alder cycloaddition product (dihydropyridazine) with complete consumption of the olefin. The new MOF, UMCM-1-L5A, remained highly crystalline, stable, and microporous, as evidenced by single-crystal XRD, PXRD, TGA, and gas sorption analysis, respectively (Figure 3.12). The BET surface area of UMCM-1-L5A was determined to be ~2800±125 m^2g^{-1}, which is lower than that of the parent UMCM-1-NH_2, but consistent with the introduction of bulky substituents into the pores of this MOF.

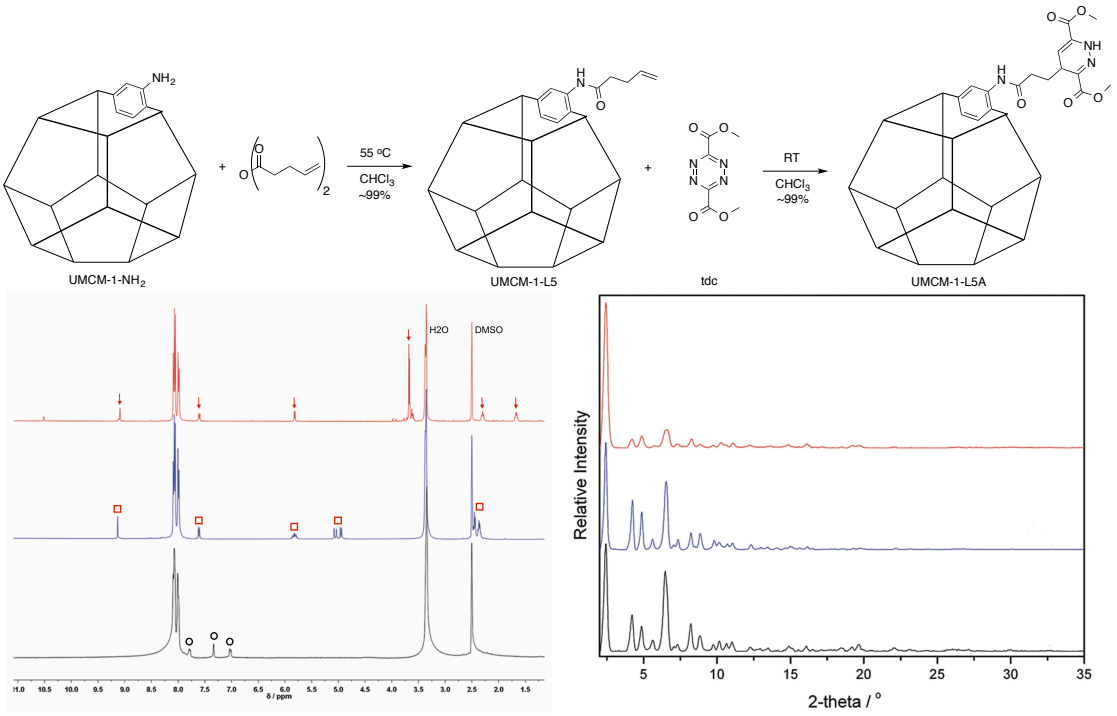

Figure 3.11. PSM functionalization of UMCM-1-NH_2 to UMCM-1-L5 and subsequently to UMCM-1-L5A after a Diels Alder cycloaddition (top). ^{1}H NMR of digested UMCM-1-NH_2 (black, highlighted by black circles) with the three distinct resonances between 7-8 ppm for the NH_2-bdc ligand and the large btb peak at 8.2 ppm for reference (bottom left). UMCM-1-L5 (blue, highlighted by red squares) with the distinct allyl resonances between 4.5-6 ppm and shifting of the aryl peaks from NH_2-bdc. Quantitative conversion of UMCM-1-L5 to UMCM-1-L5A after exposure to tdc is shown at top (red, highlighted by red arrows) with the disappearance of the allyl peaks. PXRD comparison of (left) UMCM-1-NH_2 (black), UMCM-1-L5 (blue), and UMCM-1-L5A (red) demonstrating the crystallinity is maintained after both PSM steps (bottom right).

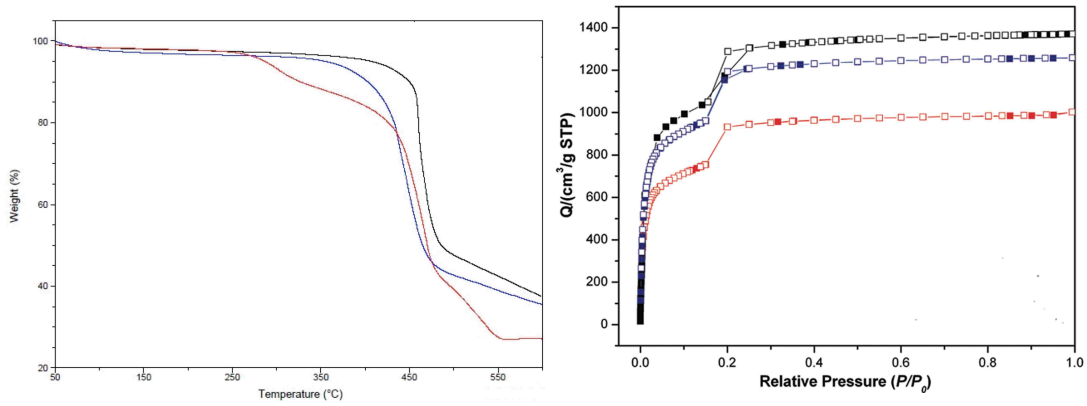

Figure 3.12. TGA traces (right) of UMCM-1-NH_2 (black), UMCM-1-L5 (blue) and UMCM-1-L5A (red) demonstrating that the PSM did not significantly affect the thermal stability of the framework until UMCM-1-L5A that starts degrading at 250 °C before the normal framework destruction at 360 °C (left). Dinitrogen isotherms for UMCM-1-NH_2 (black), post PSM to UMCM-1-L5 (blue) and lastly post PSM into UMCM-1-L5A (red) (right). The BET surface areas are 4000, 3600, and 2800 m^2g^{-1}, respectively. The lowered total capacity of nitrogen is consistent with the introduction of large functional groups.

Another tagged MOF, UMCM-1-L6, which contains an olefin group attached to the bdc ligand via a urea linkage, was prepared. UMCM-1-L6 was obtained by treating UMCM-1-NH_2 with allyl isocyanate, giving the olefin-bearing material in essentially complete conversion. UMCM-1-L6 was then treated with tdc, which underwent the cycloaddition, quantitatively converting the olefin groups to the dihydropyridazine product, UMCM-1-L6A, as confirmed by ^{1}H NMR and ESI-MS analysis (Figure 3.13). PXRD data showed that UMCM-1-L6A was highly crystalline and maintained UMCM topology thus demonstrating that other olefin groups were also found to be suitable for the tetrazine PSM reaction.

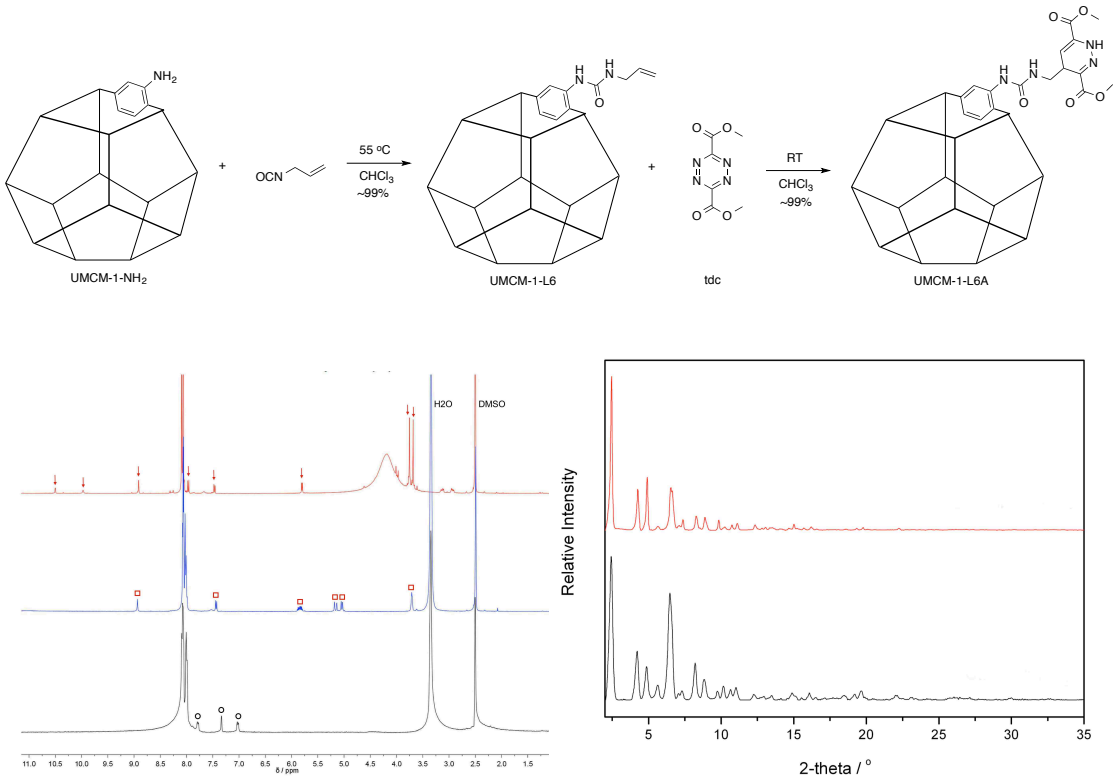

Figure 3.13. Subsequent PSM functionalization of UMCM-1-NH_2 into UMCM-1-L6 and finally into UMCM-1-L6A after the diels alder cycloaddition (top). ^{1}H NMR spectra of the digested materials before PSM (black, highlighted by black circles), after allyl isocyanate (UMCM-1-L6, blue, highlighted by red squares) and after tdc (UMCM-1-L6A, red, highlighted by red arrows) illustrating quantitative conversion for each step (bottom left). PXRD comparison of experimental (left) UMCM-1-NH_2 (black) and UMCM-1-L6A (red) demonstrating the crystallinity is maintained after both PSM steps (bottom right).

UMCM-1-L4, described above, was also exposed to the tdc ligand but showed no conversion to the cycloaddition product even at elevated temperatures (55 °C) and extended reaction times (3 d). It was hypothesized that this terminal alkene was physically too close to the framework lattice (3 atom separation between the olefin and aryl group versus 5 in L5 and L6) resulting in steric crowding (Figure 3.14). Taking into account van der Waals radii, the orientation of the allyloxy group into the smaller pore, and the geometry required for the cycloaddition to occur, the tdc molecule

may simply be too large to acquire the optimal distances from the olefin in this case to undergo the cycloaddition.

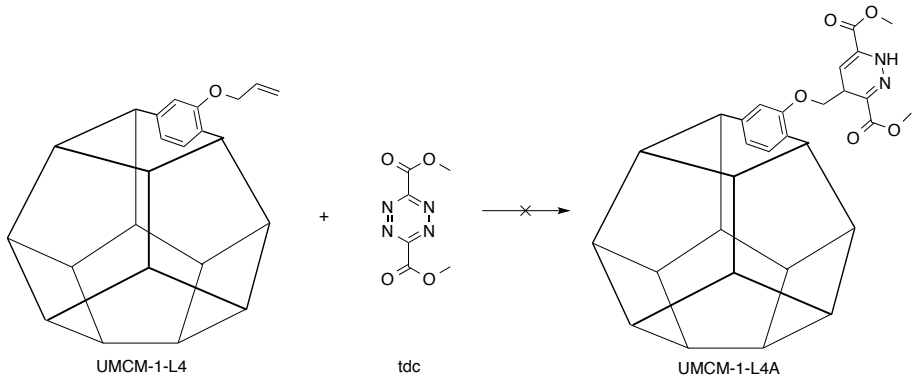

Figure 3.14. UMCM-1-L4 was exposed to tdc however no reaction took place even with heating to 55 °C and excess tdc. The olefin unit may be too close to the framework and thus prevented the formation of the cycloaddition product.

In order to further generalize these findings for other frameworks, IRMOF-3 was prepared, and quantitatively modified with pentenoic anhydride. Attempts to modify IRMOF-3-L5 with tdc demonstrated no more than ~20% conversion, even with elevated temperatures, longer reaction times, and excess tdc (Figure 3.15). This is reasonable as the IRMOF pores are smaller than UMCM and pore congestion from the addition of functional groups has been seen previously. This is manifested in a diminished BET surface area the more atoms that are introduced.[34]

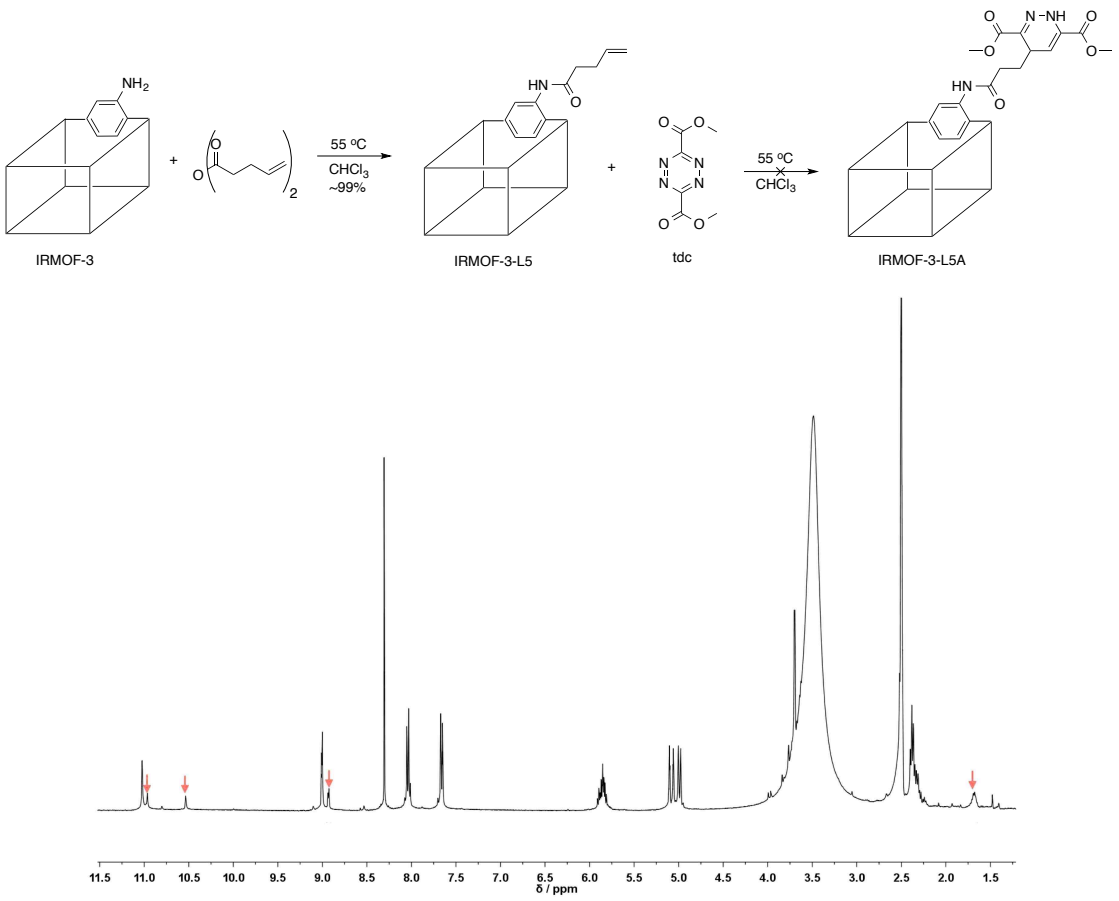

Figure 3.15. Scheme for the addition of a terminal alkene to IRMOF-3 via PSM into IRMOF-3-L5 (top) followed by reaction with tdc to obtain IRMOF-3-L5 (top). ^{1}H NMR of digested IRMOF-1-L5A (bottom). Red arrows correspond to L5A resonances showing only a small fraction of the olefin groups are modified.

The contrast between the facile reactivity of the UMCM system to the IRMOF system suggested that the smaller pore size and steric crowding of the olefin groups in the latter might be hindering the progress of the PSM reaction with tdc. To test this hypothesis, a series of mixed-ligand MOFs,[18,33,35-39] comprised of both bdc and NH_2-bdc in varying ratios, were prepared. The incorporation of bdc into the overall material decreases the density of $-NH_2$ tagged groups that are PSM capable thus modulating the amount of crowding within the pores. As found in previous reports of

mixed MOFs,[37,38] the mole fraction of NH_2-bdc in the IRMOF (obtained by ^1H NMR spectra of the digested products) shows a linear relationship with the ratio of bdc and NH_2-bdc in the solvothermal reaction mixture (Figure 3.16). In this manner, IRMOFs were prepared with 44% to 85% NH_2-bdc in the framework. Treating any of the mixed-ligand IRMOFs with pentenoic anhydride resulted in a quantitative conversion to the mixed materials containing bdc and olefin- bearing bdc ligands (i.e., IRMOF-3-L5$_n$, where n = mole fraction of the functionalized ligand;). As expected, the BET surface areas of IRMOF-3- L5$_n$ materials show a linear increase as the proportion of modified ligand decreases (i.e., as n gets smaller). This finding is consistent with earlier studies on MOFs that had undergone different degrees of PSM. The IRMOF-3-L5$_n$ materials were then further modified with tdc at 55 °C for 48 h (Figure 3.17). As shown in the ^1H NMR spectra of the digested products, when the fraction of L5 in the MOF was 66% or less, complete conversion to the cycloaddition product was obtained. The ^1H NMR data are supported by ESI-MS analysis, which shows only product ions from the dihydropyridazine-containing L5A. PXRD and single-crystal XRD indicate that the final IRMOF-3-L5A$_n$ remains highly crystalline (Figure 3.18).

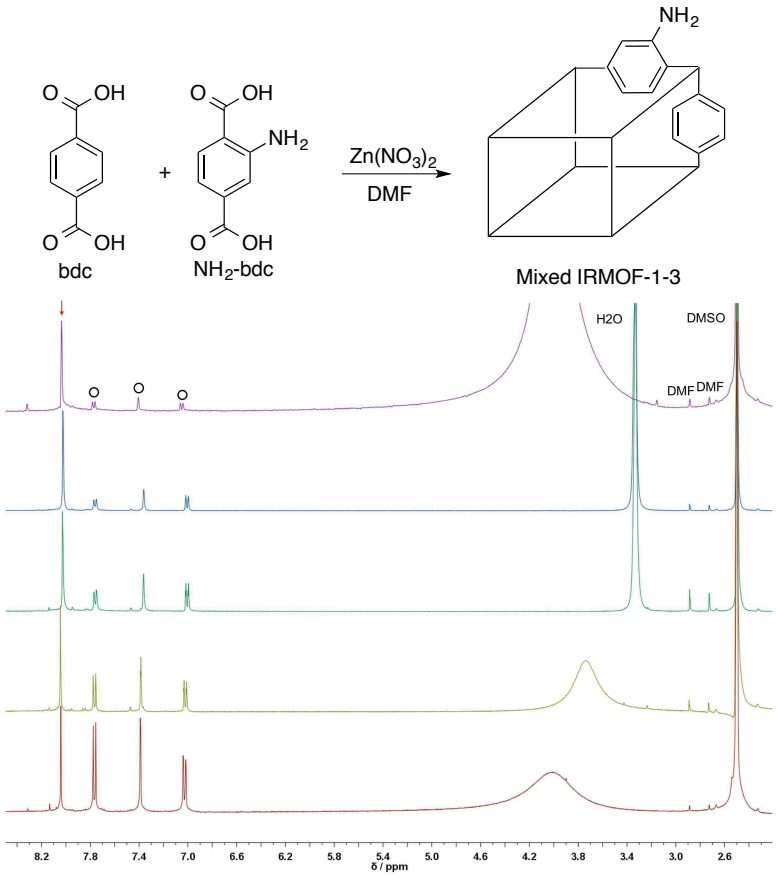

Figure 3.16. Synthesis of mixed IRMOF (top). ^{1}H NMR of digested mixed IRMOF-1-3 with varying ratios of bdc incorporation (bottom). From bottom to top 15%, 25%, 33%, 48%, and 56% bdc. The NH_2-bdc peaks (highlighted by black circles) grow substantially in comparison to the single bdc peak (highlighted by red arrow) with a higher ratio of NH_2-bdc incorporated.

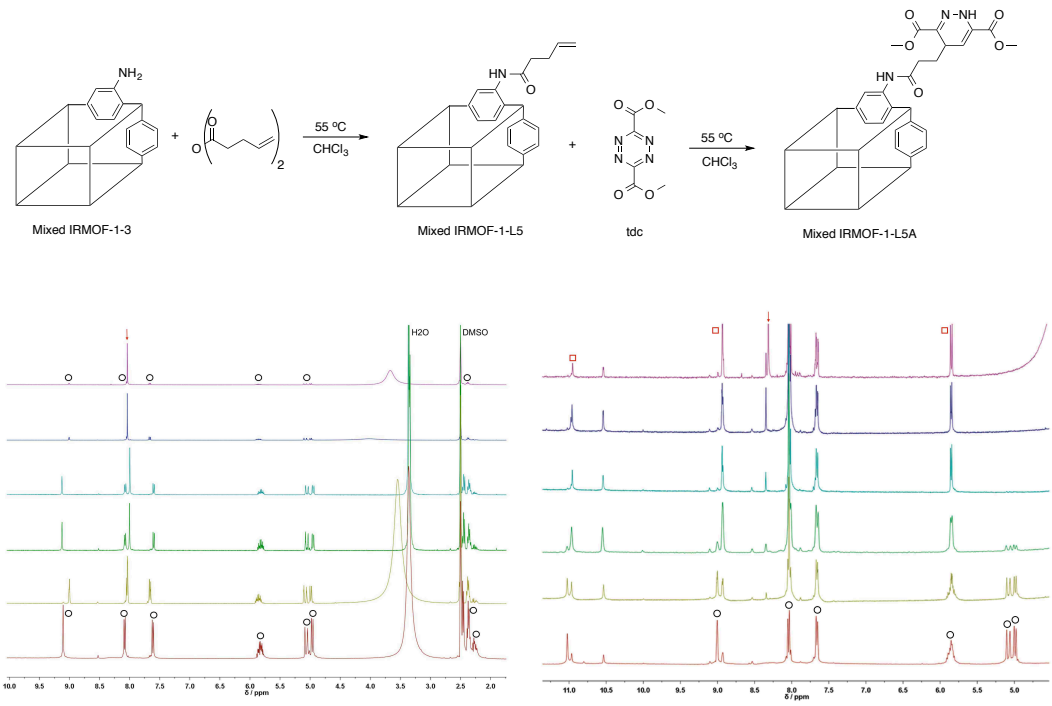

Figure 3.17. Successful PSM functionalization of the NH_2-bdc ligand in mixed IRMOF-1-3 to L5 followed by the diels alder cycloaddition reaction (top). ^{1}H NMR of digested mixed IRMOF-1-L5 with varying ratios of bdc incorporation (left, L5 resonances are highlighted by black circles). From bottom to top 15%, 25%, 33%, 48%, and 56% bdc (highlighted by a red arrow). The shifting of the NH_2-bdc resonances indicates quantitative conversion to the olefin. ^{1}H NMR spectra of mixed IRMOF-3-L5A post both PSM steps is the stacked figure (right, L5A resonances are highlighted by red squares). From bottom to top, no bdc incorporation (red), 15% bdc incorporation (yellow), 25% bdc (green), 33% bdc (teal), 48% bdc (navy), and 56% bdc incorporation (purple). Notice the remaining olefinic proton resonances between 5-6 ppm for materials with ≤ 33% bdc. The necessity for ≥ than 33% bdc in a mixed IRMOF material in order for complete conversion with the tdc ligand strongly suggests that steric crowding is preventing further reaction.

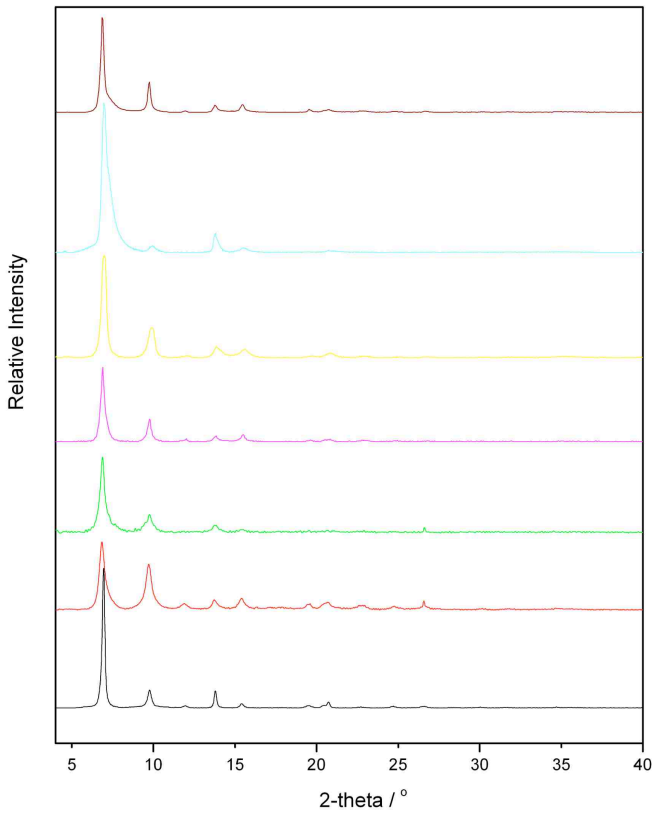

Figure 3.18. Experimental PXRD patterns for IRMOF-1 (black) and mixed IRMOF-1-L5A post PSM. From bottom to top, IRMOF-1 (black, for reference), no bdc incorporation (red), 15% bdc incorporation (green), 25% bdc (pink), 33% bdc (yellow), 48% bdc (teal), and 56% bdc incorporation (brown).

3. IV. Conclusions

In conclusion, a thioether functionality was included into MIL-68(In) using a photoinitiated thiol-ene click reaction and successfully utilized an inverse-electron-demand Diels-Alder reaction for the PSM of two different Zn-based MOF frameworks. Sulfur atoms within a Zn-carboxylate lattice were, and still are, rare and their full potential is not yet realized. Additionally, this work demonstrated that multiple reagents in a reaction, i.e. catalyst and radicals, can be tolerated within the pores of a MOF. However, optimization of multicomponent reactions can be more

cumbersome than expected. Although pre- and postsynthetic modification allowed for the synthesis of alkene tagged MOFs, only reaction conditions that fall within certain parameters can fully interact with these alkenes. The MOF lattice must be resilient to the reaction conditions, proximity of the reagents to the functional group must be reasonable, and the reagents must not fill the entire capacity of the MOF pores. Compatible PSM conditions for any given MOF material is crucial in devising a synthetic plan. For these PSM reactions in an IRMOF material, modulating the ratio of tagged linker was essential for obtaining efficient conversion simply because there was limited pore space. This highlights the importance of utilizing mixed-ligand MOFs should the incorporated functionality approach the available pore space in the material and be considered when designing MOF materials for applications. The applicability of this particular reaction should allow for PSM with MOFs bearing various dienophiles or heterodienophiles, such as electron-rich olefins, acetylenes, enol ethers, enamines, benzynes, and others. The ability to prepare diversely functionalized reagents should allow for the introduction of unprecedented, new functionality into MOFs using both of the above PSM methods. Most importantly, to increase the chance of a successful PSM in MOFs, a simpler reaction (i.e. single reagent versus multiple reagents) is generally a superior option than relying on the diffusion of multiple coreagents.

3. V. Experimental

Starting materials and solvents were purchased and used without further purification from commercial suppliers (Sigma-Aldrich, TCI, Alfa Aesar, etc.). DMF and chloroform were dried using molecular sieves. UMCM-1-NH_2 was prepared as previously described.[40]

3. V. i. Ligand Synthesis

6. Compound 1 (2 g, 9.5 mmol) and K_2CO_3 (2.6 g, 19 mmol) were dissolved in DMF (85 mL). Allyl bromide (1.4 g, 11.4 mmol) was added and the reaction was heated at 85 °C for 1 h. The mixture was cooled to room temperature, the K_2CO_3 was filtered off and water was added until a white solid precipitated out. This was isolated by filtration. Yield: 1.8 g, 77%. ^{1}H NMR ($CDCl_3$, 400 MHz, 25 °C): δ 3.92 (d, 6H; CO_2CH_3), 4.68 (s, 2H; CH_2), 5.32 (d, 1H; CH), 5.53 (d, 1H; CH), 6.06 (m, 1H; Allyl CH), 7.63 (m, 2H, ArH), 7.82 (d, 1H; ArH). ESI-MS(+): m/z 250.88 [M+H]+, 272.91 [M+NH4]+.

L4. Compound 6 (1.8 g, 7.4 mmol) was dissolved in THF (30 mL) and a 4% KOH solution (30 mL) was added. This was stirred at room temperature for 1 h. Water (50 mL) was added and the mixture was washed twice with ether (2x30 mL). The aqueous layer was acidified to pH ~ 1 with conc HCl to precipitate out a white solid. After filtration the solid was dried under vacuum with heat. Yield: 1.5 g, 93%. ^{1}H NMR (DMSO-d_6, 400 MHz, 25 °C): δ 4.71 (s, 2H; CH_2), 5.27 (d, 1H; CH), 5.47 (d, 1H; CH), 6.04 (m, 1H; Allyl CH), 7.55 (m, 2H; ArH), 7.69 (d, 1H; ArH). ESI-MS(+): m/z 222.80 [M+H]+.

L4R$_{Et}$. Compound L4 (0.2 g, 1 mmol) in 5 mL DMF with 1-ethane thiol (0.12 g, 2 mmol) and DMPA (0.013 g, 0.05 mmol) was exposed to 365 nm light for 21 h. The resulting yellow solution was washed with saturated $NaHCO_3$ (5 mL) which precipitated out a solid. After filtration, the filtrate was acidified to pH~1 with conc. HCl to precipitate out a white solid. This was collected by filtration and washed with water and dichloromethane. Yield: 0.120 g, 50%. ^{1}H NMR (DMSO-d_6, 400 MHz, 25 °C): δ 1.16 (t, 3H; CH_3), 1.95 (m, 2H; CH_2), 2.48 (m, 2H; CH_2), 2.67 (t, 2H; CH_2), 4.13 (t, 2H; CH_2), 7.52 (m, 2H, ArH), 7.67 (d, 1H; ArH). ESI-MS(-): m/z 284.07 [M-H]-.

L4R$_{iPr}$. Compound L4 (0.2 g, 1 mmol) in 5 mL DMF with 2-propane thiol (0.12 g, 2 mmol) and DMPA (0.013 g, 0.05 mmol) was exposed to 365 nm light for 21 h. The resulting yellow solution was washed with saturated $NaHCO_3$ (5 mL) which precipitated out a solid. After filtration, the filtrate was acidified to pH~1 with conc. HCl to precipitate out a white solid. This was collected by filtration and washed with water and dichloromethane. Yield: 0.23 g, 65%. ^{1}H NMR (DMSO-d_6, 400 MHz, 25 °C): δ 1.16 (d, 6H; CH_3), 1.94 (m, 2H; CH_2), 2.67 (t, 2H; CH_2), 2.91 (m, 1H; CH), 4.15 (t, 2H; CH_2), 7.55 (m, 2H, ArH), 7.67 (d, 1H; ArH). ESI-MS(-): m/z 297.00 [M-H]-.

L4R$_{Hex}$. Compound L4 (0.2 g, 1 mmol) in 5 mL DMF with 1-hexane thiol (0.12 g, 2 mmol) and DMPA (0.013 g, 0.05 mmol) was exposed to 365 nm light for 18 h. The resulting yellow solution was washed with saturated $NaHCO_3$ (5 mL) which precipitated out a solid. After filtration, the filtrate was acidified to pH~1 with conc. HCl to precipitate out a white solid. This was collected by filtration and washed with water and dichloromethane. Yield: 0.25 g, 62%. ^{1}H NMR (DMSO-d_6, 400 MHz, 25 °C): δ 0.80 (t, 3H; CH_3), 1.21 (m, 6H; CH_2), 1.48 (m, 2H; CH_2), 1.94 (m, 2H; CH_2), 2.48 (m, 4H; CH_3), 2.66 (t, 2H; CH_2), 4.15 (t, 2H; CH_2), 7.52 (m, 2H, ArH), 7.67 (d, 1H; ArH). ESI-MS(-): m/z 339.06 [M-H]-.

Dimethyl-1,2,4,5-tetrazine-3,6-dicarboxylate (tdc). Dimethyl-1,2,4,5-tetrazine-3,6-dicarboxylate was synthesized according to a published procedure.[41] Due to the toxicity of nitrous gases (disproportionated HONO) used in the original preparation, the last step of the procedure was changed, using isoamyl nitrite as the oxidation reagent. Isoamyl nitrite (2.4 mL, 17 mmol) was added slowly to a solution of dimethyl-1,4-dihydro-1,2,4,5-tetrazine-3,6-dicarboxylate (1.2 g, 6.0 mmol) in CH_2Cl_2, and the mixture was stirred at room temperature for 2 h. The solution changed color from

yellow to red. After evaporation of solvent the residue was recrystallized in $CHCl_3$ and cyclohexane (10:1). ^1H NMR ($CDCl_3$, 400 MHz, 25 °C): δ 4.23 (s, 6H, COOMe). ESI-MS(+): m/z = 197.8 [M+H]+.

3. V. ii. MOF Synthesis and MOF PSM

IRMOF-1-L4. L4 (91 mg, 0.4 mmol) and $Zn(NO_3)_2 \cdot 6H_2O$ (340 mg, 1.1 mmol) were dissolved in DMF (10 mL). This was placed in a sand bath and placed into a ramping oven and heated to 100 °C at 2.5 C °C. This was soaked for 18h and cooled to room temperature at 2.5 °C. The clear blocks (41 mg, 32% yield) were washed 3 times with DMF (10 mL) and exchanged into $CHCl_3$ (10 mL) once a day for 3 days.

IRMOF-1-L4R$_{Et}$. This reaction was attempted in DMF, toluene, benzene, chlorobenzene, and $CHCl_3$. The thiol of interest was ethane thiol, the wavelength of light was 365 nm, and the radical initiator was 2,2-dimethoxy-2-phenylacetophenone (DMPA). Despite varying ratios of all reactants with respect to IRMOF-1-OAl and UMCM-1-OAl, no appreciable conversion was determined from digestion and ^1H NMR of the materials. The decrease in the quality of the powder patterns of the materials suggested the Zn based MOFs were not able to withstand the reaction conditions.

UMCM-1-L4. L4 (60 mg, 0.3 mmol), H_3btb (39 mg, 0.09 mmol) and $Zn(NO_3)_2 \cdot 6H_2O$ (324 mg, 1.1 mmol) were dissolved in DMF (10 mL). This was placed in a sand bath and placed into an isothermal oven at 85 °C for 48 hours. The vial was taken out of the sand bath and placed on the bench top to cool to room temperature. The clear needles were washed 3 times with DMF (10 mL) and exchanged into $CHCl_3$ (10 mL) once a day for 3 days. Yield: 43 mg, 46% yield based on btb.

MIL-68(In)-L4. MIL-68(In)-L4 was synthesized following a modified literature procedure.[6,42-46] To a small Teflon Parr bomb, L4 (265 mg, 1.2 mmol), $In(NO_3)_2 \bullet xH_2O$ (400 mg, 1.35 mmol), and DMF (5 mL) was added. The bomb was sealed and placed into an oven at 100 °C for 48h. A white powder, MIL-68(In)-L4, 350 mg was obtained and washed with DMF followed by dichloromethane. The powder was transferred to a scintillation vial and between dichloromethane washings was centrifuged at 10000 RPM for 7 minutes before decanting the solvent. Afterwards this was dried under vacuum at room temperature for 3 hours before being stored in a dessicator. BET = 28 m^2g^{-1} after usual degassing methods at 105 °C overnight. The ^1H NMR digestion conditions are 10 mg of material followed by the addition of 590 μL DMSO and 10 μL DCl solution (35% by wt in H_2O).

MIL-68(In)-L4R$_{Et}$. This reaction was screened in MIL-68(In)-L4 under identical conditions to the zinc based MOFs. The most promising condition was as follows: to MIL-68(In)-OAl (35 mg, 1 mmol), DMPA (25 mg, 1 mmol) and 0.5 mL of DMF was added followed by ethane thiol (56 uL, 4 mmol). This was exposed to 365 nm light for 72 hours. The final yellow material was washed with DMF (3 x 2 mL) and DCM that had been dried with MS (2 x 2 mL) and left to soak overnight. Fresh DCM was replaced for a total of 2 days of soaking. Yield: ~25-30%. The low conversion may be due to incomplete activation and removal of trapped species prior to the reaction or problems with the diffusion of the radical species.

UMCM-1-L5. Approximately 56 mg of UMCM-1-NH_2 (ca. 0.05 mmol equiv of -NH) was placed in a vial with 0.2 mmol of pentenoic anhydride in 2 mL of $CHCl_3$. The mixture was heated in an oven at 55 °C for 24 h, after which the solution was decanted and the crystals were rinsed with 3×6 mL of $CHCl_3$. A fresh solution of

pentenoic anhydride was added to the vial again and heated for an additional 24 h. The product was washed with 3×6 mL of $CHCl_3$ and immersed in $CHCl_3$ (~10 mL) for 1 day.

UMCM-1-L5A. Fresh UMCM-1-L5 was combined with 20 mg (0.1 mmol) of dimethyl-1,2,4,5-tetrazine-dicarboxynate in 2 mL of $CHCl_3$. The sample was left at room temperature for 24 h, after which the red solution was decanted. The yellow product was washed with 5×10 mL of $CHCl_3$ and immersed in $CHCl_3$ (~10mL) for at least 3 d, during which fresh $CHCl_3$ solvent was changed every day.

UMCM-1-L6. Approximately 56 mg of UMCM-1-NH_2 (ca. 0.05 mmol equiv of -NH) was placed in a vial with 0.2 mmol of allyl isocyanate in 2 mL of $CHCl_3$. The mixture was heated in an oven at 55 °C for 24 h. The solution was decanted and the crystals were rinsed with 3×6 mL of $CHCl_3$. Then a fresh solution of allyl isocyanate was added to the vial and the mixture was heated for an additional 24 h. The resulting UMCM-1-L6 crystals were washed with 3×6 mL of $CHCl_3$ and immersed in $CHCl_3$ (~10 mL) for 3 days.

UMCM-1-L6A. Fresh UMCM-1-L6 was combined with 20 mg (0.1 mmol) of dimethyl-1,2,4,5-tetrazine-dicarboxynate in 2 mL of $CHCl_3$. After heating the sample at 55 °C for 24 h, the red supernatant was decanted. The remaining yellow crystals of UMCM-1-L6A were washed with 5×10 mL of $CHCl_3$ and immersed in $CHCl_3$ (~10 mL) for at least 3 days, during which fresh $CHCl_3$ was exchanged on a daily basis.

Mixed IRMOF-1-3. H_2bdc and NH_2-bdc with different ratios (see Table 1, total 0.4 mmol) were dissolved in 10 mL of DMF. $Zn(NO_2)_3 \bullet 6H_2O$ (0.353 g, 1.2 mmol) was then added to the solution. The mixture was sonicated for 30 min, then transferred to

a programmable oven in a sand bath and heated at a rate of 2.5 °C/min from 35 to 100 °C. The temperature was held at 100 °C for 18 h and then cooled at a rate of 2.5 °C/min to a final temperature of 35 °C. The mother liquor was decanted and the cubic-shaped crystals were washed with 3×10 mL of DMF followed by 3×10 mL of $CHCl_3$, and then finally soaked in 10 mL of $CHCl_3$ for 3 d with fresh $CHCl_3$ added every 24 h. The crystals were stored in the last $CHCl_3$ solution until needed. Yield: ~60 mg (50%) of mixed IRMOF-3.

IRMOF-3-L5$_n$. Approximately 60 mg of mixed IRMOF-1-3 was placed in a vial with 0.4 mmol of pentenoic anhydride in 2 mL of $CHCl_3$. The mixture was heated in an oven at 55 °C for 24 h, after which the solution was decanted and the crystals were rinsed with 3×6 mL of $CHCl_3$. Then a fresh solution of pentenoic anhydride was added to the vial again and the solution heated for an additional 24 h. The final product was washed with 3×6 mL of $CHCl_3$ and immersed in $CHCl_3$ (~10 mL) for 1 d.

IRMOF-3-L5A$_n$. Fresh IRMOF-3-L5$_n$ was combined with 40 mg (0.2 mmol) tdc in 2 mL of $CHCl_3$. After allowing the sample to stand at 55 °C for 2 d, the red solution was decanted. The product was washed with 5×10 mL of $CHCl_3$ and immersed in $CHCl_3$ (~10mL) for at least 3 d, during which fresh $CHCl_3$ solvent was changed every day.

3. V. iii. MOF Characterization

Material Characterization ^{1}H NMR Digestion and Analysis. Approximately 5 mg of crystalline sample was dried under vacuum at 50 °C for 3 h and then digested by sonication in 500 μL of *d*^{6} DMSO and 100 μL of dilute DCl (23μL of 35% DCl in D_2O diluted with 1000 μL of DMSO-d_6). ^{1}H NMR spectra were recorded on a Varian FT-NMR spectrometer (400MHz).

PXRD Analysis. Approximately 15 mg of crystalline sample (typically soaked in DMF or $CHCl_3$) was air dried before PXRD analysis. PXRD data were collected at ambient temperature on a Bruker D8 Advance diffractometer at 40 kV, 40 mA for Cu $K\alpha$ (λ = 1.5418 Å), with a scan speed of 1°/min, a step size of 0.02° in 2θ, and a 2θ range of 4-40°. The experimental backgrounds were corrected using the Jade 5.0 software package.

BET Surface Area Analysis. BET surface area (m^2g^{-1}) measurements were collected at 77 K with dinitrogen on a Micromeritics ASAP 2020 Adsorption Analyzer using volumetric technique. Approximately 30-60 mg of activated samples were evacuated on a vacuum line for 12 h, then transferred to a preweighed sample tube and degassed at 105 °C for approximately 18 h or until the outgas rate was <5 μmHg. The sample tube was reweighed to obtain a consistent mass for the degassed samples.

Mass Spectrometry. Mass spectra were performed using a ThermoFinnigan LCQ-DECA mass spectrometer and the data were analyzed using the Xcalibur software suite. ~10 mg of dried MOF sample was digested in 500 μL of DMSO and 100 μL of dilute 35% DCl/D_2O, followed by dilution in methanol.

Thermal Gravimetric Analysis (TGA). Approximately 10mg of sample was analyzed under a stream of dinitrogen using a TA Instrument Q600 SDT running from room temperature to 600-800 °C with a scan rate of 5 °C/min.

Single-Crystal X-ray Diffraction. Single crystals were mounted on a nylon loop with Paratone oil and placed under a nitrogen cold stream (200 K). Data was collected on a Bruker Kappa Apex II diffractometer using either Mo $K\alpha$ (λ = 0.71073 Å)

or Cu $K\alpha$ (λ = 1.54178 Å) irradiation controlled using the APEX 2.0 software package. Data were solved and refined using the SHELXTL software suite. The Zn ions, O atoms, and C atoms of the bdc ligand were located and refined anisotropically. The aryl substituents and solvent atoms ($CHCl_3$) are positionally disordered and could not be located in the difference map. The SQUEEZE model in PLATON (A.L. Spek, Acta Crystallogr. Sect. A. 46 (1990) C34) was applied to treat the electron density associated with the amide substituents and for partially occupied or disordered solvent within the porous framework. Hydrogen atoms were included in the empirical formula and formula weight except for those of solvent molecules.

3. VI. Acknowledgements

Texts, schemes, and figures in this thesis are, in part, reprints of the material in the following publication: Chao, C.; Allen, C. A..; Cohen, S. M. Tandem Postsynthetic Modification of Metal-Organic Frameworks Using an Inverse-Electron-Demand Diels-Alder Reaction *Inorg. Chem.* **2011**, *50*, 10534-10536. The dissertation author and co-author both contributed to the research. Permission to reproduce these publications was granted by the American Chemical Society, copyright 2011.

3. VII. Appendix

Table 3.1. Crystal data and structure refinement for UMCM-1-L5A and IRMOF-3-L5A$_{0.67}$.

Identification code	UMCM-1-L5A	IRMOF-3-L5A$_{0.67}$
Temperature	200(2) K	200(2) K
Wavelength	1.54178 Å	0.71073 Å
Crystal system	Hexagonal	Cubic
Space group	*P63/m*	*Fm-3m*
Unit cell dimensions	$a = b$ = 40.9234(3) c = 17.3329(3) Å $\alpha = \beta = 90°$ $\gamma = 120°$	$a = b = c$ = 25.6065(4) Å $\alpha = \beta = \gamma = 90°$
Volume	25138.8(5) Å^3	16790.0(5) Å^3
Z	6	8
Absorption coefficient	0.583 mm-1	1.184 mm^{-1}
F(000)	3042	5280
Crystal size (mm^3)	0.40 x 0.05 x 0.05	0.30 x 0.30 x 0.25
Theta range	1.25 to 50.47°.	1.38 to 23.23°.
Reflections collected	104460	13710
Independent reflections	9151 [R(int) = 0.0827]	658 [R(int) = 0.0296]
Completeness to theta = 46.06°	99.8 %	98.7 %
Refinement Method	Full-matrix least-squares on F^2	Full-matrix least-squares on F^2
Data / restraints / parameters	9151/ 92 / 332	658 / 0 / 25
Goodness-of-fit on F2	0.938	0.959
Final R indices [I>2sigma(I)]	R_1 = 0.0521, wR_2 = 0.1424	R_1 = 0.0758, wR_2 = 0.2047
R indices (all data)	R_1 = 0.0873, wR_2 = 0.1533	R_1 = 0.0887, wR_2 = 0.2178
Largest diff. peak and hole	0.399 and -0.233 e.Å^{-3}	0.860 and -0.306 e.Å^{-3}

3. VIII. References

(1) Deshpande, R. K.; Minnaar, J. L.; Telfer, S. G. *Angew. Chem., Int. Ed.* **2010**, *49*, 4598.

(2) Garibay, S. J.; Wang, Z. Q.; Tanabe, K. K.; Cohen, S. M. *Inorg. Chem.* **2009**, *48*, 7341.

(3) Seidel, W. W.; Hahn, F. E.; Lügger, T. *Inorg. Chem.* **1998**, *37*, 6587.

(4) Gadzikwa, T.; Lu, G.; Stern, C. L.; Wilson, S. R.; Hupp, J. T.; Nguyen, S. T. *Chem. Commun.* **2008**, 5493.

(5) Goto, Y.; Sato, H.; Shinkai, S.; Sada, K. *J. Am. Chem. Soc.* **2008**, *130*, 14354.

(6) Savonnet, M.; Bazer-Bachi, D.; Bats, N.; Perez-Pellitero, J.; Jeanneau, E.; Lecocq, V.; Pinel, C.; Farrusseng, D. *J. Am. Chem. Soc.* **2010**, *132*, 4518.

(7) Gadzikwa, T.; Farha, O. K.; Malliakas, C. D.; Kanatzidis, M. G.; Hupp, J. T.; Nguyen, S. T. *J. Am. Chem. Soc.* **2009**, *131*, 13613.

(8) Dondoni, A. *Angew. Chem., Int. Ed.* **2008**, *47*, 8995.

(9) Hoyle, C. E.; Bowman, C. N. *Angew. Chem., Int. Ed.* **2010**, *49*, 1540.

(10) Lowe, A. B. *J. Polym. Sci., Part A: Polym. Chem.* **2010**, *1*, 17.

(11) Campos, L. M.; Killops, K. L.; Sakai, R.; Paulusse, J. M. J.; Damiron, D.; Drockenmuller, E.; Messmore, B. W.; Hawker, C. J. *Macromolecules* **2008**, *41*, 7063.

(12) Connal, L. A.; Kinnane, C. R.; Zelikin, A. N.; Caruso, F. *Chem. Mater.* **2009**, *21*, 576.

(13) He, J.; Yee, K.; Xu, Z.; Zeller, M.; Hunter, A. D.; Chui, S. S.; Che, C. *Chem. Mater.* **2011**, *23*, 2940.

(14) He, J.; Zha, M.; Cui, J.; Zeller, M.; Hunter, A. D.; Yiu, S.; Lee, S.; Xu, Z. *J. Am. Chem. Soc.* **2013**, *135*, 7807.

(15) Yee, K.; Reimer, N.; Liu, J.; Cheng, S.; Yiu, S.; Weber, J.; Stock, N.; Xu, Z. *J. Am. Chem. Soc.* **2013**, *135*, 7795.

(16) Burrows, A. D.; Frost, C. G.; Mahon, M. F.; Richardson, C. *Chem. Commun.* **2009**, 4218.

(17) Hindelang, K.; Kronast, A.; Vagin, S. I.; Rieger, B. *Chem.--Eur. J.* **2013**, *19*, 8244.

(18) Deng, H.; Doonan, C. J.; Furukawa, H.; Ferreira, R. B.; Towne, J.; Knobler, C. B.; Wang, B.; Yaghi, O. M. *Science* **2010**, *327*, 846.

(19) Henke, S.; Schneemann, A.; Wütscher, A.; Fischer, R. A. *J. Am. Chem. Soc.* **2012**, *134*, 9464.

(20) Kaczmarek, H.; Gałka, P.; Kowalonek, J. *J. Appl. Polym. Sci.* **2010**, *115*, 1598.

(21) Cavka, J. H.; Jakobsen, S.; Olsbye, U.; Guillou, N.; Lamberti, C.; Bordiga, S.; Lillerud, K. P. *J. Am. Chem. Soc.* **2008**, *130*, 13850.

(22) Devaraj, N. K.; Weissleder, R.; Hilderbrand, S. A. *Bioconjugate Chem.* **2008**, *19*, 2297.

(23) Saracoglu, N. *Tetrahedron* **2007**, *63*, 4199.

(24) Devaraj, N. K.; Upadhyay, R.; Haun, J. B.; Hilderbrand, S. A.; Weissleder, R. *Angew. Chem., Int. Ed.* **2009**, *48*, 7013.

(25) Schoch, J.; Wiessler, M.; Jäschke, A. *J. Am. Chem. Soc.* **2010**, *132*, 8846.

(26) Tucker, M. J.; Courter, J. R.; Chen, J.; Atasoylu, O.; Smith, A. B.; Hochstrasser, R. M. *Angew. Chem., Int. Ed.* **2010**, *49*, 3612.

(27) Wiessler, M.; Waldeck, W.; Kliem, C.; Pipkorn, R.; Braun, K. *Int. J. Med. Sci.* **2010**, *7*, 19.

(28) Hansell, C. F.; Espeel, P.; Stamenović, M. M.; Barker, I. A.; Dove, A. P.; Du Prez, F. E.; O'Reilly, R. K. *J. Am. Chem. Soc.* **2011**, *133*, 13828.

(29) Volkringer, C.; Cohen, S. M. *Angew. Chem., Int. Ed.* **2010**, *49*, 4644.

(30) Wang, Z.; Cohen, S. M. *Angew. Chem., Int. Ed.* **2008**, *47*, 4699.

(31) Koh, K.; Wong-Foy, A. G.; Matzger, A. J. *Angew. Chem., Int. Ed.* **2008**, *47*, 677.

(32) Tanabe, K. K.; Cohen, S. M. *Angew. Chem., Int. Ed.* **2009**, *48*, 7424.

(33) Burrows, A. D. *CrystEngComm* **2011**, *13*, 3623.

(34) Tanabe, K. K.; Wang, Z. Q.; Cohen, S. M. *J. Am. Chem. Soc.* **2008**, *130*, 8508.

(35) Burrows, A. D.; Fisher, L. C.; Richardson, C.; Rigby, S. P. *Chem. Commun.* **2011**, *47*, 3380.

(36) Kim, M.; Cahill, J. F.; Prather, K. A.; Cohen, S. M. *Chem. Commun.* **2011**, *47*, 7629.

(37) Kleist, W.; Jutz, F.; Maciejewski, M.; Baiker, A. *Eur. J. Inorg. Chem.* **2009**, *2009*, 3552.

(38) Koh, K.; Wong-Foy, A. G.; Matzger, A. J. *Chem. Commun.* **2009**, 6162.

(39) Wang, C.; Xie, Z.; deKrafft, K. E.; Lin, W. *J. Am. Chem. Soc.* **2011**, *133*, 13445.

(40) Wang, Z.; Tanabe, K. K.; Cohen, S. M. *Inorg. Chem.* **2009**, *48*, 296.

(41) Boger, D. L.; Coleman, R. S.; Panek, J. S.; Huber, F. X.; Sauer, J. *J. Org. Chem.* **1985**, *50*, 5377.

(42) Volkringer, C.; Meddouri, M.; Loiseau, T.; Guillou, N.; Marrot, J.; Ferey, G.; Haouas, M.; Taulelle, F.; Audebrand, N.; Latroche, M. *Inorg. Chem.* **2008**, *47*, 11892.

(43) Canivet, J.; Aguado, S.; Bergeret, G.; Farrusseng, D. *Chem. Commun.* **2011**, *47*, 11650.

(44) Barthelet, K.; Marrot, J.; Ferey, G.; Riou, D. *Chem. Commun.* **2004**, 520.

(45) Pera-Titus, M.; Savonnet, M.; Farrusseng, D. *J. Phys. Chem. C* **2010**, *114*, 17665.

(46) Fateeva, A.; Horcajada, P.; Devic, T.; Serre, C.; Marrot, J.; Greneche, J. M.; Morcrette, M.; Tarascon, J. M.; Maurin, G.; Ferey, G. *Eur. J. Inorg. Chem.* **2010**, 3789.

4. Chemically Crosslinked Metal-Organic Frameworks

4. I. Introduction

Chapters 2 and 3 have explored the introduction of new functional groups using a combination of presynthetic and PSM methods. Both approaches can be useful for introducing complex functional groups into MOFs. One of the goals of the thiol-ene chemistry explored Chapter 3 was to use PSM to 'stitch together' MOFs that had two olefin moieties per organic strut. Chapter 4 will discuss methods to 'stitch' together bdc subunits in a presynthetic approach (Figure 4.1).

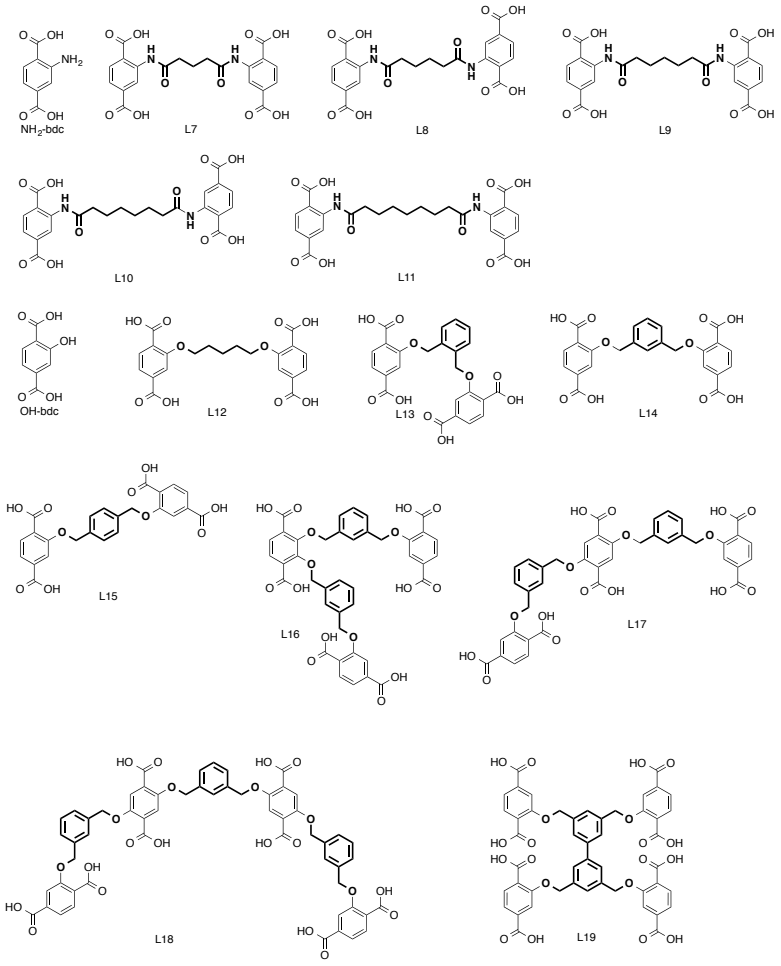

Figure 4.1. Crosslinked ligands discussed in Chapter 4. The bold portions highlight the variety of crosslinking moieties that were studied.

Crosslinking of a MOF was first reported over a decade ago. Lee and coworkers explored the stability and characteristics of a chemically crosslinked coordination solid based on Ag(I) ions and tritopic nitrile ligands (Figure 4.2).[1] Using PSM, Lee's seminal study clearly demonstrated that ligands within an intact coordination solid could be directly crosslinked resulting in enhanced framework stability. More recently, Sada and coworkers[2] transformed a crystalline MOF into a polymer gel by PSM crosslinking, followed by removal of the metal component (Figure 4.3).[3] The level of chemical crosslinking achieved was sufficient that upon removal of the structural metal ions from the SBUs, the overall morphology of the crystal was preserved in the polymer gel monolith. In a distinct but complementary route, Zaworotko and co-workers prepared MOFs using discrete metal-organic polyhedra (MOPs) connected by a linker (Figure 4.4).[4] The difference in this crosslinking approach is that the topology is dictated by the ligand-polyhedra connectivity as well the ligand geometry as opposed to the linkers being a separate entity from the framework shape. These studies bridge 'hard' crystalline with 'soft' polymeric materials allowing for the creation of a new area of materials research that harbor characteristics of both classes of compounds.[5-7]

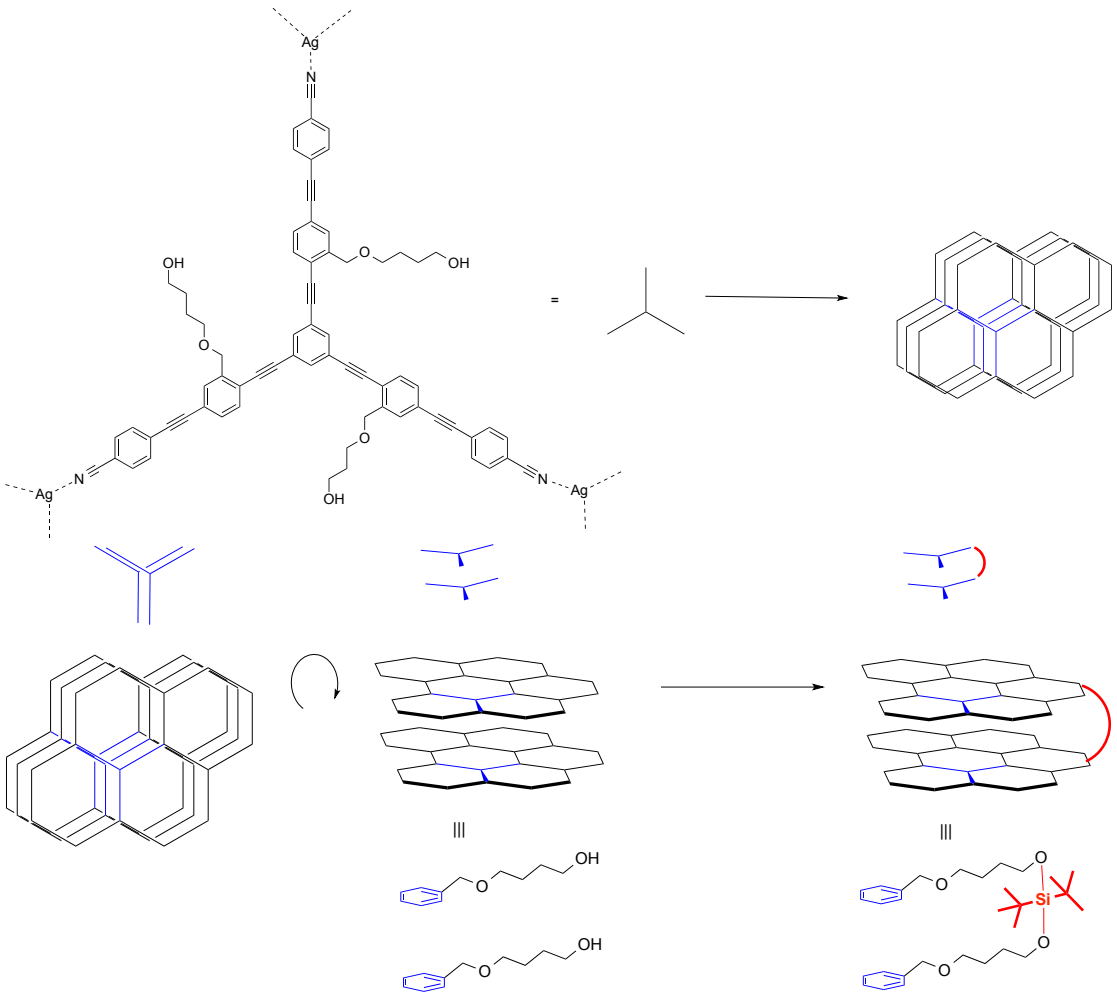

Figure 4.2. Tritopic nitrile ligand utilized in the coordination polymer that forms a honeycomb lattice (top). The alcohol group was chemically crosslinked with a silyl group (bottom). Thermal stability was increased upon the addition of crosslinks.

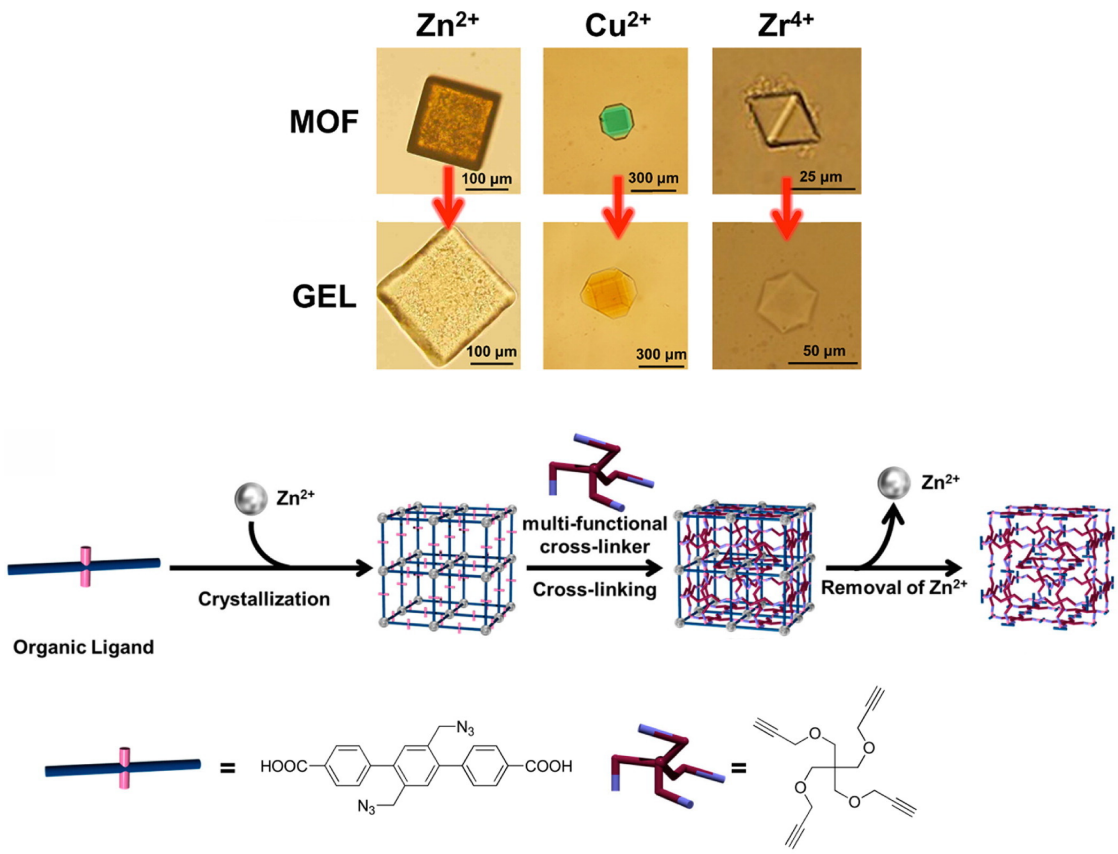

Figure 4.3. Sada's work converting a MOF to a gel of the same morphology by using click chemistry (top). Adapted with permission from Ishiwata, T., Furukawa, Y., Sugikawa, K., Kokado, K., and Sada, K., 'Transformation of Metal-Organic Framework to Polymer Gel by Cross-Linking the Organic Ligands Preorganized in Metal-Organic Framework,' *J. Am. Chem. Soc.*, **2013**, *135*, 5427-5432. Copyright 2013 American Chemical Society.

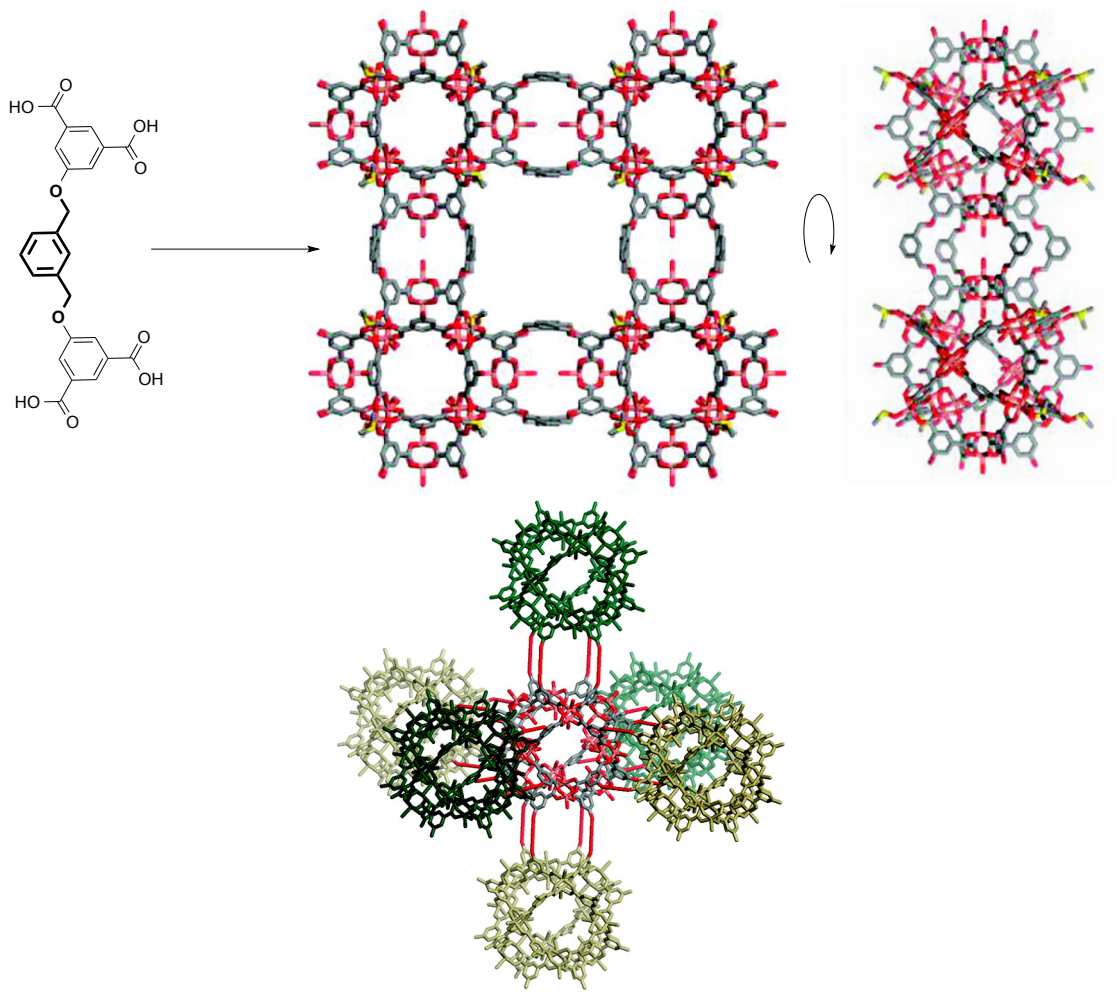

Figure 4.4. Zaworotko's use of a crosslinking moiety to bridge polyhedral 'nanoballs' depicted in varying shades of green. The red elongated sections represent the xylene linker. Adapted with permission from J. IV, J., Kravtsov, V. C., McManus, G. J., and Zaworotko, M. J., 'Bottom Up Synthesis That Does Not Start At The Bottom: Quadrule Covalent Cross-Linking of Nanoscale Faceted Polyhedra,' *J. Am. Chem. Soc.*, **2007**, *129* (33), 10076-10077. Copyright 2007 American Chemical Society.

4. II. Chemical Crosslinking in IRMOFs

Our initial attempts to produce crosslinked MOFs employed a PSM strategy. Specifically, crystals of the canonical IRMOF-3, which contain free aniline groups, were treated with diacylchlorides in an attempt to link pairs of NH_2-bdc ligands via amide

bonds (Figure 4.5). It was reasoned that such an approach should be effective based on a number of studies showing that the amine groups in IRMOF-3 can be readily acylated by anhydrides.[8] However, all attempts to react IRMOF-3 with diacylchlorides resulted in framework degradation, likely due to the HCl byproduct generated during the PSM reaction.

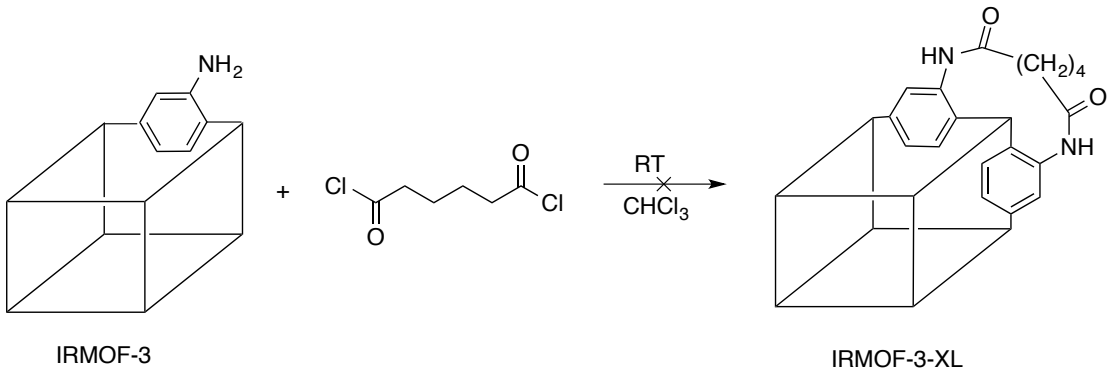

Figure 4.5. The attempted PSM crosslinking of IRMOF-3 with adipoyl dichloride. This reaction was not successful; likely due to the production of HCl during the reaction that can degrade Zn-carboxylate based MOFs.

In an alternative approach, a series of crosslinked NH_2-BDC ligands were prepared prior to MOF synthesis. These ligands contain 5-9 atoms (3-7 methylene groups and two carbonyl groups) between the amine groups of the NH_2-bdc ligands. All of the ligands were straightforward to prepare, in good yields, on a multigram scale. Simply combining different length diacylchlorides with the methyl ester of NH_2-bdc provided the tetra methyl ester variant of all the crosslinked ligands. Using a 1:1 v:v mixture of 4% $KOH_{(aq)}$ and THF, hydrolysis of the methyl ester was achieved to yield the desired products (L7-L11, Scheme 4.1).

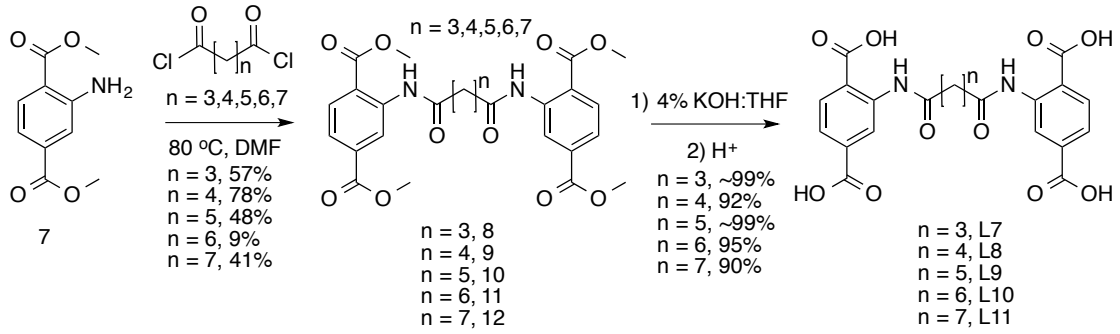

Scheme 4.1. Synthesis of crosslinked NH_2-bdc ligands L7-L11. Dimethyl 2-aminoterephthalate (7) was combined with acid dichlorides with a variety of alkyl chain lengths to create L7-L11 with 5-9 atoms crosslinking the bdc units.

Using these crosslinked, tetracarboxylic acid ligands, the direct solvothermal synthesis of a series of IRMOFs was pursued. Surprisingly, all of ligands, L7-L11, produced the desired IRMOF analogues (designated as IRMOF-3-L*n*) under standard solvothermal synthesis conditions. IRMOF-3-L7 (78%) and IRMOF-3-L8 (46%) formed as colorless, block crystals after 18 h. Longer linkers required longer reaction times (48 h) to obtain optimal yields, producing IRMOF-3-L9 (75%), IRMOF-3-L10 (72%), and IRMOF-3-L11 (52%) as small, cubic crystals, with the IRMOF-3-L11 producing a truncated cube morphology (Figure 4.6).

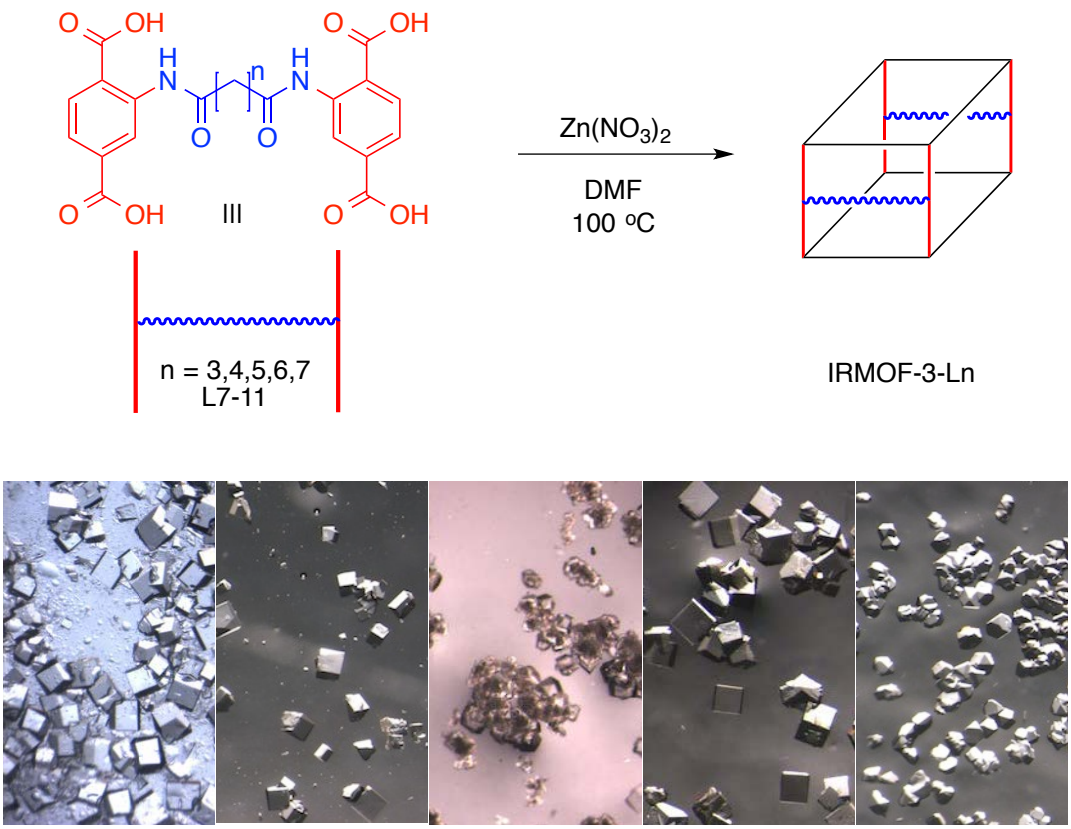

Figure 4.6. Synthesis of crosslinked IRMOFs from their precursor ligands (top). Optical microscopy photographs of IRMOF-3-(L7-11) (from left to right) showing mostly cubic morphology (bottom).

All of the crosslinked IRMOFs were characterized using PXRD, TGA, ^{1}H NMR, and gas adsorption studies. Single-crystal XRD structures of all IRMOF-3-L*n* MOFs unambiguously confirmed the formation of the desired IRMOF topology; however, electron density for the linker groups could not be assigned in any of the structures due to severe disorder of the crosslinking substituents. The PXRD patterns of all IRMOF-3-L*n* samples matched the simulated IRMOF-3 powder patterns (Figure 4.7).

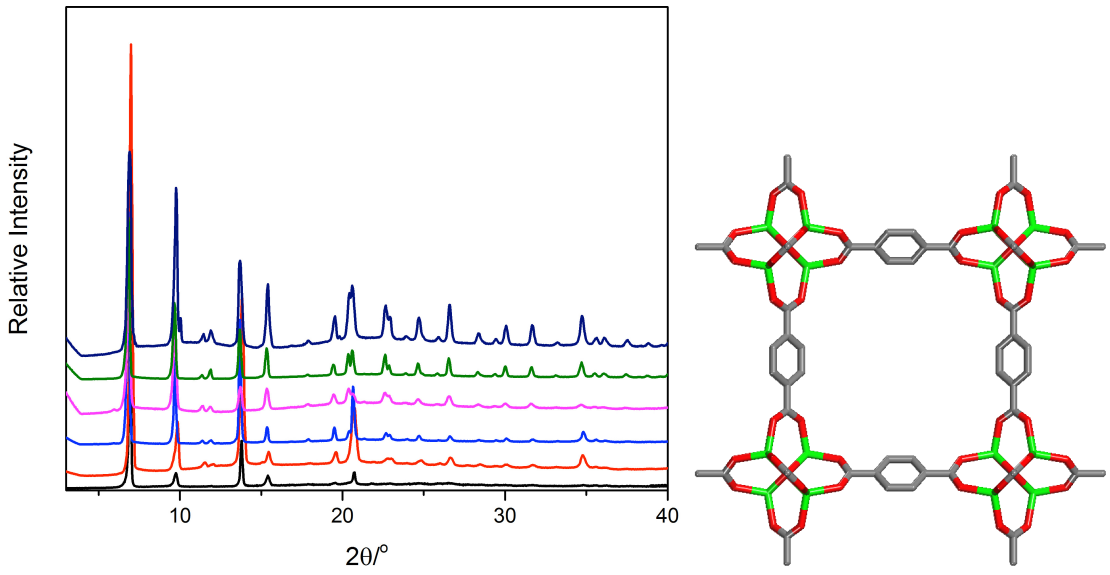

Figure 4.7. PXRD patterns for as-synthesized IRMOFs in comparison to uncrosslinked IRMOF-3 (black). IRMOF-3-L7 (red), IRMOF-3-L8 (blue), IRMOF-3-L9 (pink), IRMOF-3-L10 (green), and IRMOF-3-L11 (navy) (left). IRMOF lattice from the XRD structure verifying the topology (right). Unfortunately, no electron density for the crosslinking substituents was located. Carbon atoms are in grey, oxygen is in red, and zinc is in green.

The relative thermal stabilities of the crosslinked IRMOFs, as gauged by TGA, were similar to with IRMOF-3, with framework degradation occurring at ~400 °C. This is in contrast with the earlier work by Lee and co-workers, who noted that their fragile coordination network became more thermally stable upon crosslinking.[1] Although no enhancement in thermal stability was observed for our crosslinked IRMOFs, presumably due to the thermal lability of simple alkyl chains, a measurable difference in thermal activation was found. For activation at 105 °C, TGA analysis revealed trapped, residual guests in IRMOF-3-L8, which is discussed in more detail below.

Standard activation for IRMOFs involves three days of solvent exchange with $CHCl_3$ (i.e. soaking the crystals in $CHCl_3$) followed by heating at 105 °C under vacuum. This procedure results in the displacement of DMF for $CHCl_3$ giving full activation of IRMOF-3 as evidenced by TGA, ^1H NMR, and gas sorption analysis. 'Full activation' is achieved when the material is essentially devoid of residual solvent (DMF, $CHCl_3$, etc.). This standard thermal treatment at 105 °C can fully activate IRMOF-3, as well as all of the IRMOF-3-L*n*s, except for that derived from L8. Activation of IRMOF-3-L8 at 105 °C resulted in a material that showed a significant weight loss (12% mass loss) at ~140 °C (Figure 4.8) and ^1H NMR analysis indicated the retention of DMF in the MOF that is notably absent in the other systems (Figure 4.9). The residual DMF comes from the solvothermal synthesis process despite extensive washing of the crystals with $CHCl_3$. When activated at 150 °C, IRMOF-3-L8 showed no substantial mass loss at temperatures below 350 °C and no residual DMF in the ^1H NMR, suggesting complete desolvation and activation.

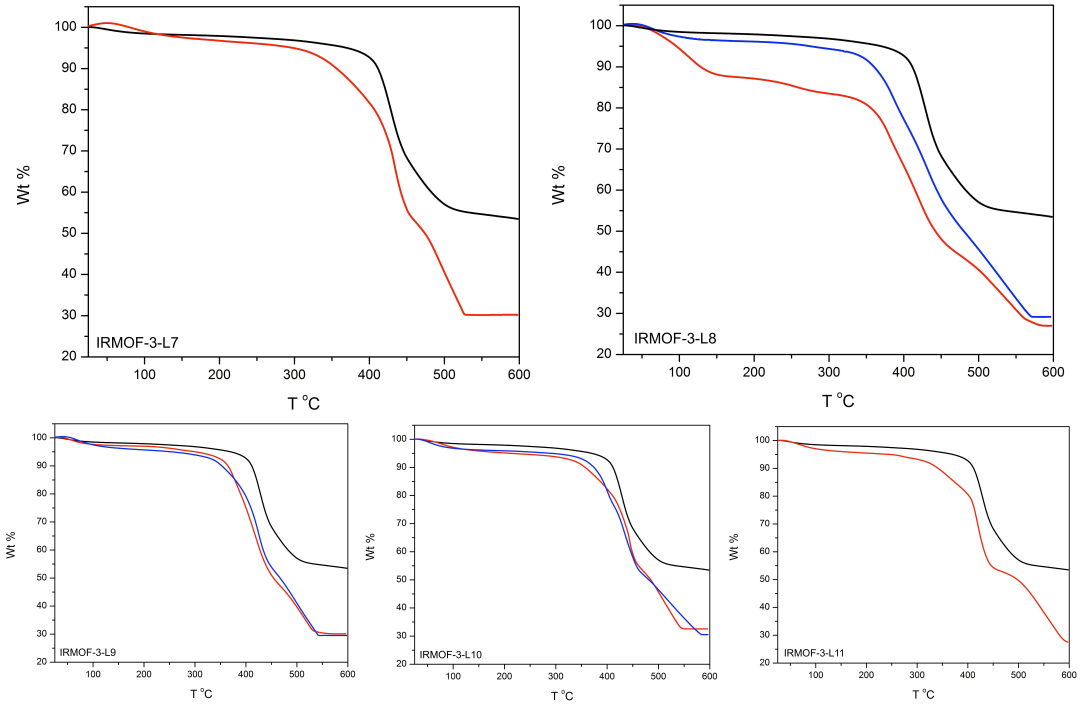

Figure 4.8. TGA traces of uncrosslinked IRMOF-3 (black) in comparison to the MOF samples after activation at 105 °C (red) and 150 °C (blue) for IRMOF-3-L7 (top left), IRMOF-3-L8 (top right), IRMOF-3-L9 (bottom left), IRMOF-3-L10 (bottom middle), and IRMOF-3-L11 (bottom right). Of note is the large mass loss for IRMOF-3-L8 of the red trace prior to framework degradation ~400 °C indicative of the trapped DMF molecules.

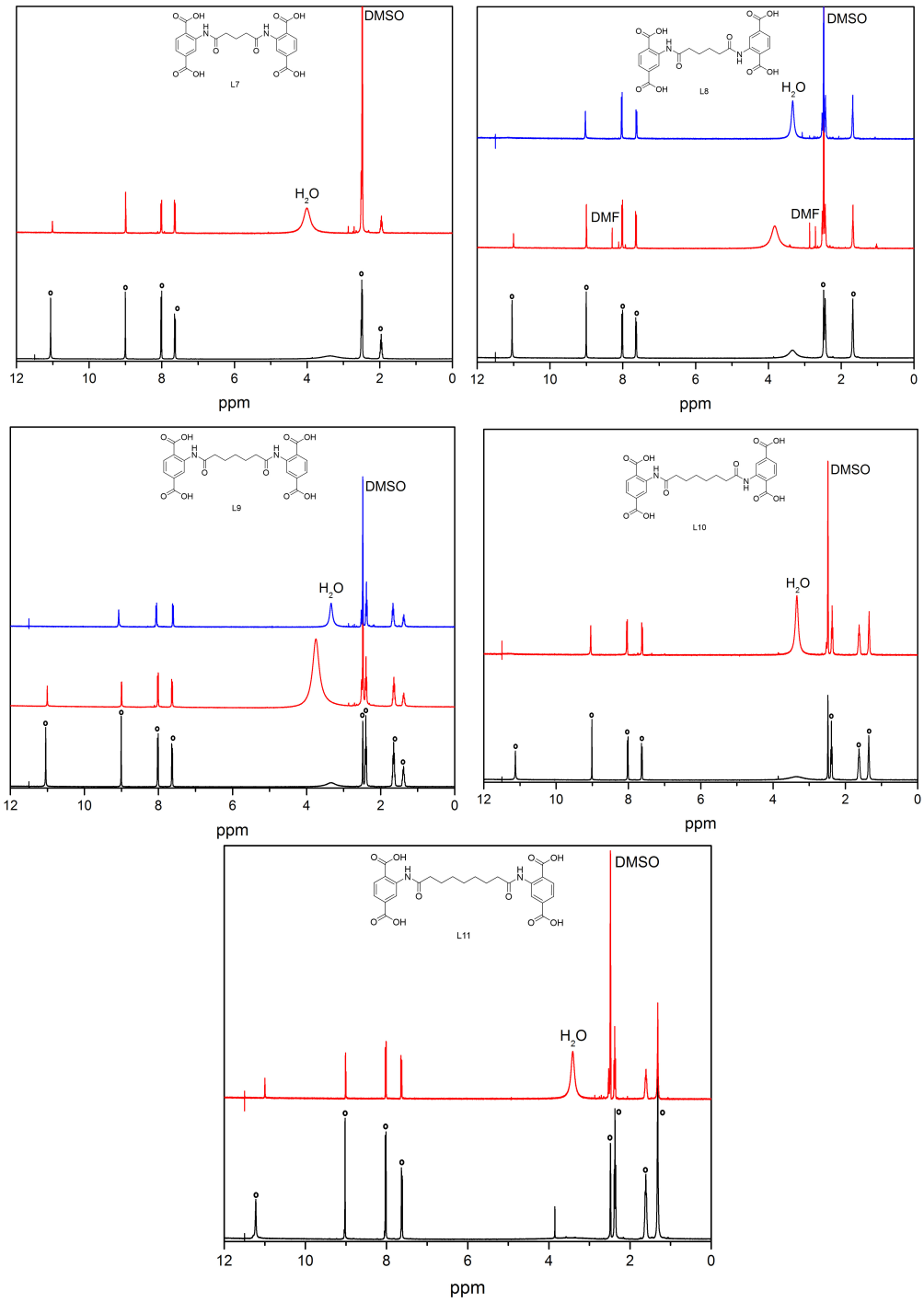

Figure 4.9. ^{1}H NMR of the ligands (black) in comparison to the digested MOF samples after activation at 105 °C (red) and 150 °C (blue) for IRMOF-3-L7 (top left), IRMOF-3-L8 (top right), IRMOF-3-L9 (middle left), IRMOF-3-L10 (middle right), and IRMOF-3-L11 (bottom). The important ligand resonances are marked with black circles. More DMF is found in IRMOF-3-L8 after activation at 105 °C.

DMF entrapment was further evidence by BET surface area measurements. After activation at 105 °C under vacuum, IRMOF-3-L*n* (where *n* = 7, 9-11) samples show surface areas ~1575-2000 m^2g^{-1}, reflective of the IRMOF structure (Figure 4.10). The values obtained were independent of the activation temperature (105 °C versus 150 °C) and consistent with those obtained for similarly acylated IRMOF-3 structures with IRMOF-3-L7, -L9, -L10 and -L11 giving BET values of 2049±8, 1636±55, 1827±23, and 1575±49 m^2g^{-1}, respectively.[9] It remains undetermined why IRMOF-3-L10 has a higher BET value than IRMOF-3-L9, but this could be due to the better quality of the crystals based on uniformity of the crystallites and sharpness of the PXRD pattern. IRMOF-3-L8 gave different surface area values depending on the activation temperature. When activated at 105 °C, IRMOF-3-L8 gave a BET surface area of 1618±21 m^2g^{-1} even after 48 h of heating. When activated at 150 °C, the BET surface area measurably and reproducibly increased by ~10% (1774±15 m^2g^{-1}), again indicative of better activation and complete removal of DMF (Figure 4.10). For all the crosslinked MOFs, the presence of the linkers occluding the MOF pores was observed as a monotonic decrease of the average pore size of the IRMOF-3-L*n* materials with increasing tether length; 6.72, 6.62, 6.59, 6.49, and 6.41 Å for L7-L11 respectively based on the Horvath-Kawazoe pore filling model.

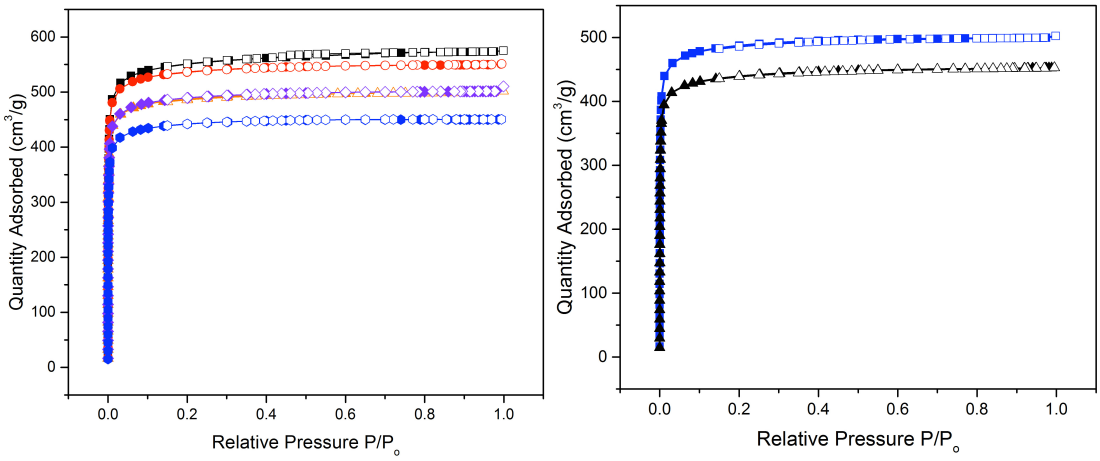

Figure 4.10. Dinitrogen isotherms of IRMOF-3-Ln materials activated at 105 °C (left). Filled and open symbols represent the absorption and desorption curves, respectively, for IRMOF-3-L7 (black), IRMOF-3-L8 (orange), IRMOF-3-L9 (red), IRMOF-3-L10 (purple) and IRMOF-3-L11 (blue). Specifically, IRMOF-3-L8 activated at both 105 °C (black) and 150 °C (blue) (right). There is a substantial increase in adsorption capacity after full removal of the solvent.

It is somewhat remarkable that a single carbon difference in the tether length (IRMOF-3-L8) can elicit a clearly measurable difference in the encapsulation properties of the MOF. However, previous studies on alkyl-decorated flexible MOFs have also shown similarly subtle differences. When varying the length of the alkyl substituent on a series of flexible MOFs, 'breathing' behavior, a measurable open and closing of the MOF channels, was observed only for one out of the six studied, while other chain lengths did not induce such structural plasticity into the MOF.[10] The data obtained here on IRMOF-3-L8 again show that even very small changes in ligand substituents can result in measurable differences in physical behavior. We anticipate that further exploration of linker lengths, structure, and composition will lead to more unanticipated MOF properties.

Several observations and experiments were performed to confirm these ligands were truly crosslinking the framework and to exclude the possibility that only one half of the ligand was participating in MOF formation. That is, it is possible that only one bdc component was structurally incorporated into the MOF lattice, with the tether and second bdc group simply behaving as a dangling substituent within the MOF pores (Figure 4.11). Combustion analysis data obtained clearly indicate that the carbon content of the MOF is consistent with both bdc groups participating in lattice formation (Table 4.1). If the tether and one of the bdc units was acting simply as a 'free' substituent the carbon content would be nearly double that measured by combustion analysis (Table 4.2). In addition, the BET gas sorption data support both bdc groups are used structurally in the MOF. If the tether and one bdc group was dangling within the MOF pores, the BET values would be much lower than those obtained, as evidence by several previous studies on IRMOFs containing bulky substituents within the pores.[9]

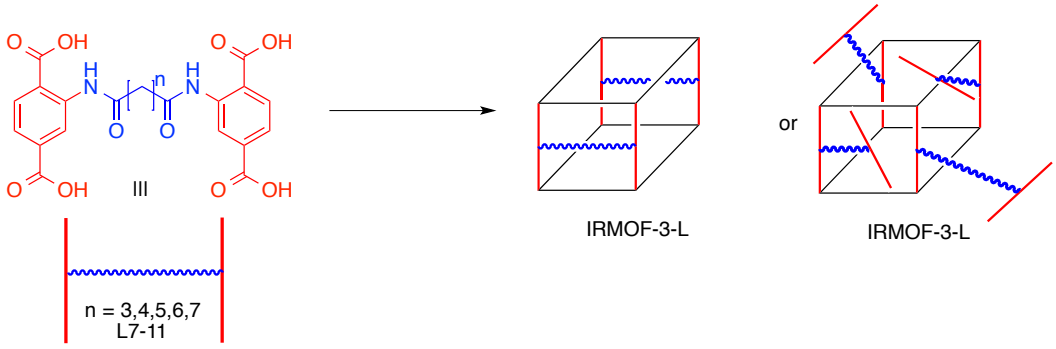

Figure 4.11. Schematic representation of both bdc portions being structurally incorporated (MOF left) in comparison to only a single side being incorporated (MOF right). Indirect characterization methods (BET and EA) indicate both ends are incorporated.

Table 4.1. Elemental Analysis of activated (at 105 °C, unless noted) IRMOF-3-L*n* materials calculated with both BDC ends structurally incorporated into the MOF.

n[a]	Molecular Formula	Wt% Calc	Wt% Exp	Difference
7	$Zn_4O(C_{21}H_{14}N_2O_{10})_{3/2}$	952.81		
	C	39.67%	39.72%	-0.05%
	H	2.22%	3.20%	-0.98%
	N	4.40%	5.34%	-0.94%
8	$Zn_4O(C_{22}H_{16}N_2O_{10})_{3/2}$	973.83		
	C	40.66%	39.98%	0.68%
	H	2.48%	3.27%	-0.79%
	N	4.31%	5.07%	-0.76%
8 (150)	$Zn_4O(C_{22}H_{16}N_2O_{10})_{3/2}$	973.83		
	C	40.66%	39.76%	0.90%
	H	2.48%	3.18%	-0.70%
	N	4.31%	4.93%	-0.62%
9	$Zn_4O(C_{23}H_{18}N_2O_{10})_{3/2}$	994.86		
	C	41.60%	41.24%	0.36%
	H	2.73%	3.24%	-0.51%
	N	4.22%	4.81%	-0.59%
10	$Zn_4O(C_{24}H_{20}N_2O_{10})_{3/2}$	1015.88		
	C	42.52%	41.78%	0.74%
	H	2.97%	3.28%	-0.31%
	N	4.13%	4.57%	-0.44%
11	$Zn_4O(C_{25}H_{22}N_2O_{10})_{3/2}$	1036.9		
	C	43.39%	42.97%	0.42%
	H	3.20%	3.64%	-0.44%
	N	4.05%	4.50%	-0.45%

Table 4.2. Elemental Analysis of activated (at 105 °C, unless noted) IRMOF-3-L*n* materials calculated with only 1 BDC end structurally incorporated into the MOF.

n[a]	Molecular Formula	Wt% Calc	Wt% Exp	Difference
7	$Zn_4O(C_{21}H_{14}N_2O_{10})_3$	1639.95		
	C	46.09%	39.72%	6.37%
	H	2.95%	3.20%	-0.25%
	N	5.12%	5.34%	-0.22%
8	$Zn_4O(C_{22}H_{16}N_2O_{10})_3$	1682		
	C	47.08%	39.98%	7.10%
	H	3.23%	3.27%	-0.04%
	N	4.99%	5.07%	-0.08%
8 (150)	$Zn_4O(C_{22}H_{16}N_2O_{10})_3$	1682		
	C	47.08%	39.76%	7.32%
	H	3.23%	3.18%	0.05%
	N	4.99%	4.93%	0.06%
9	$Zn_4O(C_{23}H_{18}N_2O_{10})_3$	1724.05		
	C	48.02%	41.24%	6.78%
	H	3.50%	3.24%	0.26%
	N	4.87%	4.81%	0.06%
10	$Zn_4O(C_{24}H_{20}N_2O_{10})_3$	1766.09		
	C	48.92%	41.78%	7.14%
	H	3.76%	3.28%	0.48%
	N	4.75%	4.57%	0.18%
11	$Zn_4O(C_{25}H_{22}N_2O_{10})_3$	1808.14		
	C	49.77%	42.97%	6.80%
	H	4.01%	3.64%	0.37%
	N	4.64%	4.50%	0.14%

The bulk analytical methods used to characterize these new IRMOFs (e.g. TGA, BET) do not reveal the conformation of the different linkers across the pore of each IRMOF. XRD data also failed to provide assignable electron density for the linkers. Depending on length, the linkers can be arranged is several possible ways across the pore of the MOF. By examining the size of the tethers and trying to place them within the distance constraints defined by the crystal structure, it was apparent that IRMOF-3-L7 and IRMOF-3-L8 can only connect adjacent ligands ('isomer 1') and are not sufficiently long to bisect the pore of the IRMOF ('isomer 2') (Figure 4.12). However, IRMOF-3-L9, -L10, and -L11 are able to reach across the pore, and hence multiple crosslinking conformations might be possible.

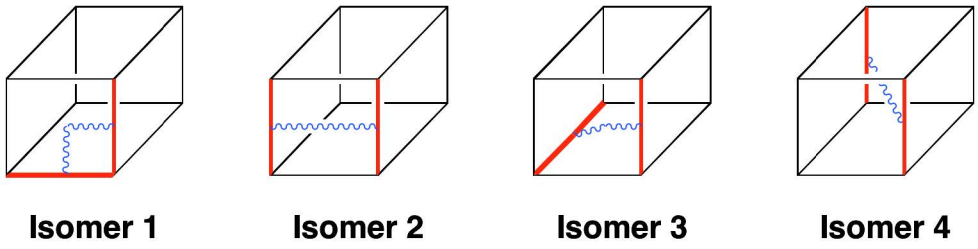

Figure 4.12. Possible linkage isomers for IRMOF-3-Ln. Curved blue lines represent the linker and bold red lines represent the crosslinked ligand. L7 and L8 can only produce isomer 1; L9 can produce isomer 1 and 2; L10 can produce to isomer 1, 2, and 3; and L11 has access to all possible isomers. These are based on bond lengths and angles of each of the ligands in addition to computational studies.

To explore which of the four isomers are possible for any given aliphatic chain, in silico modeling of the IRMOF unit cell was performed by Dr. Jordi Cirera and Prof. Franceso Paesani (UCSD). As expected, the crosslinked ligands with shorter chains can only be modeled in the isomer 1 configuration. Although both systems are stable

through the molecular dynamic (MD) simulations, small distortions of the unit cell can be observed due to the tension introduced by the crosslinking. This is particularly clear in the L7, which has the shortest aliphatic chain, thus introducing maximum tension in the framework. L9 is the first ligand that can be modeled in configurations for isomers 1 and 2. Again, MD simulations are stable in both isomers. It must be noted that the length between edges in the crystallographic IRMOF structure is approximately ~10Å, which is very similar to the maximum length that L9 can attain (~10.5Å). Thus, although possible, isomer 2 introduces a certain degree of tension between edges that can be followed during the MD simulation. L10 can be modeled in isomers 1, 2 and 3 configurations. No substantial differences are observed during the simulations. Finally, only L11 can be modeled in all four possible isomer configurations. Although the MD simulations provide insight in the possible configurations that can be obtained as a function of linker length, they cannot rule out more complex scenarios such as combinations of isomers within one lattice. The following rest of the Chapter will focus on controlling the formation of these isomers.

4. III. Exploration of Chemically Crosslinked MOFs

Above, we described a presynthetic approach to crosslinked MOFs. Experimental and computational data concluded that the NH_2-bdc tethers were structurally incorporated into the framework, but the flexibility of the linkers resulted in a random orientation of the crosslinking alkyl groups. It was proposed that at least four distinct crosslink orientations were possible for some of these alkyl bridges.[11] To mitigate the varying isomer possibilities, the ligands discussed below are geometrically preorganized to reliably form the prototypical IRMOF-1 lattice with a single linker orientation (isomer 1, Figure 4.12). More importantly, these crosslinked ligands allowed

for the rational design of oligomeric ligands that also produced the canonical IRMOF-1 structure.

The first target of this study was an alkyl linked OH-bdc (L12), which was similar to our previously reported systems,[11] but utilizes an ether, rather than an amide linker. This target ligand is an analogue to the shortest tether previously described (L7),[11] and was designed to confirm that small changes in the chemical composition of the crosslink (i.e. ether vs. amide) would be tolerated during IRMOF formation. Using the well-established Williamson ether synthesis gram quantities of L12 were readily obtained (Scheme 4.2).[12] Consistent with our earlier findings, L12 produces the desired crosslinked IRMOF as transparent blocks (IRMOF-1-L12) under standard solvothermal procedures for an IRMOF material (Figure 4.13).[13] Extrapolation from the previous computational analysis suggested that this short tether must force the bdc monomers into an adjacent, orthogonal conformation (isomer 1) based on length and geometric requirements (Figure 4.12). PXRD of IRMOF-1-L12 match that of IRMOF-1 and the connectivity and topology was unambiguously confirmed by single-crystal XRD (Figure 4.14, Table 4.6). As expected, the alkyl linker was disordered and could not be located, but was determined to be present and intact by ^{1}H NMR and ESI-MS analysis of acid digested IRMOF-1-L12. After extensive rinsing with $CHCl_3$ and heating to 150 °C under vacuum, significant amounts of DMF remained trapped in IRMOF-1-L12, similar to that observed IRMOF-3-L8 described above (Figure 4.15).[11] TGA showed a ~5% weight loss at just under 200 °C, indicative of trapped solvent, followed by decomposition of the framework at ~380 °C which is typical for IRMOFs (Figure 4.14). Activated IRMOF-1-L12 gave a BET surface areas of 1711±56 m^2g^{-1} and 1450±92 m^2g^{-1} when activated at 150 °C and 105 °C, respectfully, consistent with greater solvent trapping at a lower activation temperature (Figure 4.18). As described above,

unlinked IRMOFs will release all solvent guests under the aforementioned activation conditions.[8]

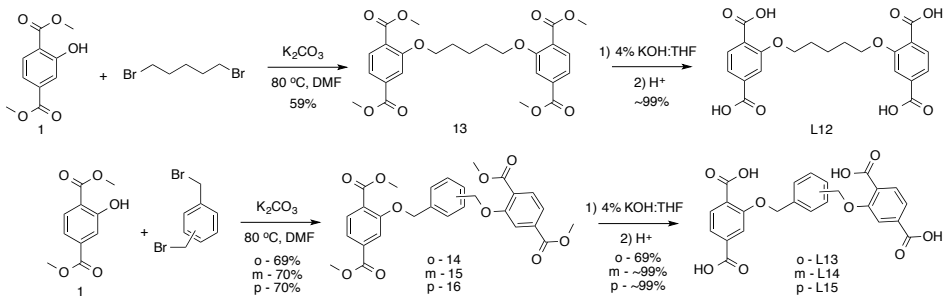

Scheme 4.2. Synthesis of crosslinked ligands L12-L15.

In an effort to control the orientation and improve the organization of the crosslinking group, ligands with more rigid tethers were designed and prepared. *Ortho*-, *meta*-, and *para*- xylene dibromides were used to prepare three new ligands (L13, L14, L15) in good yields (Scheme 4.2). Of these, the *m*-xylene derivative creates a crosslink that is roughly identical in length to L12, but with a more rigid structure.[14]

Using standard solvothermal synthetic conditions, only L14 produced the desired MOF (IRMOF-1-L14) as clear truncated blocks (Figure 4.13). These crystals displayed the expected PXRD pattern for an IRMOF (Figure 4.14). Despite numerous attempts, under a variety of solvothermal conditions, no crystalline materials were obtained using L13 or L15 (Table 4.3). Under some conditions, L13 and L15 produced white powders that were amorphous as gauged by PXRD (data not shown). To obtain the desired ligand orientation (isomer 1), the angle between the linked bdc struts would appear to be too acute with L13 and too obtuse with L15. Only L14 is capable of attaining the correct geometry to facilitate formation of the IRMOF lattice.

Furthermore, L13 and L15 are too short to allow for the formation of other crosslinked isomers and most likely too sterically encumbered to only incorporate one bdc end into an IRMOF (Figure 4.11, Figure 4.12).

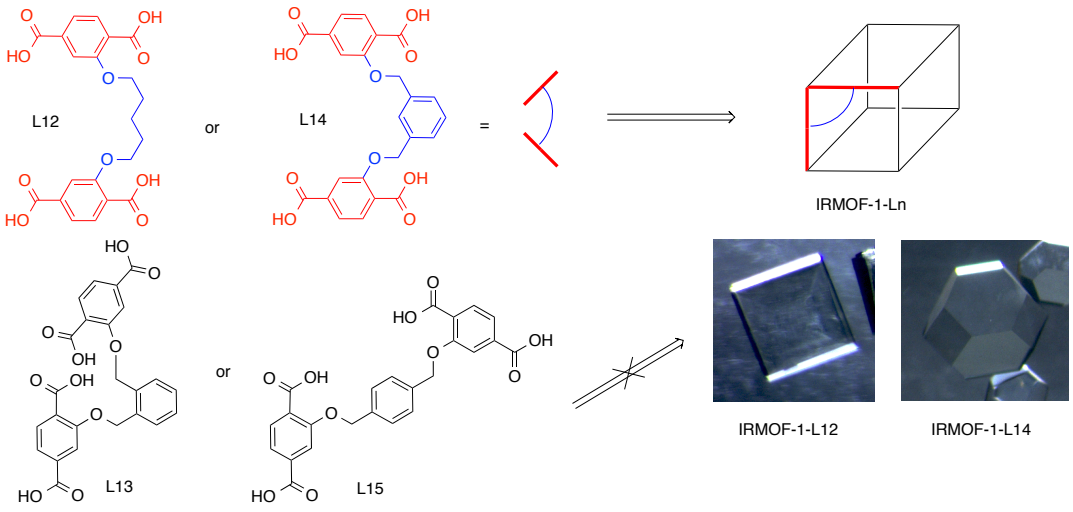

Figure 4.13. A schematic representation of L12 and L14 forcing orthogonal placement of the two bdc ends inside IRMOF that L13 and L15 cannot achieve (top). L13 and L15 in black are to indicate that both bdc units cannot be part of a single framework due to their orientation to one another. Optical microscopy photographs of the single crystalline materials are included (bottom).

.

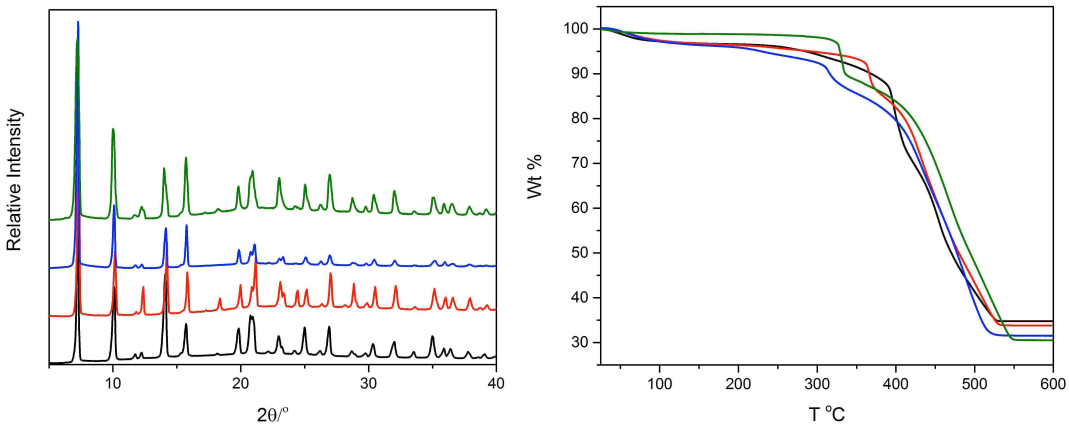

Figure 4.14. PXRD patterns for IRMOF-1-L12 (black), IRMOF-1-L14 (red), IRMOF-1-L16 (blue), and IRMOF-1-L17 (green) (left) followed by TGA traces of 105 °C activation for IRMOF-1-L12 (black), IRMOF-1-L14 (red), IRMOF-1-L16 (blue), and IRMOF-1-L17 (green) (right).

IRMOF-1-L14 gave a BET surface area of 1619±113 m^2g^{-1} after activation at 105 °C under vacuum. The ^1H NMR spectra of digested samples of IRMOF-1-L14 showed a significant amount of DMF was trapped in the material under these activation conditions (Figure 4.15). However, the DMF could be removed by heating the material at 150 °C overnight (under vacuum) giving a BET value of 2121±54 m^2g^{-1} (Figure 4.18). TGA analysis of IRMOF-1-L14 activated at 105 °C shows a 4% weight loss from 50-100 °C, but not when activated at 150 °C indicative of complete activation (Figure 4.14). Activation at either temperature results in a steep 10% weight loss at 350 °C followed by framework degradation at 360 °C. We attribute the 10% weight loss at 350 °C to degradation of the *m*-xylene linker unit. Again, the trapping of solvent in IRMOF-1-L14 at lower temperatures is suggestive of the potential gating behavior of these materials (Figure 4.15).

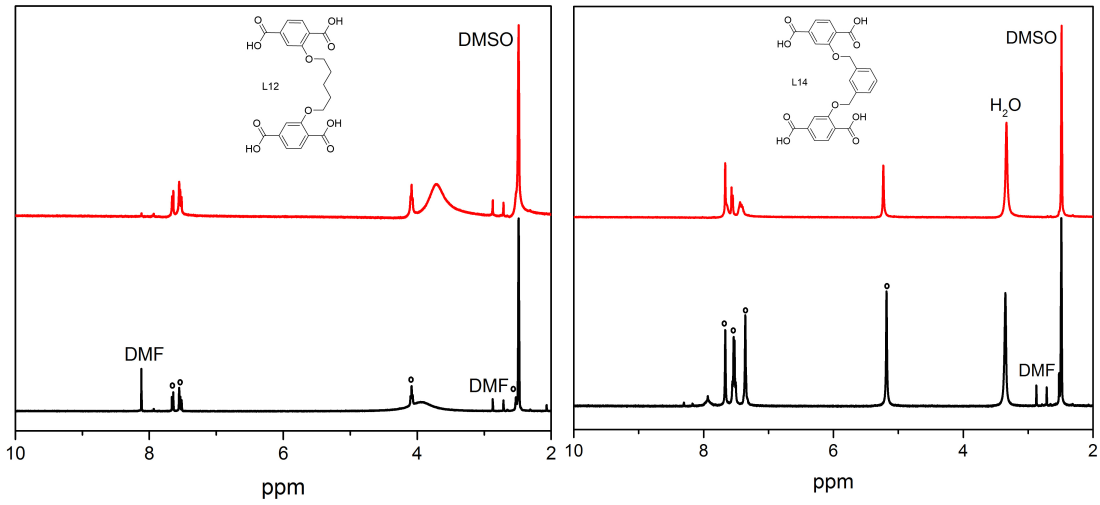

Figure 4.15. ^{1}H NMR spectra of IRMOF-1-L12 (left) and IRMOF-1-L14 (right) of the digested materials after being activated at 105 °C (black) and 150 °C (red) are shown. DMF is clearly present in both samples for IRMOF-1-L12 where it is no longer present for IRMOF-1-L14 after 150 °C. The ligand resonances are marked with black circles.

XRD structure determination of IRMOF-1-L14 verified the IRMOF topology, but also revealed that parts of the *m*-xylene crosslinker could be located in the difference map (Figure 4.16). Location of substituents by XRD data is very unusual in the highly-symmetric IRMOF system,[15] and demonstrates that the rigid crosslink is confined to a specific geometry inside the MOF pores. There is some disorder of the crosslinker, but electron density was located for the linker in the expected isomer 1 conformation, confirming our computational and design analysis (Figure 4.12). This suggests that by designing ligands that restrict the orientation of the bdc subunits, an increased level of organization and structural predictability can be engineered into the MOF topology.

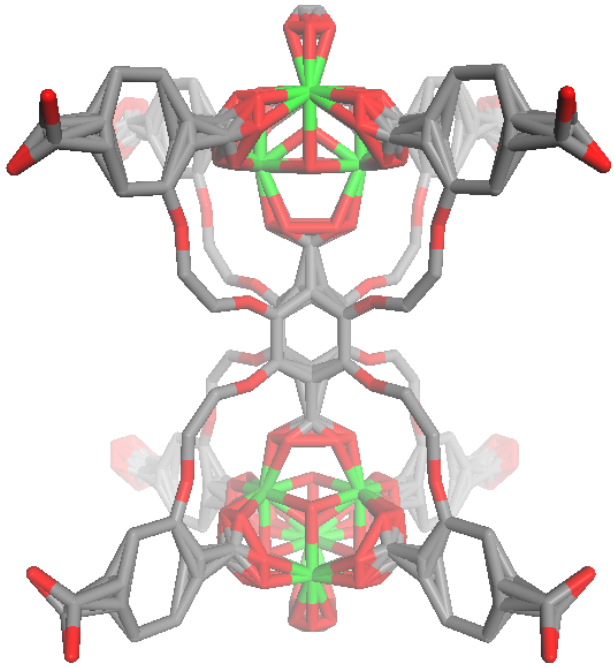

Figure 4.16. X-ray crystal structure of IRMOF-1-L14. The rigidity of the linker forces the SBU to twist slightly creating additional disorder. Additionally, the electron density for the crosslink can be seen, but not resolved, in the face of the pore. Hydrogen atoms have been omitted for clarity. Carbon atoms are in grey, oxygen is in red, and zinc is in green.

Successful incorporation of L14 into the IRMOF structure led to the expansion and evolution of L14 into ligands L16 and L17. These 'oligomeric' type ligands connect three bdc monomers via two *m*-xylene crosslinkling units. L16 and L17 are 2,3- and 2,5-substitutional isomers of one another, but both limit the bdc units to the isomer 1 orientation. These ligands were synthesized using similar procedures to L14. A Williamson ether synthesis using an excess of 1,3-dibromoxylene provided an intermediate competent for a second coupling in good yields. Coupling of the newly synthesized substituted benzyl bromide with one of two diol intermediates, followed by hydrolysis, produced L16 and L17 in reasonable yields (Scheme 4.3).

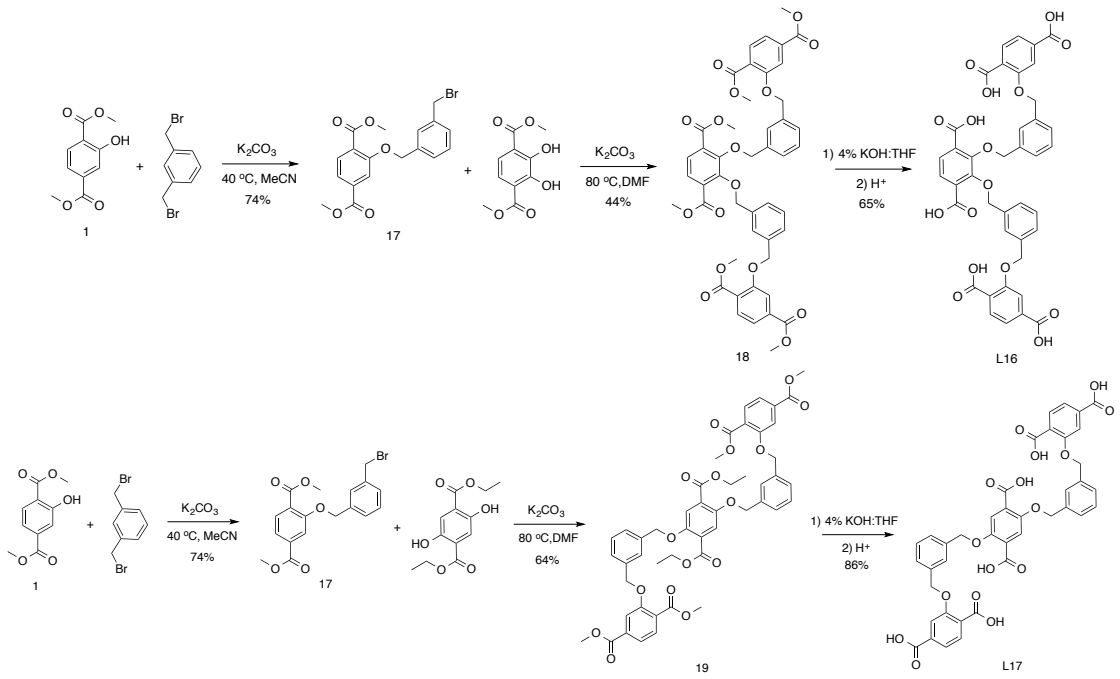

Scheme 4.3. Synthesis of oligomeric triply linked bdc L16 (top) and L17 (bottom).

The crosslinked ligands described earlier in this chapter required minimal, if any, screening efforts to form IRMOFs. While ligands L16 and L17 form IRMOF under standard solvolthermal conditions, it was found that improved crystal quality and uniformity was achieved by heating with slower temperature ramping (0.5 °C/min instead of 2.5) and the use of more equivalents of metal salt during the solvothermal synthesis. The need for slower ramping is consistent with a more demanding 'annealing' process that would be required with these oligomeric structures.

Upon combining a 1:12 ratio of L16 with $Zn(NO_3)_2{\cdot}6H_2O$ in DMF and heating to 100 °C for 24 h, yellow cubes were obtained that were suitable for single-crystal XRD (Figure 4.17). IRMOF-1-L16 displayed the expected cubic topology, as demonstrated by both the XRD structure and PXRD patterns (Figure 4.14). Unfortunately, the xylene

linker could not be located in the difference map. However, ^{1}H NMR and mass spectral analysis of digested samples confirmed that the ligand remained intact (Figure 4.19). Activation of the MOF at 105 °C (under vacuum) gave a low BET value of 650±42 m^2g^{-1}, TGA analysis indicated trapped solvent as did ^{1}H NMR analysis (Figure 4.18). By heating at 150 °C (under vacuum) the BET value was raised to 1654±89 m^2g^{-1}. The increased temperature for activation was not surprising as the orientation of the xylene units may cause interference with the removal of the solvent molecules due to the packing of the ligands within the lattice.

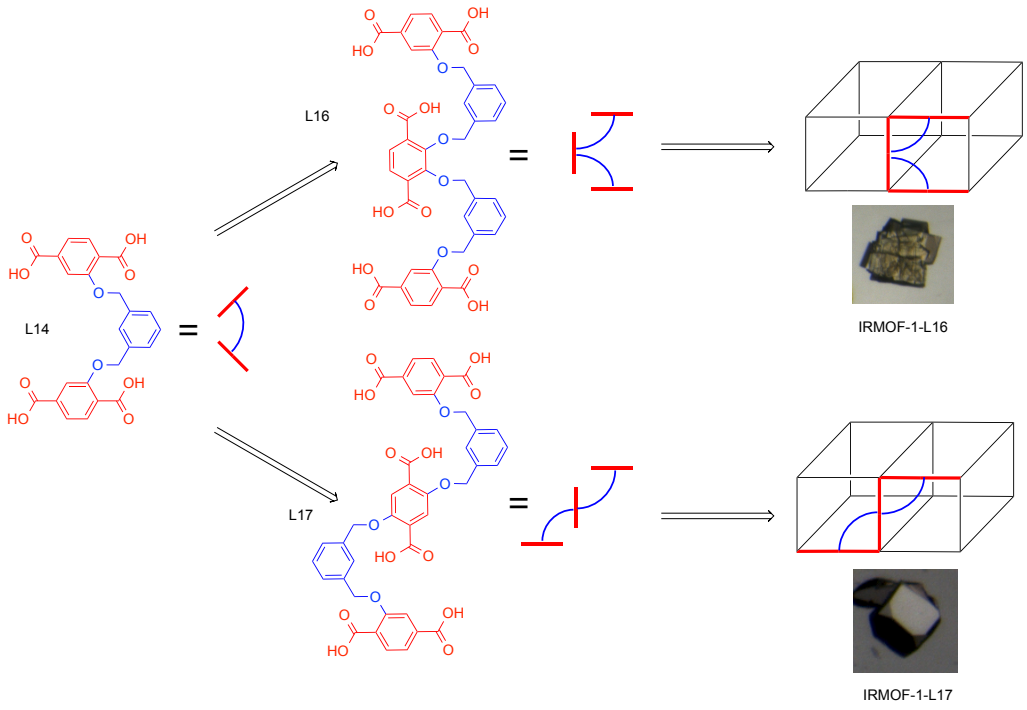

Figure 4.17. Schematic demonstrating the extension of L14 into isomeric L16 and L17 followed by how they would be incorporated into an IRMOF lattice. L16 can adhere to a 'C' configuration (top) whereas L17 must adopt a 'S' configuration (bottom). Optical microscopy photographs of the single crystalline materials are included.

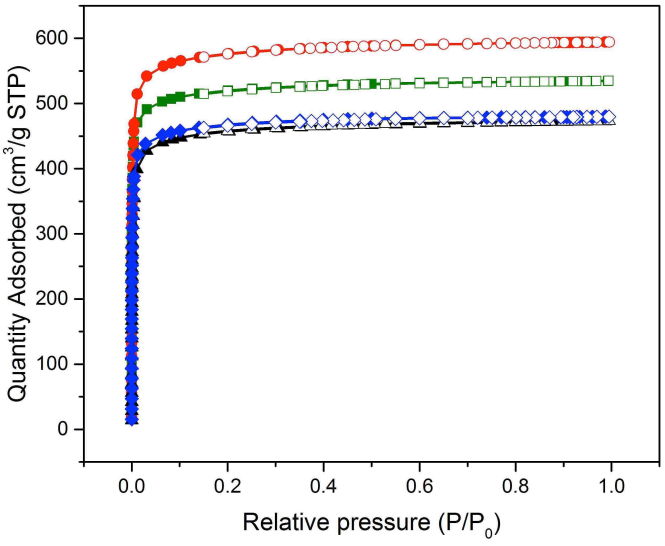

Figure 4.18. Dinitrogen adsorption isotherms for IRMOF-1-L12 (black), IRMOF-1-L14 (red), and IRMOF-1-L16 (blue) all activated at 150 °C and IRMOF-1-L17 (green) activated at 105 °C. The overlap of IRMOF-1-L12 and IRMOF-1-L16 is attributed to residual solvent trapped in IRMOF-1-L12 rendering the maximum sorption capacity similar to the triply linked IRMOF-1-L16.

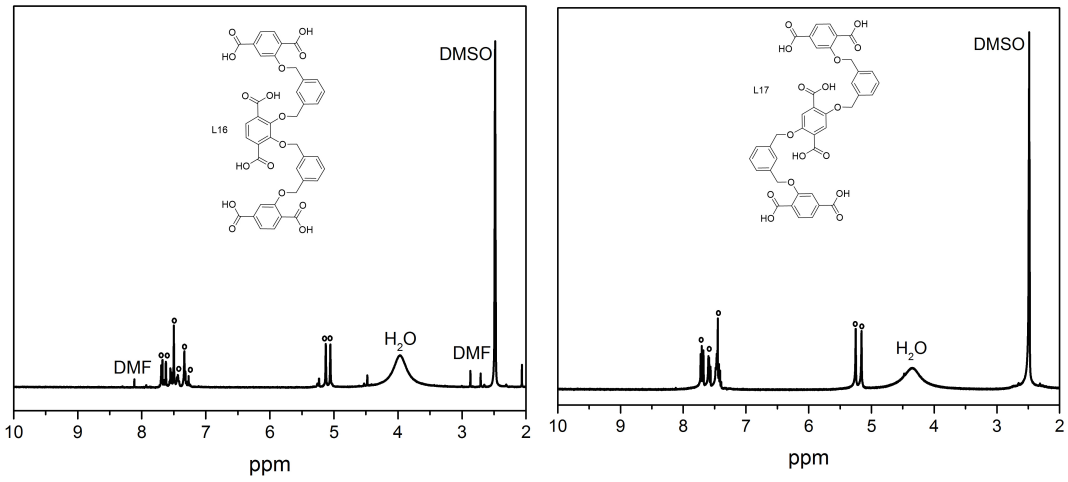

Figure 4.19. ^{1}H NMR spectra of IRMOF-1-L16 (left) and IRMOF-1-L17 (right) after activation at 105 °C is shown above. DMF is present in IRMOF-1-L16 whereas it is absent in IRMOF-1-L17. The ligand resonances are marked with black circles.

To explore how the positioning of the xylyl rings affected the MOF growth and characteristics, L17 was used in the preparation of a crosslinked IRMOF. Using a 1:10.7 L17 to zinc ratio, under slow ramping conditions (0.5 °C/min), clear blocks were obtained after 24 h at 100 °C (Figure 4.17). XRD failed to locate the xylene electron density in the difference map, but again, the IRMOF topology was verified by XRD and PXRD (Figure 4.14). Interestingly, heating at 105 °C was sufficient for complete activation of IRMOF-1-L17 as corroborated by the high BET value of 1948±34 m^2g^{-1} (Figure 4.18). TGA analysis confirmed no solvent loss at <150 °C followed by MOF degradation at around ~380 °C. ^{1}H NMR of the digested material also verified the intact ligand and no residual solvent (Figure 4.19). Even though the overall number of xylyl groups incorporated is the same as in IRMOF-1-L16, the change in orientation of the groups manifests itself in subtly different physical properties of the material, i.e. activation temperatures.

4. IV. Preliminary Results on Continuing Work

Due to the success of L16 and L17, two ligands (L18 and L19) were designed that linked four bdc units together in two distinct but complementary fashions. An extended linear 'S' shaped L18 was synthesized that allows for the necessary degrees of freedom of the bdc ligands to construct an IRMOF lattice. In this manner, all four bdc units must be orthogonal to one another in an IRMOF lattice with only two linked bdc per unit cell. Utilizing similar chemistry for previous ligands, two halves of the molecule were obtained. A final Williamson ether synthesis combined the two halves to create the esterified version that was hydrolyzed to the final L18 (Scheme 4.4).

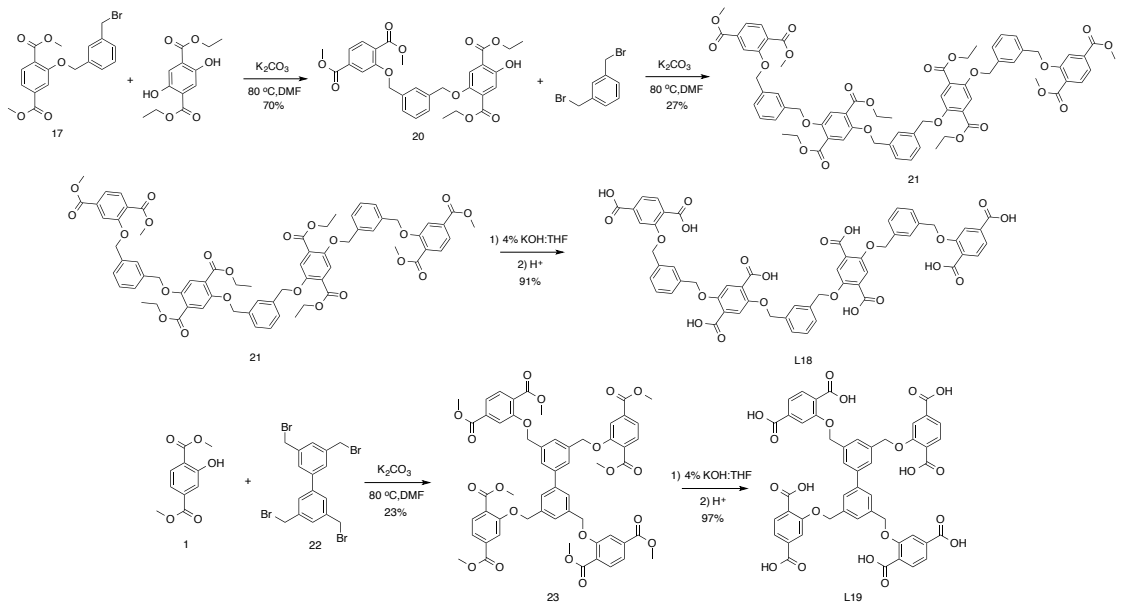

Scheme 4.4. Synthesis of isomeric tetra(bdc) ligands L18 (top) and L19 (bottom).

While L18 is a linear extension of L17, L19 takes a different approach by linking four bdc units to a single biphenyl linker. Utilization of a single Williamson ether synthesis, with 1 and 22, gave the octa(methyl ester) that could be hydrolyzed to the final L19 (Scheme 4.4). By linking two L14 molecules in the 5-position, this biphenyl crosslink should take up an entire face of the cube forcing a paneling effect within the lattice (Figure 4.20). This should dictate the overall positioning of the ligands as two edge sharing faces cannot both be paneled assuming all four bdc struts are forming the IRMOF.

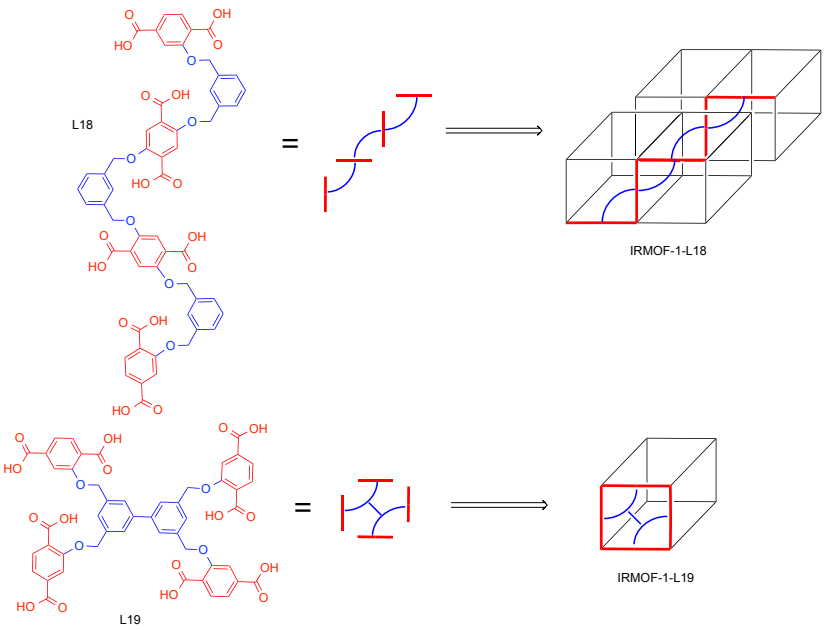

Figure 4.20. Schematic representation of how L18 and L19 would orient all the bdc tethers inside a single IRMOF lattice. L18 must adopt an elongated 'S' configuration (top) while L19 would create a paneling effect as it would occupy the entire face of a unit cell (bottom).

This level of positional design and interconnectedness of the organic struts within crystalline MOF materials is completely unique and understudied. Pending the successful incorporation of one or both ligands, the specific design and shape elements built into L18 and L19 can probe the mechanism of formation for IRMOFs. Preliminary screening with L18 and L19 produce clear cubes that have PXRD patterns similar to other IRMOFs (Figure 4.21). Additionally, preliminary BET measurements indicate that they can easily be evacuated at 105 °C and remain porous to nitrogen with BET values of 1595 and 1766 m^2g^{-1} for IRMOF-1-L18 and IRMOF-1-L19, respectively. These beginning stages, utilizing a top down approach to explore the boundaries between polymeric and crystalline porous materials, are complemented by the

incorporation of a polymeric organic ligands into a periodic and rigid framework that is also being studied.

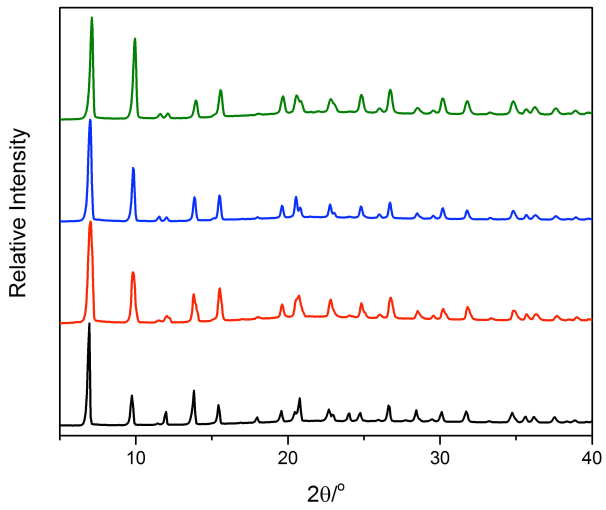

Figure 4.21. Experimental PXRD patterns of IRMOF-1-L14 (black), IRMOF-1-L16 (red), IRMOF-1-L18 (blue) and IRMOF-1-L19 (green) are shown.

The future work on this project would be to extend the linear, 2,5-dihydroxy based ligands through the addition of a single bdc unit. This way, two, three, and four, linked bdc units can be directly compared to longer five, six, seven, etc. ligands. Once the starting materials are no longer distinctly oligomeric but a blend between oligomers and polymers, then exploration of soft and hard coordination polymers based on organic polymers would begin. Additionally, this work has focused solely on IRMOF lattices because of their highly crystalline nature; development of this 'presynthetic' crosslinking approach into other MOFs would be useful to gauge the generality of our findings.

Another avenue of interest is to functionalize the crosslinking moieties. The position and orientation of the crosslink can be designed specifically to interact with

the SBU or guest molecules within the lattice. This could be a unique method to place catalytic sites or specific gas adsorption contacts directly in the pores while still leaving the struts available. In this latter example, it is known that the greater number of positive contacts embedded into your material, generally, the higher the affinity for a particular guest molecule. One method has been to create interpenetrated frameworks, where multiple nets are intertwined.[16-18] However, the porosity of these materials suffers greatly as the density of the material has at least doubled (with a 2 interpenetrated nets). Incorporating these contacts through carefully chosen crosslinking moieties would provide access to materials that are less dense than the interpenetrated lattices, but have more surface area to interact with guest molecules than without the crosslinks. To date, there has been no method to access materials with this set of characteristics.

4. V. Conclusions

In this chapter, a variety of new crosslinked ligands revealed design criteria that allowed for the formation of crosslinked IRMOF materials under standard solvothermal conditions. This seemingly benign finding has implications into the mechanism of MOF formation. Additionally, it demonstrates how little we know about the tolerance of these materials for certain type of geometric restrictions.

Simple diacylchlorides with alkyl chains of varying lengths were used to synthesize crosslinked ligands (L7-L11). In general, the properties of these MOFs are similar to the parent IRMOF-3; however, a notable difference in guest entrapment was observed with IRMOF-3-L8. The robust inclusion of DMF in this MOF suggests that the physical properties of the MOF can be substantially altered by even very small changes in tether length.

Then, L12 and L14 were designed and synthesized, as they should be capable of adhering to the restraints of a cubic lattice. Both crosslinks, pentane and *m*-xylene, accommodate a specific orientation of the two bdc units in a similar fashion to the L7-11. However, L13 and L15 that employ *o*- and *p*-xylene linkers were not able to attain the proper geometry and this was corroborated by an inability to isolate crystalline materials. The characteristics required for successful incorporation of tethered bdc molecules were used to rationally design extended, oligomeric ligands L16 and L17, each possessing six carboxylic acid units per ligand.

Lastly, more elaborate oligomeric ligands, L18 and L19, were designed from the successful incorporation of L16 and L17 into an IRMOF lattice. Both contain four individual bdc units that are linked through *m*-xylene units in two unique arrangements to probe the tolerance of this MOF to a variety of restrictions during the solvothermal synthesis. Preliminary results suggest these extended linkers can also form an IRMOF lattice, similarly to the shorter versions. These observations, combined with the ability to incorporate additional chemical functionality into the tethering group, opens up a new subclass of MOFs with even more control over the chemical and physical properties within the pores. While PSM and PSD excel in the incorporation of particular functional groups for certain applications, crosslinking can dictate where each portion of a ligand is in relation to one another due to the tethering and its affect on the crystallization process. In addition to the tools developed for modifying MOFs previously, chemical crosslinking is another complementary strategy that may enhance our control over the placement of functional groups within crystalline and porous materials thus providing an avenue of creating highly tailorable materials but also has the capacity to provide information about the mechanism of formation.

4. VI. Experimental

General. Starting materials and solvents were purchased and used without further purification from commercial suppliers (Sigma-Aldrich, Alfa Aesar, EMD, TCI, Cambridge Isotope Laboratories, Inc., and others). Chromatography was performed using a CombiFlash *R*f 200 automated system from TeledyneISCO (Lincoln, USA). ^{1}H NMR were recorded by a Varian FT-NMR spectrometer (400 MHz). Chemical shifts were quoted in ppm referenced to the appropriate solvent peak.

4. VI. i. Ligand Synthesis

General Synthesis for 8-12. Dimethyl-2-aminoterephthalate (7) (1.0 g, 4.6 mmol) was dissolved in 10 mL DMF. The dichloride (2.2 mmol) was added and stirred overnight. The DMF solvent was removed by rotary evaporation and the residue was washed with acetone, filtered, and dried overnight to obtain the protected ligand as a white powder. Running the reaction on a larger scale often resulted in lower yields; however, multiple batches of the protected ligand could be combined into single hydrolysis reactions to produce large quantities of the desired ligands.

General Hydrolysis to L7-L11. The tetra ester (8-12) was dissolved in THF (varying amounts depending on the scale of the reaction) and an equal volume of 4% $KOH_{(aq)}$. This was stirred for 1 h, the aqueous layer was collected and acidified to pH ~2 with 1 M HCl. A white precipitate formed, which was washed with water, filtered, and dried at room temperature under vacuum overnight.

8. Yield: 630 mg (57%). ^{1}H NMR ($CDCl_3$, 400 MHz, 25 °C): δ 2.23 (t, 2H; C*H*$_2$), 2.62 (t, 4H; C*H*$_2$), 3.93 (d, 12H; CO_2CH_3), 7.72 (d, 1H; Ar*H*), 8.07 (d, 1H; Ar*H*), 9.34 (s, 1H; Ar*H*), 11.06 (s, 2H; N*H*). ESI-MS(+): *m*/z 514.84$[M+H]^+$, 531.76$[M+NH_4]^+$.

L7. Yield: 7.9 g, 15.2 mmol (99%). ^{1}H NMR (DMSO-d_6, 400 MHz, 25 °C): δ 1.95 (t, 2H; CH_2), 2.48 (t, 4H; CH_2), 7.64(d, 1H; Ar*H*), 7.99 (d, 1H; Ar*H*), 8.97 (s, 1H; Ar*H*), 11.05 (s, 2H; N*H*). ESI-MS(-): *m*/z 457.07[M-H]$^-$, 479.07[M+Na-2H]$^-$, 496.07[M+K-2H]$^-$.

9. Yield: 890 mg (78%). ^{1}H NMR ($CDCl_3$, 400 MHz, 25 °C): δ 1.88 (t, 4H; CH_2), 2.53 (t, 4H; CH_2), 3.93 (d, 12H; CO_2CH_3), 7.72 (d, 1H; Ar*H*), 8.06 (d, 1H; Ar*H*), 9.33 (s, 1H; Ar*H*), 11.05 (s, 2H; N*H*). ESI-MS(+): *m*/z 528.90[M+H]$^+$, 545.83[M+NH_4]$^+$.

L8. Yield: 8.23 g, 17.42 mmol (92%). ^{1}H NMR (DMSO-d_6, 400 MHz, 25 °C): δ 1.68 (t, 4H; CH_2), 2.44 (t, 4H; CH_2), 7.63 (d, 1H; Ar*H*), 8.01 (d, 1H; Ar*H*), 8.99 (s, 1H; Ar*H*), 11.04 (s, 2H; N*H*). ESI-MS(-): *m*/z 471.11[M-H]$^-$, 493.12[M+Na-2H]$^-$.

10. Yield: 560 mg (48%). ^{1}H NMR ($CDCl_3$, 400 MHz, 25 °C): δ 1.52 (m, 2H; CH_2), 1.84 (m, 4H; CH_2), 2.49 (t, 4H; CH_2), 3.93 (d, 12H; CO_2CH_3), 7.74 (d, 1H; Ar*H*), 8.07 (d, 1H; Ar*H*), 9.35 (s, 1H; Ar*H*), 11.03 (s, 2H; N*H*). ESI-MS(+): *m*/z 542.96[M+H]$^+$, 559.85[M+NH_4]$^+$.

L9. Yield: 7.2 g, 14.8 mmol (99%). ^{1}H NMR (DMSO-d_6, 400 MHz, 25 °C): δ 1.39 (t, 2H; CH_2), 1.66 (t, 4H; CH_2), 2.41 (t, 4H; CH_2), 7.64 (d, 1H; Ar*H*), 8.02 (d, 1H; Ar*H*), 8.01 (s, 1H; Ar*H*), 11.05 (s, 2H; N*H*). ESI-MS(-): *m*/z 485.17[M-H]$^-$, 507.17[M+Na-2H]$^-$.

11. Yield: 100 mg (9%). ^{1}H NMR ($CDCl_3$, 400 MHz, 25 °C): δ 1.46 (m, 4H; CH_2), 1.79 (t, 4H; CH_2), 2.47 (t, 4H; CH_2), 3.93 (d, 12H; CO_2CH_3), 7.73 (d, 1H; Ar*H*), 8.07 (d, 1H; Ar*H*), 9.35 (s, 1H; Ar*H*), 11.01 (s, 2H; N*H*). ESI-MS(+): *m*/z 557.01[M+H]$^+$, 573.89[M+NH_4]$^+$.

L10. Yield: 7.8 g, 15.5 mmol (95%). ^{1}H NMR (DMSO-d_6, 400 MHz, 25 °C): δ 1.37 (t, 4H; CH_2), 1.64 (t, 4H; CH_2), 2.41 (d, 4H; CH_2), 7.67 (d, 1H; Ar*H*), 8.03 (d, 1H; Ar*H*), 9.304(s, 1H; Ar*H*), 11.05 (s, 2H; N*H*). ESI-MS(-): *m*/z 499.22[M-H]$^-$, 521.15[M+Na-2H]$^-$.

12. Yield: 500 mg (41%). ^{1}H NMR ($CDCl_3$, 400 MHz, 25 °C): δ 1.42 (m, 6H; C*H*$_2$), 1.77 (t, 4H; C*H*$_2$), 2.46 (t, 4H; C*H*$_2$), 3.93 (d, 12H; CO_2CH_3), 7.73 (d, 1H; Ar*H*), 8.08 (d, 1H; Ar*H*), 9.36 (s, 1H; Ar*H*), 11.02 (s, 2H; N*H*). ESI-MS(+): *m*/z 571.04$[M+H]^+$, 587.88$[M+NH_4]^+$.

L11. Yield: 1.7 g, 3.28 mmol (90%). ^{1}H NMR (DMSO-d_6, 400 MHz, 25 °C): δ 1.31 (t, 6H; C*H*$_2$), 1.60 (t, 4H; C*H*$_2$), 2.37 (d, 4H; C*H*$_2$), 7.64 (d, 1H; Ar*H*), 8.01 (d, 1H; Ar*H*), 8.99 (s, 1H; Ar*H*), 11.04 (s, 2H; N*H*). ESI-MS(-): *m*/z 513.14$[M-H]^-$, 535.14$[M+Na-2H]^-$.

13. Compound 1 (1.6 g, 7.7 mmol) was dissolved in DMF (15 mL). 1,5-Dibromopentane (0.5 mL, 3.67 mmol) and K_2CO_3 (2.0 g, 14.7 mmol) were added to the solution and the mixture was stirred at 80 °C overnight. After cooling to room temperature, the K_2CO_3 was filtered off, and excess water was added to precipitate out a beige solid that was isolated by vacuum filtration. Yield: 1.0 g (59%). ^{1}H NMR (400 MHz, $CDCl_3$, 35 °C): δ 1.73 (m, 2H; CH_2), 1.95 (m, 4H, CH_2), 3.89 (s, 6H, CO_2CH_3), 3.93 (s, 6H, CO_2CH_3), 4.13 (t, 4H; CH_2), 7.60 (d, 4H; ArH), 7.8 (d, 2H; ArH). ESI-MS(+): *m*/z 489.23[M+H]+, 506.22[M+NH4]+, 511.19[M+Na]+.

L12. Compound 14 (0.7 g, 1.4 mmol) was dissolved in 1:1 v:v THF:4% $KOH_{(aq)}$ solution (30 mL) and stirred overnight at room temperature. The aqueous layer was collected and acidified to pH ~1 with 1M HCl. A white precipitate formed that was collected by vacuum filtration. Yield (0.61 g, ~99%). ^{1}H NMR (400 MHz, DMSO-d_6, 35 °C): δ 1.61 (m, 2H; CH_2), 1.77 (m, 4H, CH_2), 4.08 (t, 4H; CH_2), 7.52 (m, 4H; ArH), 7.65 (d, 2H; ArH). ESI-MS(-): *m*/z 431.40[M-H]-.

General Synthesis for L13-15. Compound 1 (2.0 g, 9.5 mmol) was dissolved in DMF (100 mL). The appropriate bis(bromomethyl)benzene isomer (1,2-; 1,3-; or 1,4-; 1.2 g, 4.5 mmol) and K_2CO_3 (2.5 g, 18 mmol) were added and the mixture was stirred at

80 °C overnight. After cooling to room temperature the K_2CO_3 was filtered off. Excess water was added to precipitate out a white solid that was isolated by vacuum filtration and washed with minimal acetone. The resulting intermediate was dissolved in 1:1 v:v THF:4% $KOH_{(aq)}$ solution (30 mL) and stirred overnight at room temperature. The aqueous layer was collected and acidified to pH ~1 with 1M HCl. A white precipitate formed that was collected by vacuum filtration.

14. Yield: 1.63 g (69%). ^{1}H NMR (400 MHz, $CDCl_3$, 35 °C): δ 3.85 (s, 6H; CO_2CH_3), 3.92 (s, 6H, CO_2CH_3), 5.41 (s, 4H, CH_2), 7.40 (m, 2H, ArH), 7.62 (m, 4H; ArH), 7.74 (s, 2H; ArH), 7.81 (d, 2H; ArH). ESI-MS(+): m/z 539.94[M+NH4]+, 545.13[M+Na]+.

L13. Yield: 0.9 g (69%). ^{1}H NMR (400 MHz, DMSO-d_6, 35 °C): δ 5.46 (s, 4H; CH_2), 7.38 (m, 2H; ArH), 7.56 (d, 2H; ArH), 7.68 (m, 6H; ArH). ESI-MS(-): *m/z* 465.05[M-H]-.

15. Yield: 1.65 g (70%). ^{1}H NMR (400 MHz, $CDCl_3$, 35 °C): δ 3.92 (d, 12H; CO_2CH_3), 5.25 (s, 4H, CH_2), 7.47 (m, 3H, ArH), 7.60 (s, 1H; ArH), 7.66 (s, 2H; ArH), 7.68 (s, 2H; ArH), 7.85 (d, 2H; ArH). ESI-MS(+): *m/z* 540.12[M+NH4]+, 545.23[M+Na]+.

L14. Yield: 1.0 g (~99%). ^{1}H NMR (400 MHz, DMSO-d_6, 35 °C): δ 5.26 (s, 4H; CH_2), 7.43 (m, 1H; ArH), 7.48 (m, 2H; ArH), 7.57 (d, 2H; ArH), 7.59 (s, 1H; ArH), 7.70 (m, 4H; ArH). ESI-MS(-): *m/z* 465.37[M-H]-.

16. Yield: 1.67 g (70%). ^{1}H NMR (400 MHz, $CDCl_3$, 35°C): δ 3.92 (d, 12H; CO_2CH_3), 5.24 (s, 4H, CH_2), 7.54 (s, 4H, ArH), 7.65 (d, 2H; ArH), 7.70 (s, 2H; ArH), 7.84 (d, 2H; ArH). ESI-MS(+): *m/z* 539.91[M+NH4]+, 545.98[M+Na]+.

L15. Yield: 1 g (~99%). ^{1}H NMR (400 MHz, DMSO-d_6, 35°C): δ 5.26 (s, 4H; CH_2), 7.56 (m, 6H; ArH), 7.69 (m, 4H; ArH). ESI-MS(-): *m/z* 465.20[M-H]-.

17. Compound 1 (2.9 g, 13.8 mmol) was dissolved in MeCN (150 mL). 1,3-Bis(bromomethyl)benzene (7.3 g, 27.7 mmol) and K_2CO_3 (2.3 g, 16.6 mmol) were added and the mixture was stirred at 40 °C overnight. After cooling to room temperature, the K_2CO_3 was filtered off, and the solvent removed under vacuum to reveal a beige solid. A SiO_2 column using 5% ethyl acetate (EtOAc) in hexanes as eluent was used to remove excess dibromide and eluent was changed to 100% CH_2Cl_2 to liberate the product as a white solid upon removal of solvent. Yield: 4.0 g (74%). ^{1}H NMR (400 MHz, $CDCl_3$, 35 °C): δ 3.94 (s, 6H; CO_2CH_3), 4.52 (s, 2H, CH_2), 5.22 (s, 2H, CH_2), 7.36 (m, 2H; ArH), 7.43 (d, 1H; ArH), 7.56 (s, 1H; ArH), 7.66 (m, 2H; ArH), 7.86 (d, 1H; ArH). ESI-MS(+): *m/z* 392.79[M+H]+, 409.70[M+NH4]+.

18. Compound 2 (0.52 g, 2.3 mmol)[19] was dissolved in DMF (100 mL). 17 (2.0 g, 5.1 mmol) and K_2CO_3 (1.3 g, 9.3 mmol) were added and the mixture was stirred at 80 °C overnight. After cooling to room temperature, the K_2CO_3 was filtered off, and the solvent removed under vacuum to yield a beige solid. The product was purified by trituration with acetone followed by vacuum filtration to give a white solid. Yield: 1.0 g (44%). ^{1}H NMR (400 MHz, $CDCl_3$, 35 °C): δ 3.88 (t, 16H; CO_2CH_3), 5.09 (s, 4H, CH_2), 5.14 (s, 4H, CH_2), 7.36 (s, 4H; ArH), 7.48 (s, 4H; ArH), 7.58 (s, 2H; ArH), 7.62 (s, 4H; ArH), 7.80 (d, 2H; ArH). ESI-MS(+): *m/z* 873.17[M+NH4]+, 874.18[M+Na]+, 889.10[M+K]+.

L16. Compound 18 was dissolved in 1:1 v:v THF:4% KOH(aq) solution (30 mL) and stirred overnight at room temperature. The aqueous layer was collected and acidified to pH ~1 with 1M HCl. A white precipitate formed that was collected by vacuum filtration. Yield: 0.4 g (65%). ^{1}H NMR (400 MHz, DMSO-d_6, 35 °C): δ 5.05 (s, 4H; CH_2), 5.12 (s, 4H, CH_2), 7.33 (s, 4H; ArH), 7.43 (d, 2H; ArH), 7.48 (t, 4H; ArH), 7.50 (d, 2H;

ArH), 7.62 (s, 2H; ArH), 7.68 (d, 2H; ArH). ESI-MS(-): *m*/z 765.21[M-H]-, 787.10[M+Na-2H]-, 803.11[M+K-2H]-, 809.10[M+2Na-3H]-.

19. Diethyl-2,5-dihydroxyterephthalate (0.44 g, 1.7 mmol) was dissolved in DMF (100 mL). Compound 17 (1.5 g, 3.8 mmol) and K_2CO_3 (0.96 g, 6.9 mmol) were added and the mixture was stirred at 80 °C overnight. After cooling to room temperature, the K_2CO_3 was filtered off, and the solvent removed under vacuum to reveal a beige solid. The product was purified by trituration with acetone followed by vacuum filtration to give a white solid. Yield: 1.1 g (64%). ^{1}H NMR (400 MHz, $CDCl_3$, 35 °C): δ 1.31 (t, 6H; CH_2CH_3), 3.9 (d, 12H; CO_2CH_3), 4.34 (q, 4H; CH_2CH_3), 5.16 (s, 4H, CH_2), 5.24 (s, 4H, CH_2), 7.43 (m, 2H; ArH), 7.49 (s, 6H; ArH), 7.58 (s, 2H; ArH), 7.70 (d, 2H; ArH), 7.83 (s, 2H; ArH), 7.85 (d, 2H; ArH). ESI-MS(+): *m*/z 901.22[M+Na]+.

L17. Compound 19 was dissolved in 1:1 v:v THF:4% KOH(aq) solution (30 mL) and stirred overnight at room temperature. The aqueous layer was collected and acidified to pH ~1 with 1M HCl. A white precipitate formed that was collected by vacuum filtration. Yield: 1.6 g (86%). ^{1}H NMR (400 MHz, DMSO-d_6, 35 °C): δ 5.15 (s, 4H; CH_2), 5.24 (s, 4H, CH_2), 7.44 (m, 8H; ArH), 7.56 (m, 4H; ArH), 7.69 (m, 4H; ArH). ESI-MS(-): *m*/z 765.16[M-H]-, 787.09[M+Na-2H]-, 803.09[M+K-2H]-, 809.17[M+2Na-3H]-.

20. Diethyl-2,5-dihydroxyterephthalate (4.85 g, 19 mmol) and K_2CO_3 (1.2 g, 9.15 mmol) was dissolved in DMF (100 mL) at 60 °C. Compound 17 (3 g, 7.6 mmol) was dissolved in DMF (100 mL) and dripped into the above reaction. Upon disappearance of the broom via TLC, the reaction was cooled to room temperature, the K_2CO_3 was filtered off, and the solvent removed under vacuum to reveal a beige solid. A SiO_2 column, using 15-25% ethyl acetate (EtOAc) in hexanes as eluent, was used to liberate the product as a white solid upon removal of solvent. Yield: 2.99 g (70%). ^{1}H NMR (400

MHz, $CDCl_3$, 35 °C): δ 1.32 (t, 3H; CH_2CH_3), 1.42 (t, 3H; CH_2CH_3), 3.91 (d, 6H; CO_2CH_3), 4.34 (q, 2H; CH_2CH_3), 4.41 (q, 2H; CH_2CH_3), 5.13 (s, 2H, CH_2), 5.24 (s, 2H, CH_2), 7.36 (s, 1H; ArH), 7.44 (m, 4H; ArH), 7.58 (s, 1H; ArH), 7.68 (m, 2H; ArH), 7.86 (d, 1H; ArH), 10.4 (s, 1H; OH). ESI-MS(+): m/z 589.21[M+Na]+.

21. Compound 20 (2 g, 3.53 mmol), 1,3-bis(bromomethyl)benzene (0.42 g, 1.6 mmol) and K_2CO_3 (0.55 g, 4.0 mmol) were dissolved in DMF (150 mL) and stirred at 85 °C. Upon disappearance of 21 via TLC, the reaction was cooled to room temperature, the K_2CO_3 was filtered off, and the solvent removed under vacuum to reveal a beige solid. A SiO_2 column using 35-65% EtOAc in hexanes as eluent was used to liberate the product as a white solid upon removal of solvent. Yield: 0.21 g (27%). ^{1}H NMR (400 MHz, $CDCl_3$, 35 °C): δ 1.26 (t, 12H; CH_2CH_3), 3.9 (d, 12H; CO_2CH_3), 4.34 (q, 8H; CH_2CH_3), 5.16 (s, 8H, CH_2), 5.24 (s, 4H, CH_2), 7.43 (m, 2H; ArH), 7.50 (d, 10H; ArH), 7.58 (d, 4H; ArH), 7.67 (m, 4H; ArH), 7.86 (d, 2H; ArH).

L18. Compound 21 (1.7 g, 1.3 mmol) was dissolved in 1:1 v:v THF:4% $KOH_{(aq)}$ solution (130 mL) and stirred overnight at room temperature. The aqueous layer was collected and acidified to pH ~1 with 1M HCl. A white precipitate formed that was collected by vacuum filtration. Yield: 1.2 g (91%). ^{1}H NMR (400 MHz, DMSO-d_6, 35 °C): δ 5.16 (s, 8H; CH_2), 5.25 (s, 4H, CH_2), 7.45 (m, 13H; ArH), 7.56 (t, 5H; ArH), 7.70 (t, 4H; ArH). ESI-MS(-): *m/z* 1065.32[M-H]-, 1087.24[M+Na-2H]-, 1103.24[M+2Na-3H]-, 1125.27[M+Na+K-3H]-.

23. Compound 22[20] (1.13 g, 2.16 mmol), 1 (2.0 g, 9.71 mmol)) and K_2CO_3 (1.8 g, 12.95 mmol) were dissolved in DMF (150 mL) and was stirred at 80 °C overnight. After cooling to room temperature, the K_2CO_3 was filtered off, and the solvent removed under vacuum to yield a beige solid. The product was purified by column

chromatography eluting in 35-60% EtOAc in hexanes. Yield: 0.48 g (23%). ^{1}H NMR (400 MHz, $CDCl_3$, 35 °C): δ 3.84 (s, 12H; CO_2CH_3), 3.91 (s, 12H; CO_2CH_3), 5.33 (s, 8H; CH_2), 7.66 (m, 6H; ArH), 7.75 (s, 4H; ArH), 7.89 (m, 8H; ArH). ESI-MS(+): m/z 1065.28[M+Na]+.

L19. Compound 25 (0.50 g, 0.48 mmol) was dissolved in 1:1 v:v THF:4% KOH(aq) solution (130 mL) and stirred overnight at room temperature. The aqueous layer was collected and acidified to pH ~1 with 1M HCl. A white precipitate formed that was collected by vacuum filtration. Yield: 0.43 g (97%). ^{1}H NMR (400 MHz, DMSO-d_6, 35 °C): δ 5.34 (s, 8H; CH_2), 7.60 (d, 4H; ArH), 7.70 (m, 10H; ArH), 7.88 (s, 4H; ArH). ESI-MS(-): *m/z* 464.39[M-2H]2-, 929.31[M-H]-, 951.26[M+Na-2H]-.

4. VI. ii. MOF Synthesis

IRMOF-3-L7. L7 (1.88 g, 4.1 mmol) and $Zn(NO_3)_2{\cdot}6H_2O$ (6.84 g, 23 mmol) were dissolved in DMF (200 mL). These were separated into 20 scintillation vials (10 mL/ea) and heated in a sand bath inside a temperature-controlled oven at 2.5 °C/min from 35 °C to 100 °C, held at 100 °C for 18 h, and then cooled to room temperature at 2.5 °C/min. The resulting colorless, block crystals were washed with DMF (3×10 mL) and $CHCl_3$ (10 mL). The $CHCl_3$ was exchanged once a day for three full days of washing. Yield: 101 mg (78%).

IRMOF-3-L8. L8 (1.93 g, 4.1 mmol) and $Zn(NO_3)_2{\cdot}6H_2O$ (6.84 g, 23 mmol) were dissolved in DMF (200 mL). These were separated into 20 scintillation vials (10 mL) and heated in a sand bath to 100 °C at 2.5 °C/min, left for 18 h, and cooled to room temperature at 2.5 °C/min. The colorless, block crystals were washed with DMF (3×10 mL) and $CHCl_3$ (10 mL). The $CHCl_3$ was exchanged once a day for a total of three days of soaking. Yield: 60 mg (46%).

IRMOF-3-L9. L9 (0.5 g, 1.03 mmol) and $Zn(NO_3)_2{\cdot}6H_2O$ (1.7 g, 5.74 mmol) were dissolved in DMF (50 mL). These were separated into 5 scintillation vials (10 mL) and heated in a sand bath to 100 °C at 2.5 °C/min, left for 48 h, and cooled to room temperature at 2.5 °C/min. The colorless, semi-opaque crystals were washed with DMF (3×10 mL) and $CHCl_3$ (10 mL). The $CHCl_3$ was exchanged once a day for a total of three days of soaking. Yield: 101 mg (75%).

IRMOF-3-L10. L10 (0.51 g, 1.03 mmol) and $Zn(NO_3)_2{\cdot}6H_2O$ (1.7 g, 5.74 mmol) were dissolved in DMF (50 mL). These were separated into 5 scintillation vials (10 mL) and heated in a sand bath to 100 °C at 2.5 °C/min, left for 48 h, and cooled to room temperature at 2.5 °C/min. The beige, block crystals were washed with DMF (3×10 mL) and $CHCl_3$ (10 mL). The $CHCl_3$ was exchanged once a day for a total of three days of soaking. Yield: 99 mg (72%).

IRMOF-3-L11. L11 (0.1 g, 0.2 mmol) and $Zn(NO_3)_2{\cdot}6H_2O$ (0.34 g, 1.15 mmol) were dissolved in DMF (10 mL) in a scintillation vial. This was heated in a sand bath to 100 °C at 2.5 °C/min, left for 48 h, and cooled to room temperature at 2.5 °C/min. The beige, block crystals were washed with DMF (3×10 mL) and $CHCl_3$ (10 mL). The $CHCl_3$ was exchanged once a day for a total of three days of soaking. Yield: 73 mg (52%).

IRMOF-1-L12, IRMOF-1-L14. $Zn(NO_3)_2{\cdot}6H_2O$ (0.342 g, 1.15 mmol) and a crosslinked ligand (L12, L14, 0.2 mmol) were dissolved in DMF (5 mL) in a scintillation vial (20 mL). The vial was placed in a sand bath that was placed in a programmable oven. The temperature was raised from room temperature to 100 °C at 2.5 °C/min, held for 24 h, and cooled at 2.5 °C/min to room temperature. Clear blocks (L12) or truncated cubes (L14) were formed. Once the vial cooled to room temperature, the mother liquor was decanted and the crystals were washed with DMF (3×10 mL), rinsed

with $CHCl_3$ (2×10 mL), and left to soak for 3 d with fresh $CHCl_3$ added every 24 h. The crystals were stored in $CHCl_3$ until needed. Yield: IRMOF-1-L12 186 mg (>100% due to trapped solvent, FW 920.04 g/mol for $Zn_4OL12_{1.5}$). IRMOF-1-L14 147 mg (76%, FW 971.07 g/mol for $Zn_4OL14_{1.5}$). Under the same reaction conditions, and a variety of others (Table 4.3) L13 gave no crystals or precipitate and L15 gave only an amorphous powder.

Table 4.3. Synthesis attempts for IRMOF-1-L13 and IRMOF-1-L15.

Ligand (mmol)	$Zn(NO_3)_2$•$6H_2O$ (mmol)	Solvent (5 mL)	Temp (°C)	Incubation (h)	Ramping (°C/min)
L13 (0.2)	1.15	DMF	100	24	2.5
L13 (0.2)	1.15	DEF	100	24	2.5
L13 (0.2)	1.15	DMF	100	48	2.5
L13 (0.2)	1.15	DEF	100	48	2.5
L13 (0.2)	1.15	DMF	120	24	2.5
L13 (0.2)	1.15	DEF	120	24	2.5
L13 (0.2)	1.15	DMF	120	48	2.5
L13 (0.2)	1.15	DEF	120	48	2.5
L15 (0.2)	1.15	DMF	100	24	2.5
L15 (0.2)	1.15	DEF	100	24	2.5
L15 (0.2)	1.15	DMF	100	48	2.5
L15 (0.2)	1.15	DEF	100	48	2.5
L15 (0.2)	1.15	DMF	120	24	2.5
L15 (0.2)	1.15	DEF	120	24	2.5
L15 (0.2)	1.15	DMF	120	48	2.5
L15 (0.2)	1.15	DEF	120	48	2.5

IRMOF-1-L16. $Zn(NO_3)_2{\cdot}6H_2O$ (0.29 g, 0.97 mmol) and L16 (0.063 g, 0.08 mmol) were dissolved in DMF (5 mL) in a scintillation vial (20 mL). The vial was placed in a sand bath that was placed in a programmable oven. The temperature was raised from room temperature to 100 °C at 0.5 °C/min, held for 24 h, and cooled at 0.5 °C/min to room temperature. The product formed as transparent yellow blocks. Yield: 22 mg (22%, FW 1038.13 g/mol for Zn_4OL16).

IRMOF-1-L17. $Zn(NO_3)_2 \cdot 6H_2O$ (0.257 g, 0.86 mmol) and L17 (0.063 g, 0.08 mmol) were dissolved in 5 mL DMF in a scintillation vial (20 mL). The vial was placed in a sand bath that was placed in a programmable oven. The temperature was raised from room temperature to 100 °C at 0.5 °C/min, held for 24 h, and cooled at 0.5 °C/min to room temperature. The product formed as clear blocks. Yield: 55 mg (53%, FW 1038.13 g/mol for Zn_4OL17).

IRMOF-1-L18. $Zn(NO_3)_2 \cdot 6H_2O$ (0.031 g, 0.10 mmol) and L18 (0.034 g, 0.032 mmol) were dissolved in 5 mL DEF in a scintillation vial (20 mL). The vial was placed in a sand bath that was placed in a programmable oven. The temperature was raised from room temperature to 100 °C at 0.5 °C/min, held for 48 h, and cooled at 0.5 °C/min to room temperature. The product formed as clear blocks. Yield: 29 mg (84%, FW 1073.13 g/mol for $Zn_4OL18_{3/4}$).

IRMOF-1-L19. $Zn(NO_3)_2 \cdot 6H_2O$ (0.342 g, 1.15 mmol) and L19 (0.094 g, 0.101 mmol) were dissolved in 5 mL DMF in a scintillation vial (20 mL). The vial was placed in a sand bath that was placed in a programmable oven. The temperature was raised from room temperature to 100 °C at 0.5 °C/min, held for 48 h, and cooled at 0.5 °C/min to room temperature. The product formed as clear blocks. Yield: 96 mg (98%, FW 1038.13 g/mol for $Zn_4OL19_{3/4}$).

4. VI. iii. MOF Characterization

BET Surface Area Analysis. ~60-100 mg of MOF (stored in $CHCl_3$) was evacuated on a vacuum line for <1 min at room temperature. The sample was transferred to a preweighed sample tube and degassed at 105 or 150 °C (depending on chain length, see main text) for a minimum of 12 h or until the outgas rate was < 5 μmHg. The sample tube was re-weighed to obtain a consistent sample mass. BET

surface area (m^2g^{-1}) measurements were collected on at least three independent samples of each MOF at 77 K using dinitrogen and the volumetric technique.

BET Surface Area Analysis. ~35-60 mg of IRMOF (previously soaking in $CHCl_3$) was evacuated on a vacuum line for ~1 min at room temperature. The sample was then transferred to a preweighed sample tube and degassed at 105-150 °C on an Micromeritics ASAP 2020 Adsorption Analyzer for a minimum of 12 h or until the outgas rate was <5 μmHg. The sample tube was re-weighed to obtain a consistent mass for the degassed sample. BET surface area (m^2g^{-1}) measurements were collected on three independent samples, unless residual solvent was still present, of each MOF at 77 K with dinitrogen on an Micromeritics ASAP 2020 Adsorption Analyzer using the volumetric technique.

Digestion and ^1H NMR Analysis. ~5 mg of MOF was used immediately following BET analysis and digested in 500 μL of DMSO-d_6 and 100 μL of dilute DCl (23 μL of 35% DCl in D_2O diluted with 1.0 mL of DMSO-d_6) prior to ^1H NMR analysis.

Analysis by ESI-MS. ESI-MS was performed using a ThermoFinnigan LCQ-DECA mass spectrometer and the data was analyzed using the Xcalibur software suite. Samples for ESI-MS analysis were prepared by diluting 10 μL of digested ^1H NMR solution in 1 mL of MeOH.

Thermal Analysis. ~10-15 mg of IRMOF (dried after gas sorption analysis) was used for TGA measurements. Samples were analyzed under a stream of dinitrogen (10 ml/min) using a TA Instrument Q600 SDT running from room temperature to 600 °C with a scan rate of 5 °C/min.

PXRD Analysis. ~15 mg of IRMOF (soaked in DMF) was air dried (~10 min) before PXRD analysis. Powder X-ray diffraction (PXRD) data were collected at ambient temperature on a Bruker D8 Advance diffractometer using a LynxEye detector at 40 kV, 40 mA for Cu Kα (λ = 1.5418 Å), with a scan speed of 1 sec/step, a step size of 0.02 in 2θ and a 2θ range of 5-40°.

Single Crystal X-ray Diffraction. Single crystals of IRMOF-1/3-Ln were mounted on nylon loops with Paratone oil and placed under a nitrogen cold stream (200-250 K). Increased temperature notably improved the diffraction of the crystals as has been seen previously.[21] The resolution of the diffraction is approximately 1.1 Å and the data was collected up to 0.95 Å. All structures were assigned in *Fm*-3*m* by SHELXTL however for L9/10, a solution for the data could not be determined until solved in *F*-43*m*. A semiempirical method utilizing equivalents was employed to correct for absorption. All data collections were solved and refined using SHELXTL and treated with the "SQUEEZE" protocol in PLATON to account for electron density associated with the alkyl linkers and disordered solvent molecules (e.g. DMF, $CHCl_3$) within the framework.

4. VI. iv. Computational Details

Computational Details. All molecular dynamics simulations were performed with DL_POLY2[22] on an IRMOF-1[23] structure consisting of 27 unit cells with periodic boundary conditions. We have used the MM3 force field[24,25] specifically parameterized for IRMOF-1 by Schmid and co-workers,[26,27] adding the missing term for the linkers from the original MM3 force field. Partial charges for the crosslinked ligands were fitted to the calculated electrostatic potential using the CHELPG scheme[28] after a full optimization of the ligand using the B3LYP[29] functional with the triple-ζ basis set[30] from Ahlrichs and co-workers on all atoms, using the Gaussian09 code.[31] The short-

range interactions were truncated at an atom-atom distance of 9.0Å. The isoreticular MOFs were modeled from the crystallographic data on IRMOF-1, modifying a pair of bdc ligands to become bounded via the amide based linkers. The different isomers were generated in silico, and allowed to relax during a molecular dynamics simulation of 100ps in the canonical (NVT) ensemble. After the relaxation, 500ps were run in the constant stress and constant temperature (NσT) ensemble, at 77 K and 1 atm. Temperature and pressure were maintained using a Hoover thermostat with relaxation times of 1ps for both temperature and pressure. The equations of motion were propagated with a time step of 1fs.

4. VII. Appendix

Table 4.4. Crystallographic data tables for IRMOF-3-(L7-9).

Identification code	IRMOF-3-L7	IRMOF-3-L8	IRMOF-3-L9
Empirical formula	$C_{31.5}$ $H_{25.6}$ N_3 O_{16} Zn_4	C_{33} O_{16} Zn_4 H_{27} N_3	$C_{34.5}$ H_{30} N_3 O_{16} Zn_4
Formula weight	766.79	759.72	763.77
Temperature	200(2) K	250(2) K	250(2) K
Wavelength	1.54178 Å	0.71073 Å	1.54178 Å
Crystal system	Cubic	Cubic	Cubic
Space group	*Fm*-3*m*	*Fm*-3*m*	*F*-43*m*
Unit cell dimensions	$a = b = c =$ 25.5827(7) Å $\alpha = \beta = \gamma = 90°$	$a = b = c =$ 25.543(2) Å $\alpha = \beta = \gamma = 90°$	$a = b = c =$ 25.6341(6) Å $\alpha = \beta = \gamma = 90°$
Volume	16743.2(8) $Å^3$	16666(3) $Å^3$	16844.3(7) $Å^3$
Z	8	8	8
Density (calculated)	0.608 Mg/m^3	0.604 Mg/m^3	0.602 Mg/m^3
Absorption coefficient	1.494 mm-1	1.159 mm^{-1}	1.485 mm^{-1}
F(000)	3016	2944	2992
Crystal size (mm^3)	0.20 x 0.15 x 0.15	0.10 x 0.10 x 0.05	0.08 x 0.05 x 0.05
Theta range	2.99 to 46.06°.	3.19 to 19.72°.	2.99 to 68.33°.
Reflections collected	374	2430	8625
Independent reflections	374 [*R*(int) = 0.0229]	430 [*R*(int) = 0.0326]	1489 [*R*(int) = 0.0380]
Completeness to theta = 46.06°	90.1 %	98.6 %	99.8 %
Refinement Method	Full-matrix least-squares on F^2	Full-matrix least-squares on F^2	Full-matrix least-squares on F^2
Data / restraints / parameters	374 / 2 / 25	430 / 0 / 25	1489 / 2 / 49
Goodness-of-fit on F2	1.329	1.132	1.225
Final R indices [I>2sigma(I)]	*R*1 = 0.1085, *wR*2 = 0.3319	*R*1 = 0.0900, *wR*2 = 0.2624	*R*1 = 0.0995, *wR*2 = 0.2994
R indices (all data)	*R*1 = 0.1188, *wR*2 = 0.3420	*R*1 = 0.1108, *wR*2 = 0.2908	*R*1 = 0.1087, *wR*2 = 0.3213
Largest diff. peak and hole	0.316 and -0.290 $e.Å^{-3}$	0.466 and -0.540 $e.Å^{-3}$	1.115 and -0.288 $e.Å^{-3}$

Table 4.5. Crystallographic data tables for IRMOF-3-(L10-11).

Identification code	IRMOF-3-L10	IRMOF-3-L11
Empirical formula	$C_{36}H_{33}N_3O_{16}Zn_4$	$C_{37.5}H_{36}N_3O_{16}Zn_4$
Formula weight	763.77	757.72
Temperature	250(2) K	250(2) K
Wavelength	0.71073 Å	0.71073 Å
Crystal system	Cubic	Cubic
Space group	*F*-43*m*	*Fm*-3*m*
Unit cell dimensions	$a = b = c = 25.741(3)$ Å $\alpha = \beta = \gamma = 90°$	$a = b = c = 25.654(19)$ Å $\alpha = \beta = \gamma = 90°$
Volume	17055(3) $Å^3$	16884(22) $Å^3$
Z	8	8
Density (calculated)	0.595 Mg/m^3	0.596 Mg/m^3
Absorption coefficient	1.132 mm^{-1}	1.144 mm^{-1}
F(000)	2992	2944
Crystal size	0.10 x 0.10 x 0.08 mm^3	0.40 x 0.40 x 0.20 mm^3
Theta range	1.58 to 21.68°.	2.63 to 19.70°.
Reflections collected	3726	1773
Independent reflections	1018 [*R*(int) = 0.0252]	418 [*R*(int) = 0.1061]
Completeness to theta = 21.68°	99.5 %	95.7 %
Refinement method	Full-matrix least-squares on F^2	Full-matrix least-squares on F^2
Data / restraints / parameters	1018 / 0 / 49	418 / 1 / 21
Goodness-of-fit on F^2	1.100	1.107
Final R indices [I>2sigma(I)]	*R*1 = 0.0668, *wR*2 = 0.1999	*R*1 = 0.1074, *wR*2 = 0.2889
R indices (all data)	*R*1 = 0.0769, *wR*2 = 0.2063	*R*1 = 0.1454, *wR*2 = 0.3421
Largest diff. peak and hole	0.518 and -0.753 $e.Å^{-3}$	0.718 and -0.744 $e.Å^{-3}$

Table 4.6. Crystallographic data for IRMOF-1-L12 and -L14.

Identification code	IRMOF-1-L12	IRMOF-1-L14
Empirical formula	$C_{24}O_{13}Zn_4$	$C_{34.63}O_{23}Zn_4$
Formula weight	757.72	1045.33
Temperature	100(2) K	100(2) K
Wavelength	1.54178 ≈	1.54178 ≈
Crystal system	Orthorhombic	Cubic
Space group	Fmmm	Fm-3m
Unit cell dimensions	$a = b = c$ = 25.6676(7) Å $\alpha = \beta = \gamma$ = 90°	$a = b = c$ = 25.5228(12) Å $\alpha = \beta = \gamma$ = 90°
Volume	16910.5(5) $Å^3$	16625.9(14) $Å^3$
Z	8	8
Density (calculated)	0.595 Mg/m^3	0.835 Mg/m^3
Absorption coefficient	1.479 mm^{-1}	1.697 mm^{-1}
F(000)	2944	4094
Crystal size	0.40 x 0.40 x 0.20 mm^3	0.40 x 0.40 x 0.40 mm^3
Theta range	4.87 to 67.92°.	3.00 to 68.35∞.
Reflections collected	3136	818
Independent reflections	3136 [R(int) = 0.0000]	818 [R(int) = 0.0000]
Completeness to theta = 67.92°	75.7 %	98.7 %
Refinement method	Full-matrix least-squares on F^2	Full-matrix least-squares on F^2
Data / restraints / parameters	3136 / 0 / 97	818 / 19 / 57
Goodness-of-fit on F^2	1.145	2.247
Final R indices [I>2sigma(I)]	R1 = 0.0670, wR2 = 0.2132	R1 = 0.1658, wR2 = 0.4315
R indices (all data)	R1 = 0.0714, wR2 = 0.2217	R1 = 0.1730, wR2 = 0.4678
Largest diff. peak and hole	0.753 and -0.362 e. $Å^{-3}$	2.267 and -2.307 e. $Å^{-3}$

Table 4.7. Crystallographic data for IRMOF-1-L5 and -L6.

Identification code	IRMOF-1-L5	IRMOF-1-L6
Empirical formula	$C_{24}O_{13}Zn_4$	$C_{24}O_{13}Zn_4$
Formula weight	757.72	757.72
Temperature	100(2) K	100(2) K
Wavelength	0.71073 ≈	0.71073 ≈
Crystal system	Cubic	Cubic
Space group	Fm-3m	Fm-3m
Unit cell dimensions	$a = b = c$ = 25.5553(18) Å $\alpha = \beta = \gamma$ = 90°	$a = b = c$ = 25.5193(14) Å $\alpha = \beta = \gamma$ = 90°
Volume	16689(2) Å ^{3}	16619.1(16) Å ^{3}
Z	8	8
Density (calculated)	0.603 Mg/m^3	0.606 Mg/m^3
Absorption coefficient	1.157 mm^{-1}	1.162 mm^{-1}
F(000)	2944	2944
Crystal size	0.30 x 0.10 x 0.10 mm^3	0.40 x 0.40 x 0.40 mm^3
Theta range	1.38 to 25.35°.	1.38 to 21.94°.
Reflections collected	830	567
Independent reflections	830 [R(int) = 0.0000]	567 [R(int) = 0.0000]
Completeness to theta = 67.92°	99.8 %	99.8 %
Refinement method	Full-matrix least-squares on F^2	Full-matrix least-squares on F^2
Data / restraints / parameters	830 / 0 / 25	567 / 0 / 25
Goodness-of-fit on F^2	1.015	1.162
Final R indices [I>2sigma(I)]	R1 = 0.0615, wR2 = 0.1896	R1 = 0.0742, wR2 = 0.2351
R indices (all data)	R1 = 0.0847, wR2 = 0.2001	R1 = 0.0860, wR2 = 0.2547
Largest diff. peak and hole	0.467 and -0.421 e. Å $^{-3}$	0.989 and -0.376 e. Å $^{-3}$

4. VIII. Acknowledgements

Texts, schemes, and figures in this chapter are, in part, reprints of the material in the following publications: Allen, C. A..; Cohen, S. M. Exploration of Chemically Crosslinked Metal-Organic Frameworks *Inorg. Chem.* **2014**, *53* (13), 7014-7019. Allen, C. A..; Boissonnault, J. A.; Cirera, J.; Paesani, F.; Gulland, R.; Cohen, S. M. Chemically Crosslinked Metal-Organic Frameworks *Chem. Commun.* **2013**, *49*, 3200-3202. The dissertation author was the primary researcher and author on the publications listed above. The co-authors listed also contributed to the research. Permission to reproduce these publications was granted by the American Chemical Society, copyright 2014, and The Royal Society of Chemistry, copyright 2013.

4. IX. References

(1) Kiang, Y. H.; Gardner, G. B.; Lee, S.; Xu, Z. *J. Am. Chem. Soc.* **2000**, *122*, 6871.

(2) Ishiwata, T.; Furukawa, Y.; Sugikawa, K. *J. Am. Chem. Soc.* **2013**, *135*, 5427.

(3) Ishiwata, T.; Furukawa, Y.; Sugikawa, K.; Kokado, K.; Sada, K. *J. Am. Chem. Soc.* **2013**, *135*, 5427.

(4) IV, J. J.; Kravtsov, V. C.; McManus, G. J.; Zaworotko, M. J. *J. Am. Chem. Soc.* **2007**, *129*, 10076.

(5) Schubert, U. *Chem. Soc. Rev.* **2011**, *40*, 575.

(6) Furukawa, Y.; Ishiwata, T.; Sugikawa, K.; Kokado, K.; Sada, K. *Angew. Chem., Int. Ed.* **2012**, *51*, 10566.

(7) Appel, E. A.; Del Barrio, J.; Loh, X. J.; Scherman, O. A. *Chem. Soc. Rev.* **2012**, *41*, 6195.

(8) Garibay, S. J.; Wang, Z. Q.; Tanabe, K. K.; Cohen, S. M. *Inorg. Chem.* **2009**, *48*, 7341.

(9) Tanabe, K. K.; Wang, Z. Q.; Cohen, S. M. *J. Am. Chem. Soc.* **2008**, *130*, 8508.

(10) Wang, Z.; Cohen, S. M. *J. Am. Chem. Soc.* **2009**, *131*, 16675.

(11) Allen, C. A.; Boissonnault, J. A.; Cirera, J.; Gulland, R.; Paesani, F.; Cohen, S. M. *Chem. Commun.* **2013**, *49*, 3200.

(12) Huh, S.; Jin, J.; Achard, M. F.; Hardouin, F. *Liq. Cryst.* **1998**, *25*, 285.

(13) Eddaoudi, M.; Kim, J.; Rosi, N.; Vodak, D.; Wachter, J.; O'Keeffe, M.; Yaghi, O. M. *Science* **2002**, *295*, 469.

(14) Perry, J. J.; Kravtsov, V. C.; McManus, G. J.; Zaworotko, M. J. *J. Am. Chem. Soc.* **2007**, *129*, 10076.

(15) Dau, P. V.; Polanco, L. R.; Cohen, S. M. *Dalton Trans.* **2013**, *42*, 4013.

(16) Prasad, T. K.; Suh, M. P. *Chem.--Eur. J.* **2012**, *18*, 8673.

(17) Pachfule, P.; Chen, Y.; Jiang, J.; Banerjee, R. *J. Mater. Chem.* **2011**, *21*, 17737.

(18) Getman, R. B.; Bae, Y.; Wilmer, C. E.; Snurr, R. Q. *Chem. Rev.* **2011**, *112*, 703.
(19) Tanabe, K. K.; Allen, C. A.; Cohen, S. M. *Angew. Chem., Int. Ed.* **2010**, *49*, 9730.

(20) Vogtle, F.; Hohner, G.; Weber, E. *J. Chem. Soc., Chem. Commun.* **1973**, 366.

(21) Dau, P. V.; Kim, M.; Cohen, S. M. *Chem. Sci.* **2013**, *4*, 601.

(22) Smith, W.; Forester, T. R. *J. Mol. Graphics* **1996**, *14*, 136.

(23) Li, H.; Eddaoudi, M.; O'Keeffe, M.; Yaghi, O. M. *Nature* **1999**, *402*, 276.

(24) Allinger, N. L.; Yuh, Y. H.; Lii, J. H. *J. Am. Chem. Soc.* **1989**, *111*, 8551.

(25) Lii, J. H.; Allinger, N. L. *J. Am. Chem. Soc.* **1989**, *111*, 8566.

(26) Tafipolsky, M.; Amirjalayer, S.; Schmid, R. *J. Comput. Chem.* **2007**, *28*, 1169.

(27) Amirjalayer, S.; Schmid, R. *J. Phys. Chem. C* **2012**, *116*, 15369.

(28) Breneman, C. M.; Wiberg, K. B. *J. Comput. Chem.* **1990**, *11*, 361.

(29) Becke, A. D. *J. Chem. Phys.* **1993**, *98*, 5648.

(30) Schäfer, A.; Huber, C.; Ahlrichs, R. *J. Chem. Phys.* **1994**, *100*, 5829.

(31) Gaussian, I. In *Revision A. 1*; Gaussian, Inc.: Wallingford, CT, 2009.